8-2018

Thermo-mechanical analysis of iron-chromium-aluminum (FeCrAl) alloy cladding for light water reactor fuel elements

Ryan Terrence Sweet
University of Tennessee, rsweet1@vols.utk.edu

To the Graduate Council:

I am submitting herewith a dissertation written by Ryan Terrence Sweet entitled "Thermo-mechanical analysis of iron-chromium-aluminum (FeCrAl) alloy cladding for light water reactor fuel elements." I have examined the final electronic copy of this dissertation for form and content and recommend that it be accepted in partial fulfillment of the requirements for the degree of Doctor of Philosophy, with a major in Nuclear Engineering.

Brian D. Wirth, Major Professor

We have read this dissertation and recommend its acceptance:

Jess C. Gehin, Kurt A. Terrani, William J. Weber

Accepted for the Council:

Dixie L. Thompson

Vice Provost and Dean of the Graduate School

(Original signatures are on file with official student records.)

Thermo-mechanical analysis of iron-chromium-aluminum (FeCrAl) alloy cladding for light water reactor fuel elements

A Dissertation Presented for the
Doctor of Philosophy
Degree
The University of Tennessee, Knoxville

Ryan Terrence Sweet
August 2018

ACKNOWLEDGEMENTS

I have had the privilege of working alongside many talented and hardworking individuals across several institutions throughout my graduate studies. Firstly, I would like to thank my graduate committee chair and graduate advisor, Professor Brian Wirth, whose guidance over the past five years have been invaluable to both my professional development and my approach to solving challenging problems.

This research would not have been possible without insight and efforts of my collaborators. I would like to thank my graduate committee Dr. Jess Gehin, Dr. Kurt Terrani, and Dr. Bill Weber. Dr. Nathan George, formerly at the University of Tennessee, was instrumental in delivering results from neutronics calculations used for many of these simulations. Dr. Rich Williamson at the Idaho National Laboratory was a gracious host, allowing to me to make several trips to work with the BISON team over the course of my graduate study. Dr. Joe Rashid and Dr. Wenfeng Liu at Structural Integrity Associates, Inc. provided guidance with fuel performance modeling techniques.

I would like to thank the many other graduate students and staff that I have had the privilege of sharing an office with. In particular, I would like to thank Dr. Aaron Kohnert, Dr. Nathan Capps, Dr. Dwaipayan Dasgupta, and Dr. Daniel Schappel for their advice and discussions.

I would like to thank my family and friends, whose encouragement and support helped me set and achieve my goals.

This work would not have been possible without the financial support of the U.S. Department of Energy through The Consortium for the Advanced Simulation of Light Water Reactors, the Accident Tolerant Fuels Program of the Advanced Fuels Campaign, and a Nuclear Engineering University Program Fellowship.

ABSTRACT

Alternative cladding materials have been proposed to replace the currently used zirconium (Zr)-based alloys, in order to improve the accident tolerance of light water reactor (LWR) fuel. Of these materials, there is a particular focus on iron-chromium-aluminum (FeCrAl) alloys that exhibit much slower oxidation kinetics in high-temperature steam than Zr-alloys. This behavior should decrease the energy release due to oxidation and allow the cladding to remain integral longer in the presence of high temperature steam, making accident mitigation more likely.

This dissertation documents efforts to develop fuel performance capabilities to assess the behavior of FeCrAl cladding during normal and transient reactor operating scenarios. Within this work, simulations were performed for FeCrAl cladding using constitutive models and representative reactor operating conditions implemented into the finite-element fuel performance code BISON.

Simulations were performed targeting the cladding behavior during normal operation of a boiling water reactor using boundary conditions derived from neutronics data. These simulations indicate that the fuel compliance plays a much larger role in the evolution of the cladding stress state after gap closure for the FeCrAl cladding than for Zircaloy. Individual sensitivity analyses of the fuel and cladding creep responses were then performed, which indicated the influence of compliance for each material, separately, on the stress state of the fuel cladding.

To improve calculations of the fuel expansion and compliance, an additional investigation was performed to assess the role of creep, relocation, and explicit fracture in the fuel. Fuel rods using each of these models are simulated under representative conditions and compared to test rod measurements. This analysis provides a start toward the development and incorporation of explicit fracture in fuel performance analysis.

Additionally, performance and stability under transient conditions must also be demonstrated for FeCrAl cladding. This analysis focused on modeling the integral thermo-mechanical performance of FeCrAl clad uranium dioxide fuel during transient reactor operation. Results from this simple analysis show similar bursting time and temperature between both FeCrAl and Zircaloy cladding, however, beyond cladding burst in these conditions, the superior high temperature oxidation kinetics of the FeCrAl cladding significantly reduce hydrogen gas production and provide longer fuel integrity.

Keywords: BISON, fuel performance, fuel modeling and simulation, accident tolerant fuels, FeCrAl

TABLE OF CONTENTS

LIST OF TABLES

LIST OF FIGURES

CHAPTER 1: INTRODUCTION

1.1 History of Zircaloy as Reactor Fuel Cladding

Zirconium alloy cladding has been the primary cladding material in commercial light water reactors since the Shippingport pressurized water reactor was first operated in 1957 (Clayton, 1993). The decision to use zirconium cladding for naval reactors and Shippingport was made by Admiral Rickover because it exhibits a low thermal neutron absorption cross-section, superior corrosion resistance in LWR conditions, and dimensional stability in the irradiation environment (Adamson, 2010). Since the nearly 60 years since its development, over 100 commercial nuclear reactors have been built and operated in the United States, regularly utilizing Zircaloy cladding.

In a nuclear reactor, the fuel cladding is the first barrier to the release of radionuclides to the coolant system. This cladding generally consists of a 4-meter-long tube that is about a centimeter in diameter and approximately 600 microns thick. Ensuring that the cladding tubes in the reactor remain intact for various irradiation cycles, sometimes up to 8 years, is especially important to ensuring consistent reactor operation.

As operational experience with the zirconium-based cladding has grown, operating procedures have been implemented, and coolant chemistry has been controlled, utilities have continually managed to reduce the occurrence of failed fuel rods. From the 1980's to the mid-2000's, there was a large decrease in the number of leaking fuel rods due to industry-led programs to improve fuel cycle economics and plant performance (Yang et al., 2006). Figure 1 shows the number of US LWRs that reported fuel rods with defects from the mid-2000's to present. Again, much of this improvement was supported by industry-initiatives, such as the Fuel Integrity Initiative, a response to the Institute of Nuclear Power Operations' (INPO) goal of zero fuel failures by 2010 (EPRI, 2008). Since the beginning of 2010, nearly 90% of U.S. reactors have reported defect-free fuel.

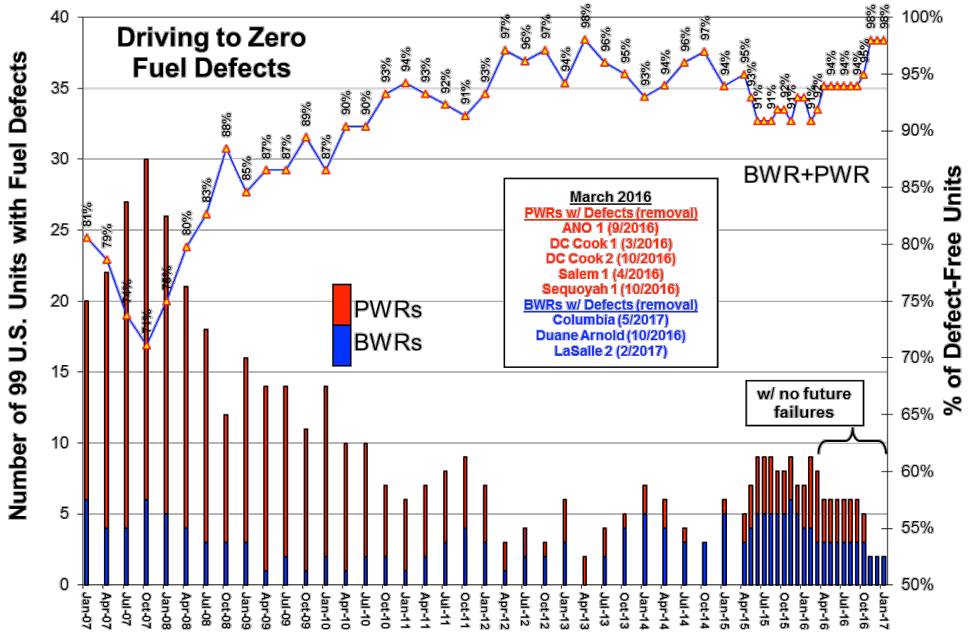

Figure 1. Number of U.S. LWRs reporting fuel defects from 2007-2017, where the blue and red bars report data from PWR versus BWR, respectively. The percentage of defect-free reactors is represented by the right axis. [Reproduced from (Mader, 2016)]

Because of the increasing reliability of zircaloy cladding and the better recognition of the reactor operating margins, the NRC is granting utilities extended power uprates, allowing reactors to operate at higher powers than they were originally licensed for (IAEA, 2011), while fuel discharge burnups continue to increase (IAEA, 2010). Benefitting from this extensive operational experience has led to an increase in the capacity factor for the US fleet of nuclear reactors to over 90% (U.S. EIA, 2018).

However, despite its superior operational history during normal reactor conditions, Zircaloy exhibits very adverse behavior when it reaches high-temperatures during beyond-design basis accidents.

1.2 Motivation for Nuclear Fuels with Enhanced Accident Tolerance

During a severe accident scenario, such as a beyond design basis loss-of-coolant-accident, the radial temperature gradient inside the fuel rod rapidly decreases to a nearly uniform temperature distribution once the fission reaction is shutdown (Terrani et al., 2014a). However, the average temperature begins to increase, quickly reaching temperatures sufficient to boil off the coolant. This reduces the coolant level in the core and eventually uncovers the fuel, also significantly reducing the heat transfer coefficient, further increasing the average fuel temperature. In the case of traditional zirconium-based alloys, when the cladding temperature reaches ~1200˚C, rapid oxidation kinetics occur (Cathcart et al., 1977; Moalem and Olander, 1991). This highly exothermic oxidation reaction

consumes and embrittles the Zr-alloy cladding while releasing large amounts of H_2 gas into the reactor vessel (Hofmann, 1998), as well as releasing significant heat which further increases fuel temperatures.

After the accident at the Fukushima Daiichi Nuclear Generating Station, the first large-scale nuclear accident in several decades, the U.S Department of Energy began a large research and development program, *the U.S. Fuel Cycle Research and Development Advanced Fuels Campaign*, tasked with identifying possible fuel-cladding systems with enhanced accident tolerance (Carmack et al., 2013), and developing them to commercialization. The operational goals for these candidate fuel systems include a reduced hydrogen generation rate, enhanced fission product retention, structural integrity in high temperature steam, and reduced fuel-cladding chemical and mechanical interaction. This work ultimately led to the identification, testing, and development of the iron-chromium-aluminum alloy cladding material.

1.3 Iron-Chromium-Aluminum Alloys as Nuclear Fuel Cladding

In order to increase the safety margin of LWR fuel in severe accident scenarios, several alternative cladding materials have been proposed (Zinkle et al., 2014). Of these materials, there is a particular focus on a class of iron-chromium-aluminum (FeCrAl) alloys because they exhibit significantly slower oxidation kinetics in high-temperature steam than zirconium-based alloys (Terrani et al., 2014b). An Arrhenius plot of the oxidation kinetics for various cladding materials are shown in Figure 2. This shows that in high-temperature steam, FeCrAl cladding will possess nearly 100× slower oxidation than zirconium alloys and type-304 stainless steels.

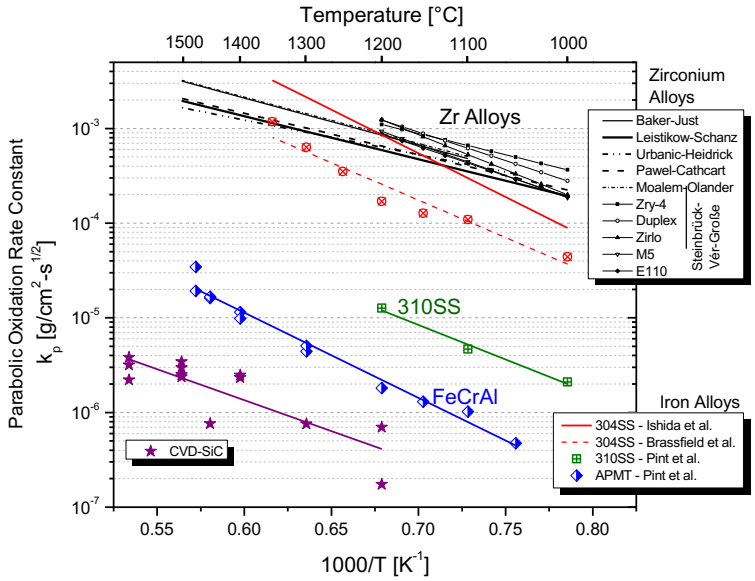

Figure 2. Parabolic oxidation rate constant for various proposed and utilized cladding materials shown here against reciprocal temperature. [reproduced from (Terrani, 2018)]

Increased oxidation resistance may give more time to mitigate any further damage resulting from an accident. For example, MELCOR simulations have indicated several hours of additional coping time for a short-term station black-out accident scenario, in which the FeCrAl cladding would delay the onset of lower head dryout to 8.5 hours from 4 hours (Ott et al., 2014; Robb, 2015). Additionally, FeCrAl cladding may also offer benefits during normal operations, recent corrosion tests have been performed demonstrating favorable oxidation behavior in LWR coolant chemistry tests (Terrani et al., 2016a).

FeCrAl alloys are much stronger than zirconium alloys, providing the option to use thinner cladding to achieve similar mechanical performance. It has been suggested that, because of its strength, stainless steel cladding may exhibit better resistance to PCMI failure than zircaloy (Strasser et al., 1982). However, as discussed later in Chapter 2, the creep behavior of FeCrAl and Zircaloy, are also very different, and this results in differences in the expected fuel rod gap closure behavior and mechanical interaction of the fuel and cladding, which will also impact the PCMI failure resistance.

By replacing the Zr-alloy fuel cladding with a FeCrAl alloy, the core neutronics will change. FeCrAl alloys have a thermal neutron cross-section nearly ~12-16 times larger than Zr-alloys. This decreases the reactivity of the core, subsequently decreasing the potential cycle length for operation (George et al., 2015b). To counteract this, increased fuel enrichment or increased fuel mass have been considered. Alternatively, because of the higher strength of FeCrAl, it is also possible to decrease the cladding thickness to reduce the neutronic penalty from using the alloy. Figure 3 (Terrani et al., 2014b) shows a contour plot of the end-of-cycle change in the reactivity for a FeCrAl cladded fuel assembly for a PWR based on a change in the cladding thickness or fuel enrichment. This shows that for a typical Zircaloy cladding thickness in a PWR, ~570μm, the reactivity would be greatly reduced by $\Delta k_{inf} > 0.03$ In order to achieve an equivalent cycle length, shown where $\Delta k_{inf} = 0$, the cladding thickness would have to be nearly half of the expected thickness for Zircaloy, or the fuel enrichment would have to be increased past 5%. This presents a challenge because many fuel fabrication facilities are currently licensed to a enrichment of 5% (Bragg-Sitton et al., 2016). For a high-Cr FeCrAl, similar to APMT, most of the thermal neutron absorption in the cladding will come from iron-56 (%66) and chromium-53 (%15) (Younker and Fratoni, 2016). Additionally, chromium-53 could be isotopically de-enriched from the cladding alloy, which would result in a slight reduction to the reactivity penalty. In this study, we have performed modeling analysis in which changes to the fuel mass, cladding thickness and fuel enrichment were considered.

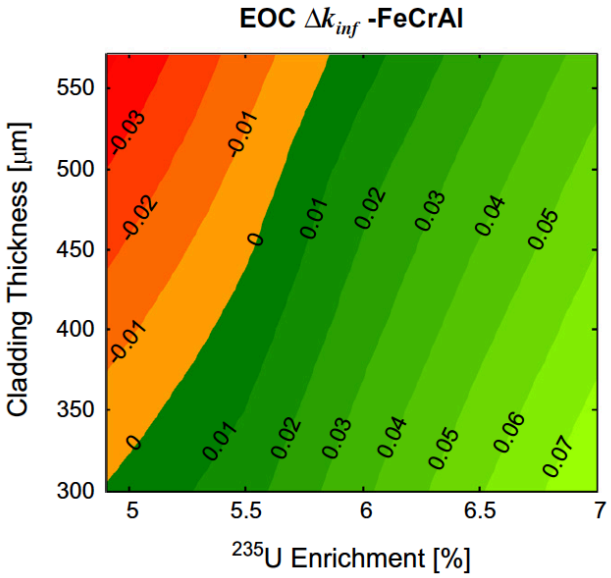

Figure 3. The change in the reactivity for a 17 x 17 PWR fuel assembly using FeCrAl compared to Zircaloy cladding at the End of Cycle (EOC) as a function of cladding thickness and fuel enrichments [Reproduced from (Terrani et al., 2014b)]

Because of its BCC crystal structure, FeCrAl alloys exhibit increased hydrogen permeation when compared to Zircaloy (Hu et al., 2015). This may lead to a concern associated with an increased concentration of tritium, formed during tertiary fission in the fuel, released into the coolant. It has been shown that while forming an alumina layer by pre-oxidation of the FeCrAl cladding may present an effective barrier to release, the alumina layer must be formed on the cladding interior, as it may dissolve in the hydrogenated water chemistry of a BWR (Rebak, 2018).

Before these alloys are considered it must be demonstrated that not only do they perform better than zircaloy in accident conditions, but that they also perform just as well under normal operation (Bragg-Sitton et al., 2016).

There is currently no commercial experience to draw from for FeCrAl alloys, however there is brief experience with stainless steels during early development of LWRs, which are expected to behave somewhat similarly.

1.4 History of Stainless Steels Used in Reactors

Various 300-series Fe-Cr-Ni based stainless steel variants (304, 316, 347, 348, etc.) have been used as nuclear fuel cladding in several early LWRs including: Connecticut Yankee, Yankee Rowe, San Onofre, and Indian Point (Strasser et al., 1982). These steels were initially used due to the high cost of Zirconium cladding, and while the performance of the stainless steel cladding improved, reactors gradually migrated away from using steel cladding due to their poor neutronic properties (Karoutas et al., 2018).

The operation of stainless steel cladding is generally thought to have been successful, at least for PWRs, despite a number of fuel failures. Namely, there were specific groups of fuel failures at the Connecticut Yankee and Sena reactors. Stainless steel cladding was operated in Yankee Rowe, San Onofre, and Indian Point with very few fuel failures (Strasser et al., 1982). Many of the problems with this cladding were eventually addressed, but not before a significant transition to zircaloy cladding had already started.

At the Connecticut Yankee reactor, increased coolant activity was observed, indicating radionuclide release from fuel rods, at the end of cycle 7. Subsequent examination was performed after cycle 8, which indicated fuel cladding failure. Although the failures were somewhat extensive (with 36 out of 48 assemblies in the cycle 8 affected), subsequent analyses indicated this was due to inconsistent fuel behavior (reduction in fuel densification and chipped fuel), and not necessarily due to the steel cladding. This ultimately led to better surveillance of fuel for defects and consistency in fuel manufacturing, and the application of power maneuvering guidelines (Pasupathi and Klingensmith, 1981).

The La Crosse BWR utilized type-348 stainless steel cladding and extensive fuel failures were reported (~71% of assemblies affected within the first five cycles), however as operation continued, performance was considerably improved (~1 failed fuel rod per cycle for the remaining two cycles) (Roberts, 2013; Strasser et al., 1982). Fuel failures from the La Crosse BWR were generally attributed to PCI and intergranular stress corrosion cracking, similar to failures from Big Rock Point, Dresden-1, and Humbolt Bay. After the implementation of power restrictions, the cladding failure rate decreased.

These examples of stainless steel cladding failure, in particular at the Connecticut Yankee PWR and the La Crosse BWR, demonstrate that the stainless-steel cladding was not necessarily the limiting factor. It should also be pointed out that these fuel rods were operated at comparatively lower linear heat rates (maximum average LHR at 15 kW/m) than zircaloy-cladded fuel (~%75), however many did not contain the fuel rod pre-pressurization, fuel pellet dishing and chamfering, and ramp rate restrictions that are exercised today (Strasser et al., 1982).

At the time stainless steel fuel cladding was retired, there was remarkable reduction to the fuel failure rate of the cladding due to better operational guidelines. The FeCrAl cladding materials that are suggested for use as alternative cladding material to Zircaloy are very different than the stainless steels described here. Recent tests have shown that high chromium ferritic, BCC alloys offer superior stress corrosion cracking resistance compared to austenitic steels like the 300-series stainless steel variants described in this section (Andresen et al., 2014).

1.5 Fuel Performance Modeling

An important aspect of the evaluation of nuclear reactor fuel designs is the ability to determine the fuel rod behavior during operation in the reactor. To assess the thermo-

mechanical behavior of the fuel and cladding under both normal and transient reactor operating conditions, computational tools are commonly developed and used.

Fuel performance codes are used to improve fuel reliability by evaluating fuel designs under anticipated conditions against established metrics to determine operating margins (Yang et al., 2006). In order to accomplish this, constitutive thermal and mechanical models for the materials, derived from experiments, must be implemented into the code. Figure 4 shows an arrangement of calculated values from various models in a fuel performance code connected to models they directly impact. This shows how interrelated many of these models are and how each model must be verified carefully to develop predictive capabilities.

There are numerous codes that have been developed to date in order to simulate various types and designs of nuclear fuel such as: ALCYONE (Thouvenin et al., 2006),BISON (Hales et al., 2014), COMETHE (Hoppe et al., 1995), ENIGMA (Jackson et al., 1990), FALCON (Rashid et al., 2004), FEMAXI (Suzuki and Saitou, 1997), FRAPCON (Geelhood et al., 2011) / FRAPTRAN (Cunningham et al., 2001),PAD5 (Long et al., 2013), PRIME (GNF-A, 2010), TRANSURANUS (Lassmann et al., 1995), among many others. These codes use a variety solution methods and coordinate systems to evaluate the coupled thermo-mechanical response.

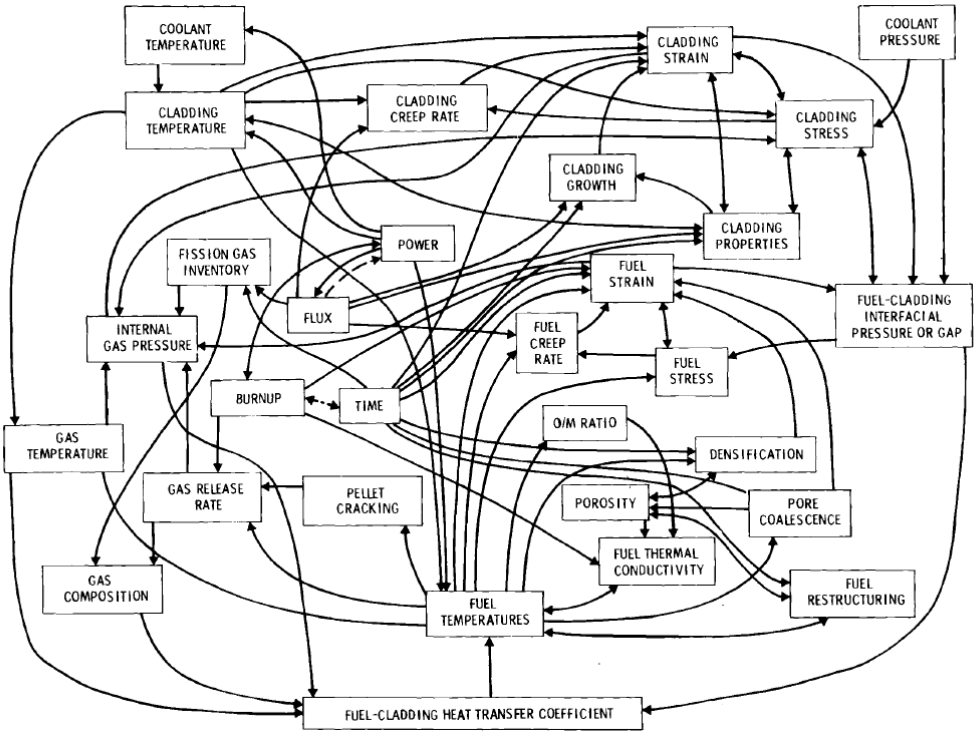

Figure 4. The models used in a fuel performance code are complex and interlinked. [Reproduced from (Beyer et al., 1975)]

In order to simulate these complex problems, a number of simplifications must be made based on the fuel geometry, the physics coupling, and the temporal scale (Lassmann, 1980). Fuel geometries are normally simplified into planar geometry or a series of linear geometries to reduce the degrees of freedom in the system, although 3D geometries are sometimes used for specialized analyses. This decreases computational costs and allows much faster calculations.

Generally, codes solve for thermal and mechanical solutions using either "loose coupling", by using an iterative solution to evaluate each model until a convergence criterion is reached, or "tight coupling", where all of the models are solved simultaneously. These models include heat conduction, species diffusion, nonlinear mechanics, and mechanical contact. Again, this is based on the computational resources available and the desired fidelity.

These models are solved under specified conditions representing the reactor operation, and then they are advanced through time to provide temporal resolution. Because fuel rods are typically operated in reactors for long periods of time (5-8 years), compromise must be made between the temporal resolution of the simulation and solve time.

While fuel performance codes are not yet predictive to a quantitative scale, they can assess fuel rod designs and provide a bounding analysis of the expected behavior. A brief introduction to the BISON fuel performance code, the code chosen for this analysis, is provided in Chapter 2. Since little is known regarding the performance of FeCrAl alloy based LWR fuel cladding, it is necessary to confirm both normal in-reactor performance, as well as the transient or accident behavior of this fuel. Thus fuel performance simulations have been performed using the BISON code (Williamson et al., 2012). While the database on material properties and complex mechanical fuel-cladding interactions are not yet complete for this class of alloys, we have evaluated a range of possible behaviors using a parametric approach to help identify key unknowns and uncertainties that will require further experimental and computational modeling investigation

1.6 Organization

The content of this dissertation is organized as the following:

Chapter 2 describes the material models that are used in these analyses. This includes an overview of the fuel and cladding geometry and behavioral models used in the BISON fuel performance code.

Chapter 3 discusses the thermo-mechanical analysis of FeCrAl and Zircaloy cladding under various steady-state operating conditions for the Peach Bottom BWR. This includes sensitivity analyses targeting the creep behavior of the fuel and cladding, as well as a parametric analysis focused on the fuel rod geometry.

Chapter 4 provides an assessment of the impact of various explicit fracture models on the determination of the cladding performance for both Zircaloy and FeCrAl cladding.

Chapter 5 discusses the thermo-mechanical analysis of FeCrAl and Zircaloy cladding under representative high-temperature reactor accident conditions.

Chapter 6 provides a summary for the work performed and discusses the ongoing activities to advance the fuel mechanical models as well as plans for improving the FeCrAl alloy models for high-temperature analyses.

CHAPTER 2: THERMO-MECHANICAL MODELING APPROACH

2.1 Overview

BISON is a finite-element simulation tool for nuclear fuel elements that is based on the Multiphysics Object Oriented Simulation Environment (MOOSE) framework (Williamson et al., 2012). It utilizes a Jacobian-Free Newton-Krylov method to solve coupled systems of non-linear partial differential equations while leveraging the scalability of parallel computing. Because of the expandability of the MOOSE framework (Gaston et al., 2009), BISON can incorporate a host of materials as well as behavioral models for integral fuel performance modeling. It has the capability to model complex thermo-mechanical behavior from both discrete and smeared pellet fuel meshes, the fuel-cladding gap and plenum, and the evolution of various fuel and cladding materials over their operation.

In order to discuss the model development and approach later in this chapter, a brief overview of the application of these models is provided in this section. The results herein document the evaluation and improvement of models used to perform thermo-mechanical analysis for three distinct types of fuel performance simulations. These calculations for FeCrAl cladded fuel rods start with the cladding performance under normal conditions, then identify sensitivity and data needs in the conventional fuel mechanics models, and conclude with an analysis of the cladding behavior under transient operating conditions.

The first analysis, described in Chapter 3, focuses on the performance of FeCrAl cladding during normal reactor operation. This evaluates the sensitivity of the integral fuel rod behavior to changes in the constitutive models used for the FeCrAl cladding and compares this behavior to Zircaloy cladding. In order to compare the predicted in-reactor performance of FeCrAl cladding with traditional Zircaloy cladding, and assess effects from irradiation creep, thermal creep, and swelling, several geometric and material models were implemented in the BISON fuel performance code.

Chapter 3 is separated into several sections based on the operating conditions, the material models evaluated, and the method used to evaluate them. Section 3.2 provides a comparison of FeCrAl versus Zircaloy-4 fuel cladding for three different scenarios of boiling water reactor power operation. This analysis compares the Zircaloy cladding, using previously developed cladding models in BISON with recently implemented constitutive models for FeCrAl cladding. These new models are also used to examine the effects of thermal and irradiation creep and irradiation swelling on the in-reactor performance of the fuel cladding. This study expands upon a previous core equivalence study (George et al., 2015a) targeting the cycle length effects of using iron-chromium-aluminum alloys as alternative fuel cladding for the Peach Bottom BWR by incorporating aspects of integral fuel performance. Data from this previous study was used in order to create representative reactor operation data for the fuel simulations performed with BISON described in Sections 3.2 and 3.3.

The second analysis is motivated by this initial comparison of FeCrAl to Zircaloy cladding

for the different BWR power operation scenarios and consists of individual examination of the creep models used for the FeCrAl cladding and UO_2 fuel. For this analysis, separate evaluations are conducted to identify the sensitivity of the FeCrAl cladding behavior to changes in the thermal and irradiation creep models, and the fuel creep model is evaluated for changes in calculating specific creep contributions. FeCrAl creep properties are examined to provide performance bounds for future FeCrAl alloy development, where available data is currently sparse. Fuel creep is assessed due to uncertainty in modeling fuel compliance. This evaluation aims to identify a range of expected fuel behavior by examining the irradiation and thermal creep rate currently implemented in BISON and described in MATPRO (Hagrman et al., 1995). Without sufficient stress relief mechanisms, such as cracking, the calculated fuel creep might be greatly over predicted; this can influence the mechanical interaction between the fuel and cladding and ultimately result in a prediction of very high, overly conservative cladding hoop stresses.

The third part of this analysis, described in Section 3.7 focuses on identifying the potential thermal and mechanical impacts of altering the radial fuel rod geometry specifications. This is performed in order to evaluate previous assumptions for the geometry of the FeCrAl cladded fuel rod. For these simulations, the fuel-cladding gap was parametrically varied while maintaining a constant cladding outer radius and cladding thickness. This analysis was performed with and without modeling fuel creep to provide bounding values for the expected behavior of the FeCrAl cladding under constant operating conditions.

Finally, Section 3.8 describes and compares improvements made to the cladding material models to reflect the behavior observed during mechanical testing of FeCrAl. This includes, specifically, modifications to the cladding thermal and irradiation creep models. To compare the influence of these modifications, additional comparisons are performed using constant operating conditions from a BWR.

Motivated by the results from the fuel creep analysis, a more in-depth study of the fuel mechanics models and the impact of explicit fuel fracture was conducted, described in Chapter 4. In this analysis, cracking models were implemented and models which induce diametral expansion due to fracture in the fuel, specifically fuel relocation, were examined. As previously mentioned, this is performed in order to correctly determine the fuel diametric expansion and the compliance in the fuel after mechanical contact with the cladding occurs. This influences the stress-state and radial expansion of the cladding, which is a focal point of this work documenting the expected mechanical performance of FeCrAl cladding. In order to determine how the fuel expansion directly affects the cladding deformation, a series of simulations are executed each with different fracture models for conditions from the OSIRIS H09 integral fuel rod test. This is a full-length, Zircaloy-cladded fuel rod from the OSIRIS test reactor, selected from the International Fuel Performance Experiments (IFPE) database (Sartori et al., 2010) for its documentation and end-of-life cladding diametric profilimetry measurements.

Finally, in Chapter 5, the cladding performance under transient reactor operating conditions is analyzed. For these simulations, material specific constitutive models are implemented

as well as cladding oxidation models, in order to elucidate cladding behavior at high-temperatures. Operating conditions, such as the axial linear heat generation rate, and boundary conditions, such as the cladding outer surface temperature, are adapted from a previous study on the role of fuel thermal conductivity on LWR accident progression (Terrani et al., 2014a).

General geometric, material, and behavioral models used for the analysis in Chapter 3 are described in this chapter. Additional modifications to the geometric and material models for specific evaluations are described in detail in the appropriate section.

2.2 Geometric Models

Geometric models for this study are based on available data for the Peach Bottom BWR (Larsen, 1978). Where data is unavailable, representative values have been assumed. Two-dimensional, axisymmetric fuel rod geometries (shown in Table 1) were created for both Zircaloy and FeCrAl. The cladding thickness, fuel radius, and fuel enrichment for the FeCrAl cladded rod were chosen based on the impact of the neutronic penalty over the reactor cycle, while maintaining the same cladding outer radius. In this study, the FeCrAl cladding is half the thickness of the Zircaloy cladding and the initial cladding fuel gap has been kept the same to increase fuel mass as a partial offset to the neutronic penalty of FeCrAl. Additionally, this is partially motivated by the greater strength of the FeCrAl alloy. This results in ~14% more fuel mass. Additional fuel enrichment was also added (~.57%) to further improve the fuel reactivity.

These geometric models are simplified by using smeared pellet fuel meshes (mesh example shown in Figure 5). Meshes are generated using second-order elements. A sensitivity analysis has been previously performed and documented in the literature (Williamson et al., 2016) regarding the mesh refinement and solution precision of the BISON fuel performance code, and based on the results of that analysis, we conclude that the current mesh is sufficiently refined to accurately assess the fuel and cladding thermal-mechanical behavior. In the figure, elements in the UO_2 fuel region are shown in green, and elements in the cladding region are shown on the right, in grey.

Table 1. Fuel geometry specifications for 2D axisymmetric fuel performance analyses.

Cladding Material	Fuel Radius (μm)	Gap Thickness (μm)	Cladding Thickness (μm)	Fuel Length (m)	Cladding Length (m)	Enrichment (% U-235)
Zircaloy	4400	100	600	3.66	4.08	4.11
FeCrAl	4700	100	300			4.68

- This produces a total outer radius of 5100μm for both cladding types.

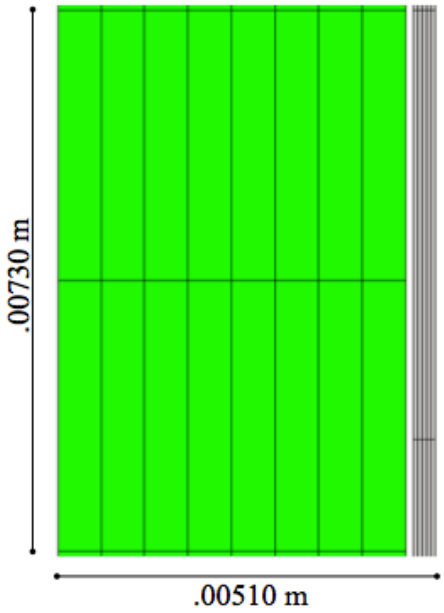

Figure 5. Segment of axisymmetric mesh for 300μm FeCrAl Cladding

2.3 Boundary Conditions and Simulation Input Parameters

A neutronics analysis was performed to provide power histories to BISON, in the form of input and boundary conditions. These include axial power profiles of the fuel and temperature profiles of the cladding outer surface. The power and temperature data generated was represented by the highest power fuel rod in the highest power fuel assembly at each depletion step in the calculation, effectively the most limiting rod in the core, and was modeled in effective full power seconds. This data is organized as a fuel rod average power history and a series of axial power profiles. Figure 6 shows the rod average power history for both the FeCrAl and Zircaloy cladded fuel rods and a set of selected axial power profiles from the FeCrAl-cladded fuel. These axial power profiles, shown on the right in Figure 6 have been averaged and show the wide variation in power along the axial length of the fuel rod over time.

In order to target the average fuel rod behavior using this operational data, a separate set of fuel rods was run using an 80% power version of these histories. The dashed lines in Figure 6 (a) show the reduced power histories for these fuel rods.

It is important to note that this operational data does not simulate reactor shutdown between cycles, which may cause increased degradation on the fuel rod from repeated power ramping. These power histories cover three 18-month cycles and extend into a 4th cycle (~2100 days for FeCrAl, 1770 days for Zry). In order to meet cycle length requirements, the FeCrAl fuel rod design had to be altered and its enrichment increased. Because of this, differing power histories and limiting rod locations are used between the FeCrAl and Zircaloy-cladding cases.

Using the full-core optimization software LWROpt, coupled to the nodal diffusion simulator NESTLE, control blade patterns and lattice batch configurations were optimized (George et al., 2017). This was performed for three 18-month cycles in order to maximize fuel lifetime, maintain low radial and axially peaking factors, and of course, sustain criticality. However, as the lifecycle of the fuel designs continue, axial and radial power shifts within the core are inevitable. This is presented in the following figure as the axial power profile varies from beginning of life to end of life.

Simplified simulation data was constructed from the average rod power in order to more easily disseminate changes in the fuel rod over operation. In order to perform this analysis, a simplified power history and axial profile are used. This power history and axial power profile are shown in Figure 7 and consists of a relatively quick (~12 hours) ramp to power with a simple axial power shape. After the initial power ramp, fuel rod power is then held constant at ~18 kW/m (this represents the average power). For the analysis of this power operation, a constant coolant temperature profile of 560 K was applied axially along the cladding.

Boundary conditions were used to apply coolant temperature profiles to the outside of the cladding along with the coolant pressure, and to apply the plenum pressure to the inside surface of the cladding and the outside of the fuel. The reactor operating pressure (7.136 MPa) was taken from the design document and also applied as a boundary condition to the outside of the cladding. The initial plenum pressure for the fuel rod is 5 ATM (~.5 MPa), derived from a GE-9 fuel assembly, as data was not available for GE-12 or GE-14 fuel assemblies (Moore and Notz, 1989).

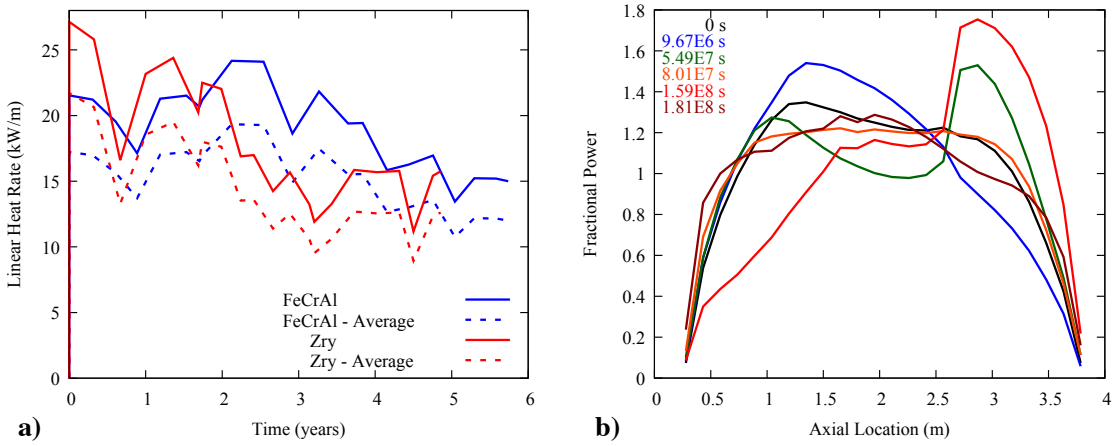

Figure 6. The power history for limiting and average rod operation for both cladding types (a) shows the difference in the linear heat rate caused by optimizing the fuel and cladding for FeCrAl to meet cycle length requirements. Selected axial power profiles of FeCrAl clad fuel rods (b) show axial variability in the power generation rate over time.

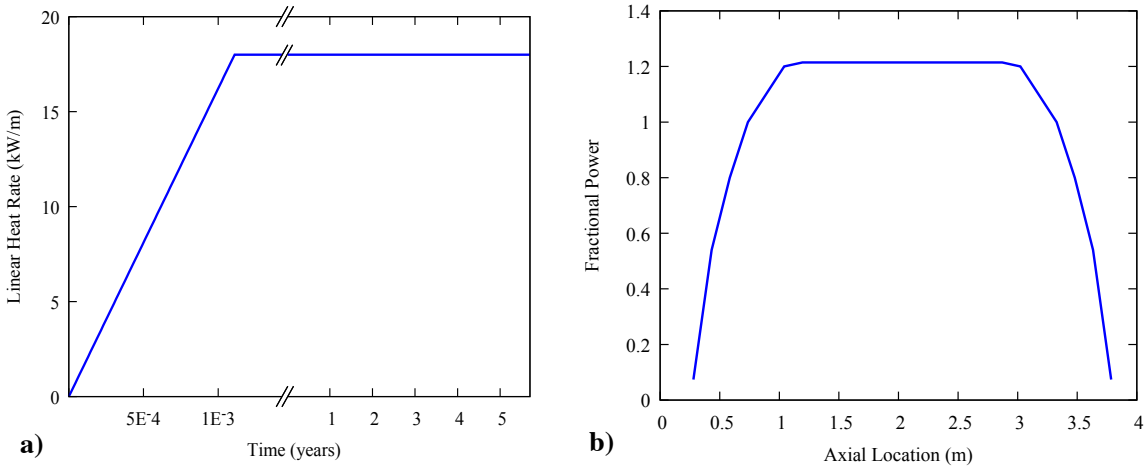

Figure 7. The power history (a) and axial power profile (b) for constant-power rod operation show a ramp to 18kW/m and a simplified axial power distribution. These were chosen to more easily disseminate results from operation.

2.4 Constitutive and Behavioral Models

While BISON already contains many established material models for fuel performance, models for FeCrAl cladding had to be developed and implemented; it is important to also note that similar activities were performed elsewhere, as described by Wu et al. (Wu et al., 2015). Constitutive models are already established for UO_2 fuel, gap/plenum behavior, and Zircaloy cladding, although FeCrAl investigation involves different fuel geometry than conventional LWR fuel to compensate for the higher parasitic neutron absorption in FeCrAl cladding.

To simulate the UO_2 fuel, we have implemented material properties that have been previously developed, including; NFIR data (Marion, 2006) on thermal properties (based on temperature and burnup dependence); temperature dependent mechanical properties; fuel densification, relocation, and solid fission product swelling (Hagrman et al., 1995); gaseous fission product swelling and fission gas release (Hales et al., 2014). In our fuel simulations, the fuel was initially modeled as an elastic material to isolate and understand cladding behavior. This was subsequently followed by a separate and systematic analysis of the influence of fuel thermal and irradiation creep on the predicted fuel and cladding stress levels.

The gap and plenum of the fuel are modeled by using the gap conductance model, fission gas release, and plenum pressure model developed by Williamson and co-workers (Williamson et al., 2012). The plenum pressure is determined based on the amount of initial plenum fill-gas as well as fission gas released, and the evolving plenum volume. Mechanical interactions between the fuel and cladding surfaces in these simulations follow a penalty formulation to prevent surfaces from overlapping, and in this model we have assumed frictionless contact between surfaces (Hales et al., 2014). This simplification

implies that there will be no axial elongation in the cladding due to fuel ratcheting or additional elongation as the fuel expands during mechanical contact (Olander, 1976).

Models used for the Zircaloy-4 cladding include thermal and mechanical properties based on temperature, neutron fluence, initial oxygen concentration, and cold-working factor; thermal and irradiation creep; and irradiation growth. These are standard models in BISON and described by (Hagrman et al., 1995) and (Hales et al., 2014).

Material models for FeCrAl cladding were developed based on available data for the FeCrAl alloys Kanthal Alkrothal 720 (Kanthal) and Kanthal APMT (Kanthal). Because of their high-Cr content, these alloys may lose ductility (embrittle) in a nuclear reactor environment due to the formation of Cr-rich precipitates (Field et al., 2015). Although these alloys may undergo embrittlement, they are expected to share many thermal and mechanical properties with the FeCrAl-class of alloys currently under development for nuclear applications. The radiation hardening and embrittlement behavior of these alloys are not considered in these simulations. Although this will affect plastic deformation of the FeCrAl cladding, there is not enough data to satisfactorily infer this behavior up to the doses expected in the cladding. Thus, radiation hardening in the cladding is not currently included in this work.

Material properties from the datasheets were fit to curves based on the published dependencies and implemented into BISON. These models are based on available thermo-physical, mechanical, and irradiation properties and include: thermal conductivity, specific heat, elastic modulus, Poisson's ratio, density, thermal creep, and irradiation swelling. The work presented herein on the steady-state performance of FeCrAl cladding does not consider cladding oxidation or corrosion behavior. At this time, a method for evaluating the mechanical and thermal impact from uniform oxidation and cladding consumption is not implemented in the BISON fuel performance code. In the previous analysis by Gamble et al. (Gamble et al., 2017), it is shown that under similar conditions in a pressurized water reactor (PWR) a <10 μm thick layer of oxide will form on the FeCrAl cladding over ~4 years, and an ~80 μm thick layer of oxide will form on the Zircaloy cladding. This is expected to be significantly diminished for a BWR (Hagrman et al., 1995). The next Section 2.5 provides additional information on the thermal and irradiation creep and dimensional changes for both Zircaloy and FeCrAl.

2.5 Implementation of Cladding Creep, Growth, and Swelling Models

Important models for determining the reactor performance of FeCrAl cladding include irradiation creep, thermal creep, and irradiation swelling. These are compared with corresponding Zircaloy models to identify expected cladding deformation behavior under various stress, temperature, and neutron flux conditions.

The deformation in the FeCrAl cladding over time, is calculated as the sum of the elastic, thermal, swelling, and creep strains, as:

$$\varepsilon_{total} = \varepsilon_e + \varepsilon_{th} + \varepsilon_s + \varepsilon_c \quad (1),$$

where ε_e describes the elastic strain by Hooke's law, ε_{th} describes the strain induced by a change in temperature, and ε_s and ε_c describe the swelling and creep, respectively, and are described later in this section. While Eq. (1) is the same for Zircaloy cladding, ε_s must be replaced by an expression that captures the anisotropic irradiation growth at constant volume (ε_g), rather than isotropic irradiation induced swelling.

Models for the irradiation swelling and irradiation creep strain (shown below in Equations 2 and 3, respectively**)** for FeCrAl were used to reflect estimates of the material response for ferritic alloys (Garner et al., 2000). Note that the creep contribution from swelling has been neglected in this model, based on the lack of swelling or cavity nucleation observed in FeCr and FeCrAl in the temperature/dose range anticipated for LWR cladding. Thus, the irradiation-swelling model for FeCrAl is expressed as a simple linear scaling with dose:

$$\varepsilon_s = A \cdot \varphi \quad (2),$$

where ε_s is the volumetric strain due to irradiation swelling, A is a volumetric swelling constant (0.05%-dpa^{-1}) and φ is the cumulative irradiation damage in the cladding in displacements-per-atom (dpa). The damage rate in these models is adapted from the expected displacement damage at the mid-plane of a BWR core over an effective-full-power-year (Heinisch et al., 2004) and converted to the fast neutron fluence. This conversion is performed because BISON does not calculate the neutron energy spectrum from fission, and therefore cannot calculate the displacement damage. Because of the low maximum dose expected for the FeCrAl cladding in these simulations (<20 dpa), steady-state swelling is not anticipated to occur. Instead, this model is intended to provide a conservative estimation of the transient swelling regime before the onset of steady-state swelling. Thus, a volumetric swelling constant of 0.05%-dpa^{-1} is used instead of 0.2%-dpa^{-1}, which Garner suggests for the steady-state swelling of BCC alloys (Garner et al., 2000).

The creep strain, ε_c, can be further divided into two distinct contributions for thermal, $\varepsilon_{c,th}$, and irradiation creep, $\varepsilon_{c,irr}$. The irradiation creep model is:

$$\varepsilon_{c,irr} = B \cdot \varphi^m \cdot \sigma^n \quad (3),$$

where B is the irradiation creep pre-factor, and we use a value of 5×10^{-7} MPa^{-1}-dpa^{-1}, φ is the displacement damage in the cladding (dpa), and σ is the effective stress (MPa). In Eq. (3), the exponent of both displacement damage, m, and stress, n, are assumed equal to 1 for FeCrAl.

The steady-state thermal creep strain for the FeCrAl alloy is based on a power-law creep law equation to describe dislocation creep (as shown in Equation 4), which is adapted from a FeCrAl alloy with a yttrium addition (Saunders et al., 1997). The strain for this model is expressed as:

$$\varepsilon_{c,th} = C \cdot \sigma^n \cdot \exp\left(-\frac{Q}{kT}\right) \cdot t \quad (4),$$

where C is the creep pre-exponential (5.96×10^{-24} s^{-1}–Pa^{-n}), σ is the effective stress in Pa, n is the stress exponent fitting parameter (5.5), Q is the creep activation energy (~4.062 eV), T is the temperature in K, t is the time in seconds, and k is the Boltzmann constant (eV-K^{-1}). It is important to note that the value of creep pre-exponential, C, used in Eq. (4) has been modified from the original value (5.96×10^{-27} s^{-1}–Pa^{-n}) published by Saunders and co-authors (Saunders et al., 1997), in order to match experimental results more accurately (Terrani et al., 2015).

For Zircaloy, the steady-state irradiation and thermal creep expression are provided below in Equations (5) and (6) and are obtained from Limback and Andersson (Limbäck and Andersson, 1996). The irradiation creep expression is implemented analogously to the expression for FeCrAl, however, with different values of the material constants.

$$\varepsilon_{c,irr} = D \cdot \varphi^m \cdot \sigma^n \cdot t \quad (5).$$

In Eq. (5), the irradiation creep constant, D, for Zircaloy is 9.88×10^{-28} (Pa^{-1}-m^2-s^{-1}) and the irradiation creep strain is a function of φ, the fast neutron flux (#-m^{-2}-s^{-1}), t, the time (in seconds), and σ, the effective stress (MPa). The flux exponent, (m), is sub-linear with a value of 0.85, and a linear dependence on stress is observed, with an exponent, (n), of 1.

The thermal creep for Zircaloy is expressed based on the Matsuo model (Matsuo, 1987), with constants modified to include irradiation hardening and better reflect data on Zircaloy-4 (Limbäck and Andersson, 1996), as described in Eq. (6). This thermal creep expression includes a contribution from irradiation hardening, which acts to slow the creep rate, as described by Eq. (7).

$$\varepsilon_{c,th} = F \cdot \left(\frac{E}{T}\right) \cdot \left(\sinh\frac{a_i \cdot \sigma}{E}\right)^2 \cdot \exp\left(-\frac{Q}{kT}\right) \cdot t \quad (6)$$

$$a_i = 650 \cdot \left(1 - 0.56 \cdot \left(1 - \exp(-8.8334e^{-}33 \cdot \Phi^{1.3})\right)\right) \quad (7)$$

where F is the thermal creep pre-factor (3×10^5 K-MPa^{-1}-s^{-1}), E is the elastic modulus in MPa, a_i is the contribution to irradiation hardening, σ is the effective stress, Q is the creep activation energy (~2.083 eV), T is the temperature in K, t is the time in seconds, and k is the Boltzmann constant (eV-K^{-1}). The reduction of the thermal creep rate from irradiation hardening is dependent on the fluence in the material, Φ (#-m^{-2}).

The irradiation growth, ε_g, expression used (Equation 8) is the Franklin model (Franklin, 1982), as described by Rashid (Rashid et al., 2004) and implemented in BISON.

$$\varepsilon_g = 9.088e^{-}25 \cdot (\Phi)^{.845} \quad (8)$$

Where Φ is the fast neutron fluence in (#-m^{-2}). Irradiation growth conserves the overall volume of the material; therefore, as the cladding elongates along the growth direction it reduces size in the other directions. Therefore, a corresponding strain acting to reduce the cladding radius and thickness will develop.

Figure 8 shows a comparison between the irradiation and thermal creep behavior of FeCrAl versus Zircaloy at stress levels of 50, 150 or 300 MPa, as function of fast flux and temperature, respectively. Figure 8(a) displays the irradiation creep rate between the cladding materials, emphasizing a slight difference in the scaling of the creep rate and a large difference in the creep rate magnitude. For the illustration in Figure 8(b), the elastic modulus of Zircaloy is assumed to be 75 GPa and neither material includes a contribution from irradiation hardening in the thermal creep rate.

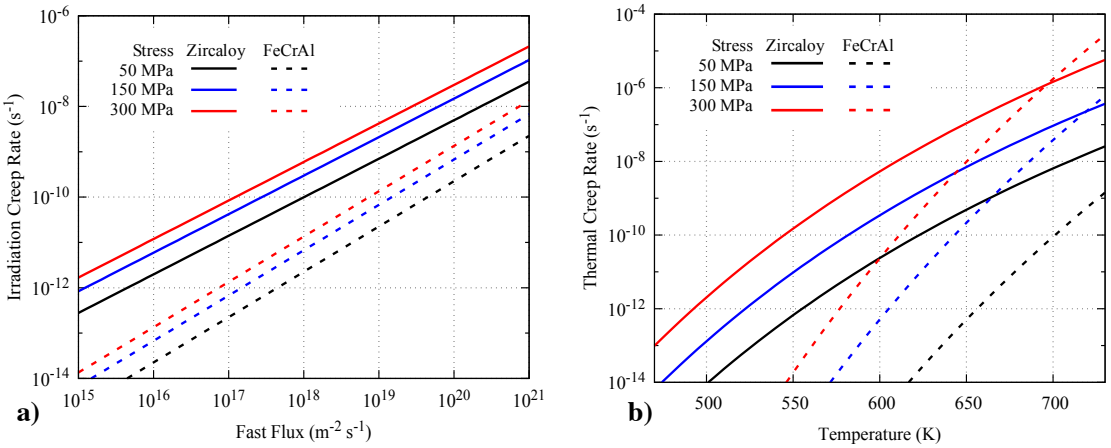

Figure 8. Comparison of creep rates of Zircaloy (solid lines) versus FeCrAl (dashed lines) for conditions of (a) Irradiation creep as a function of neutron fast flux (E > 0.1 MeV) and (b) thermal creep as a function of temperature. These plots illustrate the large difference in the creep behavior between materials under identical conditions.

Figure 8 clearly demonstrates the large difference in the creep behavior of FeCrAl alloys relative to Zircaloy over a variety of anticipated reactor operating conditions and at varying stresses. Correspondingly, FeCrAl cladding will experience much less creep deformation, and in the absence of instantaneous plasticity, should experience less stress relief during fuel-cladding mechanical contact than the Zircaloy-4 cladding.

Figure 9 shows the difference between both cladding types in the anticipated irradiation induced stress-free dimensional change as a function of fast neutron flux (a) and the thermal expansion as a function of temperature (b). For the Zircaloy, because it possesses a hexagonal-close-packed crystal structure, there are two values for both phenomena based on the orientation of the crystal structure in the individual alloy grains (or the alloy texture). Figure 9(a) shows the irradiation growth in the axial direction, and the absolute value of the corresponding retraction (offset) in the perpendicular direction. This shows that as the Zircaloy cladding elongates due to irradiation growth, the fuel-cladding gap is reduced as

the cladding is restricted during this volume conservative dimensional change. This also shows that the Zircaloy will axially expand more than the FeCrAl alloy will. Because the FeCrAl alloy is BCC, it expands isotropically due to irradiation swelling, thus, there is only a single value for the dimensional change. Figure 9(b) shows the thermal expansion for both alloys, and much like the irradiation-induced dimensional change, there are two separate curves for the Zircaloy due to the crystal anisotropy. The thermal expansion for the FeCrAl alloy is much larger than the thermal expansion for the Zircaloy. This results in a larger fuel cladding radius, and thus a larger gap size, after the rise to operating temperature in the FeCrAl cladding.

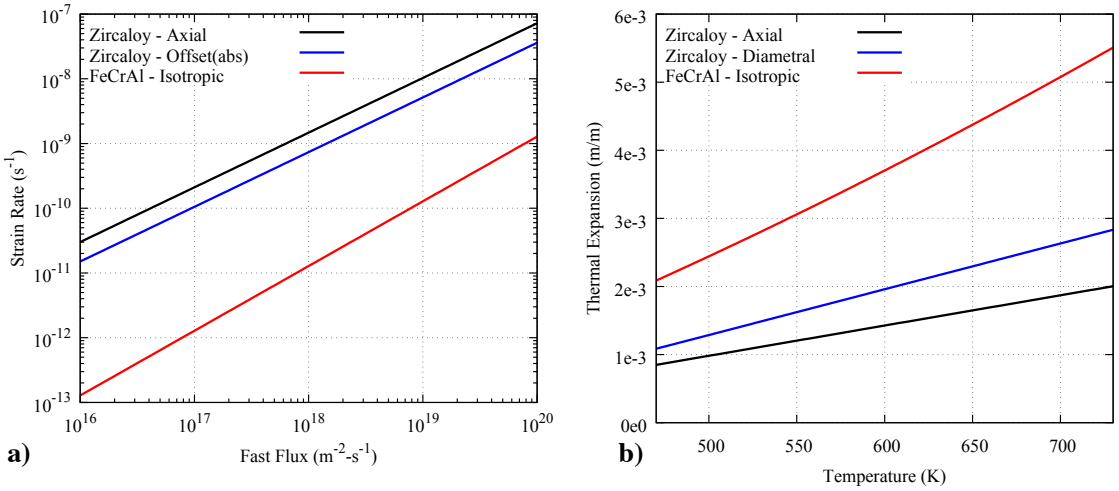

Figure 9. a) The irradiation-induced strain rate for dimensional change of Zircaloy in the axial and offset directions compared to FeCrAl, and b) the thermal expansion for Zircaloy and FeCrAl.

2.6 UO_2 Fuel Creep Model

The combined UO_2 thermal and irradiation creep strain rate model (Eq. 9) described by Hagrman et al. (Hagrman et al., 1995) is used in these integral pin thermo-mechanical calculations. This equation is evaluated in order to identify the impact of fuel compliance, specifically the contribution from fission-induced creep, on cladding stress state. This model is defined as the summation of the three separate creep rate contributions shown in Eq. 9; fission-enhanced thermal creep (first term), thermal creep (second term), and fission-induced creep (third term).

$$\dot{\varepsilon}_{total}^{fuel} = \frac{A_1+A_2\dot{F}}{(A_3+D)G^2}\sigma e^{\left(\frac{-Q_1}{kT}\right)} + \frac{A_4}{(A_6+D)}\sigma^{4.5}e^{\left(\frac{-Q_2}{kT}\right)} + A_7\dot{F}\sigma e^{\left(\frac{-Q_3}{kT}\right)} \quad (9)$$

Where the various A parameters are fitting constants, $\dot{F}$ is the fission rate (m^{-3}-s^{-1}), σ is the effective stress (Pa), the Q variables are creep activation energies (eV), T is the temperature (K), k is the Boltzmann constant (eV-K^{-1}), D is the percent of theoretical fuel

density, and G is the grain size (μm). While there is an effect of the fuel stoichiometry on the creep activation energies (Q) for this model, only an oxide-to-metal ratio of 2 is considered in this analysis. Fitting constants and creep activation energies used in this analysis are provided in Table 2.

Table 2. Tabulated constants for the fuel creep (Hagrman et al., 1995) and (Hales et al., 2014) and modified fission-induced creep (Solomon et al., 1971)

Parameter	Value	Units
A_1	0.3919	μm^2-Pa^{-1}-s^{-1}
A_2	1.31e-19	μm^2-m^3-Pa^{-1}
A_3	-87.7	*dimensionless*
A_4	2.0391e-25	$Pa^{-4.5}$-s^{-1}
A_6	-90.5	*dimensionless*
A_7	3.72264e-35	m^3-Pa^{-1}
A_8	1.49977e-36	m^3-Pa^{-1}
Q_1	3.903	eV
Q_2	5.725	eV
Q_3	0.225	eV

The fission-induced creep contribution is generally thought to be athermal (Solomon et al., 1971), although there is some variability in reporting a temperature dependence (Dienst, 1977). This is especially important because the contribution from fission-induced creep dominates the total creep response approaching 1000˚C, where irradiation-enhanced creep becomes dominant.

In order to determine the differences from including athermal fission-induced creep in the creep rate calculation, the contribution in Eq. 9 was replaced by one from Solomon et al., shown in Equation 10. Figure 10 shows the individual contributions in the combined thermal and irradiation creep model and Eq. 10.

$$\dot{\varepsilon}_{3,b} = A_8 \dot{F} \sigma \tag{10}$$

Where the A parameter is a fitting constant, $\dot{F}$ is the fission rate (m^{-3}-s^{-1}), and σ is the effective stress (Pa).

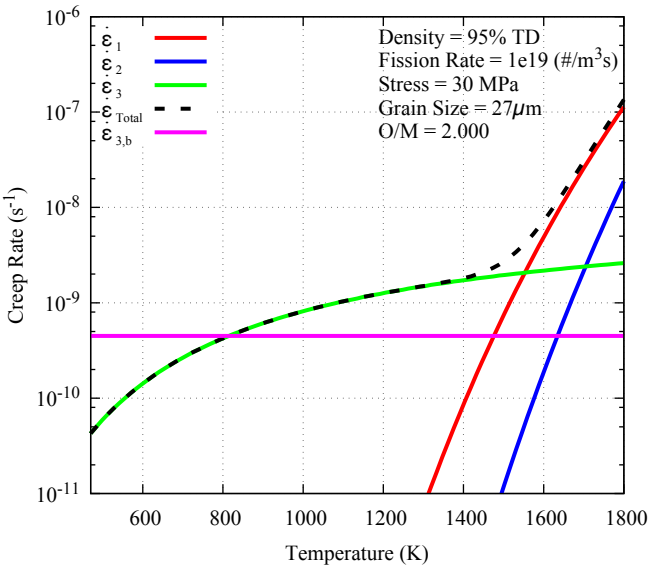

Figure 10. Plot of the individual contributions ($\dot{\varepsilon}_1, \dot{\varepsilon}_2, \dot{\varepsilon}_3$) to the total fuel creep rate versus temperature ($\dot{\varepsilon}_{Total}$) in the model described by Hagrman (Hagrman et al., 1995) and a comparison with the athermal irradiation-induced fuel creep ($\dot{\varepsilon}_{3,b}$) contribution described by Solomon (Solomon et al., 1971).

For the fuel creep analysis described later in Section 3.6, three separate calculations are performed to determine the individual effects of fuel creep and the modified athermal irradiation-induced creep term. These include modeling the fuel as an elastic material without creep versus using the creep model as described by Hagrman or with the fuel creep model including the modified fission-induced creep.

CHAPTER 3: STEADY-STATE OPERATION

3.1 Simulation Summary and Fuel Performance Analysis Metrics

In total, five different fuel performance simulations were performed for different reactor operating scenarios, in which the fuel was modeled as elastic only. As shown in Table 3, four simulations were performed for FeCrAl cladding, each of which corresponds to performing a systematic incorporation of different material models, along with a single simulation for Zircaloy cladding using established material models implemented in BISON. The variations in fuel performance simulations performed for FeCrAl cladding were performed to distinguish integral effects from individual properties of the FeCrAl cladded fuel rods during reactor operation and compare to the Zircaloy cladding.

From these simulations, several parameters were utilized to determine the state of the fuel and cladding. These metrics were chosen to reflect current fuel safety criteria as described by the OECD/NEA (OECD, 2012) and include: peak and average fuel centerline temperatures, cladding axial elongation, maximum cladding radial displacement, fission gas production and release, plenum pressure and volume, and maximum cladding hoop stress.

Peak fuel centerline temperatures give an indication whether the fuel is approaching its melting temperature. The relation used for the melting temperature of UO_2 as the fuel is utilized is shown in Equation 11 and described by Rashid et al. (Rashid et al., 2004).

$$T_m = 3120.15 - 0.76 \cdot bu \tag{11}$$

Where, T_m is the fuel melting temperature in Kelvin and Bu is the local fuel burnup in MWd/kgU. BISON calculates the local burnup radially and axially over the fuel using the axial power distribution provided in the simulation input and a radial power profile determined from the TUBRNP model developed by Lassman et al. (Hales et al., 2014; Lassmann et al., 1994). The peak local burnup across all of the work in this chapter is approximately 170 MWd/kgU, and is located in the rim region at the periphery of the fuel pellet. This establishes a conservative minimum fuel melting temperature of nearly 2990K. This is used to show that the peak fuel centerline temperatures from these results are continuously below the fuel meting temperature.

Table 3. Summary of material models included in each fuel performance simulation

Cladding Material	Elastic Properties	Thermal Creep	Irradiation Swelling	Irradiation Creep	Irradiation Growth
FeCrAl	**X**	**X**	**X**	**X**	
FeCrAl	**X**	**X**	**X**		
FeCrAl	**X**	**X**			
FeCrAl	**X**				
Zircaloy	**X**	**X**		**X**	**X**

Axial average centerline temperatures describe the behavior of the fuel rod much better for assessing thermally activated phenomena. While the peak temperature is directly limiting (because of the fuel melting temperature), the average temperature better reflects the integral fuel rod behavior.

Calculating the dimensional change in the fuel is important for assessing deformation limits on the cladding (e.g. retaining fuel rod pitch for heat transfer or preventing axial constraints that can cause bowing). Limits described by the OECD/NEA include a 1% hoop strain limit and 2.5% equivalent strain limit. Limits on the cladding deformation as imposed by the U.S. Nuclear Regulatory Commission (U.S. Nuclear Regulatory Commission, 2007) include a 1% uniform strain limit (excluding strains from cladding creep down and irradiation growth).

Fission gas accumulation in the plenum can lead to increased fuel rod internal pressure, which may act to rupture the fuel cladding in high temperature and pressure conditions (ballooning and bursting). Accumulation of fission products in the plenum volume also degrades the thermal conductivity of the fill gas and contributes to higher fuel temperatures.

The cladding hoop stress is an extremely important indicator for assessing the condition and probable failure of cladding materials, as well as assessing the effects of mechanical contact on the fuel cladding. Sections 3.2-4 describe the results obtained for each of the different reactor operating scenarios investigated. Sections 3.5 and 3.6 provide systematic study on the sensitivity of the cladding stress state to variations in the cladding and fuel creep behavior. Section 3.7 describes a parametric evaluation of the fuel radial geometry in order to assess differences in the integral fuel rod behavior from changes in the fuel radius and gap thickness. Section 3.8 documents gradual improvements to the FeCrAl material models and compares the cladding behavior using new material models for the experimental C35M alloy.

3.2 Limiting-Power Operation

Figure 11 presents the peak and average fuel centerline temperatures for the most limiting power operation. Figure 11(a) compares the peak fuel centerline temperatures for the different FeCrAl mechanical behavior models, as compared to Zircaloy cladding. Figure 11(b) compares the peak and average fuel centerline temperatures of the full FeCrAl-cladded simulation and the Zircaloy-cladded fuel rod. As shown in Figure 11(b), there is a very small change in fuel centerline temperature for the FeCrAl clad fuel, when evaluating the effect of different mechanical behavior models during the simulated reactor operation. A slight (~40 K) change is observed from one to three years in the model with isotropic FeCrAl swelling, as a result of the clad diameter expansion that slightly increases the fuel-cladding gap thickness. Increasing the gap thickness decreases the heat transfer from the fuel and therefore results in higher fuel temperatures. However, as the fuel swells and closes the gap, the increased gap conductance lowers fuel temperatures, and the fuel temperatures predicted by these different models converge. As well, there is a slight change

in the fuel temperature (~20 K) for the case of the elastic model beginning about the fourth year of the operating history. This arises because the cladding in this particular simulation (Elastic, blue dashed line) only includes elastic deformation, and therefore restricts the fuel from expanding more than the other models. Aside from this, the fuel centerline temperatures of the fuel rods with FeCrAl cladding overlap for much of the simulation. This indicates that the difference in models for the FeCrAl mechanical behavior and dimensional stability have a limited effect on the fuel centerline temperatures.

However, a large difference in fuel temperature profiles with operating time exists between the fuel rods with Zircaloy vs FeCrAl cladding. These differences are due to the differing power histories and axial profiles that resulted from optimization of the full-core neutronics simulations for each cladding material. The difference between the peak and the average fuel centerline temperatures, shown in Figure 11(b), occurs due to variations in the axial power profiles. It is important to note that the FeCrAl simulations maintain a consistently higher average temperature than the Zircaloy rods beginning at about 16 months of operation. Such increases in fuel temperature have a large influence on thermally driven phenomena, such as fission gas release, and will be further discussed in the chapter summary.

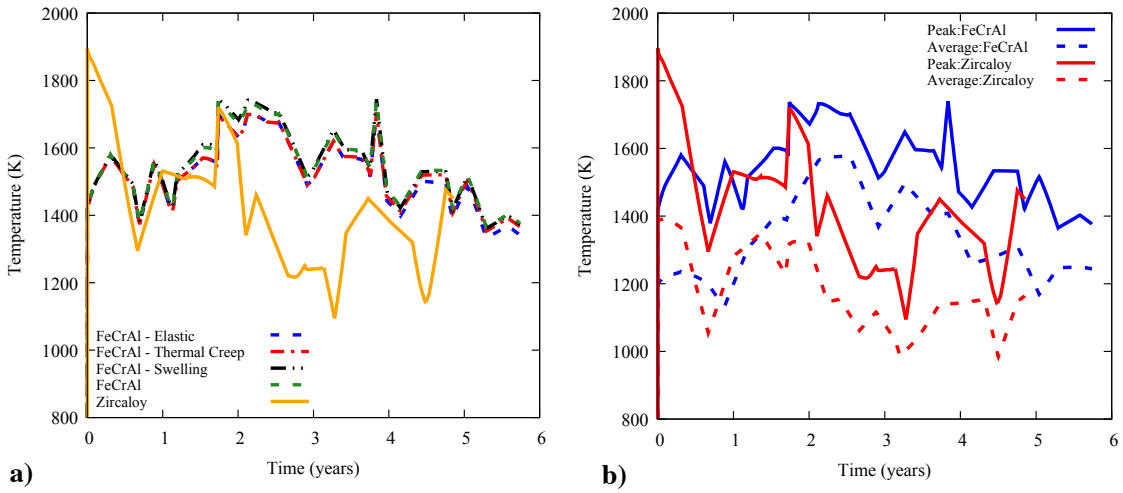

Figure 11. Peak (a) and average (b) fuel centerline temperatures during the limiting power simulation. The slight difference in peak centerline temperatures among FeCrAl cladded fuel rods primarily indicate the effect of irradiation swelling by increasing the fuel-cladding gap size. The average fuel centerline temperatures are much different than the peak centerline temperatures because of the axial power distribution.

Figure 12 compares the cladding displacement, including both the axial elongation and maximum radial displacements. The initial axial elongation in both FeCrAl and Zircaloy clad fuel rods is driven by the thermal expansion of the cladding during its rise to reactor coolant temperature, and subsequently, the fuel operating temperature. Immediately after the initial thermal expansion, there is a noticeable deviation between the different mechanical behavior models for the FeCrAl cladding based on the irradiation swelling of

the cladding. In the cases without swelling, the cladding axial elongation is relatively constant until mechanical contact occurs. After mechanical contact, there is a reduction in cladding length as the fuel expands the cladding radially, due to Poisson's effect. This is similar for the model that includes the FeCrAl irradiation-swelling model, however, the axial swelling appears to nearly offset the length reduction from radial expansion. The fuel rods with Zircaloy cladding show a similar axial elongation effect until mechanical contact occurs, but this is caused by the anisotropic irradiation growth of Zircaloy. There is a small effect from the addition of thermal and irradiation creep models in the FeCrAl cladding. Creep deformation allows the cladding to relax stresses that form during the mechanical interaction with the fuel. This allows the cladding radius to increase, subsequently decreasing the axial elongation.

Similar to the axial elongation, the initial radial expansion in the FeCrAl and Zircaloy-cladded fuel rods is due to thermal expansion. Figure 12(b) shows the radial displacements, and the values plotted are the maximum value that is observed along the length of the rod. While these values are only for the cladding tube itself, the ends of the tube near the end caps affect them. Because the end caps do not creep down as much as the tube itself, these values are only sampled in the cladding along the length of the fuel.

For the Zircaloy cladded fuel rod, the cladding radius immediately begins to decrease. This is largely due to both anisotropic irradiation growth and cladding creep down. This can be identified in Figure 12(b), as the displacement decreases after thermal expansion and before the fuel-cladding mechanical contact. The FeCrAl cladding, however, does not experience the same magnitude of creep deformation as the Zircaloy cladding under these conditions, and therefore, the cladding radius is not reduced.

Gap closure and subsequent mechanical contact occurs in the Zircaloy fuel rod after ~301 days, while in the FeCrAl fuel rods, gap closure does not occur until ~760 days. The gap closure is easily identified by the transition from compressive to tensile cladding hoop stress shown in Figure 13. Further, after mechanical contact between the fuel and the FeCrAl-cladding, the radial displacement quickly begins to increase as the fuel swells. The simulation that only considers elastic cladding behavior indicates that the cladding constricts the fuel and undergoes no plastic deformation. Simulations including creep deformation allow the cladding to relieve stresses formed during mechanical contact by radial expansion of the cladding.

For both cladding materials, the cladding elongation is less than 2.5 cm over the 4 m cladding tube (~.6%) and the maximum radial displacement is nearly 70 μm (~1.4% of the cladding radius) for the FeCrAl cladding versus about 40 μm (~0.8% of the cladding radius) for the Zircaloy cladding. This indicates that, while all of these rods satisfy the requirement of maintaining an equivalent strain below 2.5%, the hoop strain for the FeCrAl-cladded fuel rods is greater than the 1% limit at the end of life. It is important to note that the high FeCrAl cladding hoop stresses are a result of this initial fuel modeling in which the fuel pellet is treated as elastic only, e.g., no smeared cracking or fuel creep is included here, which produces much larger stress and strain in the cladding than expected.

The impact of fuel creep has been systematically evaluated and is described later in a Section 3.6.

Figure 13 plots the maximum cladding hoop stress as a function of time. The cladding is initially in a compressive stress state caused by the difference in the rod plenum pressure and the reactor coolant pressure. Because the FeCrAl cladding thickness is one- half the thickness of the Zircaloy cladding, the hoop stresses that develop are nearly double in the FeCrAl cladding. The cladding stress remains compressive, with minor contributions from increasing plenum pressure or the different FeCrAl mechanical behavior models until mechanical contact occurs. As the cladding is irradiated, irradiation swelling acts to expand the cladding. Azimuthal expansion of the cladding slightly prolongs the onset of gap closure, while radial expansion of the cladding reduces formation of tensile hoop stresses.

Because the magnitude of thermal and irradiation creep for Zircaloy cladding is so large, the Zircaloy cladding tube begins to slowly collapse around the fuel in order to relieve compressive stress from the pressure differential across it; this is known as 'cladding creep-down' (OECD, 2012). The hoop stress in the Zircaloy reaches a tensile value of 160 MPa after extended mechanical contact, and generally maintains a value between 150 and 200 MPa. As mentioned in the material model descriptions in Chapter 3, the creep strain rate of FeCrAl cladding is nearly 4 orders of magnitude lower than Zircaloy at relevant reactor conditions. Thus, the FeCrAl cladding does not experience any significant creep-down, and fuel swelling dominates the gap closure. After mechanical contact occurs in the FeCrAl-cladded fuel rods, the hoop stresses rapidly increase due to both a lack of compliance in the fuel and the cladding. Again, this initial model considers the fuel to be an elastic material.

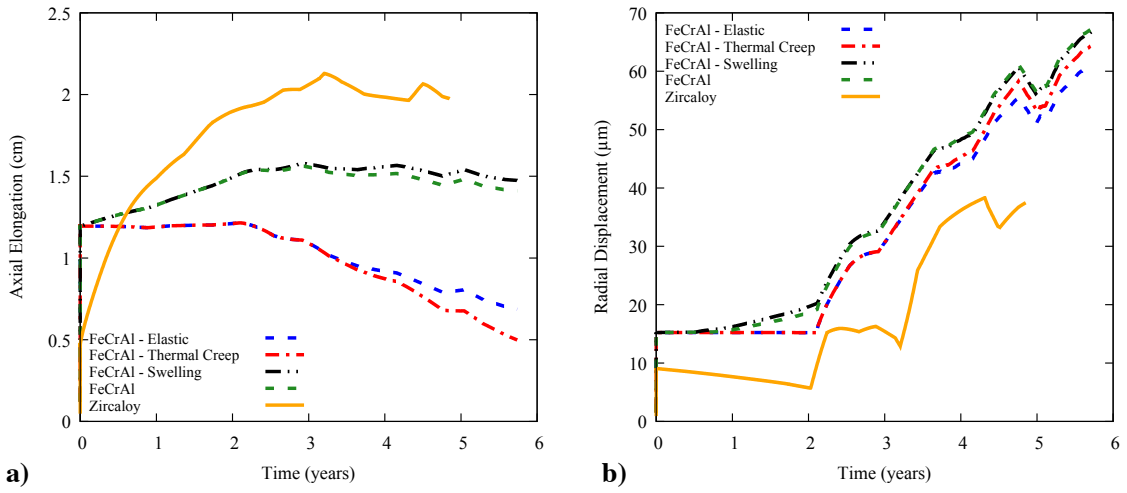

Figure 12. The axial elongation (a) and maximum radial displacement (b) of the cladding is initially due to thermal expansion as the cladding is heated to operating temperature, then, as the cladding begins to creep down, contributions from irradiation swelling for FeCrAl and irradiation growth for Zircaloy become dominant until mechanical contact.

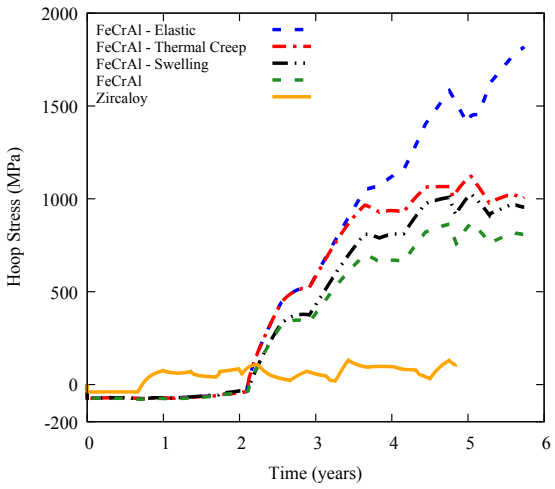

Figure 13. The maximum hoop stress in the cladding as a function of time, comparing the Zircaloy with the different models of FeCrAl cladding. Very large hoop stresses are predicted for FeCrAl cladding in elastic simulations, which are reduced by taking into account thermal creep and swelling but are still much larger than Zircaloy.

A large reduction in the hoop stress at the end of the fuel rod simulations (~750 MPa) can be identified due to the inclusion of the thermal creep model because of its sensitivity to high stresses (the stress exponent in Equation 4 is 5.5), with modest effects from both irradiation creep and swelling. Many of the fluctuations in the hoop stress histories are caused by temperature variations across the length of the fuel as the axial power profiles change. This leads to the development of local areas of increased fuel temperatures that can increase the fuel thermal expansion and swelling. Increased temperatures along the fuel cladding also increase stress relaxation in those areas by increasing the thermal creep rates, because they are also very sensitive to temperature. While this analysis indicates high tensile stresses in the FeCrAl above the alloy yield strength; it is important to note that this is an overly conservative analysis due to modeling the fuel as elastic only without considering fuel creep or smeared cracking.

Fission gas production and release behavior for these fuel rods is shown in Figure 14. Fission gas production (in mol-m^{-3}) is shown in Figure 14(a), and remains very similar for both cladding materials, although there is a slight difference due to the total power produced for each rod. The variation between the Zircaloy and FeCrAl cladded rods is due to the increased power production in the Zircaloy cladded rod towards the beginning of life and the FeCrAl-cladded rod much later. Because all fuel rods with the FeCrAl cladding follow the same power history, the amount of fission gas generated in the fuel is identical.

Fission gas release behavior, however, is observed to be very much different between the FeCrAl and Zircaloy rods, as well as between the different mechanical behavior models for FeCrAl. Figure 14(b) shows the fission gas released to the fuel rod plenum, as a percentage of the fission gas produced. The fission gas release in the FeCrAl cladded fuel

rods increases sharply beginning at 16 months (Figure 14(b)), and is consistent with a sharp rise in the rod average temperature (Figure 11(b)). A substantial effect from irradiation swelling can also be seen beginning at ~2 years and throughout the fuel rod lifetime. This is presumably because of the radial expansion of the fuel cladding and the subsequently increased fuel temperature from a larger fuel-cladding gap. The fission gas released in the FeCrAl cladded rods increases to nearly 4x the amount in the Zircaloy-cladded rods. Later in life, the percentage of gas released then begins to taper off as the fission gas release rate decreases. This occurs because the fuel temperature is cooler later in life, and thus, more fission gas is calculated to remain in the fuel matrix.

Fission gas release in Zircaloy-cladded fuel rods is much different because the power history and correspondingly, the temperature, varies significantly in comparison to the FeCrAl cladded fuel rods. At the beginning of life, the fuel centerline temperature ramps to 1900 K, and the rod immediately experiences significant fission gas release. From there the percentage of gas released decreases until the fuel experiences elevated temperatures again at ~20 months. In this mode of operation, it is difficult to perceive effects from fission gas on the overall performance of the fuel rod. Nonetheless, it can be used to help identify behavior of the plenum pressure in the fuel rod.

The plenum pressure and volume are shown in Figure 15. As mentioned previously in Section 2.3, the initial rod fill-gas pressure is .5 MPa in the rod at standard temperature and pressure. This quickly increases as the fill gas is heated and the fuel and cladding thermally expand during startup. At approximately ~1 year, the FeCrAl cladded fuel rods begin significant fission gas release from the fuel into the plenum, greatly increasing the fuel rod plenum pressure. Because the Zircaloy cladded fuel rods experience much less fission gas release, the plenum pressure remains lower. The scatter in these curves is largely due to the shifting temperature of the fuel and gap regions, where thermal expansion has a pronounced effect. The difference in the FeCrAl family of curves is due to irradiation swelling and the effect it has on fuel temperatures. The plenum pressure in the FeCrAl cladded rods remains below the reactor coolant pressure for the entire 3 cycles, indicating the cladding hoop stress generated from the pressure differential between the fuel rod and coolant pressure is compressive. This is important, as generation of a plenum pressure greater than the system coolant pressure can result in a condition of cladding outward expansion known as “cladding lift-off” (OECD, 2012). In this condition, the internal rod pressure acts to expand the cladding, thus, reopening the fuel-cladding gap, which can begin a thermal-feedback effect with the amount of fission gas released and the plenum pressure.

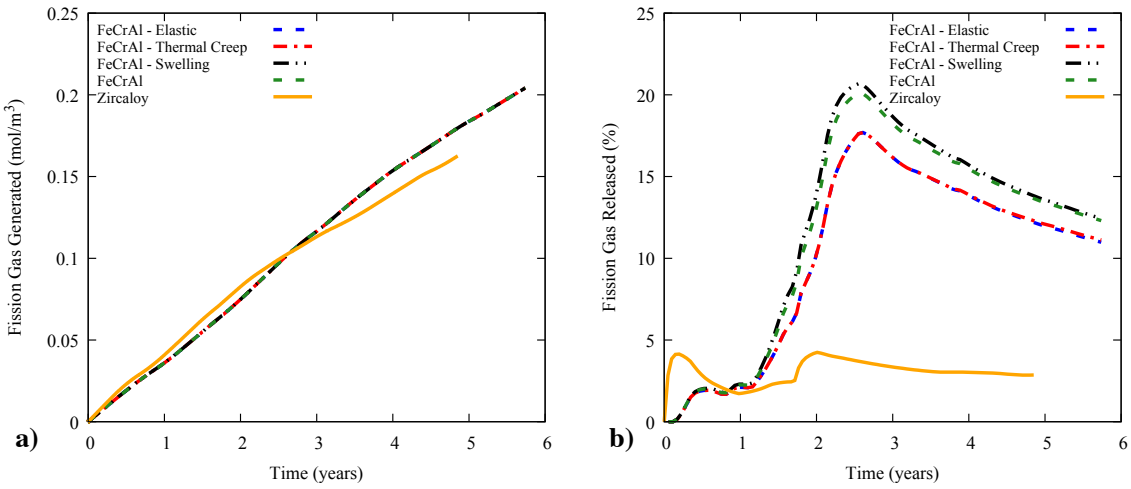

Figure 14. (a) Fission gas generation in the fuel as a function of time for the different, and (b) fission gas release, which is greater for FeCrAl cladded rods, specifically those with irradiation swelling.

Plenum volume shows the effects of dimensional change of both the fuel and the cladding. The volume initially decreases as the fuel expands more than the cladding during the initial rise to operating temperature. The fuel then begins densification, leading to a small increase in the plenum volume. This is more evident in the FeCrAl-cladded fuel rods as the there is a greater volume of fuel to densify and the cladding is less susceptible to creep deformation. The subsequent decrease in plenum volume is largely the axial and radial swelling of the fuel. There is a slight increase in the volume of some FeCrAl rods as irradiation swelling makes a small contribution to cladding dimensions.

Both the FeCrAl and the Zircaloy cladded fuel rods have an initial 100-µm gap between the fuel and inner cladding surface. However, the FeCrAl fuel rods have a larger plenum volume since they have a larger gap radius due to greater fuel mass and decreased cladding thickness. This means that even after mechanical contact has closed the gap between the fuel and the cladding, the FeCrAl cladded rods will contain greater volume in the plenum regions of the fuel rod.

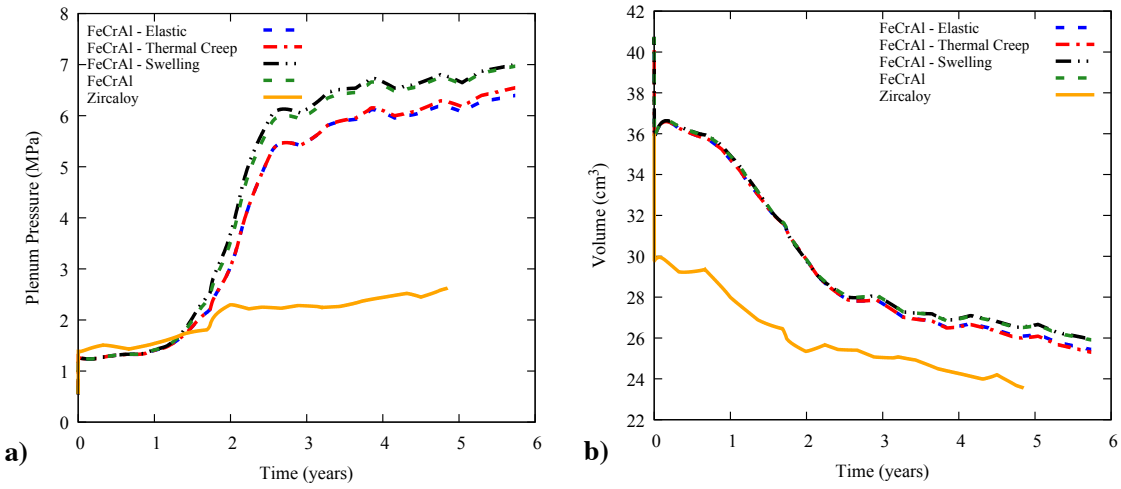

Figure 15. (a) The fuel rod internal plenum pressure as a function of time for the Zircaloy versus FeCrAl rods, which initially increases as the gas is heated from room temperature and begins to increase further as more fission gas is released, shown most prominently by the FeCrAl cladded fuel rods with irradiation swelling models. (b) The plenum volume decreases as the fuel expands and continues to swell, eventually decreasing less as the fuel and cladding achieve mechanical contact.

3.3 Average-Power Operation

In order to more closely model the average fuel rod operation, the linear heat rates from the most limiting cases are scaled by 80%, as described in Section 2.3, to demonstrate operation of an average BWR fuel rod. The peak and average fuel centerline temperatures are shown in Figure 16. Similar to the results from the *Limiting-Power Operation,* there is very slight difference in the maximum fuel centerline temperatures among the FeCrAl clad fuel rods shown in Figure 16(a). A noticeable difference (~40 K) develops at ~2 years, corresponding to a rapid release of fission gas into the rod plenum, shown in Figure 20(b). This acts to degrade the gap conductivity, further increasing the fuel centerline temperature. The effect of gas release is larger in fuel rods that include irradiation swelling, where the fuel-cladding gap is much larger due to isotropic swelling and does not close until later.

The large difference in operating power between the Zircaloy and FeCrAl clad fuel, as mentioned in Section 2.3, is due to the differing power history and axial power profiles generated from the neutronics analysis and implemented into BISON. The average fuel centerline temperatures (shown in Figure 16(b)) among the fuel rods using the two cladding materials are also much different. As shown in Figure 16(b), the FeCrAl cladded fuel rods maintain a much greater average fuel centerline for much of the operation, beginning at about ~2 years, which is similar to the behavior noted in Section 3.2.

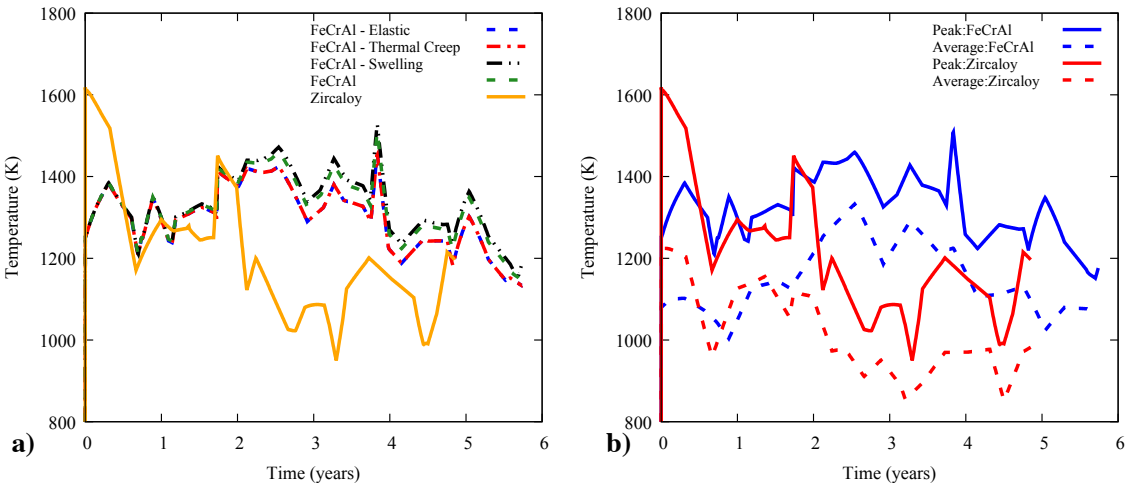

Figure 16. (a) Peak and (b) average fuel centerline temperatures for the different cladding models as a function of time during the average-power operation conditions. These results show a similar overall behavior to the limiting power operation, however, because gap closure occurs much later, there is a more noticeable effect from the inclusion of the irradiation swelling model.

The dimensional change in the fuel rods is altered significantly by reducing the power produced by the fuel rods. Figure 17 shows the axial elongation (Figure 17(a)) and the maximum radial displacement (Figure 17(b)) for the cladding during average-power operation. The immediate increase in axial elongation for all rods is due to thermal expansion of the cladding during the rise to operating temperature. Much like the FeCrAl cladded rods in the *Limiting-Power* operation, irradiation swelling has a substantial effect on cladding elongation. However, the FeCrAl-cladded rods do not achieve fuel-clad mechanical contact until late in life; consequently, the cladding is allowed to elongate without any radial deformation caused by fuel-cladding contact. The onset of fuel-clad mechanical interaction is delayed because the fuel swells and thermally expands much less in this average power condition. This is expected behavior as the gaseous fission product swelling model is sensitive to fuel temperatures. The Zircaloy clad fuel rod also exhibits similar axial elongation characteristics to the *Limiting-Power* companion. Irradiation growth allows the fuel rods to expand axially until mechanical contact occurs, at which point, radial deformation of the cladding begins to reduce the cladding length.

With less fuel expansion, it follows that there is also less radial expansion in the cladding. Figure 17(b) shows the radial displacement of the cladding over its life. The initial increase in the cladding displacement is due to the thermal expansion during the rise to power. The FeCrAl-cladded rods without swelling, (Elastic and Thermal Creep, blue and red dashed lines, respectively), undergo no significant change in the cladding radius until gap closure. However, the rods that include the swelling model quickly begin to expand as the cladding swells isotropically. This acts to increase the fuel rod gap thickness and subsequently delays gap closure. There is a small effect to close the gap from irradiation creep, which

acts to help relieve stress by collapsing the cladding down around the fuel. In this simulation, creep contributes to a decrease in the cladding radius because the coolant system pressure is much larger than the rod internal gas pressure. Effects from irradiation growth and cladding creep-down largely dominate radial deformation of Zircaloy cladding during this mode of operation. After the initial thermal expansion in the cladding, the cladding radius continues to decrease due to anisotropic irradiation growth and cladding creep-down until gap closure.

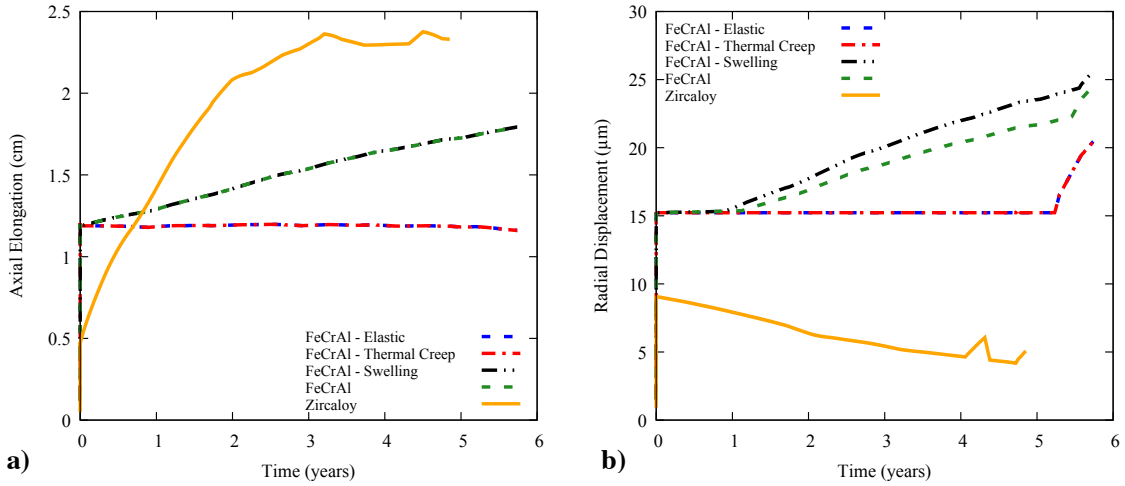

Figure 17. The axial elongation (a) and maximum radial displacement (b) of the cladding as a function of time for the different cladding models. The behavior is similar to the case of *limiting power observation*, although the delayed gap closure leads to greater elongation of the FeCrAl at later times and a decreased radial displacement.

Figure 18 shows the maximum cladding hoop stress that develops during average power operation. Again, the cladding hoop stress is initially in a compressive state due to the pressure differential between the coolant system and the fuel rod plenum. In the FeCrAl-cladded rods, there is a very slight reduction in the hoop stress due to the increase in plenum pressure from fission gas release. Because fission gas release is greater in fuel rods where the cladding includes isotropic irradiation swelling, this reduction in the compressive hoop stress can be can be seen starting at approximately 2 years. Much of the fluctuation in the cladding hoop stresses appears because of the variation in the axial power profiles during operation. At approximately 4.5 years, gap closure and subsequent cladding radial deformation occur in the FeCrAl clad fuel rods without the irradiation swelling model. This occurs because a hot spot in the axial power profile enhances local fuel expansion producing an increase in hoop stress as the fuel pushes on the cladding. This interaction is short-lived, which results with the cladding stress returning to its compressive state determined by the differential pressure across the cladding. Full gap closure occurs in these fuel rods slightly after 5 years, and hoop stresses in the cladding quickly increase immediately after onset. The FeCrAl-cladded rods that include swelling undergo gap closure nearly half a year later due to the associated cladding radial expansion, and the

Zircaloy clad fuel undergoes gap closure about a quarter year sooner due to cladding creep-down. Gap closure behavior is significantly suppressed in the FeCrAl–cladded rods during average power operation. Here, it occurs much later at ~5 years, as opposed to ~2 years during the *Limiting*-Power operation. The maximum cladding hoop stress at the end of life is also reduced when compared with fuel rods from the *Limiting-Power* operation because the radial deformation of the cladding is much smaller.

The Zircaloy cladding develops a much lower initial hoop stress because it is twice the thickness of the FeCrAl cladding and has a slightly smaller effective radius. This means nearly half the compressive stress should develop in the cladding from the pressure differential. The cladding hoop stress remains in this state until gap closure occurs slightly after one year of operation. This is very similar to the behavior seen during the *Limiting-Power* operation. Because the thermal creep rate will remain comparable and the irradiation creep rate will scale with the power, cladding creep-down occurs at a similar rate. The hoop stress after mechanical contact occurs in the Zircaloy-cladded fuel rod also fluctuates as the axial power profile influences radial expansion in the fuel.

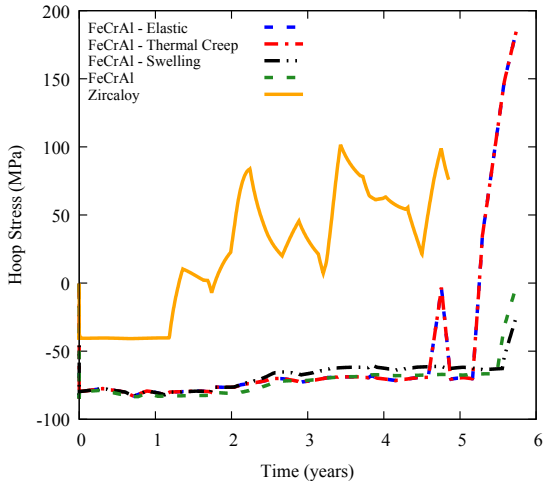

Figure 18. The maximum cladding hoop stress as a function of time for the different cladding models for average power operation conditions. The stress levels are considerably less that those generated in the limiting power operation due to less thermal and fission product swelling in the fuel. Full gap closure for the FeCrAl clad fuel rods is achieved at near the end of the fuel lifetime before considerable stresses have developed.

The amount of fission gas produced in the fuel and the percentage of the gas released to the plenum during average-power operation are shown in Figure 19(a) and Figure 19(b), respectively. As expected, the fission gas generated in the fuel during the *average-power* operation is scaled by 80% relative to the *limiting-power* operation. Because the power produced is the same for all of the FeCrAl-cladded fuel rods, the curves line up exactly.

As a result of the high fuel temperatures the Zircaloy clad fuel experiences at the beginning

of life, fission gas release begins immediately. The percentage of fission gas released increases to a peak at nearly 1.2% and tapers off as more fission gas generated in the fuel. This is similar behavior, while decreased in magnitude, to the *Limiting-Power* operation. The FeCrAl-cladded fuel rods do not release an appreciable amount of fission gas until the second year of operation. Here, fission gas release begins to rapidly increase as the fuel temperature begins to increase. There is a large effect due to the inclusion of the irradiation swelling and a more moderate effect from irradiation creep models. Irradiation swelling acts to expand the cladding and increase the gap thickness, which impedes heat-transfer from the fuel to the cladding. This increase in fuel temperature subsequently increases the fission gas release. Irradiation creep counteracts this by allowing the cladding to creep-down and decrease the gap thickness.

At the end of life in average-power operation, the FeCrAl-cladded rods release ~2.5 - 5% of gas generated, compared to ~10 - 13% during the *Limiting-Power* operation. Fission gas release in the Zircaloy clad fuel is significantly lower at ~.5% for average-power operation and ~3% during limiting-power operation. As a result of the lower fuel temperatures for much of the later life, the Zircaloy-cladded fuel rod releases much less fission gas that its FeCrAl-cladded companion.

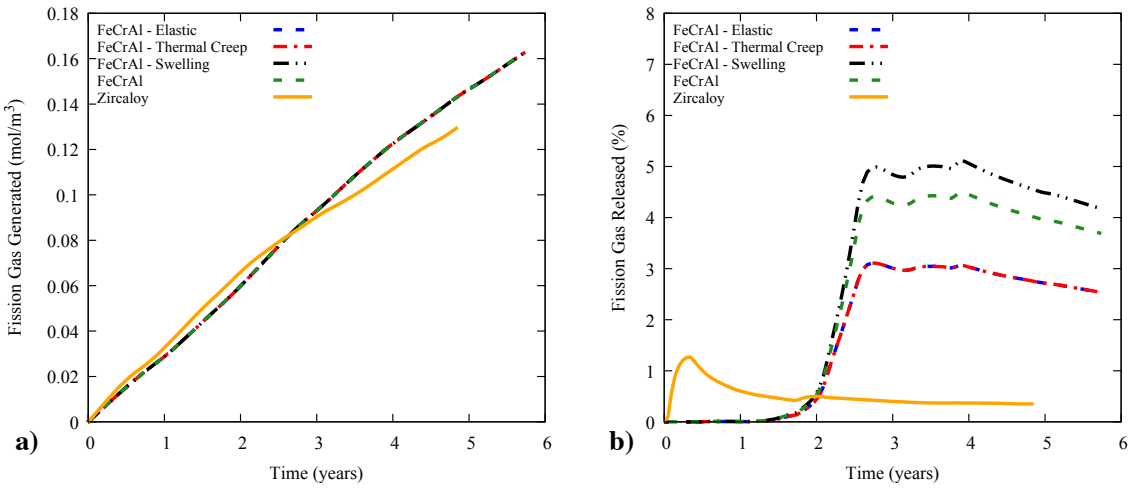

Figure 19. (a) The amount of fission gas generated in the fuel, and (b) fraction of fission gas released to the plenum during average power operation conditions. The amount of fission gas produced scales perfectly by 80% compared to the *Limiting-Power Operation***,** while the percentage of fission gas released is greatly reduced due to lower fuel temperatures.

Fuel rod plenum pressure and plenum volume are shown in Figure 20. The initial fill-gas pressure for these rods is .5 MPa, which quickly increases as the fuel rod heats to operating temperature. After the initial ramp to power, the plenum pressure for the FeCrAl-cladded fuel rods remains relatively unchanged until fission gas release occurs just after two years of operation. Because the plenum pressure is sensitive to the amount of gas present,

features from the amount of fission gas released (Figure 19(b)) can be seen clearly in the plot of plenum pressure (Figure 20(a)). More fission gas is released in the FeCrAl clad fuel rods which include the irradiation swelling model, due to their increased fuel temperatures. The contribution of the fission gas to the plenum pressure in the Zircaloy-cladded fuel rods is relatively insignificant, as such; changes in the plenum pressure show similar features to the plenum volume. These plenum pressures remain much lower than the rods shown in the *Limiting-Power* operation, due to the decreased fission gas release and the fuel temperatures.

The plenum volume, shown in Figure 20(b), initially decreases as the fuel rod is heated to operating temperature. This occurs as the fuel thermally expands more than the cladding. Immediately after the initial ramp to operating power, the fuel begins densification, thereby increasing the plenum volume as the fuel contracts. When the fuel has completed densification, fission product swelling and fuel pellet relocation then begin to help expand the fuel. After fuel cladding contact has occurred, the plenum volume is then decreased as the fuel swells and temperatures vary causing axial variation in the pellet stack height.

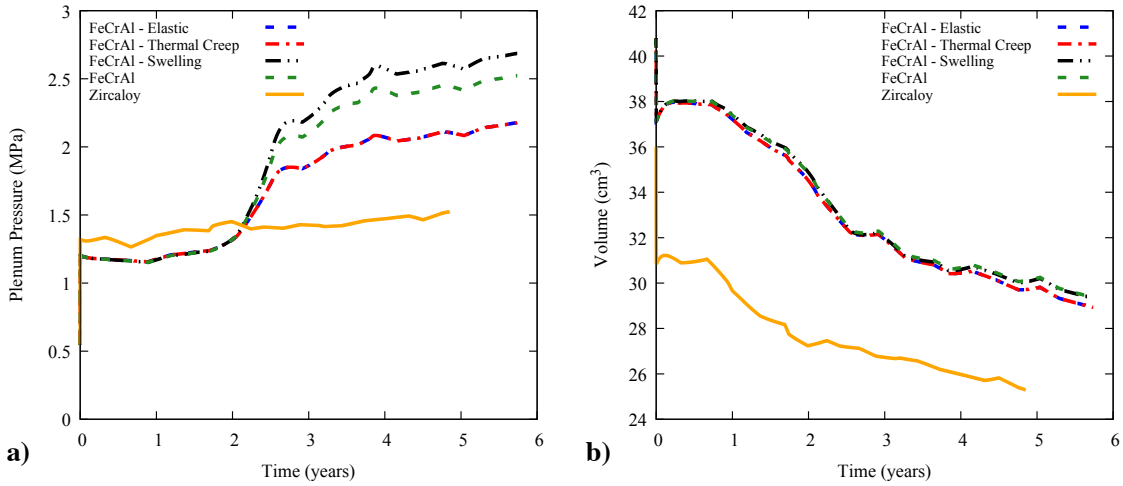

Figure 20. (a) The fuel rod plenum pressure and (b) plenum volume as a function of time and the cladding model during average power operating conditions. The plenum pressure increases rapidly for FeCrAl cladded fuel rods corresponding to an increase in the amount of fission gas released, with greater effects in simulations where the cladding model includes irradiation swelling. Because the Zircaloy clad fuel does not release an appreciable amount of fission gas, the plenum pressure remains much lower than the FeCrAl cladded fuel rods. The plenum volume (b) shows similar features to the *Limiting-Power operation*, where the fuel densifies and begins to expand reducing the cladding volume.

3.4 Simplified-Power Operation

For this analysis, the fuel rods were ramped to a linear heat rate of 18 kW/m and held at this power to a rod average burnup of 60 MWd/kgU. This operation was performed to investigate the integral and coupled behavioral evolution of the fuel rods.

Figure 21 displays a comparison between the peak fuel centerline temperatures (Figure 21a) between all five of the fuel rods and a comparison of the average fuel centerline temperatures (Figure 21b) of the full FeCrAl-cladded rod and the Zircaloy-cladded rod. The fuel centerline temperatures initially increase from room temperature as the rod ramps up to steady-state power. Fuel temperatures in the FeCrAl-cladded rods begin to increase as the fuel thermal conductivity begins degradation. This also affects the Zry-cladded fuel rods, but reduction of the gap region due to creep deformation in the cladding acts to counteract this. Because the FeCrAl has very little creep deformation, the gap thickness between the fuel and cladding is largely dictated by fuel displacement. Figure 21(a) shows a significant temperature increase for the FeCrAl-cladded rods that include irradiation swelling, and a much small reduction in temperature from the inclusion of irradiation creep. This is due to the increased gap size that develops as the cladding diameter increases from irradiation swelling. The simulation including the irradiation creep shows counteracting gap closure. These effects can also be seen in the maximum radial displacement shown in Figure 22(b).

At approximately 20 MWd/kgU, fission gas release from the fuel begins to degrade the gap conductivity, and the fuel centerline temperatures begin to increase. These temperatures reach a maximum near ~35 MWd/kgU, where fuel expansion begins to close the gap enough to counteract the effects of fission gas release on gap conductivity. The maximum fuel centerline temperatures decrease as the fuel and cladding undergo mechanical interaction along the rod, beginning at ~45 MWd/kgU. The final increase in temperature at the end of the simulation is a result of the degraded thermal conductivity of the fuel and the poor gap conductivity where gap closure has not occurred.

The difference in fuel centerline temperatures among FeCrAl clad fuel is due to the irradiation-induced swelling in the cladding. By increasing the diameter of the cladding, the size of the fuel-cladding gap is increased impeding heat transfer from the fuel to the cladding. This causes increased temperatures, which because of model sensitivity contributes to greater fission gas release. The Zircaloy clad fuel, however, behaves much differently than its FeCrAl clad counterpart. After the initial power ramp, the cladding begins to creep-down toward the fuel due to the pressure differential between the rod fill gas pressure and the reactor coolant pressure. This allows gap closure to occur much sooner than the FeCrAl rods at approximately 25 MWd/kgU. By reducing the gap size, the temperatures of the fuel are reduced. Because the Zircaloy contains less fuel mass, the rod burn-up increases faster. This causes the thermal conductivity of the fuel in the Zircaloy to degrade faster, seen in Figure 21(a) after ~25 MWd/kgU. In this case, lower fuel temperatures delay the onset of large-scale fission gas release from the fuel, thereby limiting the degradation of gap conductivity before mechanical interaction.

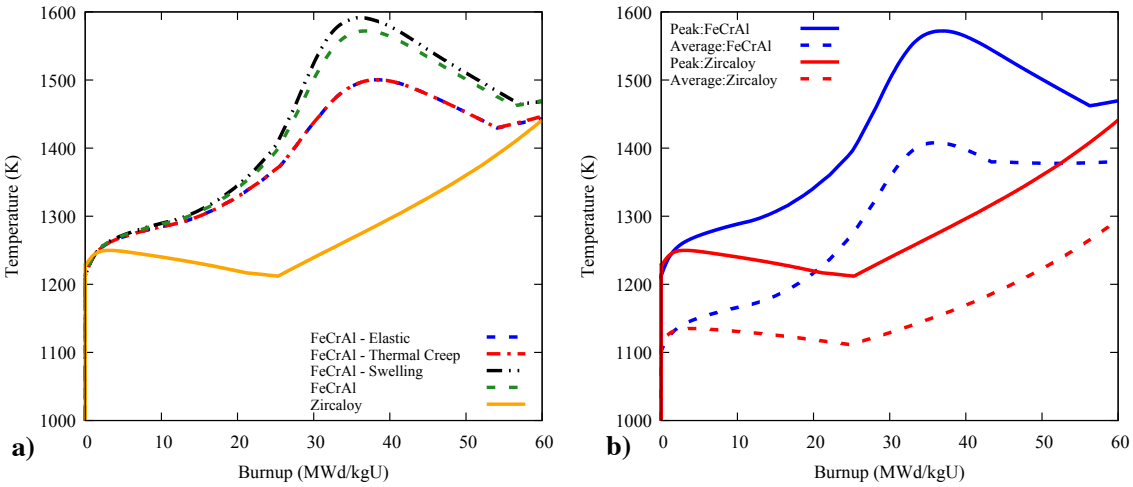

Figure 21. Peak (a) and average (b) fuel centerline temperatures as a function of burnup for simplified power operation. The peak fuel centerline temperature behavior for FeCrAl is nearly unaffected by the inclusion of thermal creep, however there is a large increase in temperatures from the inclusion of irradiation swelling and a much smaller effect from irradiation creep. Zircaloy cladding remains much cooler as the fuel cladding gap begins to close much sooner. The average centerline temperatures for these simulations are significantly lower than the peak centerline temperatures because of the axial power profile shape (shown in Figure 7(b))

The axial elongation and maximum radial displacement of the fuel rod cladding under simplified operation are shown in Figure 22. After the initial thermal expansion, the FeCrAl cladding shows very clear elongation due to irradiation swelling in the cladding, even after mechanical contact has occurred at ~42 MWd/kgU. Zircaloy shows a similar trend due to irradiation growth, where the cladding elongates until significant fuel-cladding mechanical contact begins to increase the fuel radius, counteracting the axial elongation. The FeCrAl-cladded fuel rods that do not include irradiation swelling remain essentially the same length until mechanical interaction occurs.

The FeCrAl-cladded fuel rods modeled with irradiation swelling also show much more radial expansion. FeCrAl-cladded rods without irradiation swelling simply remain the same radius after initial thermal expansion until mechanical interaction. Zircaloy, as mentioned in Section 2.5, experiences several orders of magnitude more thermal and irradiation creep than FeCrAl under identical conditions. This allows the Zircaloy-cladding to slowly collapse around the fuel due to the pressure differential between the plenum pressure and the reactor coolant pressure. It is worth noting again that, in the Zircaloy-cladded rod, gap closure occurs before the sharp increase in radial displacement because the cladding tube wall near the ends does not creep down as much as the other areas. This is due to the additional structure that the cladding end caps provide.

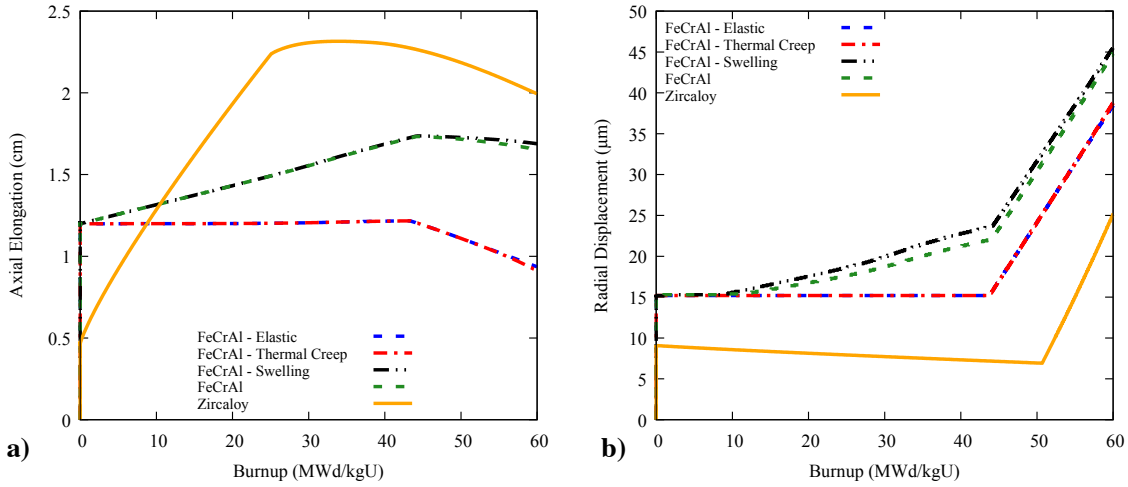

Figure 22. The axial elongation (a) and maximum radial displacement (b) for the Zircaloy versus FeCrAl cladding as a function of burnup for simplified power operation. The axial elongation of FeCrAl cladding is largely determined by irradiation swelling until mechanical contact occurs, where the elongation is reduced as the fuel pushes the cladding out radially. For Zircaloy, a similar relationship exists for irradiation growth, where axial elongation is counteracted by mechanical contact. The maximum radial displacement for the FeCrAl cladding is increased by the presence of isotropic irradiation swelling until mechanical contact occurs. The maximum radial displacement for Zircaloy is slowly reduced due to anisotropic irradiation growth in the axial direction until mechanical contact occurs.

The maximum hoop stress, shown in Figure 23, as with the other operational cases, is compressive due to the pressure differential across the cladding until gap closure. It shows a small reduction in compressive hoop stress due to an increase in plenum pressure as fission gas is released from the FeCrAl clad fuel beginning at 25 MWd/kgU. After gap closure occurs, the hoop stresses quickly become tensile as the fuel starts expanding against the cladding.

Much like the other modes of operation, the hoop stress in the FeCrAl cladding rapidly increases after the onset of gap closure. Figure 23 shows the effects of including each of the FeCrAl material models and the difference in stress reduction between types. At the end of the simulation, slight stress relaxation from irradiation creep can be observed. Just as the previous operational modes showed, the Zircaloy-cladded rod undergoes mechanical contact much sooner than the FeCrAl-cladded rods (~20 MWd/kgU earlier), although the maximum hoop stress saturates at a much lower value. For the Zircaloy-cladded fuel rod, gap closure occurs before fission gas release becomes prominent.

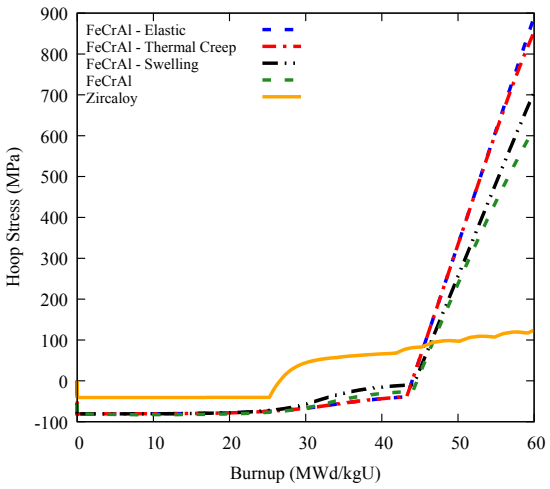

Figure 23. The maximum hoop stress in the cladding as a function of time, comparing the Zircaloy with the different models of FeCrAl cladding for simplified power operations. The maximum hoop stress in the Zircaloy cladding saturates at nearly 100 MPa, while the Hoop stress in the FeCrAl cladding rapidly increases. There is a small reduction due to irradiation swelling, and a further reduction from irradiation creep.

The fission gas generated for both cladding types is shown in Figure 24(a). The fission gas generated is different for the FeCrAl-cladded fuel rods and the Zircaloy because of the difference in fuel mass between the rod geometries. Because the FeCrAl-cladded fuel rods contain greater fuel mass, they will generate more fission gas than the Zircaloy-cladded rods at a specified fuel utilization.

The amount of fission gas released is heavily dependent on temperature, and therefore varies greatly, even among FeCrAl-cladded fuel rods. Irradiation swelling causes large expansion of the cladding radius, increasing fuel temperatures and further accelerating the amount of fission gas released. For the FeCrAl-cladded fuel rods, significant fission gas release begins around 20 MWd/kgU and increases until 40 MWd/kgU where it begins to plateau. The Zircaloy clad fuel, however, remains cooler through much of the fuel operation thus the onset of fission gas release is significantly delayed.

The fuel rod plenum pressure and volume are shown in Figure 25. The constant power operation allows the effects of the individual material models to be seen quite clearly. Plenum pressure, shown on the left, initially increases from .5 MPa at the beginning of the simulation, to ~1.2 MPa after the fuel rods heat up. Because the plenum volume (Figure 25(b)) is quite large, a reduction in available volume for the fission gas only causes a minor pressure increase. The FeCrAl-cladded fuel rods show large pressure increases corresponding at the onset of fission gas release and continue to increase with fuel utilization.

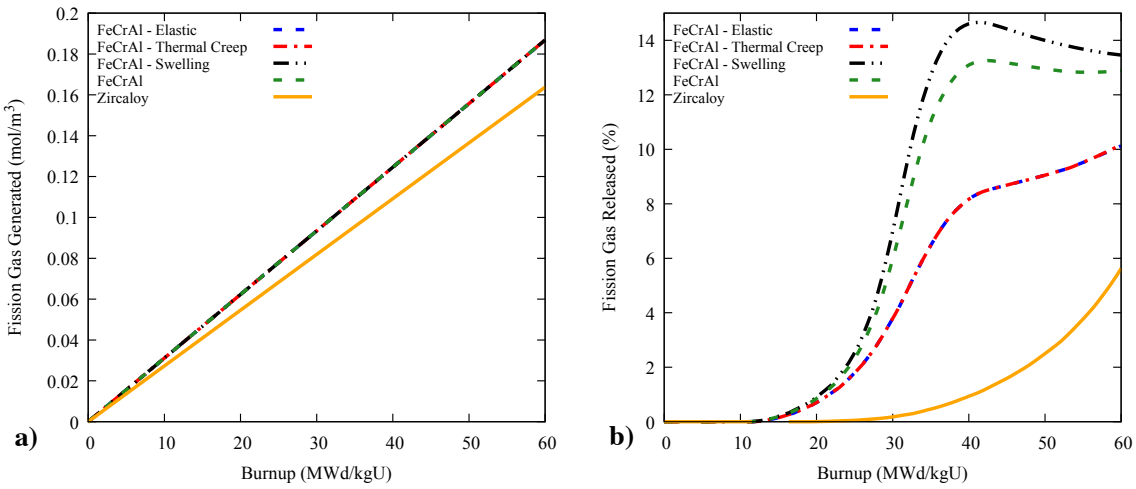

Figure 24. a) Fission gas generation in the fuel as a function of burnup for the different fuel cladding, and (b) fission gas release for simplified power operation. There is a slight difference in fission gas production between FeCrAl and Zircaloy cladded fuel due to the difference in fuel mass, and the gas generation linearly increases with burnup. The amount of fission gas released to the fuel rod plenum is strongly dependent on the fuel temperatures, and rapidly increases as the fuel temperatures increase.

There is a large difference in the plenum pressure evolution of these rods based on the mechanical behavior of the different FeCrAl models and the coupled effects of fuel temperature and gap size on fission gas release. As the FeCrAl-cladded rods approach 60 MWd/kgU, they approach the coolant operating pressure of 7.136 MPa. This is concern for safely operating these rods at higher temperature and burnup because the plenum pressure should not exceed the coolant system pressure. Doing so causes a change in the creep behavior of the fuel rod and allows the cladding to begin to creep away from the fuel due to the pressure differential. This can increase the fuel temperatures as the gap reopens and further exacerbate the temperature-pressure feedback. The Zircaloy-cladded fuel rod shows a similar trend of increasing plenum pressure sharply as more fission gas is released from the fuel, although the pressure increase is not quite as large as that of the FeCrAl-cladded fuel rods.

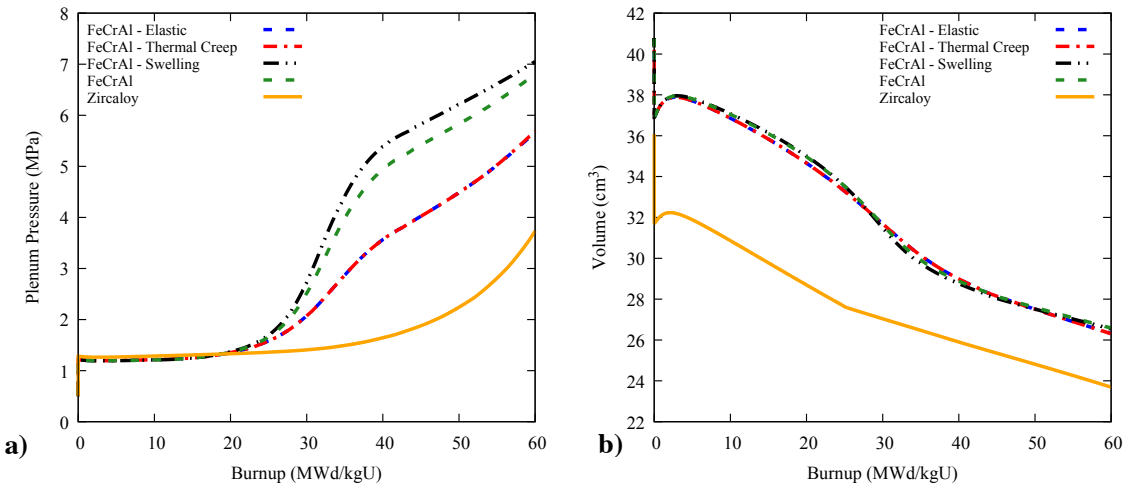

Figure 25. The fuel rod plenum pressure (a) remains relatively constant until fission gas begins to release into the plenum. At this point, the fission gas release correlates directly to a plenum pressure increase. The plenum volume (b) initially decreases as the fuel thermally expands more than the cladding during startup. There is a small increase in volume as the fuel densifies, and a continued decrease as the fuel begins to expand, reducing the cladding volume.

The plenum volume is shown in Figure 25(b). As the fuel is initially heated, it begins to expand into the gap and plenum regions. Immediately, the fuel begins densification, reaching a maximum at ~4 MWd/kgU. At this point fuel swelling and relocation begin to control the reduction in plenum volume. This fuel expansion behavior is similar for both cladding materials, however, because of differing fuel rod geometries and cladding creep responses, the plenum volume for the FeCrAl clad fuel rod is predicted to have a much greater reduction over the same fuel utilization.

3.5 Cladding Thermal and Irradiation Creep Analysis

Our initial analysis, albeit without smeared cracking or fuel creep included in the fuel, predicts very large tensile hoop stresses forming in the FeCrAl cladding which in some instances were prohibitively large during normal operation. This was determined to arise due to a lack of compliance in both the fuel and cladding materials. Because stress-relief mechanisms, such as smeared cracking, were not implemented in modeling the fuel behavior, which is known to fracture during the rise to power. The fuel pellet radius dimensions used here are non-prototypic, and, thus, constitutive models for fuel thermal and irradiation creep were not considered.

In order to mitigate these large stresses, the influence of cladding compliance was analyzed through a systematic variation of thermal and irradiation creep models for the FeCrAl cladding. Based on the results of the operational analysis and the belief that the thermal creep rate model used was conservative, it was suggested to identify what creep rates would

be necessary to significantly reduce the maximum hoop stresses formed in the FeCrAl cladding.

In order to perform this analysis, a series of simulations were performed to identify effects of varying parameters from the irradiation (Equation 3) and thermal (Equation 4) creep rates. The irradiation creep pre-factor was varied along with the thermal creep pre-exponential and activation energy. The simulations performed used the simple axial power profile and constant 18 kW/m linear heat rate, as well as the same geometry used for all FeCrAl-cladded fuel simulations.

Figure 26 shows contour plots of the maximum cladding hoop stresses at the end of the fuel rod operation as a function of the thermal creep activation energy and pre-exponential terms. The plots demonstrate the variation in the irradiation creep. Figure 26(a) uses the same irradiation creep pre-factor used in previous analysis (0.5×10^{-6} MPa^{-1}-dpa^{-1}), while Figure 26(b) uses the pre-factor increased by an order of magnitude (0.5×10^{-5} MPa^{-1}-dpa^{-1}).

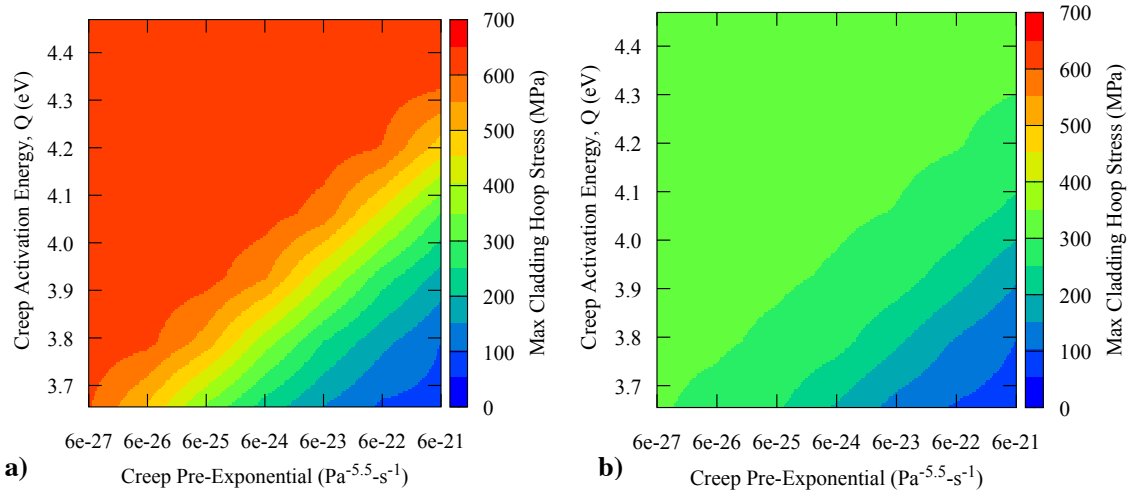

Figure 26. Contour plots of the maximum cladding hoop stress at 60 MWd/kgU as a function of thermal creep pre-exponential and activation energy for irradiation creep pre-factors of 0.5×10^{-6} (a) and 0.5×10^{-5} (b) show the sensitivity of the cladding stress state to combinations of thermal and irradiation creep parameters and creep regimes where cladding stress is relieved.

Current FeCrAl cladding thermal and irradiation creep models are near the region where hoop stress formed during mechanical contact is relieved. Significant changes to the irradiation creep rates lead to sizable reductions in the stress contours in all regions. This shows that small improvements in creep behavior may allow large stresses to be reduced below the yield strength of the alloy. This is important for accident or high-power scenarios where fuel swells rapidly with increasing exposure. In earlier simulations using elastic fuel, the maximum hoop stress in the FeCrAl cladding increases rapidly after mechanical contact

and does not reach a level where it saturates. The Zircaloy cladding, however, saturates due to its sensitivity of creep deformation to the applied stress. In order to design a cladding that can accommodate rapid deformation from fuel swelling, ratcheting, or relocation, alloy designs to modify the plastic response of the cladding should be considered. Cladding with little to no creep deformation will rely on fuel compliance to remain in a manageable stress range during mechanical contact events.

3.6 Fuel Creep Analysis

As discussed previously, uncertainty in the models used to simulate the fuel compliance were identified. This led to an examination of the influence of using fuel creep models (outlined in Chapter 2) currently implemented in BISON. As presented earlier in this chapter, a scoping study was performed to determine how neglecting creep deformation in the fuel would influence the cladding deformation and stress state. After consideration of the fuel creep model in Section 2.6, it was determined there is a degree of uncertainty in this model, centered on the usage of a thermal-activation term for the contribution from fission-induced creep. In order to identify the effect of changing the fission-induced creep contribution from the thermally-activated term to the athermal term on the stress state in the fuel and cladding, additional simulations were performed and are described in this section.

To preface this analysis, a short review of the available experimental data gathered from the literature was prepared. Of the original data used to develop this model, only a limited amount of raw data is currently available because many of these results were not widely published or only received limited circulation as internal institutional reports. Figure 27 shows a fit of the measured creep rate from several of these experiments (Bohaboy et al., 1969; Perrin and Wilson, 1971; Solomon et al., 1971) against the calculated creep rate using the full fuel creep model described in Chapter 2, Equation 9. The results from Bohaboy et al. were produced from thermal creep tests at intermediate stresses (10 – 100 MPa) and high temperatures (1800 – 2000 K), compared to expected LWR fuel conditions, for a variety of theoretical densities (92 – 98%) and fuel grain (4 – 35 μm) sizes. This data is generally the main source of the calibration for the thermal creep contribution in the model, although tests were only performed over a limited temperature range. None of the tests performed by Bohaboy et al. included irradiation.

Perrin et al. conducted both in-pile and out-of-pile creep tests for a variety of UO_2 samples to characterize the fuel response for use in liquid metal fast breeder reactor fuel elements. These creep tests were performed at low stresses (10 – 27 MPa) and intermediate temperatures (1400 – 1600K), compared to the expected conditions in an LWR, and with a consistent grain size (26μm) and fuel density (97.8% TD). The fission rate for the in-pile creep samples varied between 1.7e18, 4.0e18, and 1.2e19 fissions/m^3/s.

Solomon et al. provides a consolidation of several in-pile creep experiment results. The fuel samples compiled include: compression (Sykes and Sawbridge, 1969) and tension (Solomon and Gebner, 1972) of helical UO_2 springs, compression of UO_2 disks

(Brucklacher and Dienst, 1970), and three-point bend tests (Clough, 1970). Many of these tests were conducted at low to intermediate temperatures (~400K, 700 – 1200K) and low stresses (6 – 35 MPa), and each of these different tests use different fuel parameters fuel densities (<95% TD), grain sizes (8 – 30 µm) and fission rates (2e18 – 2e20 #/m^3/s). Figure 27 plots each of these data sets separately according to the reported fuel creep rates from these experiments, and the expected creep rates calculated from the fuel creep equation as its described in Hagrman et al (Hagrman et al., 1995). The unirradiated data by Bohaboy et al. (Bohaboy et al., 1969)shows good agreement with the high temperature creep relation, but the irradiated samples and much of the data from Perrin et al.(Perrin and Wilson, 1971) show large deviations from the expected result.

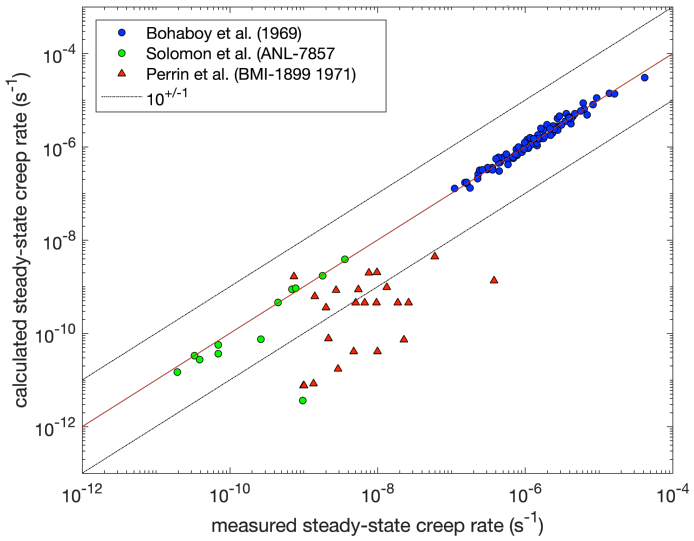

Figure 27. The calculated versus measured steady-state creep rate for the fuel shows good agreement at high creep rates for unirradiated samples (Bohaboy et al., 1969), however there is a large spread of data for both irradiated and unirradiated samples (Perrin and Wilson, 1971; Solomon et al., 1971) at low strain rates.

To determine the effect of changing the fission-induced creep contribution term, only the experimental results including irradiation are reassessed using both the thermally-activated creep term and the athermal term. Figure 28 shows the calculated vs measured creep rates for the full creep model, separately evaluating both fission-induced creep contributions. While there is generally better agreement using the Arrhenius term to describe the temperature dependence of the fission-induced creep, it is also the more likely model to under predict the experimental fuel creep rate, at least for the conditions of these experiments. The solid black lines in these figures demonstrate boundaries of an order of magnitude above and below the ideal solution, shown as a solid red line.

On a side note, the outlying point in the Solomon et al. data in Figure 28(a) is the lowest temperature test data available (~383K). As shown in Figure 28(b) the calculated creep rate for this test is increased by approximately two orders of magnitude using the athermal creep

term, implying that this may more accurately describe the low temperature UO_2 behavior. While a single data point is inconclusive and the temperature is much lower than normal operating temperatures in the fuel periphery, this highlights an operational regime where additional fuel creep tests are needed.

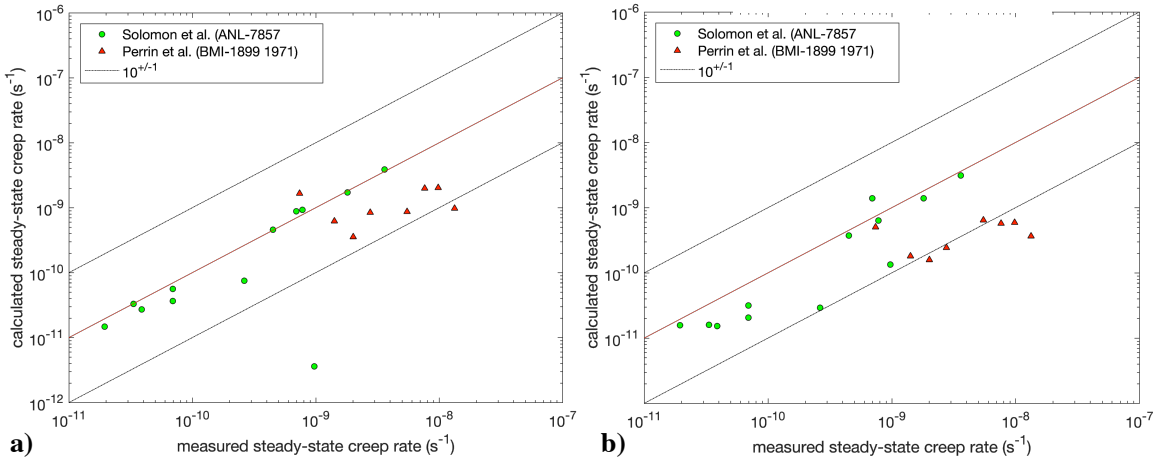

Figure 28. The calculated vs measured fuel creep rate using the thermally-activated fission-induced creep term (a) and the athermal fission induced creep term (b) for in-pile fuel creep tests.

In order to provide a qualitative estimate of the effects of variations in the fuel creep model on the FeCrAl cladding stress state, a rudimentary simulation was performed. In this simulation, the fuel creep rate was varied using a scale factor under the constant operating conditions utilized earlier in this chapter and described in Chapter 2. The fuel creep rate in these simulations was scaled using the model as its implemented, reducing the creep rate by one and two orders of magnitude, and finally by neglecting the fuel creep model altogether. The cladding hoop stress for this comparison is shown in Figure 29. This demonstrates that by decreasing the fuel creep by a single order of magnitude, the cladding stresses quickly begin to resemble those calculated using the elastic fuel approximation, and it further emphasizes how sensitive the FeCrAl cladding stress-state is to fuel compliance.

In the previous sections of this chapter, the fuel was modeled without thermal and irradiation creep, as explicit fracture models were not considered. This assumption was motivated by the expectation that fuel creep would be greatly over-predicted without modeling fracture and the accompanying stress relief. In this section, the fuel creep rate model is varied in order to determine the impact of this assumption on the cladding deformation and stress state. This analysis was performed using the same geometric models and reactor operation as in Section 3.4-5. The fuel was simulated at a constant linear heat rate of 18 kW/m to a rod average burnup of 60 MWd/kgU. However, for this analysis, the fuel is modeled: as an elastic material without creep, using the creep model as described

by Hagrman in Section 2.6, and with the fuel creep model including the modified fission-induced creep.

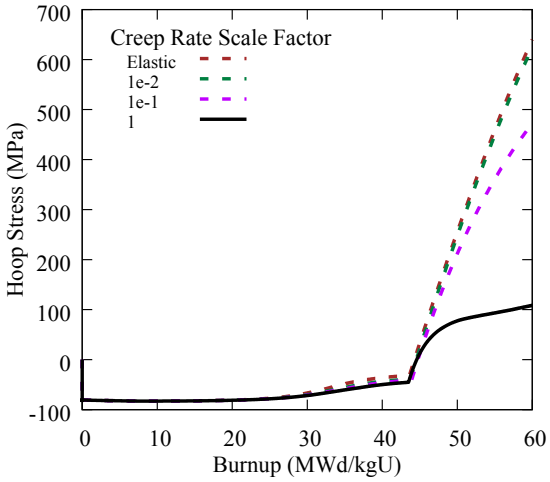

Figure 29. The FeCrAl cladding hoop stress is initially in a compressive state due to the pressure differential between the plenum pressure and the coolant system pressure. As gap closure occurs, the cladding hoop stress quickly becomes tensile. By gradually decreasing the scale factor for the fuel creep rate, the maximum cladding hoop stress increases until it reaches the elastic fuel approximation.

Figure 30 shows the maximum cladding radial displacement and cladding hoop stress for both Zircaloy and FeCrAl, with and without the fuel creep model enabled. The radial displacement of both cladding materials, shown in Fig. 17a, increases due to thermal expansion as the fuel rods ramp up to steady-state operation. For Zircaloy, the cladding displacement immediately begins to decrease due to a combination of anisotropic irradiation growth and creep down from the pressure differential between the fuel rod plenum pressure and the coolant system pressure. Zircaloy cladding continues to creep-down until mechanical contact occurs at nearly 25 MWd/kgU with and without fuel creep. It is important to note that, while these values are only for the cladding tube itself, the maximum displacement is sampled from the cladding along the length of the fuel stack. This shows that with the creep model as implemented, the Zircaloy cladding radius is actually ~10 μm smaller at 60 MWd/kgU. Modeling the fuel as an elastic material, without fuel creep, allows the fuel to push the cladding outward, resulting is an increase in the radius of ~30 μm more than the simulation with fuel creep.

FeCrAl cladding shows a stark difference in behavior after mechanical contact has occurred at ~42 MWd/kgU. By including fuel creep in the simulation, the fuel only expands a small amount, limited by the stiffness of the cladding. This decreases the radial deformation in the cladding from mechanical contact by about 15μm.

The maximum cladding hoop stress for these simulations, shown in Figure 30(b), is initially compressive, until significant amounts of fission gas are released to the fuel rod plenum or the onset of gap closure has occurred. For the Zircaloy, there is a subtle reduction in the hoop stress (~100 MPa) at 60 MWd/kgU as a result of the increased compliance from enabling the fuel creep model. The FeCrAl cladding sees a much greater reduction (~500 MPa) in hoop stress, and the stress seems to saturate around 100 MPa.

Figure 31 shows the maximum cladding radial displacement (Figure 31(a)) and cladding hoop stress (Figure 31(b)) for both Zircaloy and FeCrAl, and compares the original fuel creep model and the modified fuel creep model. These results show a much more understated change since the only difference between them is the modification of the fission-induced creep term. For Zircaloy, the maximum radial displacement is slightly increased (~10μm), and the hoop stress in the cladding (Figure 31(b)) is only slightly modified (< 10MPa). Similarly, for the FeCrAl cladding, there is a slight increase in the radial displacement, and the fuel is less compliant after modifying the creep model. Using the modified fuel creep models, the fuel deforms less due to mechanical contact, expanding the cladding further than the original model and generating somewhat higher hoop stresses in the FeCrAl cladding.

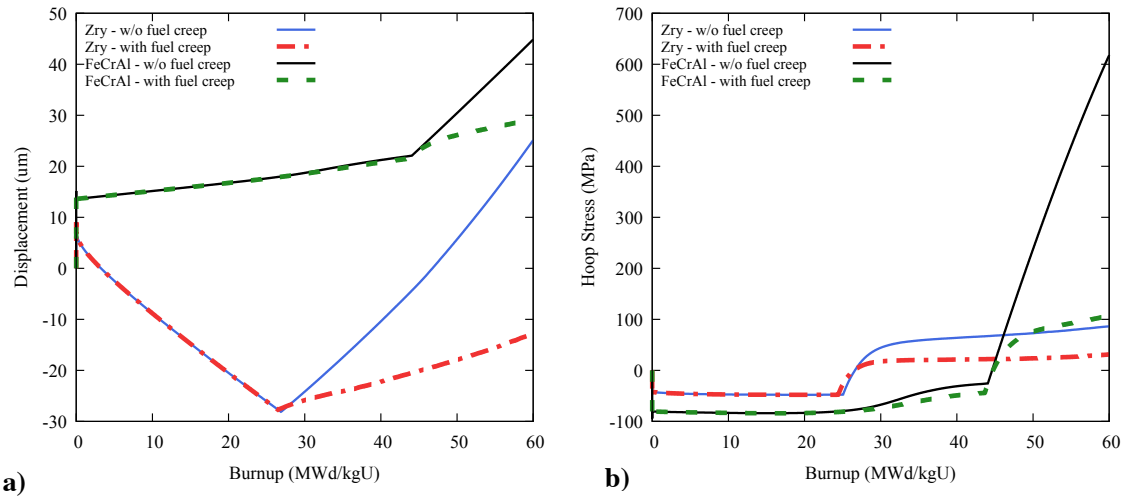

Figure 30. The maximum radial displacement (a) and maximum cladding hoop stress (b) are generally reduced for both FeCrAl and Zircaloy cladding by modeling fuel creep, as compared to fuel modeled as an elastic material. FeCrAl alloys, however, because of their limited creep response after mechanical contact with the fuel, show a much greater impact by increasing fuel compliance.

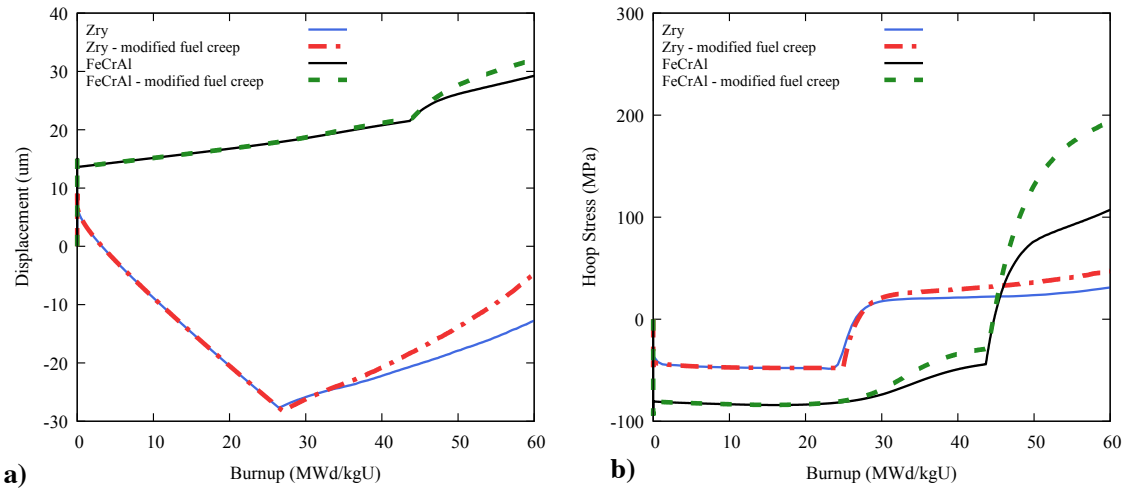

Figure 31. By modifying the fission-induced creep contribution in the fuel, the maximum radial displacement (a) for the FeCrAl alloy is increased after the onset of mechanical interaction, compared to the as implemented fuel creep model. For the Zircaloy, however, the maximum radial displacement of the cladding tube never extends beyond areas near the end caps. The maximum cladding hoop stress (b) for the FeCrAl is also increased from modifying this model, while Zircaloy, again, shows a very limited effect.

While fuel creep in this operation has nearly no effect on the burnup for gap closure to occur, it greatly changes the cladding and fuel mechanical response after the gap has closed. These results illustrate that, because FeCrAl and Zircaloy behave so differently, uncertainties that present minute effects on Zircaloy may have profound performance ramifications for FeCrAl cladding, and while the focus has been on developing cladding behavioral models, fully developing fuel constitutive models is necessary to predict cladding behavior after mechanical contact has occurred.

3.7 Parametric Analysis of Fuel Rod Design

A parametric analysis was performed on the fuel rod radial geometry specifications to determine the optimal fuel cladding gap based on the integral performance of the FeCrAl cladded fuel rods. This was motivated by the need to increase the fuel mass and change the cladding thickness in the FeCrAl cladded fuel rods to offset the neutronic penalty of the alloy, and because of the difference in the gap closure behavior of the Zircaloy and FeCrAl cladding. As shown in Sections 3.2-4, the Zircaloy cladding generally experiences gap closure much faster than the FeCrAl due to the greater magnitude of thermal and irradiation creep deformation. Because of the relatively quick gap closure of Zircaloy cladded fuel rods, these rods generally exhibit lower fuel temperatures and less fission gas release from the fuel for much of their utilization. This analysis is performed using a variety of radial fuel geometries, shown in Table 4, generated by varying the gap thickness and fuel radius in 20μm increments, while holding the cladding outer radius constant. The reactor conditions are identical to the constant operation utilized earlier in Chapter 3.4-6. These

simulations are performed with and without fuel creep in order to provide a performance boundary for fuel cladding mechanical interaction.

Table 4. Parametric Analysis Fuel Rod Geometry Specification

Gap Thickness (μm)	Fuel Radius (μm)	Cladding Thickness (μm)	Fuel Length (m)	Cladding Length (m)
100	4700			
80	4720			
60	4740	300	3.66	4.08
40	4760			
20	4780			

- This produces a total outer radius of .51cm for all fuel rods.

To begin this analysis, simulations were performed without the fuel creep model enabled in order to provide a bounding value on the cladding mechanical behavior for different fuel rod radial geometries. The results from the 100μm initial gap thickness are identical to the results from the full FeCrAl simulation described earlier in this chapter in Section 3.4. Many of the results are similar, so, in the interest of brevity, only the most salient results are reported here.

Figure 32 shows the average fuel centerline temperature (a) and the percentage of fission gas released (b) for these fuel rods, without the fuel creep model. Starting as the fuel rods reach the operating power, the fuel with the larger gap thicknesses experience consistently higher average fuel centerline temperatures. This is due to the poor conductivity of the fill gas in the gap/plenum region and the subsequent conductivity degradation it undergoes as fission gas is released from the fuel. The fuel rod with the 20μm initial gap thickness experiences gap closure nearly immediately, resulting in decreased temperatures. The average fuel centerline temperatures for the 20μm, 40μm, and 60μm gap thicknesses begin to converge as the gap conductivity is improved from fuel expansion. The average fuel centerline temperature for these rods gradually increases as the fuel thermal conductivity is degraded in the periphery due to the increase in fuel burnup.

The 80μm and 100μm cases exhibit noticeably higher temperatures because of the larger initial gap size, and eventually they experience more fission gas release than the smaller gap thicknesses. The onset of fission gas release occurs earlier in the 100μm gap geometry than the other fuel rods, resulting in an earlier degradation in gap conductivity. Degradation of the gap conductivity increases the fuel temperatures as heat transfer between the fuel and cladding is impeded, and eventually leads to a greater fission gas release rate. This begins a feedback between the fuel temperature and the amount of fission gas released to the fuel rod plenum. This is shown in Figure 32 where, as the fission gas rapidly increases for the 100μm gap geometry (Figure 32(b)) the average fuel centerline (Figure 32(a)) also begins to increase. This feedback effect subsides when the fuel cladding gap closes due to fuel expansion.

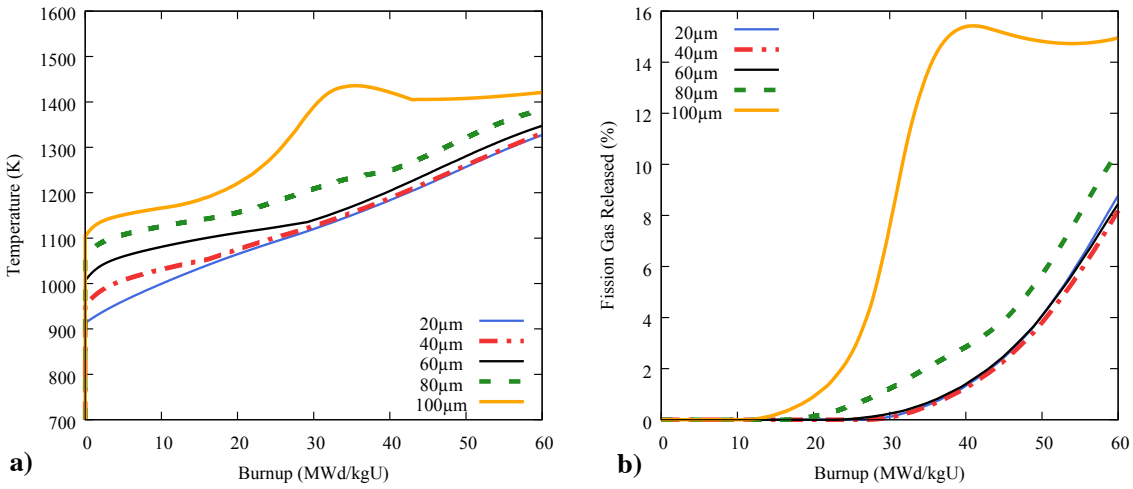

Figure 32. (a) The average fuel centerline temperatures and (b) fission gas released as a function of burnup and initial gap thickness. The fuel rods with the 80µm and 100µm gap sizes experience larger fuel temperatures leading to noticeably larger amounts of fission gas release.

As expected, gap closure occurs earlier for the fuel rods with the smaller initial gap sizes. By assuming the fuel behaves as an elastic material, as the fuel expands, it deforms the FeCrAl cladding radially. Figure 33 shows the maximum radial deformation of the cladding (a) and the corresponding maximum hoop stress (b) in the cladding. For the 20µm gap geometry, the cladding radial deformation quickly increases after gap closure which occurs nearly immediately as the fuel rises to operating power. The radial deformation increases as the fuel thermally expands and begins to decrease a small amount due to fuel densification, which is complete by ~5 MWd/kgU. At 60 MWd/kgU, the difference between the maximum cladding radial expansion for each successively smaller gap thickness is ~20 µm, demonstrating the increasing deformation (without fuel creep) is almost entirely driven by the incremental increases in the initial fuel radius. The 80µm and 100µm gap geometries experience additional cladding deformation due to increased thermal expansion from greater temperatures and the increase in gaseous fission product swelling. The fuel temperatures are increased because of the fuel temperature-fission gas release feedback and the accompanying gap conductivity degradation.

The maximum cladding hoop stresses across all fuel rods show nearly identical trends to the radial deformation due to the approximation of the fuel as an elastic material. Once mechanical contact occurs in these fuel rods, the cladding hoop stresses rapidly increase. These stresses increase as the cladding is radially deformed from fuel expansion. Because fuel creep is neglected in these simulations, the maximum cladding hoop stress for these fuel rods is artificially high.

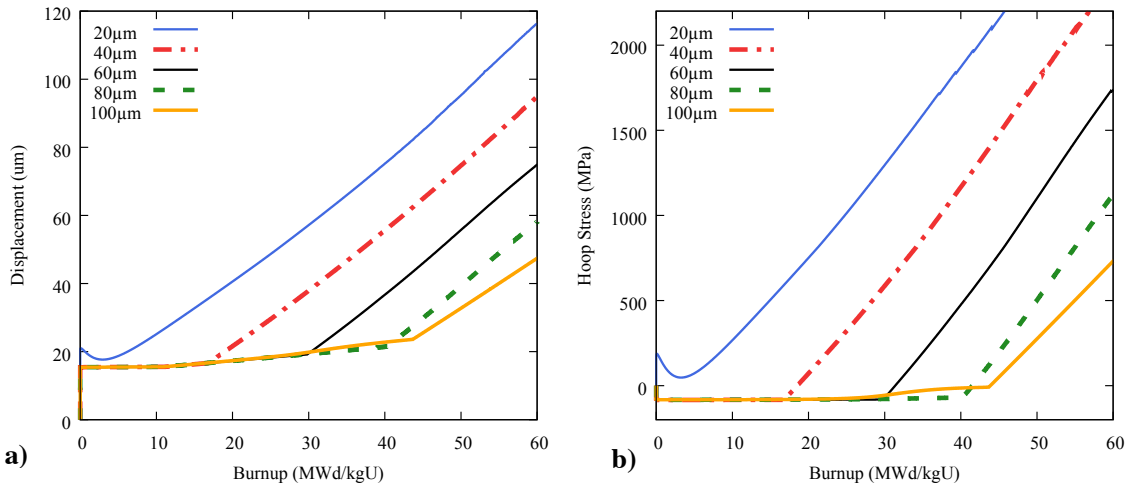

Figure 33. The maximum radial expansion (a) is larger for the fuel with the larger initial fuel radius and smaller gap size. Without fuel creep, as the fuel swells after gap closure, it expands the FeCrAl cladding. Likewise, by modeling the fuel as an elastic material, the maximum cladding hoop stress (b) continuously increases as the fuel expands.

Next, simulations were performed using identical fuel geometries, this time including the full fuel creep model as described in Section 2.6. Figure 34 shows the average fuel centerline temperatures (a) and the percentage of fission gas released (b) from the fuel rods for these simulations. Much like the simulations without fuel creep, the average fuel centerline temperatures generally converge for the smaller gap sizes as gap closure occurs. For the larger 80µm and 100µm gap thicknesses, the average fuel centerline temperatures are again increased initially due to the larger gap thickness, and eventually increased due to the gap conductivity degradation experienced from fission gas release to the gap and plenum.

By including the fuel creep model there is a small decrease in the fuel temperatures up to ~40 MWd/kgU, but due to increased fission gas release after this point, the average fuel temperatures are increased. For the 100µm gap thickness, the feedback effect between the fuel temperature and amount of fission gas released is somewhat reduced, however, the fuel rod ultimately releases a greater amount of fission gas by 60 MWd/kgU.

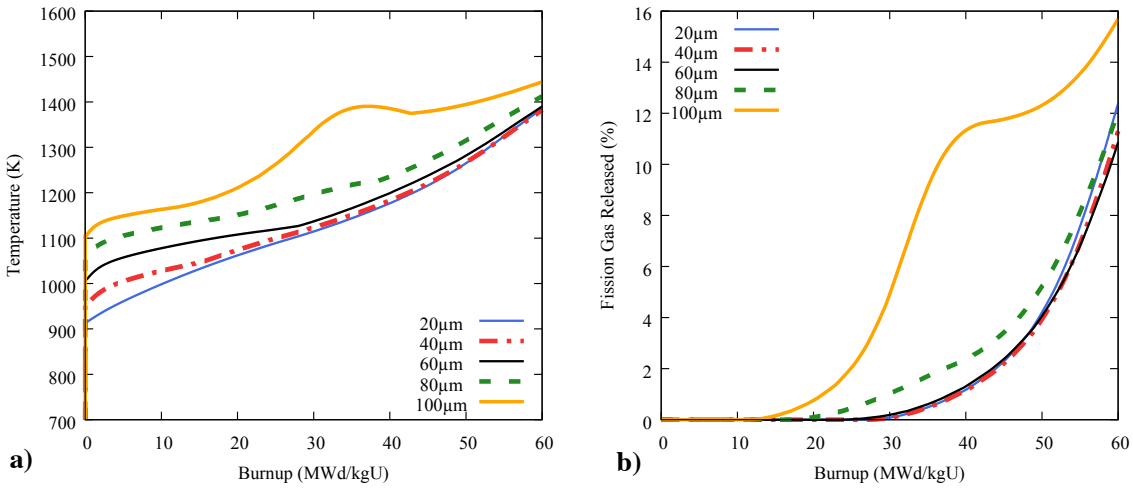

Figure 34. (a) The average fuel centerline temperature and (b) the percentage of fission gas released, with the incorporation of the full fuel creep model. The incorporation of the fuel creep model slightly reduces temperatures above 40 MWd/kgU and slightly reduce the amount of fission gas release at 20 – 50 MWd/kgU, compared to the simulations without fuel creep.

The maximum cladding radial displacement and maximum cladding hoop stress, shown in Figure 35 (a) and (b) respectively, are greatly reduced by including the fuel creep model. Much like the previous simulations, the initial deformation in the cladding is due to thermal expansion as the cladding temperature is increased to operating temperature. The fuel rod with 20µm gap thickness is almost immediately in mechanical contact with the fuel and continues in contact for the entire simulation. Because the fuel creep model allows the fuel to deform plastically, increasing the fuel compliance, the cladding does not radially expand nearly as much (~33 µm) as the previous simulations (45 – 120 µm). The maximum radial deformation for all of these fuel rod geometries increases to ~33 µm, implying that the maximum deformation when using this full fuel creep model is limited by the cladding behavior instead of the fuel expansion.

Correspondingly, the maximum hoop stress in the cladding is also greatly reduced after mechanical contact. The 20µm simulation almost immediately undergoes gap closure, and after the fuel densification, the maximum cladding hoop stress seems relatively constant until much higher fuel burnups are reached. The 100µm gap thickness shows a slight increase in the compressive cladding hoop stress as the plenum pressure is increased due to the release of fission gas from the fuel before mechanical contact occurs.

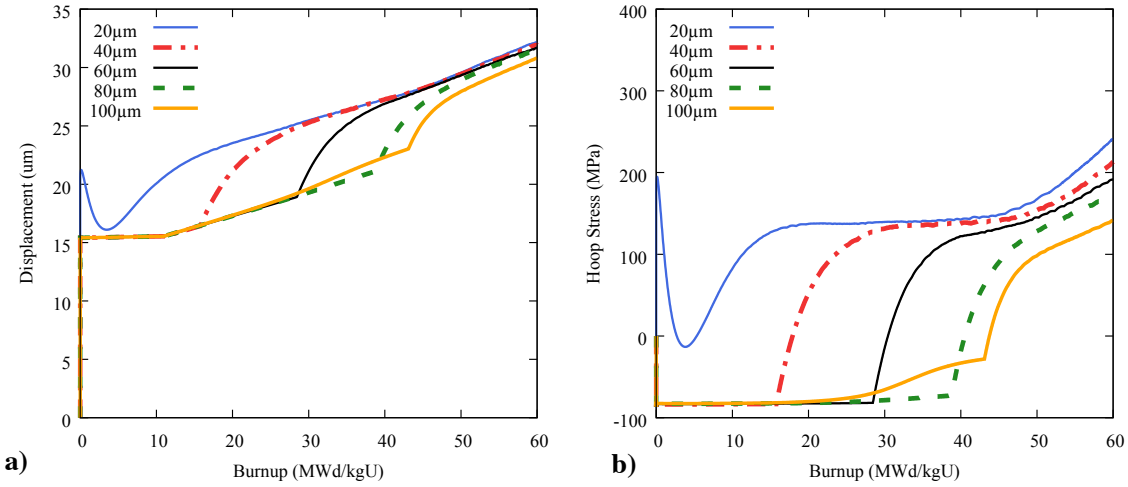

Figure 35. (a) The maximum cladding radial displacement and (b) cladding hoop stress as a function of gap thickness and burnup, with the incorporation of the full fuel creep model. The radial displacement and cladding hoop stress are both decreased significantly, compared to the simulations without fuel creep.

This simple parametric analysis on the fuel rod radial geometry provides a performance boundary for the thermal and fission gas behavior by assess various geometries with and without the fuel creep model. Although these models will greatly impact the fuel mechanical state and thus the cladding state, there is uncertainty modeling the fuel compliance. Results from this section are, therefore, more suited to provide bounding calculations for the mechanical behavior of the cladding.

The inclusion of the fuel creep model greatly affects the mechanical state of the cladding. The results without fuel creep, while artificial, again emphasize how important fuel compliance models are for modeling the FeCrAl cladding. This comparison shows that aside from the difference in the mechanical performance between the simulation types, the fuel creep model, in this case, does not greatly affect other aspects of the fuel rod performance. Both the fuel temperatures and fission gas release behavior are generally consistent among both analyses and show that reducing the gap thickness from the assumed 100µm, from the previous analyses in this chapter, generally results in more favorable fuel rod behavior and thus it is recommended that FeCrAl clad fuel rods could have a reduced gap thickness on the order of 40 to 60 µm.

3.8 Improvements to FeCrAl Cladding Material Models

In order to demonstrate the impact that the material microstructure may have on the cladding behavior and integral fuel rod performance, a comparison has been performed using the FeCrAl cladding, as described in Chapter 2, and the expected properties of a similar developmental alloy, C35M.

Preliminary data for the C35M alloy, developed at Oak Ridge National Laboratory, indicates that the alloy may experience more thermal creep and significantly more irradiation creep than discussed in Section 2.3 of this work (Terrani and Yamamoto, 2016). Material models for the C35M alloy have recently been incorporated into BISON as described by Gamble et al. (Gamble et al., 2017). Models used to simulate the C35M cladding include: C35M Elastic modulus and Poisson's ratio (Thompson et al., 2015), Kanthal APMT thermal expansion (Kanthal), C35M thermal creep, irradiation creep, and swelling (Terrani and Yamamoto, 2016). Figure 36 shows a comparison between the irradiation (Figure 36(a)) and thermal (Figure 36b) creep models suggested for the C35M alloy by Terrani et al. (Terrani and Yamamoto, 2016) and those described earlier in this work. It is anticipated that for the C35M alloy the coefficient for the irradiation creep rate model may be nearly an order of magnitude greater (0.5×10^{-5}) than that suggested by Garner et al. (0.5×10^{-6}). Generally, the thermal and mechanical properties for these cladding alloys are fairly similar, however, as shown in Figure 36, there is a large difference in the models used for the thermal creep rates (3-9× greater over 570 – 595K) and irradiation creep rates (10×).

Using these models, the C35M alloy cladding will exhibit much more creep deformation. It is expected that the maximum cladding hoop stress will remain much lower after mechanical contact and that the cladding will begin showing creep-down behavior. In order to compare these alloys and demonstrate how the creep rates will affect the integral fuel rod performance, a separate analysis is conducted. This consists of a comparison between the FeCrAl alloy implemented as described earlier in Chapters 2 and 3, the C35M alloy using the thermal and irradiation creep relations described by Terrani et al., and a simulation of the C35M alloy using an irradiation creep coefficient of 0.5×10^{-6} as suggested for BCC ferritic alloys by Garner et al. (Garner et al., 2000). The simulations performed in this analysis utilize the same fuel behavioral models and reactor operating conditions for constant operation as discussed in Section 2.4. While the hoop stress is identified to be the performance indicator of the previous sensitivity analysis, the following results show that a wide range of behaviors can be expected for the other performance indicators considered in this study.

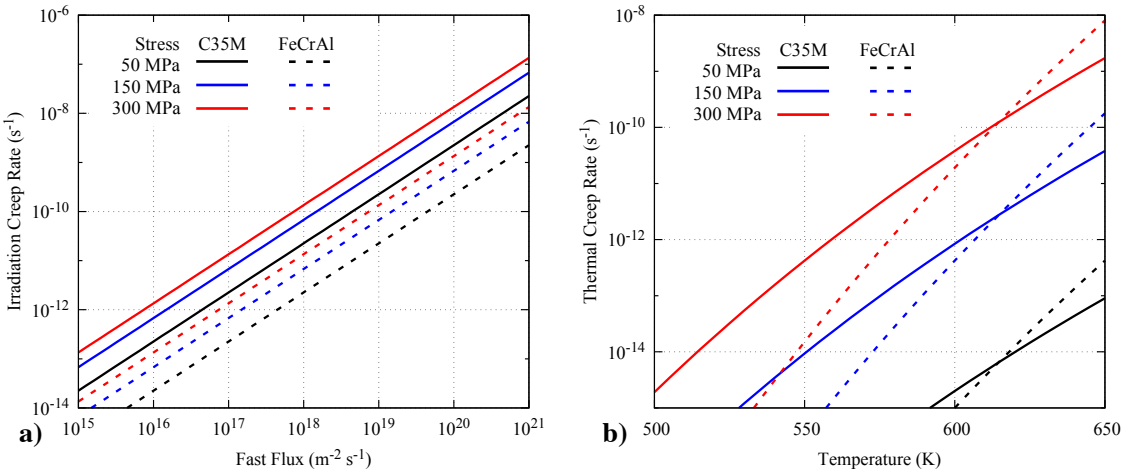

Figure 36. Comparison of creep rates of the C35M (Terrani and Yamamoto, 2016) models (solid lines) versus the FeCrAl models described in Section 2.5 (dashed lines) for conditions of **(**a) irradiation creep as a function of neutron fast flux (E > 0.1 MeV) and (b) thermal creep as a function of temperature.

The peak fuel centerline temperatures over the fuel utilization for the three simulations considered in this section are shown in Figure 37. For this analysis, the fuel rods were ramped to a linear heat rate of 18 kW/m and held at a constant power to a rod average burnup of 60 MWd/kgU. The fuel centerline temperatures initially increase as the rod ramps up to steady-state power.

Almost immediately, there is a noticeably lower fuel centerline temperature and a larger irradiation creep coefficient in the simulation with C35M cladding (blue line). The greater irradiation creep rates in this simulation allow the cladding to relieve the compressive stresses that arise due to the pressure differential between the coolant system and fuel rod plenum, which consequently reduces the cladding diameter. This is shown by the maximum radial displacement of the cladding (Figure 38(b)). Further, though the other simulations use different thermal creep models, the simulations exhibit nearly identical behavior to each other. Fuel temperatures in these simulations begin to increase as the gap thickness increases from isotropic irradiation swelling in the cladding. As the size of the fuel-cladding gap increases, heat transfer from the fuel to the cladding is further impeded.

At approximately 20 MWd/kgU, fission gas release from the fuel begins to degrade the gap conductivity, and the fuel centerline temperatures begin to increase. These temperatures reach a maximum near ~35 MWd/kgU, where fuel expansion begins to close the gap enough to counteract the effects of fission gas release on gap conductivity. This effect is dramatically subdued for the C35M alloy, for which the models predict larger irradiation creep. This is because fission gas release is thermally driven, and by reducing the fuel temperatures, less fission gas is released to the plenum. The peak fuel centerline temperatures decrease as the fuel and cladding undergo mechanical interaction along the

rod, beginning at ~42 MWd/kgU. The final increase in temperature at the end of the simulation is a result of the degraded thermal conductivity of the fuel and the poor gap conductivity where gap closure has not occurred.

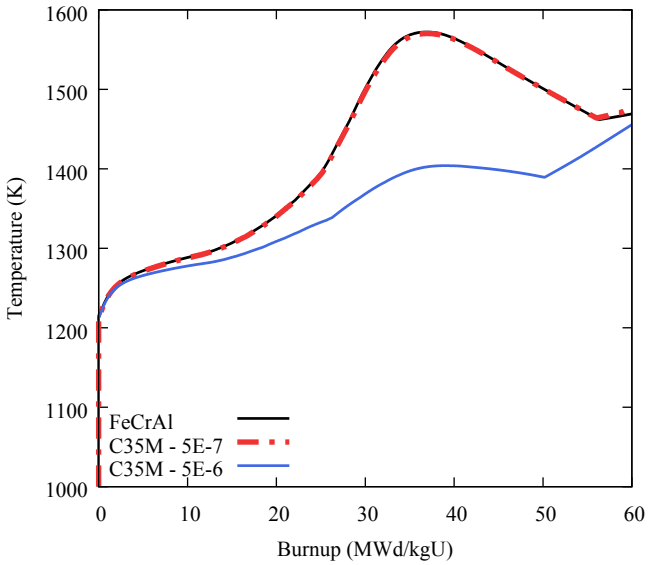

Figure 37. Variation in the peak fuel centerline temperature behavior of FeCrAl rods, based on different thermal and irradiation creep models.

The axial elongation and maximum radial displacement of the fuel rod cladding under this simplified operation are shown in Figure 38. After the initial thermal expansion, the FeCrAl cladding exhibits elongation due to irradiation swelling. As shown in Figure 38(a), cladding elongation is generally uniform until mechanical contact occurs at ~ 42 MWd/kgU. As the fuel expands and radially deforms the cladding, the cladding radius will increase. As a result, there is a strong Poisson's effect counteracting the axial elongation, thereby reducing the cladding length. By 60 MWd/kgU, an ~0.3 cm difference develops in the axial elongation among the simulations based on the cladding irradiation creep coefficient.

The maximum radial deformation of the cladding tube for these three simulations is shown in Figure 38(b). By increasing the irradiation creep pre-factor for the C35M alloy, the cladding is able to offset the expansion due to irradiation swelling and slowly collapse around the fuel due to the pressure differential between the plenum pressure and the reactor coolant pressure. The cladding radius will decrease until mechanical contact occurs and fuel expansion deforms the cladding radially. The FeCrAl and C35M simulations without increased irradiation creep (coefficient of 5E-7, red dashed line), again, show identical behavior. The cladding expands as irradiation swelling enlarges the cladding radius until mechanical contact occurs and the fuel rapidly deforms the cladding. The difference in the radial deformation among the simulations at 60 MWd/kgU is due to the temperature dependence of the gaseous fission product swelling model used. Because the temperatures

are lower for the C35M alloy with increased irradiation creep, the swelling rate is reduced, and the final fuel diameter, and thus the cladding radial displacement, is slightly smaller.

The maximum hoop stress in the cladding, shown in Figure 39, becomes very compressive as the fuel is ramped up to operating temperature due to the pressure differential between the coolant system pressure and the fuel rod internal pressure. As the simulations progress, the cladding remains compressive until significant fission gas is released or mechanical contact has occurred. Fission gas release, shown in Figure 40(a), rapidly increases in the *FeCrAl*, and *C35M - 5E-7* simulations at ~25 MWd/kgU, this increases the plenum pressure, consequently reducing the compressive hoop stress. Mechanical contact occurs at ~42 MWd/kgU for the C35M cladding with increased irradiation creep (blue line), and ~44 MWd/kgU for the other simulations. By 60 MWd/kgU the maximum hoop stress in the cladding for the C35M – 5E-6 simulation has started to saturate at ~300 MPa, while the hoop stress in the other simulations is in the 500 – 600 MPa range and seemingly still increasing. While cladding hoop stresses of this magnitude are a consequence of the elastic fuel assumption, this stress saturation behavior is still an important aspect of the cladding material.

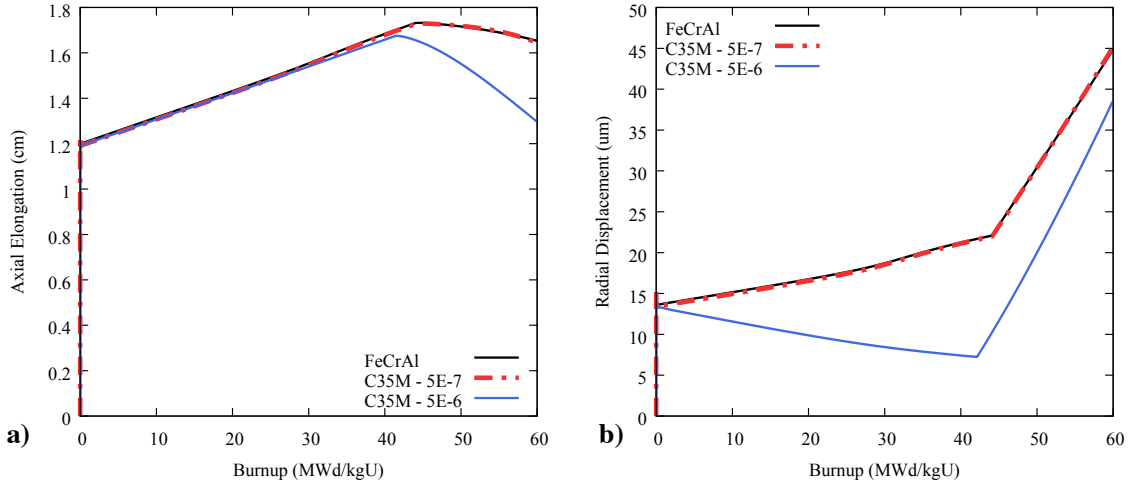

Figure 38. The axial elongation (a) for the FeCrAl cladding is largely determined by irradiation swelling until mechanical contact occurs, where the elongation is reduced as the fuel pushes the cladding out radially. The maximum radial displacement (b) for the FeCrAl cladding is also increased by the presence of isotropic irradiation swelling until mechanical contact occurs. Although, in the C35M cladding with increased irradiation creep, the maximum radial displacement is slowly reduced due to cladding creep down.

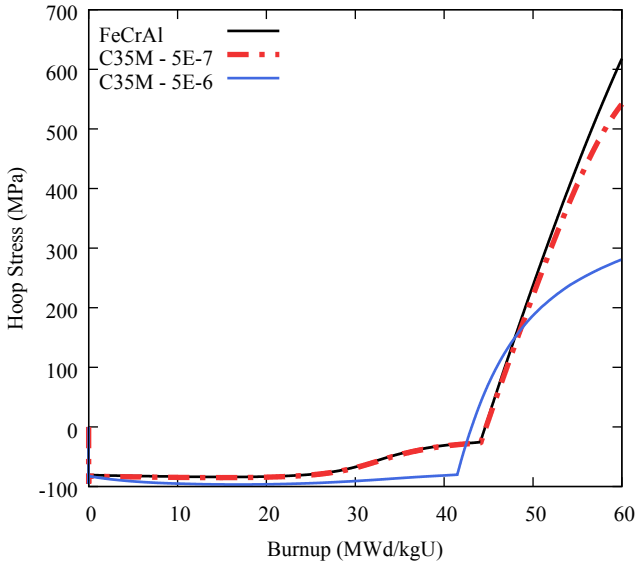

Figure 39. The maximum hoop stress in the cladding as a function of burnup, and thermal and irradiation creep model. The maximum hoop stress is slightly decreased using the C35M thermal creep model, however, a major reduction occurs in the case where the irradiation creep rate is increased.

The percentage of fission gas released in these fuel rods, shown in Figure 40(a), is heavily dependent on temperature, and therefore varies greatly among simulations. Irradiation swelling causes large expansion of the cladding radius, increasing fuel temperatures and further accelerating the amount of fission gas released. For the *FeCrAl* and *C35M – 5E-7* simulations, significant fission gas release begins around 20 MWd/kgU and increases until 40 MWd/kgU where it begins to plateau. The *C35M – 5E-6* simulation, however, remains cooler through much of the fuel operation, thus the onset of fission gas release is significantly delayed.

The fuel rod plenum pressure is shown in Figure 40(b). The fuel rod plenum pressure initially increases from .5 MPa at the beginning of the simulation, to ~1.2 MPa after the fuel rods heat up. Because the plenum volume in these fuel rods is quite large, a reduction in available volume for the fission gas only causes a minor pressure increase. Figure 40 shows a large pressure increases corresponding at the onset of fission gas release and continue to increase with fuel utilization.

As the *FeCrAl* and *C35M – 5E-7* simulations approach 60 MWd/kgU, they approach the coolant operating pressure of 7.136 MPa. This is a concern for safely operating these rods at higher temperature and burnup because the plenum pressure should not exceed the coolant system pressure. Doing so causes a change in the creep behavior of the fuel rod, and allows the cladding to begin to creep away from the fuel due to the pressure differential, although this concern is likely less significant for the reduced creep FeCrAl materials relative to Zr alloys. Up to 60 MWd/kgU, this effect is mitigated in the *C35M – 5E-6*

simulation, as the amount of fission gas, and consequently the plenum pressure, are both reduced.

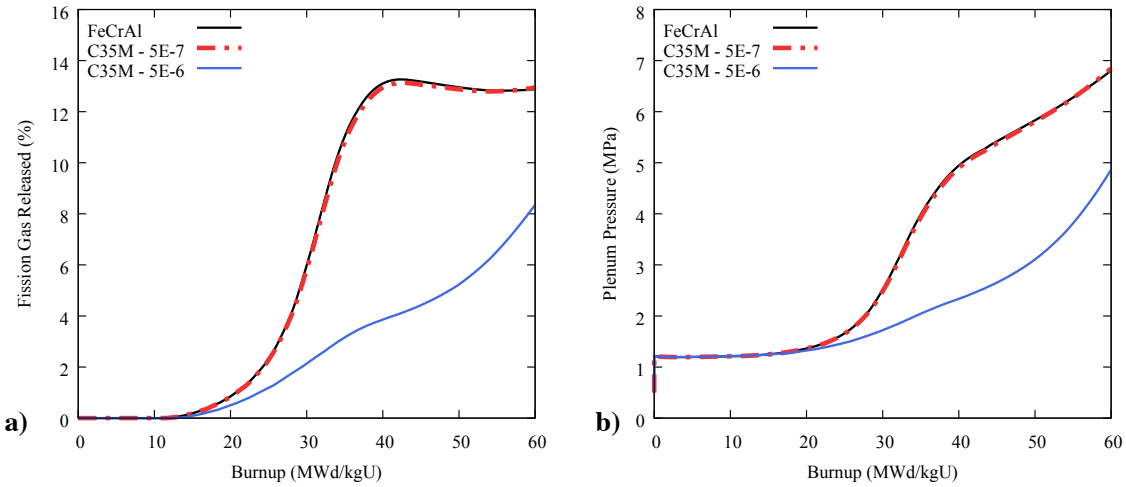

Figure 40. (a) Fractional fission gas released and (b) plenum pressure as a function of burnup, and thermal and irradiation creep model, both of which are highly sensitive to fuel temperature.

It is suggested that the increase in irradiation creep pre-factor results from larger ferrite grain size and the lack of precipitates in the C35M alloy. By increasing this creep pre-factor, the overall fuel performance was greatly improved. Such an outcome further demonstrates that the engineering of material microstructure is an important design parameter for the development of alternative cladding materials. Moreover, this study illustrates the sensitivity of integral fuel rod behavior to the deformation mechanics of the cladding and highlights the importance of continued investigation of the cladding properties.

3.9 Summary

3.9.1 Effects of fuel rod geometric and material design

The analyses in this chapter have sought to identify critical parameters for design consideration of FeCrAl alloys as a replacement for Zircaloy cladding under steady-state operating conditions. In this study, the fuel rod geometry for the FeCrAl and Zircaloy cladded fuel rods was modified. The larger fuel radius and thinner clad thickness for the FeCrAl cladded fuel rods result from optimizing the cycle length and reducing the negative reactivity impact (thermal neutron absorption) of FeCrAl. Reducing the cladding thickness by half essentially doubles the stresses that form in the cladding, while increasing the fuel enrichment and fuel pellet radius leads to a larger temperature gradient across the fuel thereby increasing the fuel expansion and fission gas release. Throughout this analysis, several different modes of power operation were considered, in which the nonconventional

fuel pellets were treated as a fully elastic material. This leads to very high stress levels within the fuel and higher fuel centerline temperatures that leads to greater fission gas release. Upon gap closure, very large hoop stresses formed in the FeCrAl cladding as a result of the fuel-cladding mechanical interaction. Subsequently, we have evaluated the thermal and irradiation creep mechanisms in the cladding and the fuel which will naturally prevent such large stress levels from occurring. To further identify possible sensitivities characteristic of the fuel design used in this chapter, an additional parametric study was performed on the fuel rod geometry.

Because FeCrAl cladding exhibits orders of magnitude less thermal and irradiation creep deformation at relevant conditions than Zircaloy cladding, gap closure is largely dominated by fuel expansion. This leads to gap closure that occurs much later in life and at much higher burnup. This is important because Zircaloy-cladded fuel rods behave very differently with respect to fuel cladding gap closure. By closing the gap, heat-transfer from the fuel to the cladding is improved, and fuel temperatures are lowered. This dramatically reduces thermally dependent phenomena, such as fission gas release and gaseous fission product swelling. In contrast, the stiffer FeCrAl-cladding does not experience as much creep deformation and may even undergo very limited swelling in this temperature and dose regime. As well, the higher CTE of FeCrAl alloys results in a larger gap once operation starts, even if the as-fabricated gap is the same as that of Zircaloy clad fuel pins. The later gap closure for FeCrAl rods, even for the same initial gap width as Zircaloy cladding, produced higher fuel temperatures which combined with the need for a larger fuel pellet, could lead to an increase in fission gas release. This scenario may necessitate fabrication of fuel rods with a smaller initial fuel-cladding gap thickness or alternate fuel concepts, such as chromia-doped fuels. Again, it is suggested that FeCrAl cladded fuel rod designs can utilize a gap thickness of 40 to 60 μm.

The case studies on cladding creep parameters show that the behavior of the cladding can vary widely with small changes to the alloy and provide insight into how experimental alloys may respond during exposure. By utilizing material properties as engineering parameters, the material response under certain conditions (high temperature, stress, or neutron fluence) may be significantly altered. This may include modifying such properties as the cladding composition, texture, grain size, or possibly the addition of a dopant in order to reduce the activation energy of thermal creep.

The parametric analysis for the fuel rod radial geometry shows that by varying the fuel radius and the gap thickness, the feedback effect between the fuel temperatures and the fission gas induced gap conductivity degradation can be subdued or altogether avoided. Building upon the previous study on the fuel creep model, simulations were performed with and without the creep model to identify the impact on the integral fuel rod behavior. The majority of this work assumes an initial gap thickness of 100μm based on the limited data available for the Peach Bottom-2 BWR. The results from this parametric analysis, however, identify the 100μm gap thickness to be in the sensitive range for this feedback effect. In order to provide a more accurate determination of the optimized fuel geometry, additional work on the fuel compliance models is needed.

3.9.2 Models for Fuel Performance

The initial results of this chapter provide a start toward determining the role of fuel creep and cracking in the evolution of the cladding stress state after mechanical contact has occurred. Developing reliable fuel mechanical behavior models to simulate fuel behavior, in particular implementing fuel creep and the effects of fuel cracking in nonconventional fuel geometries, is paramount for analyzing integral fuel rod performance and assessing safety criteria. Because fuel compliance is extremely important for modeling mechanical interaction between the fuel and cladding, additional benchmarking must be performed to ensure that these models are accurate.

It is expected that upon reactor startup, fuel pellets will generate large stresses from differential thermal expansion due to the temperature gradient across the pellet. This will put the periphery of the fuel pellet into a state of tension, where it will begin to fracture and produce radially oriented cracks. The fuel will expand or relocate a small amount, changing the effective radius of the fuel and altering the thermal and mechanical effects in that region. By neglecting fracture, the fuel creep model will over-compensate for the cracking, as it the main source of stress relief currently implemented for these simulations. In order to further improve these fuel creep models, additional model development based on experimental data is needed as well as the implementation of fracture models, which is discussed in Chapter 4.

In this chapter, several scoping analyses were conducted to provide preliminary insight on the steady-state performance of FeCrAl alloys, used as a replacement for Zircaloy cladding, and to gauge several areas of fuel and cladding creep behavior. These simulations show that because the expected creep behavior of FeCrAl alloys varies significantly from Zircaloy, the thermo-mechanical performance and consequently the integral fuel rod behavior varies as well.

While many of these simulations involved modeling the modified fuel pellet enrichment and geometry, our initial analysis treated the fuel pellets as elastic only, without fuel creep, and show very large stresses forming in the FeCrAl cladding (much larger than the yield strength at these temperatures (Yamamoto et al., 2015)), they do highlight important parameters for alloy design and fuel rod operation in high stress conditions. Due to uncertainty in modeling fuel creep and stress relief mechanisms, such as cracking, fuel creep was assessed and subsequently modified to assess its role in the stress evolution of the FeCrAl cladding. Results showed that the fuel creep model, as expected, has a profound impact on the stress state of the FeCrAl cladding after the onset of fuel rod gap closure, while showing a much smaller impact on the Zircaloy cladding.

While using larger, nonconventional fuel pellets, the expected thermal gradients across the fuel will be steeper due to the larger fuel radius and the thermal conductivity of oxide fuel. This implies that for similar operation, the amount of fission gas released to the fuel rod plenum may be greater in FeCrAl clad fuel rods, corresponding to fuel at higher temperatures. Controlling the amount of fission gas released, or the plenum pressure

increase in the fuel rod is a key design aspect to address when considering new fuel systems.

In order to optimize FeCrAl as an alternative cladding material, engineering design improvements are possible to better capitalize on the characteristic strength and creep strength of the alloys. This could involve tailoring material properties such as composition, microstructure, and in the case of fuel, microstructure and porosity. Alternatively, altering the geometric design of the fuel rod might delay the onset of gap closure or mitigate mechanical interaction altogether. In order to apply alternative cladding materials to currently operating reactors, design consideration should be given to both.

Modeling fuel creep and further detail in FeCrAl behavioral models is necessary to improve accuracy in determining integral fuel performance of FeCrAl-cladded fuel rods. Even small modifications in thermo-mechanical models and fuel rod designs can change fuel rod behavior due to the complex, coupled sensitivities inherent in fuel performance modeling. This highlights the importance for the continued development of fuel mechanics models; early efforts to begin characterization of these models and assess their influence are documented in Chapter 4.

CHAPTER 4: EFFECTS OF FUEL MECHANICS ON THE STRESS-STATE OF FUEL ROD COMPONENTS

4.1 Overview

In Chapter 3, it was demonstrated that the mechanical behavior of the cladding after gap closure is very sensitive to models associated with the fuel compliance. This emphasizes that behavior that alters the diametric expansion and elastic-plastic response of the fuel must be accounted for to develop more accurate modeling capabilities to determine the cladding mechanical response and the onset of gap closure.

As the temperature of UO_2 fuel is increased during reactor power ascension, significant thermal stresses form across the fuel pellet due to differential thermal expansion as a result of the steep radial temperature gradient that forms (Olander, 1976). These thermal stresses are tensile in the fuel periphery and transition to compressive approaching the fuel center. These large tensile hoop stresses initiate radial cracks in the fuel, starting near the fuel periphery and propagating inward. If the power in the fuel is then quickly decreased after the fuel has been plastically deformed, the stress profile is changed and the central region of the fuel transitions to a tensile state. This allows circumferentially-oriented cracks to form at radial distances about 30% from the fuel centerline (Rashid, 1974).

The formation of fuel cracks increase the apparent fuel diameter as the fragments are free to expand and eventually move outward toward the cladding (Williford et al., 1980). The movement and dispersal of these fragment is a phenomenon known as 'relocation'. As fuel temperatures are increased, more cracks are expected to form in the fuel, increasing the effect of relocation (Oguma, 1983). Currently used relocation models for fuel performance calculations are empirically-derived and include, along with fracture, other effects that alter the fuel cladding gap evolution, such as the eccentric location of fuel pellets in the gap region, which may occur without constraints to hold the fuel pellets perfectly aligned and centered (Cunningham et al., 1979).

Fracture can affect many aspects of integral fuel rod performance. While this study is focused on fuel temperatures and expansion, fracture may also increase the ability of the fuel to release fission gas to the fuel rod gap and alter the cladding stress state (Maki and Meyer, 1978). As radially-oriented cracks form, they allow the fuel to expand; reducing the fuel cladding gap and lowering fuel temperatures. Circumferential cracks, however, may impede the heat transfer from the core of the fuel to the cladding because the fuel has a higher thermal conductivity than the fill gas. A short study has been performed, as discussed in Appendix A, demonstrating that a diametral fuel increase due to cracking will reduce the fuel temperatures. This study, however, only evaluates the temperature distribution and does not consider the coupled thermo-mechanical effects or material property changes due to fuel burnup.

Cracking may also increase the release of gaseous fission products to the fuel rod plenum by increasing the free surface area to which the products may diffuse and by directly opening fission gas bubble networks intersected by the surface of the cracks. By providing a free pathway to the fuel rod gap/plenum, the fission gas inventory is expected to increase and eventually alter the gap heat transfer characteristics in the fuel rod. Although this effect is not considered in the current analysis, it is expected to alter fuel temperatures, at least before gap closure occurs.

As power in the fuel is continually cycled during operation, fuel fragments are slowly able to migrate outward radially. This 'ratcheting' behavior of the fuel fragments generally has a diminishing effect with an increasing number of power cycles and occurs until contact is established between the fuel and cladding (Rashid, 1974). Fuel fragment relocation and subsequent crack closure leads to the development of an asymmetric fuel surface in contact with the cladding. Previous work has been performed to demonstrate the tendency for large cladding stresses to form as gap closure occurs with fuel containing cracks (Gittus, 1972) and defects (Capps et al., 2016). Determining the mechanical response of the cladding after gap closure with open cracks in the fuel requires accurate calculation of the coefficient of friction between the fuel and cladding and, thus, is not considered here.

Several models have been proposed to include the effect of fracture into fuel performance simulations. These include a variety of numerical methods to approximate the fuel expansion and in some cases, the fuel property evolution.

Novel fracture models have been developed to incorporate cracking as an alteration of the bulk fuel thermal and elastic properties. This can be performed by determining whether the fuel has reached a fracture stress, and if it has, adjusting the directional (or isotropic) elastic properties based on the direction and number of cracks assumed to have formed (Jankus and Weeks, 1972). Additionally, similar methods have been suggested by applying an "effective" elastic modulus and modeling the apparent diametral expansion as an extension of the thermal expansion calculation (Williford, 1982).

A more explicit model, the smeared cracking model, is used in finite-element analysis to determine the elastic behavior of the fuel on an element-by-element basis (Rashid et al., 2004). If the single element is specified as cracked, the elastic properties of the element are reduced. This allows stress concentrations to develop in the surrounding elements as the element loses strength, and as such, a cracking pattern is able to from in the fuel. This provides a more accurate, however, much more computationally intensive fracture model.

In order to simplify the computational requirements of these models while still applying the stress relief from fracture, discrete cracking models have also been utilized. These allow prescribed discrete cracks to be applied directly to the fuel mesh before the simulation begins.

Other models simply include the diametral expansion due to fuel fracture. This can be accomplished by applying a radial strain directly to the fuel column based on the linear

heat rate, as used in many fuel performance codes including BISON. Fuel relocation not only increases the diameter of the fuel, reducing the time before the onset of gap closure, by reducing the gap thickness, but it also reduces the fuel temperatures. The models used in this analysis utilize some combination of the characteristics from the aforementioned fracture methods.

This chapter describes efforts to determine the effect of neglecting explicit fracture models on the calculation fuel expansion and compliance. The first section, Section 4.2, documents the fracture models considered in this analysis. Section 4.3 reports the results of a comparison between these fracture models for a well-characterized test fuel rod. Section 4.4 extends this analysis by applying these models to a FeCrAl cladded fuel rod using the fuel geometry described in Chapter 2.2. The findings of this analysis and possible enhancements to these models are further discussed in Section 4.5.

4.2 Fuel Mechanics Models

The current implementation of fuel relocation in BISON involves an empirical model that applies a radially-oriented strain based upon the local linear power, the cold fuel diameter and gap, and the fuel burnup. While this method predicts relocation well in specific instances, it artificially changes the fuel diameter to accomplish it. For example, by not relieving the stress during fracture, the response of other plasticity models, such as creep, is altered. In order to model fuel pellet relocation more mechanistically, explicit fracture models need to be considered. As previously mentioned, these may consist of relaxing the elastic stiffness of specific elements in the finite-element mesh as they surpass the material's fracture strength, known as smeared cracking (Figure 41(a)), or prescribing cracks directly to the finite element mesh, known as discrete cracks (Figure 41(b)).

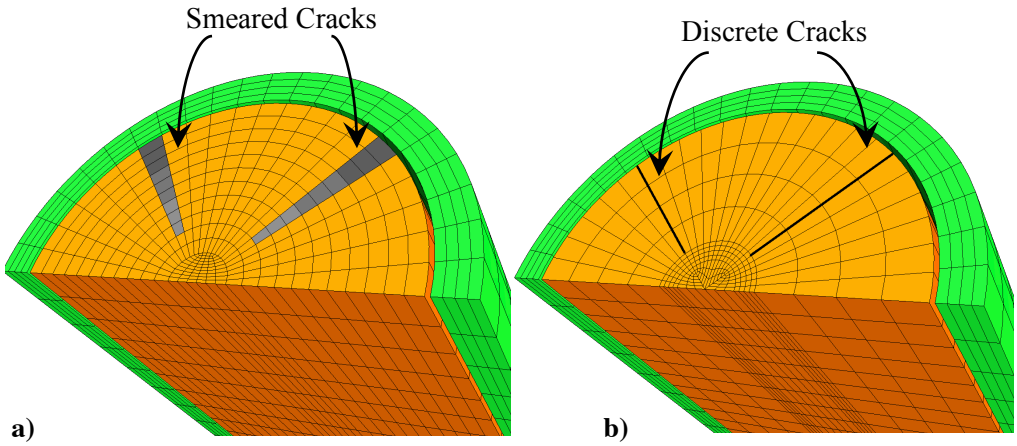

Figure 41. 3D illustration of two different fracture models commonly considered in finite element fuel performance codes. Smeared cracking (a) consists of relaxing elastic constant of the material as the stress in those elements surpasses the fracture strength. Discrete cracking (b) consists of prescribing cracks directly to the geometry.

Figure 42 shows a comparison, performed using BISON (Williamson et al., 2012), of the measured and calculated fuel centerline temperatures using relocation and smeared cracking models for a specified linear heat generation rate. It is important to note that the details of fuel creep in this assessment were not immediately available. Although this shows that smeared cracking, in this instance, does not possess the same reduction in temperature that the relocation model does, it does demonstrate that there is an impact on fuel temperature. This may indicate that other important phenomena beyond fracture may also have a significant contribution to the fuel diametral strain.

In order to more accurately model the mechanical behavior of UO_2 fuel leading up to and during pellet-cladding mechanical interaction using the BISON fuel performance code, a comparison of several fuel mechanics models has been performed. This analysis consists of a comparison between fracture models and the fuel relocation model with experimental data to determine the effect of explicitly modeling fuel fracture on cladding stress state and expansion. Along with the fuel creep model, detailed in Section 2.6, models currently implemented in BISON include fuel relocation, smeared cracking, isotropic softening.

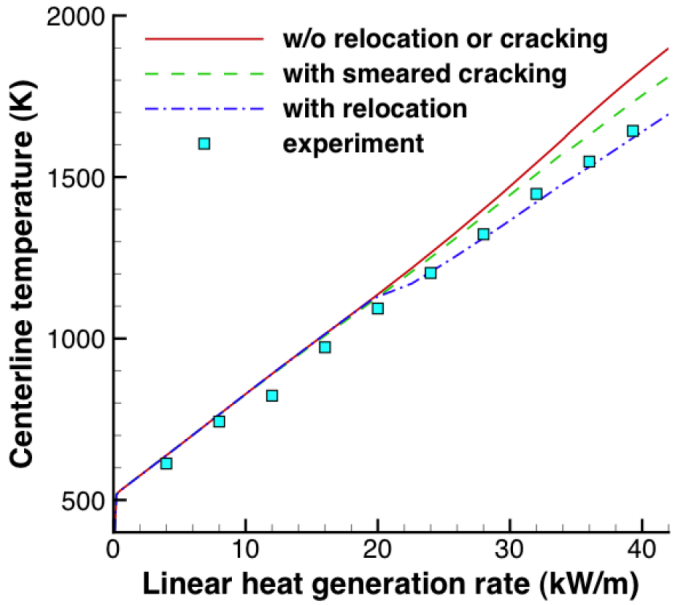

Figure 42. The predicted fuel centerline temperature as a function of linear heat generation rate for varying fuel mechanics models, as compared to experimental measurements (blue squares). The fuel temperature increases nearly linearly with the linear heat generation rate until the fracture models alter the fuel expansion, starting at nearly 20 kW/m. The models with greater fuel expansion experience lower fuel centerline temperatures. [Reproduced from (Williamson et al., 2012)]

4.2.1 Fuel Relocation

The fuel relocation model used in this analysis is based on the ESCORE model developed by EPRI (Rashid et al., 2004), although it was subsequently modified An uncertainty quantification analysis performed by (Swiler et al., 2013) determined that, for a specific subset of fuel rods (IFA-431, IFA-432) from the Halden test reactor, the most likely onset of fuel relocation occurred at a much lower linear heat rate than the ESCORE model indicated. In order to accommodate this, changes were made to the activation thresholds of the model and their functional dependence on the linear heat rate. The result of this is considered the 'Modified ESCORE' model (Hales et al., 2014). Equation 12 shows the general function for the change in the diameter relative to the initial fuel diameter.

$$\left(\frac{\Delta D}{D_O}\right) = 0.80 \cdot Q_r \cdot \left(\frac{G_t}{D_O}\right) \cdot (0.005 \cdot Bu^{0.3} - 0.20 \cdot D_O + 0.3) \tag{12}$$

In Eq. (12), ΔD is the change of the fuel diameter due to relocation (inches), D_O is the initial, as-fabricated, cold fuel diameter (inches), G_t is the initial, as-fabricated, cold diametric fuel rod gap (inches), Bu is the average fuel burnup (MWd/MTU), and Q_r is a dimensionless piecewise function based on the linear heat rate. Equation 13 describes the Q_r function for the Modified ESCORE model and Equation 14 describes the Q_r function for the unchanged ESCORE model.

$$Q_r = \begin{cases} 0 & for\ q' \leq 1.524 \frac{kW}{ft} \\ \frac{2 \cdot q'}{14} & for\ 1.524 \frac{kW}{ft} < q' \leq 14 \frac{kW}{ft} \\ \frac{q' - 10}{2} & for\ 14 \frac{kW}{ft} < q' \end{cases} \tag{13}$$

$$Q_r = \begin{cases} 0 & for\ q' \leq 6 \frac{kW}{ft} \\ (q' - 6)^{\frac{1}{3}} & for\ 6 \frac{kW}{ft} < q' \leq 14 \frac{kW}{ft} \\ \frac{q' - 10}{2} & for\ 14 \frac{kW}{ft} < q' \end{cases} \tag{14}$$

In Eqs. (12-14), Q_r is a dimensionless piecewise function and q' is the linear heat rate in kW/ft.

The difference between these models are the threshold linear heat rate where the onset of relocation begins, and the functional dependence of the Q_r term in the intermediate expansion region. The modified ESCORE model has a much lower activation energy at ~1.524 kW/ft (~5 kW/m) compared to the original model which begins at ~6 kW/ft (~19.7 kW/m), targeted toward simulating fracture at lower linear heat generation rates. Likewise, the functional dependence for the linear heat rate during the onset of relocation is also changed from a cubic term to a linear dependence. Figure 43 shows the difference in the

amount of fuel radial expansion expected between these two models for a typical PWR fuel geometry at three separate fuel burnups and a range of linear heat rates. This shows the large difference between the two models over the 5 – 20 kW/m range and a relatively small difference after ~25 kW/m. Although the Modified ESCORE model was used in this analysis, because of the limited size of the data used in the model calibration, it is uncertain whether consideration should be continued.

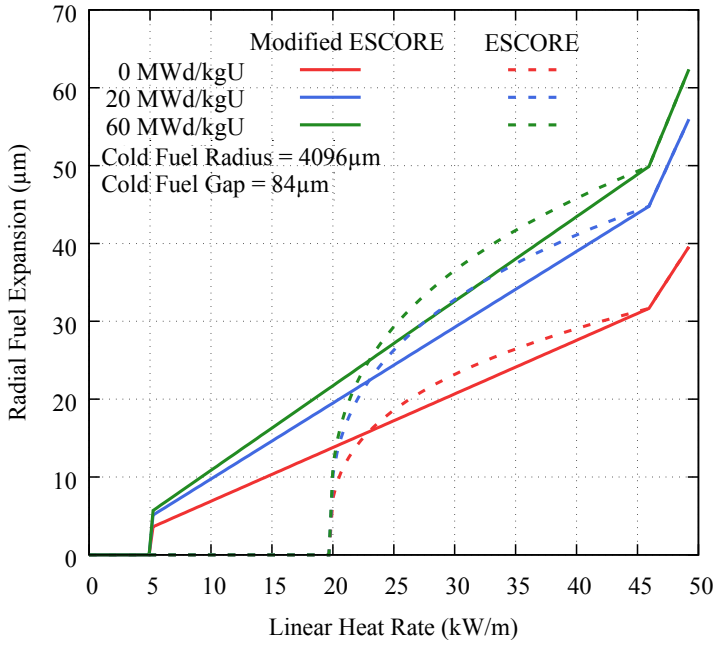

Figure 43. The original (dashed) and modified (solid) relocation models calculate a large difference in the radial fuel expansion between 5 – 20 kW/m for a typical PWR sample geometry. The modified ESCORE model features a much lower threshold where relocation is expected to begin (~5 kW/m) and a linear radial expansion as a function of linear heat rate.

4.2.2 Smeared Cracking

In order to simulate explicit fracture using a smeared cracking model, a fracture strength model for UO_2 from the MATPRO library (Hagrman et al., 1995) has been implemented. The expression, shown in Equation 15, describes the out-of-pile temperature and density dependent fracture strength as no in-pile data is currently available.

$$\sigma_f = 1.7 \times 10^8 \left[1 - 2.62(1 - D) \right]^{\frac{1}{2}} e^{\left(-\frac{1590}{8.314 \cdot T}\right)} \quad (15),$$

where σ_f is the fracture strength (Pa), D is the fractional density (fraction of theoretical density), and T is the temperature (K). This is applied for fuel temperatures up to 1000K;

beyond this temperature the strength is assumed to be constant ($\sigma_f = \sigma_f(1000K)$). In order to enhance the expected crack propagation through the fuel, a statistical approach was taken by seeding the fuel mesh with a normal distribution and applying the fracture stress. Equation 16 shows the probability density function for a normal distribution with an average value of zero.

$$f(x) = \frac{1}{\sqrt{2\pi\mu^2}} e^{\left(-\frac{x^2}{2\mu^2}\right)} \quad (16),$$

where f(x) is the probability function for a normal distribution centered at zero with a standard deviation (μ) of 19 MPa. After each element is seeded with a sample from the probability function, the temperature and density dependent fracture stress is combined to give each element in the fuel mesh a unique, normally distributed temperature dependent fracture strength. Although not considered in this analysis, including a grain size dependence on the fuel fracture strength, as described by (Hagrman et al., 1995), may additionally improve fidelity for fuel fracture. Figure 44 shows a sample distribution of the fracture strength over temperature for 95% TD UO_2 fuel. The shaded area in the figure shows the range of a single standard deviation from the average.

An example mesh using the r-θ coordinate simulation capability in BISON, similar to those used in the following analysis, is shown in Figure 45. It should be noted that the fracture strength is declared as an isotropic value within the finite-element fuel mesh.

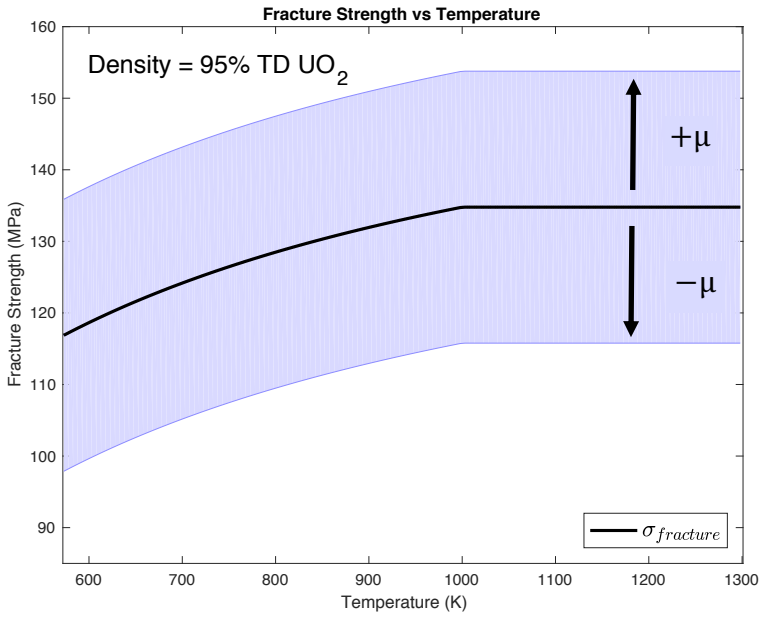

Figure 44. The fracture strength of UO_2 is shown as a function of temperature, based on out-of-pile measurements, as no in-pile data is currently available. The standard deviation of the fracture strength (shaded) is quite large as UO_2 undergoes brittle fracture. Above 1000 K, the fracture strength is assumed to be constant.

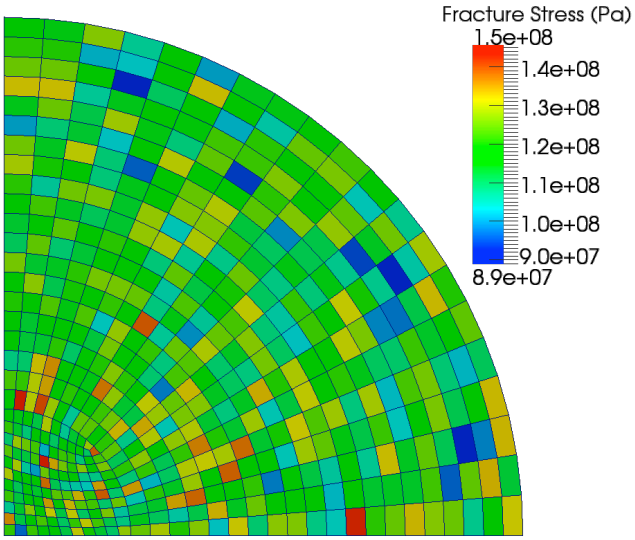

Figure 45. This quarter fuel pellet r-θ mesh demonstrates the distribution of the isotropic fracture strength at each element.

In order to simulate fracture in the fuel, a smeared cracking model (Rashid, 1968) is used. In this model, the elastic properties in an individual direction are reduced based on the crack strain or number of times an element cracks, after the fracture stress has been reached in that specific element. Because of the nonlinearity introduced into the system, a truly abrupt cracking model (where the elastic properties are immediately reduced to zero) reduces the ability of the fuel performance code solver to find convergence. This makes it extremely difficult to determine the solution, and thus alternative models are considered. The smeared cracking model implemented in BISON (Hales et al., 2014) is currently based on an exponential softening curve (Equation 17). In this model, after the aforementioned fracture strength is reached, the elastic properties of an element are exponentially reduced as the crack strain is increased. This allows the element to retain elastic properties initially; and as the crack begins to open, these are greatly reduced.

$$\sigma = \sigma_f \cdot \left(\sigma_{residual} + (1.0 - \sigma_{residual}) \cdot e^{\left(\frac{-E*\beta}{\sigma_f} * (\varepsilon_{max} - \varepsilon) \right)} \right) \qquad (17),$$

where σ is the stress in the element, σ_f is the isotropic fracture strength in the element, $\sigma_{residual}$ is the user provided residual stress in a specified direction, E is the elastic modulus, ε_{max} is the maximum strain in that specific element, β is a user specified softening factor, ε is the crack strain in the crack direction. For this analysis, the residual stresses in the axial direction and the radial plane are set to zero to allow a continued reduction of the elastic properties for each cracked element. The value of β is assumed to

be one, meaning the initial slope of the exponential model after an element has cracked is equal to the negative elastic modulus.

To further improve the robustness of the solver mechanics, an additional calculation of the fuel stress based on the number of times an element 'cracks' can be used. In this power-release model (shown in Equation 18), the elastic properties are reduced to 1/3 of the current properties every time the fuel reaches the fracture stress. The fracture stress, in turn, is based on the exponential softening curve, so after each crack forms, it becomes easier to reach the fracture strength again and reduce the elastic properties in that element, allowing the crack to open further. Thus,

$$\sigma = \left(\frac{1}{3}\right)^{n} \cdot E \cdot \varepsilon \qquad (18),$$

where σ is the stress in the element, E is the elastic modulus, n is the number of cracks in that element, and ε is the strain in that element.

Figure **46** shows a comparison of the stress-strain exponential and power release models. The main difference between the exponential (a) and power-release (b) models is how the mechanical properties are relaxed after the fracture strength has been reached. The exponential release model exponentially softens the fuel perpendicular to the crack as the crack strain increases. The power release model decreases the elastic modulus to 1/3 of the original value and utilizes the exponential strain softening curve to calculate the new fracture strength. This shows the relatively smooth release of the elastic properties for the exponential model.

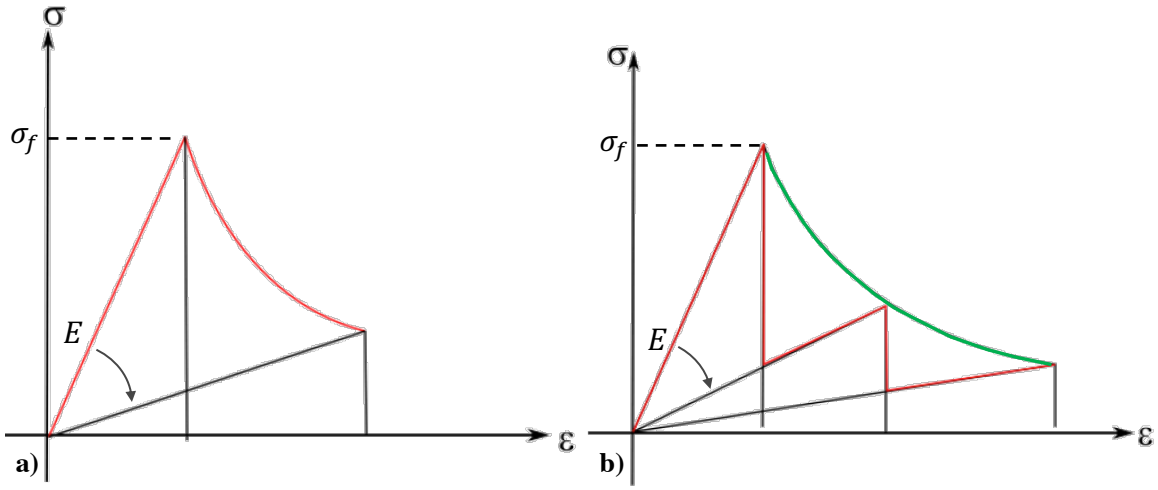

Figure 46. a) Exponential versus b) power release model, in which the red lines denote the current element stress based on the strain. For the exponential model the elastic modulus is softened gradually, while for the power release model this occurs suddenly. The green line denotes the strain softening curve from the exponential model. [Reproduced from (Liu and Rashid, 2017)].

4.2.3 Mesh Topography-Based Fracture

To compare against the smeared cracking models, another explicit fracture model, the discrete crack, is considered. Unlike smeared cracks, the mechanical properties of the fuel using the discrete crack remain unchanged during the simulation. Instead, cracks are prescribed to the mesh based on observed crack properties in the fuel before the simulation begins. Although this is a poor assumption for the early stages of the simulations, before fracture would normally occur, it is generally much less resource intensive to get a converged solution. A 90˚ r-θ mesh used in this analysis is shown in Figure 47 demonstrating the locations and geometry of the cracks in the fuel pellet. For this analysis, it is assumed eight cracks exist in the fuel (two of which are on the plane of symmetry, one in the center) which transverses the fuel at 70% of the fuel radius. The initial crack width, which is limited by the mesh generation software, is approximately 0.5˚. Cracks located on the symmetry plane are only .25˚ from the axis boundary.

An example of the hoop stress distribution in a fuel pellet with discrete cracks during a ramp to operating power is shown in Figure 48. In this demonstration, the hoop stress is reduced in the fuel pellet periphery along the cracks because the fuel is allowed to move. As the fuel is heated and expands during a power ramp, thermal stresses form in center of the cracked fuel lobes, away from the crack surfaces. Due to the increased temperature and thermal expansion at the center of the fuel, the core of the pellet is in a compressive stress state. The fuel periphery is in a tensile stress state because the core of the fuel pellet experiences more thermal expansion from the temperature gradient and expands the fuel.

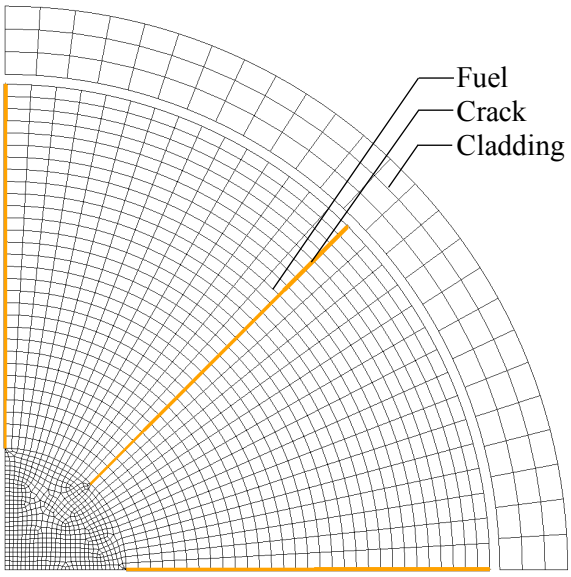

Figure 47. Finite element mesh showing the geometry used in the discrete crack fuel simulations. The cracks are noted in yellow and penetrate 70% of the fuel radius.

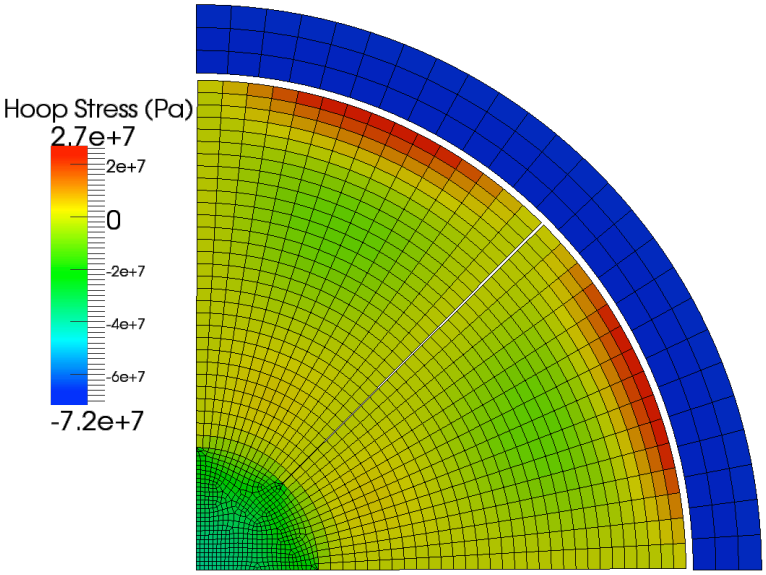

Figure 48. Distribution of hoop stress (color scale indicated spanning -72 to +27 MPa) within the fuel and cladding following an increase to a power level of 10 kW/m.

4.2.4 Isotropic Softening

Another approach to quickly modeling fuel fracture, implemented in BISON (Hales et al., 2014), is the use of a linear heat rate-based softening of the elastic properties of the fuel. As the fuel develops thermal stresses from the strong radial temperature gradients, the fuel is expected to fracture. A simple assumption can then be made to determine that if the fuel reaches a certain linear heat rate, considering the geometry to be the same, then the fuel will fracture. This work is similar to that of (Oguma, 1983), which extrapolates this cracking behavior to large linear heat rates by applying more radial cracks in each of the crack lobes, and eventually applying a circumferential crack. An illustration of this, reproduced from Oguma, is shown in Figure 49. This demonstrates the assumed step behavior of increasing fracture in UO_2 with an increasing linear heat rate. While this approach is difficult to apply to different fuel geometries (in the case of FeCrAl with much larger fuel pellets), it is also much less computationally intensive than smeared cracking models that calculate fracture based on a stress-based criterion.

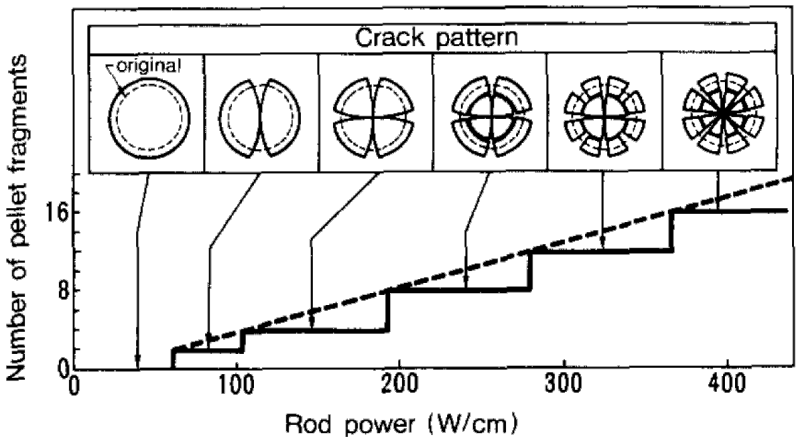

Figure 49. The expected crack patterns resulting from increases in the fuel linear heat rate. This increase in the number of cracks is predicated on the relationship between the thermal stresses that form across the fuel pellet and the fuel temperatures as the fuel linear heat rate increases, as reproduced from Ref. (Oguma, 1983).

In this isotopic softening model, the number of cracks is calculated using the linear heat rate, as shown in Equation 18. This equation is the result of fitting cracked fuel data. As shown in Figure 50, this model was fit to the experimental data of Walton and Husser, which was intended for use in a mechanistic fracture/relocation model for the FUMAC and TACO fuel performance codes (Walton and Husser, 1982). Thus,

$$N_{cr} = 1 + 10 \cdot \left(1 - exp\left(-\frac{LHR - 5}{21}\right)\right) \quad (18),$$

where N_{cr} is the number of cracks, and LHR is the fuel rod average linear heat rate in kW/m. In this equation, the first crack is assumed to form at 5 kW/m and the maximum number of cracks is assumed to be 11. Figure 50 shows a comparison between this model and the original model proposed by Oguma. Both of these models agree well with their respective data sets, although there is only limited data from Oguma for high linear heat rates. Because the fuel geometries are not available, this comparison is somewhat difficult to extrapolate to different fuel pellet sizes.

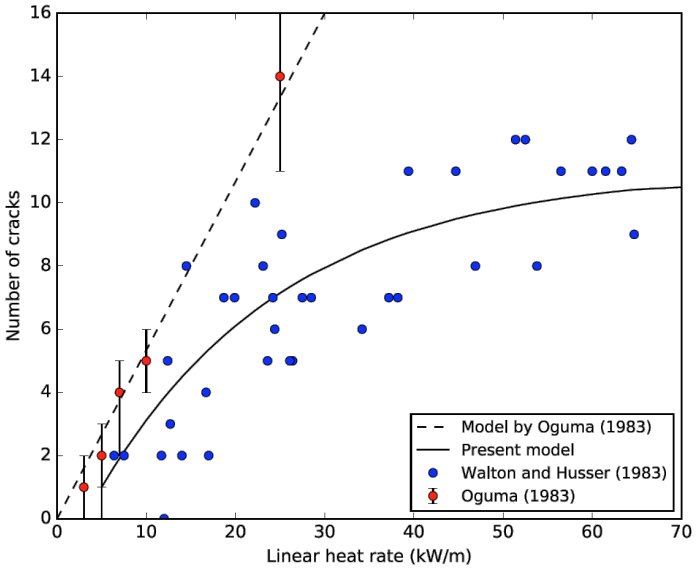

Figure 50. The number of cracks versus linear heat rate from the present model uses data from (Walton and Husser, 1982) as opposed to the Oguma model(Oguma, 1983), as reproduced from Ref. (Hales et al., 2014).

In order to reduce the elastic properties of the fuel as it fractures, the following reduction factors are applied to the elastic modulus (Equation 19) and Poisson's ratio (Equation 20) based on the number of cracks calculated in Equation 18, as:

$$f_{el} = \left[\left(\frac{2}{3}\right) \cdot \frac{(2-\nu)}{(2+\nu)(1-\nu)}\right]^{N_{cr}} \quad (19),$$

where f_{el} is the ratio of the elastic modulus remaining after cracking, and is the ν is Poisson's Ratio of the fuel. For these simulations the Poisson's Ratio of the fuel is calculated using a relation from the MAPTRO library currently implemented in BISON. The reduction factor for the fuel Poisson's Ration is calculated as:

$$f_{\nu} = \frac{1}{2^{N_{cr}} + \nu \cdot (2^{N_{cr}} - 1)} \quad (20),$$

where f_{ν} is the ratio of the remaining Poisson's ratio. Figure 51 shows these reduction factors as a function of the number of cracks in the fuel. For this simple comparison, the Poisson's ratio of the fuel is assumed to be 0.35. This shows the somewhat rapid loss of the elastic properties for the first few cracks formed at relatively low fuel linear heat rates. For example, at 10 kW/m it is assumed that ~3 cracks will be formed, reducing the elastic modulus to ~30% and Poisson's ratio to ~10%. Likewise, for an average linear heat rate of 20 kW/m, ~6 cracks are expected to be formed, reducing the elastic modulus to ~15% and Poisson's ratio to ~1%. These reduction factors show how quickly the elastic properties of the fuel are reduced after relatively few cracks (which occurs at a relatively low LHR).

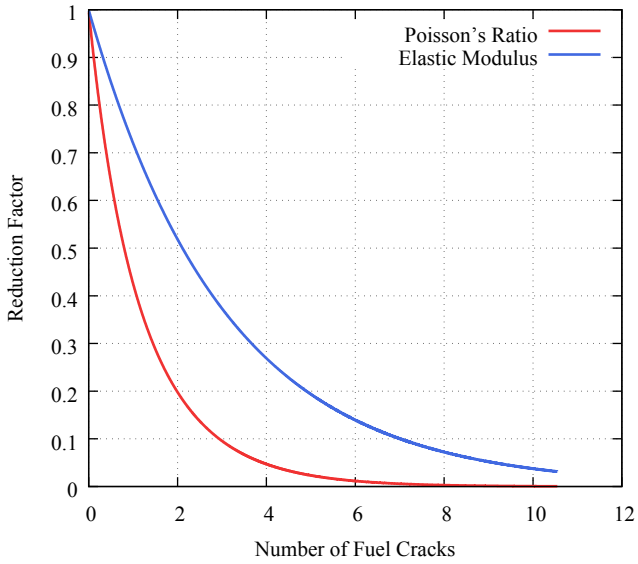

Figure 51. The reduction factors for the isotropic softening model as a function of the number of cracks formed in the fuel, which are dependent on the linear heat rate in the fuel.

To summarize, for this analysis several different methods of simulating explicit fracture in the fuel are considered. These consist of: the Modified ESCORE relocation model which empirically applies a radial strain to the fuel at a specified linear heat rate; the exponential and power-release smeared cracking models which reduce the elastic properties in a single finite-element based on the crack status and strain; the discrete meshed crack method which has an assumed crack number and geometry contained in the mesh for the finite-element simulation; and the isotropic softening model which relaxes the elastic properties of the fuel based on the number of cracks in the fuel, which is calculated by the rod average linear heat rate. The MATPRO fuel creep model (the original model, as it is implemented in Section 2.6), is also considered in this analysis, implemented either as a standalone plasticity model or in conjunction with the fracture models.

4.3 OSIRIS Rod H09 Results

To compare the accuracy of each of the fracture models, the OSIRIS Rod H09 was chosen as a benchmark case from International Fuel Performance Experiment (IFPE) Database (Sartori et al., 2010). This rod was chosen, in particular, because it is a full-length Zircaloy cladded fuel rod, the reactor operating conditions are documented, and data from the post irradiation examination contains axial profilimetry. These diametral measurements are used to compare the final diameter of the fuel rod with predictions from BISON simulations.

In order to simulate this test rod, the geometry is generated from specifications in the IFPE database, shown in Table 5, using a quarter of an r-theta slice of the fuel rod. Figure 52

shows the fuel rod mesh considered in these simulations. Because of the symmetry in this mesh, only a quarter is used (with appropriate boundary conditions) in an effort to reduce the computational requirements. The geometry and reactor conditions for the OSIRIS Rod H09 are representative of a standard PWR.

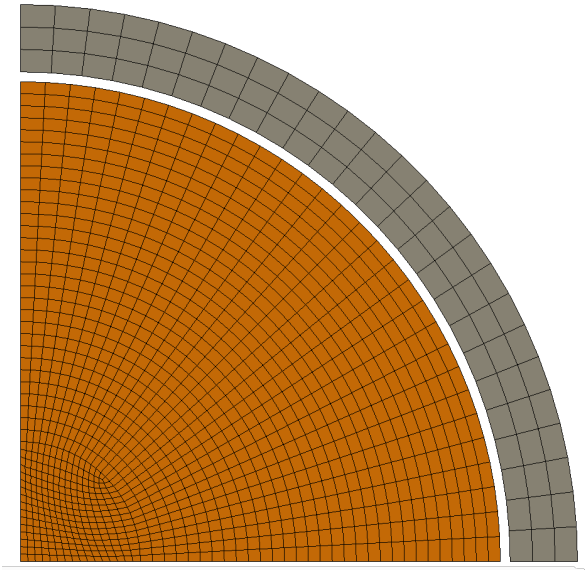

Figure 52. The quarter-rod r-theta coordinate geometry shows the fuel and cladding mesh density used in these simulations.

The r-theta geometry used in these simulations is a slice through the fuel rod, and as such, the conditions at that axial location of the slice can alter the results. For these simulations, the fuel rod operating conditions and the end-of-life fuel rod diameter are generated from the highest power axial location along the fuel rod.

Table 5. OSIRIS H09 Fuel Rod Geometry Specification

Cladding Type	Fuel Radius (μm)	Gap Thickness (μm)	Cladding Thickness (μm)
Zircaloy	4095	84	575

The power history for the OSIRIS H09 test rod is shown in Figure 53. There are four significant features in the power maneuvering of this test rod that are expected to cause fuel cracking from the development of thermally-induced stresses. The first occurs during the rise to operating power, where the fuel increases to ~23 kW/m over approximately (200 hours). It is expected that such a rapid increase in the fuel temperatures over a relatively short time will lead to the bulk of the cracking behavior in the fuel. The second is the power reduction at nearly ~1.6 years. When the fuel is operated at high temperatures for long periods of time, stresses in the fuel will relax due to thermal and irradiation creep. If the fuel power is suddenly decreased, large circumferentially-oriented cracks develop from the large radial stresses that form as the core of the fuel contracts. After this sharp decrease in

power, there is a corresponding ramp up in power. Again, during large power cycles more radial cracks are expected to form. Finally, as the fuel temperatures are decreased during reactor shutdown at the end of the power history, large circumferential cracks may form. It should be noted that shutdown between reactor cycles was not documented in the power history provided in the IFPE database. This is expected to have a similar effect on fuel fracture as the initial reactor startup and shutdown.

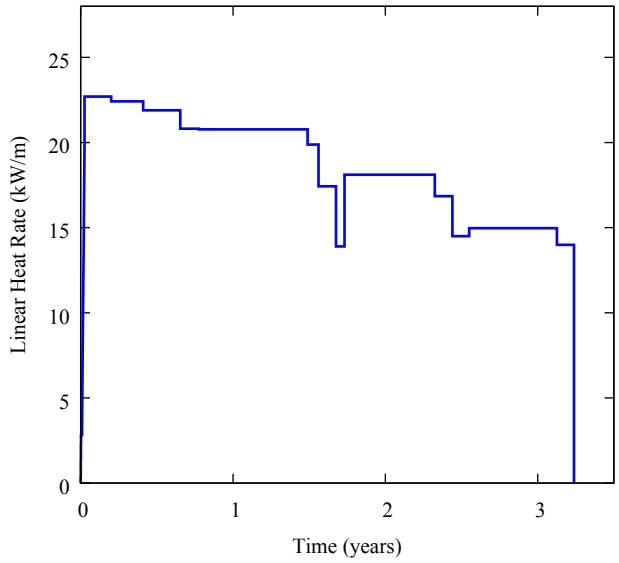

Figure 53. The power history, as reported in the IFPE Database for the OSIRIS H09 test fuel rod, shows several important features of the fuel rod operation including the rapid rise to 20 kW/m and a sharp decrease in power at ~1.6 years.

This particular fuel rod in the OSIRIS test suite was operated in a PWR for four cycles. Fuel and reactor properties are shown in Table 6. Because these r-theta geometries do not have a discrete plenum included in the mesh, it is difficult to accurately calculate the temperature and pressure of the gas in the gap/plenum. In these simulations, the gas pressure is only affected by the calculated gap temperature, there is no volumetric change from gap closure or pressure increase from fission gas release. This is performed because there is not a discrete temperature calculation for the fuel rod plenum in the r-theta geometry.

Table 6. OSIRIS H09: Reactor and Fuel Properties

Parameter	Value	Unit
Coolant Pressure	15.5	MPa
Initial Plenum Pressure	3.1	MPa
UO_2 Density	95%	T.D.

The two smeared cracking models are expected to behave somewhat differently as they calculate the reduction of the fuel elastic properties according to different criteria. Because

of the statistical application of the fracture strength to the fuel, several additional simulations have been performed to quantify the variation in the fuel diameter as result of this method.

In total, sixteen simulations were performed; four each for both of the smeared cracking models, with and without the fuel relocation model enabled. Figure 54 shows crack patterns that form by using the exponential-release model (Figure 54(a)) and the power-release model (Figure 54(b)) near the end of the simulations. This illustration shows the remaining elastic fuel properties in the azimuthal (hoop) direction as a result of the formation of perpendicular, radially-oriented cracks. Because of how quickly the elastic modulus is reduced, the exponential-release model shows fewer but more well-defined radially cracks. This agrees well with the geometric assumptions used to generate the discrete crack geometry. The power-release model, however, shows a much more diffuse reduction in elastic properties in the fuel periphery, and the crack penetration length into the fuel is shorter. Interestingly, the power-release model indicates the likely formation circumferentially-oriented cracks form during sharp reductions in power

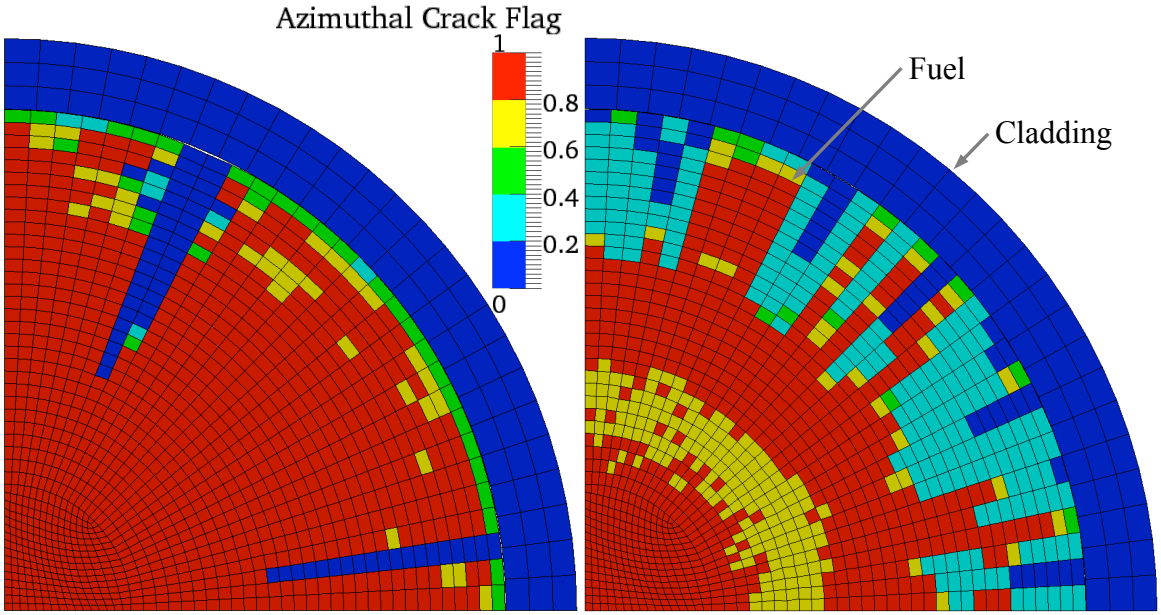

Figure 54. The exponential release model (a) shows fewer cracks that are more well-defined and penetrate further into the fuel radius. The power-release model (b) shows a more diffuse reduction in the fuel elastic properties in the fuel periphery. The plot legend, the azimuthal crack flag, shows the remaining elastic properties in the circumferential direction; the lower the value, the more crack-like the element becomes.

The maximum radial expansion of the fuel (a) and the cladding (b) are shown in Figure 55. The fuel and cladding displacements are both greatly reduced without using fuel relocation. Multiple simulations are performed here to demonstrate the variation in the fuel expansion from cracking due to the statistic application of the fracture strength. Simulations using the

power-release smeared cracking model show more fuel expansion and thus more cladding expansion by the end of life the exponential-release model. As well, there is a clearly discernable difference between the fuel expansion based on the application of the fuel relocation model, showcasing that fuel relocation is a dominant expansion contribution. The power-release smeared cracking model also consistently demonstrates significantly more expansion than the exponential release model after fuel densification occurs. By the end of life, there is an approximately 5µm deviation among the fuel expansion profiles based on crack type resulting from the statistical difference in crack formation. Before gap closure occurs, the cladding radius initially increases as the temperature is raised to operating temperature and quickly begins to decrease due to creep deformation from the pressure differential between the internal gas and the system pressure. After the onset of gap closure, the cladding radial expansion plotted in Figure 55(b) shows a deviation similar to the fuel based on the difference in fuel expansion from the cracks. Here, the power-release model shows the least cladding creep down amongst the different models, however, the predicted radial inward displacement is ~20µm greater than the measured radial expansion. It should be noted that the cladding radial expansion measurement is at room temperature, thus, it is compared to the radial displacement at the end of these simulations.

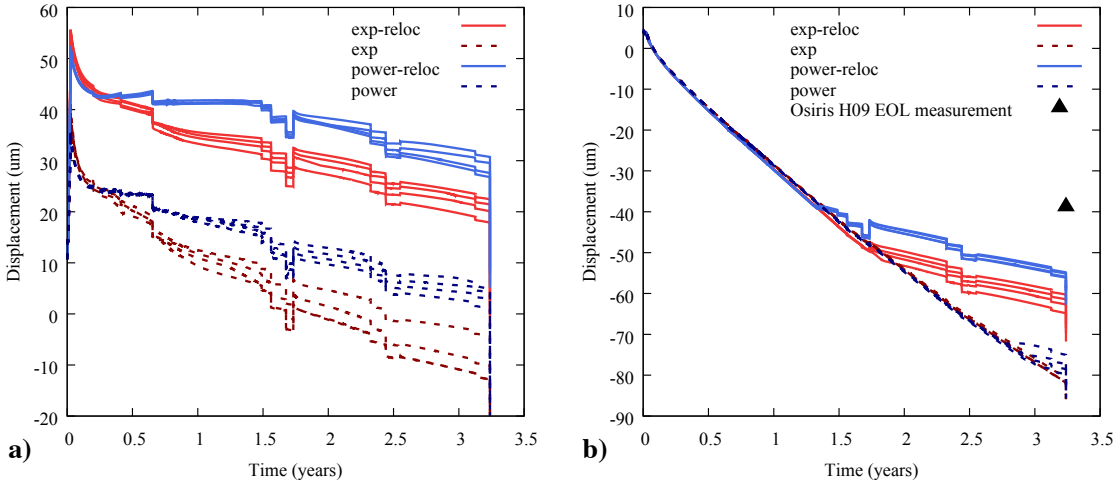

Figure 55. The fuel (a) and cladding (b) radial expansion, as a function of time following the power profile shown in Figure 53 and comparing different fuel mechanics models. The experimental cladding displacement after operation is shown with the black triangle.

Because of the larger (~10µm) fuel expansion for the power-release model over the exponential-release model, it is considered to be in better agreement with the cladding deformation measurement. For the forthcoming analysis, only the power-release model is considered where a smeared cracking model is used.

The fuel centerline temperatures for the OSIRIS H09 test fuel rod for the various fuel mechanics are shown in Figure 56. These results include: the elastic fuel properties, fuel

creep deformation (Section 2.6), the power-release smeared cracking model (Section 4.2.2), discrete meshed cracks (Section 4.2.3), and the isotropic softening model (Section 4.2.4). Additional simulations are included here without the fuel relocation model for the smeared and discrete cracking models. The variation among the fuel centerline temperatures is almost entirely due to the difference in the gap closure behavior of these fuel rods. The fuel temperatures for smeared cracking, creep, and isotropic softening models only differ a small amount initially until gap closure occurs. Because the discrete cracks are 70% of the fuel radius and included in the simulation at the beginning, they allow the fuel to expand more than the other simulations even before fracture would occur. A smaller fuel cladding gap leads to lower fuel temperatures. Eventually, however, the fuel temperatures begin to converge as gap closure occurs in all fuel rods with relocation before 1.5 years. The fuel rods without relocation show considerably higher fuel centerline temperatures, which are caused by their larger fuel cladding gap size.

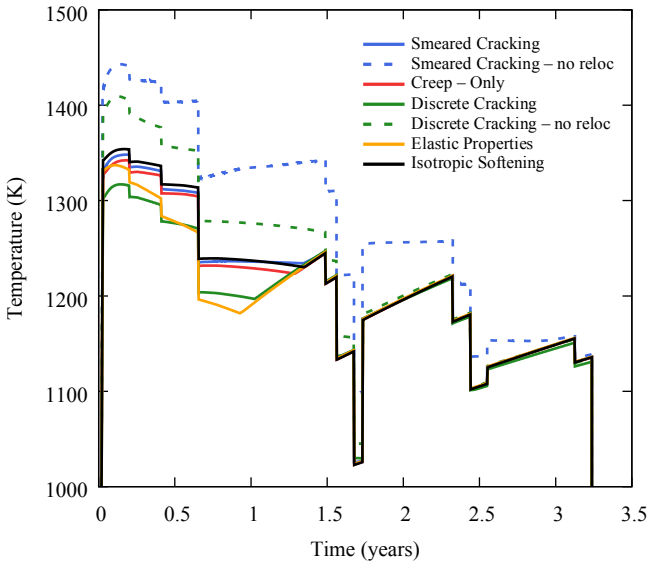

Figure 56. The fuel centerline temperature variation as a function of time as predicted by the various fuel mechanics model simulations.

Figure 53 shows the fuel radial expansion (a) and fuel rod gap thickness (b) variation amongst the different models as a function of time. Because the discrete meshed cracks are essentially fully-developed cracks, they expand more than the fracture models. After densification, the elastic fuel continues to expand from fission product swelling and fuel relocation, resulting in a much larger (>40μm) difference in the final fuel radius than the other simulations. By the end of the simulation, there is an ~10μm difference between fuel radius for the fracture models. Because the smeared cracking model implements a reduction in elastic properties corresponding to circumferential cracks, the fuel expands less than in the isotropic softening and creep-only simulations. In future iterations of these simulations, a crack healing criterion might need to be incorporated to regain the elastic properties under certain compressive stress conditions.

Similarly, gap closure occurs earliest for the fuel rods with the greatest fuel expansion. After the initial fuel expansion caused by fuel thermal expansion and densification, the fuel rod gap closes much faster than the fuel expands. This indicates that the gap closure behavior for these fuel rods is dominated by creep-down of the Zircaloy cladding. This is consistent with results reported in Chapter 3.

Without the relocation model the onset of gap closure is significantly delayed, especially for the smeared cracking where gap closure occurs at ~3 years. As the reactor is shutdown at the end of these simulations, the fuel contracts and the gap is reopened.

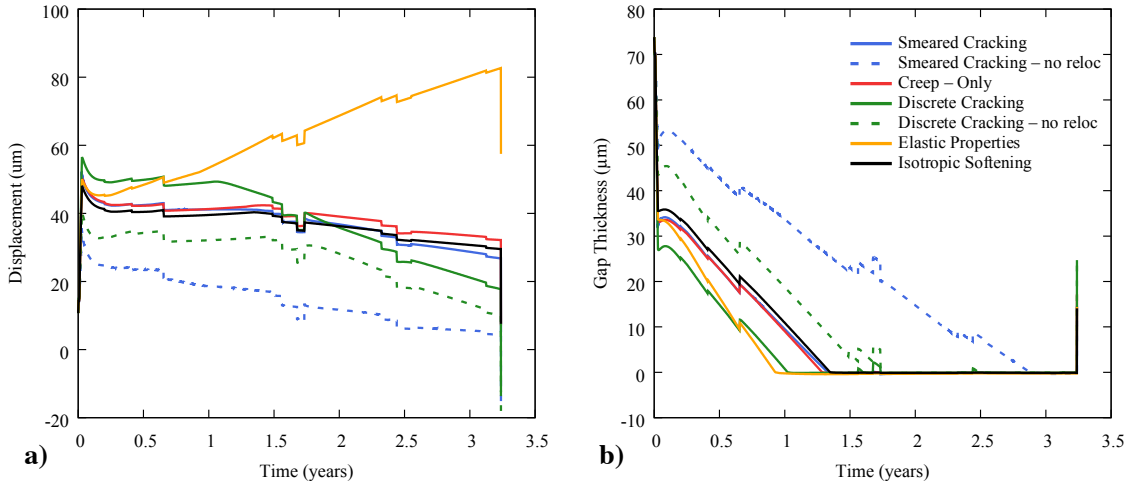

Figure 57. The fuel radial expansion (a) sharply increases initially due to thermal expansion and begins to decrease due to fuel densification where it remains relatively constant until gap closure. The gap thickness (b) sharply decreases early in the simulations until gap closure occurs.

The fuel hoop stress is very sensitive to the constitutive models used in each simulation. Figure 58 shows the fuel hoop stress over the initial rise to operating power (a) and over the full simulation. (b). The behavior of these mechanics models are best described during the rise to power. Because the elastic fuel has no stress relief due to fracture or creep, the stresses continue to increase as the temperatures increase to a steady state at operating power and fuel densification begins. As the hoop stresses increase, the fuel creep model eventually reaches a stress regime where it is sensitive and begins to deviate. After the operating temperature is reached, the stress is rapidly relieved.

The maximum hoop stresses for both smeared cracking models fluctuate near the fuel fracture strength as radial cracks form. Similarly, after the operating temperature is reached the hoop stress is relieved due to creep deformation. The isotopic softening model at the peak linear heat rate features ~7 cracks. Because the elastic properties are reduced isotropically, the hoop stress is almost immediately reduced and shows very little variation

over the rest of the operation. Likewise, because the discrete meshed cracks are able to immediately expand, there is very little build up in the hoop stress.

Figure 58(b) shows the hoop stress profiles over the entire 4 cycles of operation. This emphasizes the impact that the fuel creep and fracture models have on the fuel stress state when compared to the elastic fuel approximation. Because the elastic fuel does not include fuel creep of a fracture model to provide stress relief, the hoop stress is determined by the radial expansion. The strain from relocation is introduced as a stress-free strain, thus the hoop stress is generated by a combination of expansion from the fission product swelling and thermal strain. As such, the hoop stress in the elastic fuel cycles with the variation in the linear heat rate.

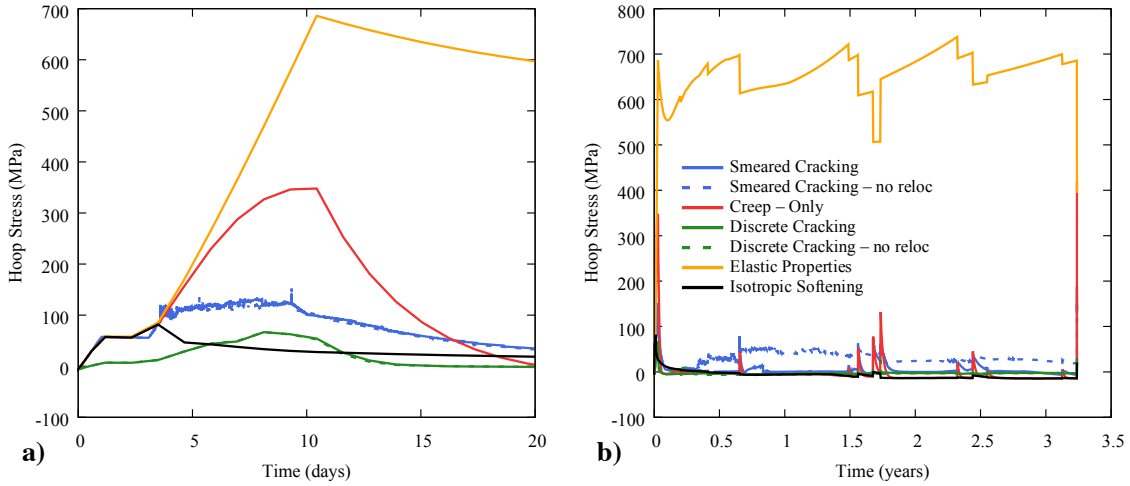

Figure 58. The fuel hoop stress over the first 20 days (a) reaches a maximum at the end of power ascension and slowly decays due to fuel densification and fuel creep. Fuel hoop stresses fluctuate over the full four-cycle (b) operation because of the power swings.

Features in the hoop stress profiles for the fracture models are better visualized by focusing on the lower hoop stress magnitudes, as shown in Figure 59. Immediately after large stresses are induced from fuel power cycling, the fuel creep model allows the fuel to deform and relive the stresses. Because the smeared cracking model can quickly reduce the elastic properties in a single fuel finite-element, stress concentration can form in the fuel. This can artificially increase the maximum hoop stress that is reported in the fuel, as the crack slowly progresses. This can be seen at nearly 0.75 years where the hoop stress is increased without any shift in the fuel temperatures.

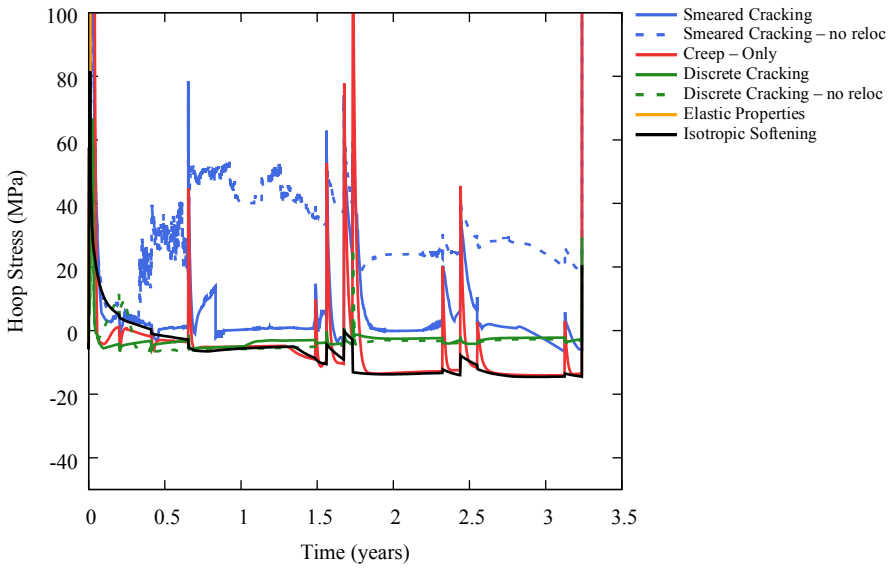

Figure 59. The maximum fuel hoop stress varies by the fracture model due to its behavior during the large shifts in power as prescribed by the power history.

As the cladding temperature increases during the rise to operating power, the cladding radius thermally expands by ~5 µm. Figure 60 shows the cladding radial expansion (a) and the maximum cladding hoop stress (b) for these simulations. Almost immediately, the cladding begins to creep-down due to the pressure differential between the coolant system and the rod internal pressure. The cladding radially expands as mechanical contact occurs for the elastic fuel first. Because the elastic fuel continues to expand, the cladding displacement continually increases. As gap closure occurs in the remaining simulations, the cladding slowly restricts the fuel. The fuel radius is slowly reduced as the linear heat rate is diminished at the end of the simulation. At the end of the operation, all of the fracture models predict significantly more inward displacement (~15 to 40 µm) as compared to the EOL experimental test rod measurement.

After the increase to operating temperature, the Zircaloy cladding is initially in a compressive state until gap closure occurs. Again, fission gas release plays little to no role in the plenum pressure calculations from these fuel rods because there is no discrete fuel plenum volume/temperature calculation. Figure 60(b) shows the cladding hoop stress for these simulations. After gap closure occurs, only the elastic fuel simulation reaches tensile cladding stresses for any appreciable time, and even these only reach a maximum of ~60 MPa. The other simulations fluctuate in a compressive state after gap closure due to the thermal cycling of the fuel. As the fuel contract during reactor shutdown, the stress rapidly increases reaching a maximum value of ~20 MPa for the isotropic softening simulation.

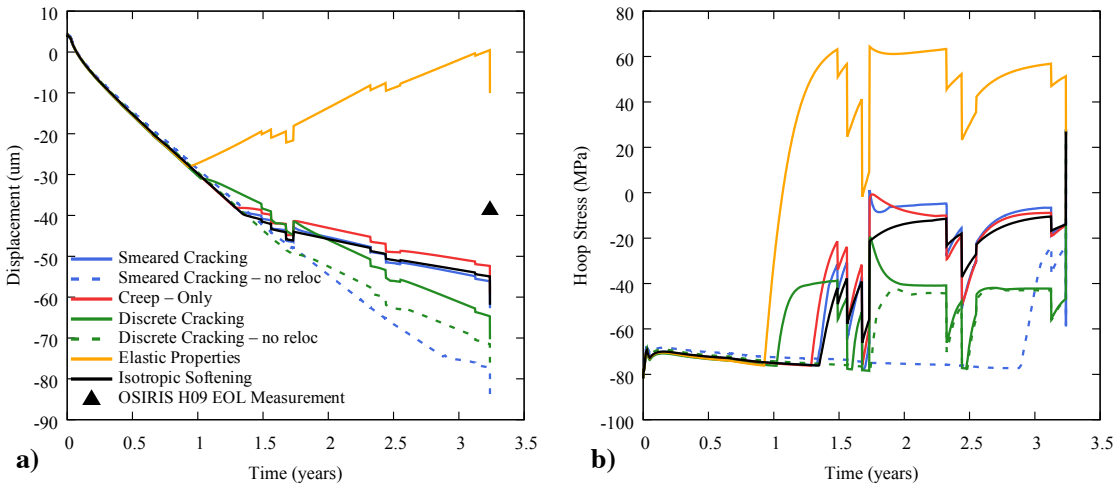

Figure 60. The cladding radial displacement (a) decreases due to creep-down from the pressure differential across the cladding until gap closure occurs. Similarly, the maximum cladding hoop stress (b) is increased after gap closure but remains in a compressive state for many of the simulations for the remaining operation.

These results show an early attempt to reconcile fracture into fuel performance simulations and determine the accuracy of several proposed models against measured fuel rod data. The smeared cracking model implemented here has several assumptions that need to be investigated more closely including the applicability of the model for plane-strain geometries and how the reduction in the elastic modulus should affect the creep compliance of the fuel. Although these results do not provide a great enhancement in the agreement with the measured data, they do provide a framework that can eventually be calibrated and improved for application to different fuel rod geometries and materials.

4.4 FeCrAl Cladding Results

The goal behind the investigation of the fuel mechanics models was to determine the accuracy of these models using a controlled experiment. Ultimately, this is performed to identify areas where these models can be improved in order to accurately simulate nonconventional fuel geometries with alternative cladding materials. This section discusses the work performed by applying these models, as they are implemented in Section 4.3, to FeCrAl cladding using the fuel geometry and conditions of interest, discussed in Chapter 3.

Figure 61 shows the fuel mesh generated using the specifications from Chapters 2 and 3, summarized in Table 7. For this analysis, the FeCrAl geometry and reactor conditions from the Peach Bottom BWR (Table 8) analysis in Chapter 3 are used in conjunction with the power history from the OSIRIS H09 test rod.

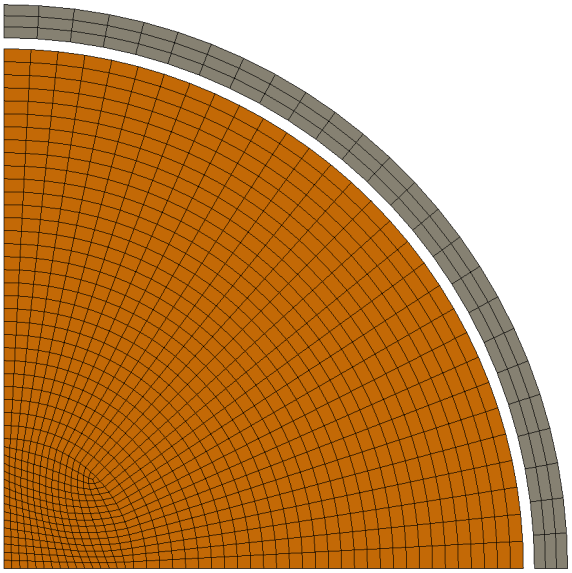

Figure 61. An r-theta fuel rod geometry using specifications from the earlier BWR analysis for the Peach Bottom BWR in Chapter 3 is made.

Table 7. FeCrAl Fuel Geometry Specifications

Cladding Type	Fuel Radius (μm)	Gap Thickness (μm)	Cladding Thickness (μm)
FeCrAl	4700	100	300

Unlike Section 4.3, BWR conditions are used in the analysis performed here. The large difference here is the initial plenum pressure and the coolant system pressure. The previous analysis used a coolant pressure of 15.5 MPa and a fuel rod plenum pressure of 3.1 MPa. Because there is no effect from the fission gas release model on the fuel rod plenum evolution for these simulations, the plenum pressure remains relatively low for the reactor operation.

Table 8. Boiling Water Reactor and Fuel Properties

Parameter	Value	Unit
Coolant Pressure	7.136	MPa
Coolant Temperature	560	K
Initial Plenum Pressure	.5	MPa
UO_2 Density	95%	T.D.

The fuel centerline temperatures are shown in Figure 62, and demonstrate that the FeCrAl cladded fuel rods behave much differently than the Zircaloy counterparts (discussed in Section 4.3). In these simulations, the fuel cladding gap does not close. Interestingly, it is the discretely cracked fuel pellet simulation which exhibits the most fuel expansion and

thus the lowest fuel centerline temperatures. The simulations without fuel relocation, as expected, show much larger temperatures than their counterparts. Generally, the other simulations share similar behavior with the exception of the smeared cracking model. After the first large drop in power at about 0.6 years, the smeared cracking model shows noticeably less fuel expansion. This occurs because elements are determined to be cracked near the core of the fuel, similar to the crack pattern shown in Figure 54(b). Because so many of these elements lose their radial strength, as temperatures increase in the core of the fuel, the fuel in these regions lose the ability to exert force on the fuel periphery and further expand the fuel.

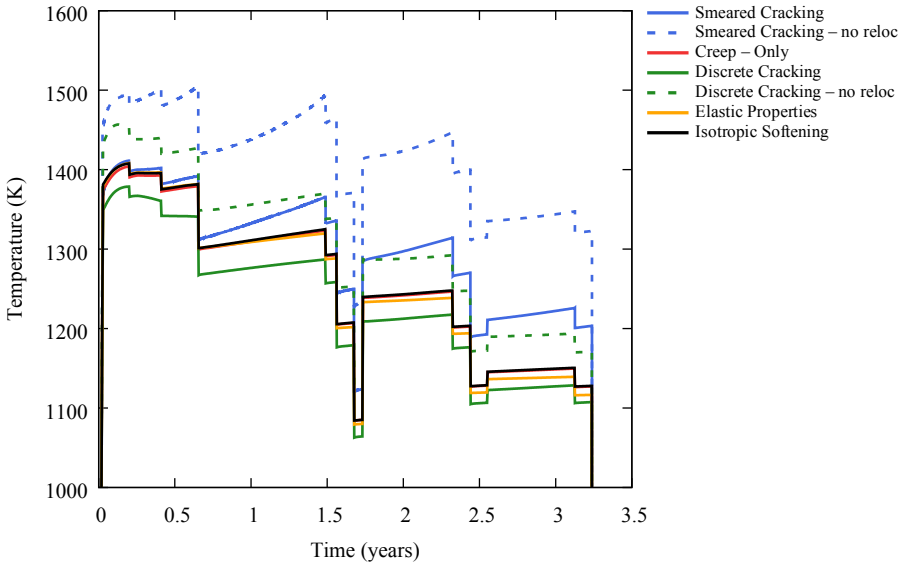

Figure 62. The fuel centerline temperature variation as a function of time as predicted by the various fuel mechanics model simulations. Over these simulations, the smeared cracking simulations show a much higher temperature.

Figure 59 plots the maximum fuel hoop stress (a) and maximum radial displacements (b), respectively. These simulations show a similar maximum hoop stress response over the reactor operation to the Zircaloy cladding. The elastic fuel simulation retains extremely large hoop stresses throughout the simulation, and the other simulations only experience large hoop stresses during large power cycles.

The fuel radial expansion (Figure 63(b)) also shows a different trend than the Zircaloy cladded fuel rods. The discrete cracked mesh exhibits more fuel expansion earlier in life and retains this expansion through the simulation. The other simulations show similar fuel expansion until the first decrease in power. As previously mentioned, at this point the fuel expansion in the smeared cracking simulations is significantly hindered.

The simulations without fuel relocation and their counterparts show similar trends, indicating that the magnitude in fuel relocation for these simulations is ~20μm and that the

fuel relocation does not change the expansion rate. This implies that the fuel expansion is largely due to fission product swelling, as the fuel continually expands while the fuel temperatures are reduced.

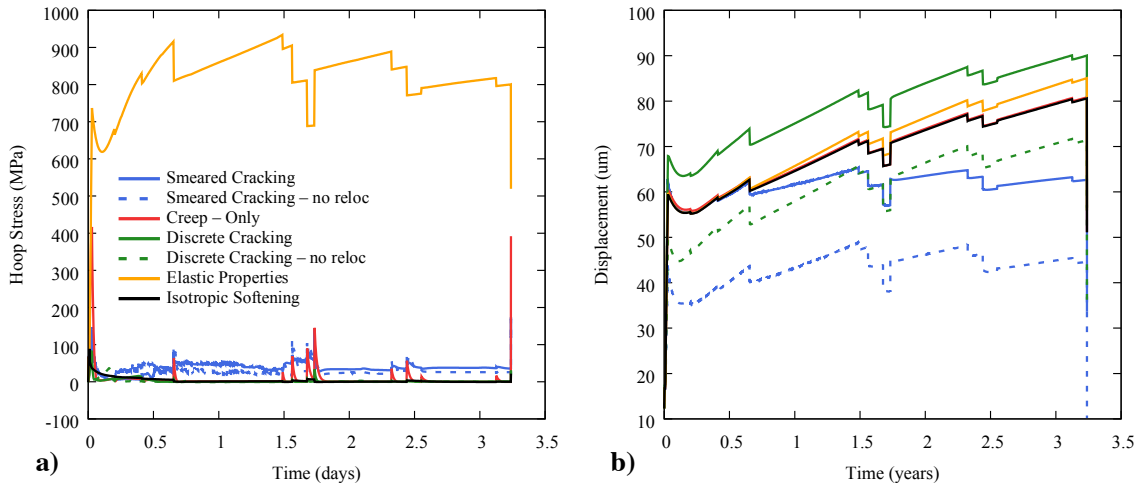

Figure 63. Similar to the previous analysis in Section 4.3, the maximum hoop stress in the fuel (a) shows spikes corresponding to large power shifts. The fuel radial expansion (b) shows a large variation between models over the four-cycle simulations.

The gap thickness for the FeCrAl cladded fuel rods is shown in Figure 64. Unlike the Zircaloy, the gap does not close quite as rapidly for the FeCrAl cladded fuel rods due to cladding creep down. While there is some creep-down due to irradiation creep in the cladding, fuel expansion dominates the gap closure behavior for these fuel rods. As previously discussed, the smeared cracking models begin to deviate after an early (~.6 years) power cycle in power and exhibits relatively little fuel expansion from that point forward. Because the discrete cracks are meshed into the fuel geometry at the beginning of the simulation, the fuel is rapidly allowed to expand which continue through much of the fuel lifetime.

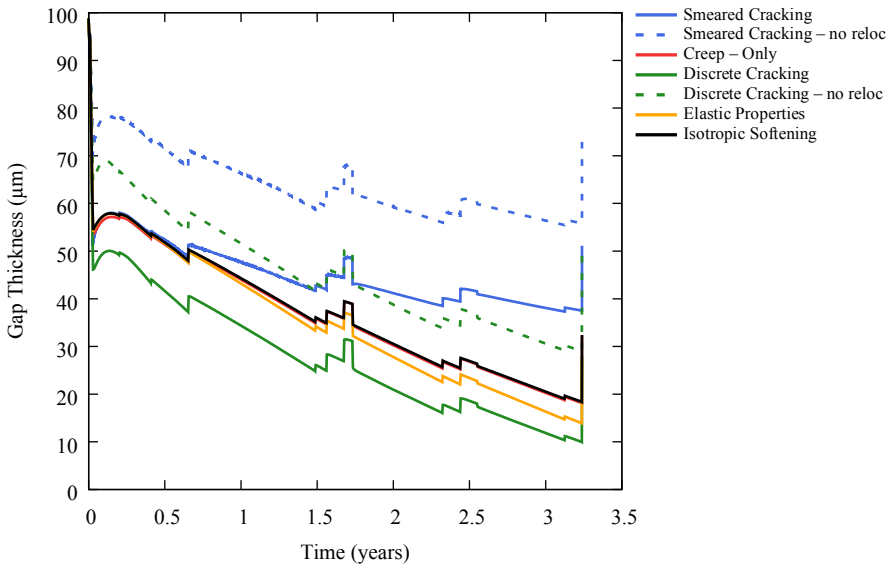

Figure 64. After the initial rise to power, the gap closure behavior varies widely by the model used, however all simulations show sharp variation according to the fuel temperatures.

Because the gap closure behavior of these fuel rods is much different than the Zircaloy rods reported in Section 4.3, the gap remains open. These results show the sensitivity of the fuel to these fracture models without gap closure, emphasizing that calibration of these models is needed for the uniquely performing alloys with non-conventional fuel geometries. This difference in fuel rod behavior demonstrates the need to develop specific test cases that not only demonstrate the power cycling that an LWR is expected to experience, but also irradiate the fuel long enough to gauge the conditions of interest. Because the FeCrAl cladded fuel rods can exhibit the onset of gap closure much later in life (Chapter 3), the greatest effect of the fuel fracture models is on the fuel temperatures. While the variations in predicted fuel temperatures are within ~25K initially, by the end of the simulation the temperatures show an ~100K difference. This is expected to change the fission gas behavior and possibly initiate the bootstrapping effect between the release rate and temperature, although this will need further investigation in full length fuel rod simulations, since the fuel plenum has not been modeled in these simulations.

4.5 Summary

In order to improve the accuracy of fuel performance simulations for nonconventional fuel geometries and alternative cladding materials, an initial investigation of the impact of including various fracture models has been performed and discussed in this chapter. This investigation includes several different methods for the incorporation of fuel fracture, an important mechanism of diametral expansion, into the fuel performance code.

Fuel fracture has been the focus of this investigation, and it was selected for evaluation because it plays a role in the evolution of the fuel cladding gap closure behavior and the subsequent mechanical interaction that determines the cladding stress state. Because many of the current relations used to determine the fuel expansion are highly empirical data fits from specific fuel tests, a more mechanistic solution is sought. In order to begin this investigation, a smeared cracking model was chosen and modified in the BISON fuel performance code. Although this model still lacks many aspects to develop a meaningful comparison representative of fracture in UO_2, it performs relatively well for Zircaloy cladding. For FeCrAl cladding, on the other hand, due to the reduced creep down of FeCrAl cladding, the impact of varying fracture models appears to be much less sensitive than the case of conventional Zr-alloy rods.

Several critical improvements are needed before this model can see widespread deployment. These include improvements in the range of parameters being scaled along with the elastic modulus, such as the Poisson's Ratio and the fuel thermal conductivity, and model improvements such development of a crack healing mechanism and possibly an augmentation to the fission gas release model.

In the current smeared cracking models, the Poisson's Ratio is calculated based on the fuel properties without any impact from fuel fracture. In order to improve the behavior of elements as they are stretched due to crack opening and closing, the Poisson's Ratio should decay using a similar method to the elastic modulus. Likewise, fuel relocation tests show that the onset of cracking is accompanied by a reduction in the thermal conductivity of nearly 30% for the fuel (Williford et al., 1980). Future work on this model will include a calibrated reduction for both smeared cracking and the Poisson's Ratio for the cracked elements.

Future crack models may need to constrain the crack direction and include crack healing. Crack healing is an important aspect of the fracture mechanics affecting re-cohesion or re-sintering of the cracked surface and may result in better agreement with the experimental results as elastic properties are able to be regained. These simulations do not currently include any expedited crack healing model, and as such they cannot exhibit the fuel "ratcheting" associated with continued power cycling. In order to include this contribution to the diametral expansion, crack healing criteria will need to be developed and implemented into the smeared cracking model.

As well, additional work may be performed to incorporate aspects from the fuel fracture model into the fission gas release model. As crack networks propagate both radially and circumferentially through the fuel pellet, new free surfaces are created which may serve as sites to allow more gaseous fission products to diffuse from the fuel (Pastore et al., 2013). Although this fission gas release mechanism has never been thoroughly evaluated through experiments, it is expected to play a role in the transient fission gas release occurring during reactor power maneuvering (Maki and Meyer, 1978).

As well, additional analyses are needed to further identify the cladding stress development due to mechanical contact between cladding and fuel cracks. Localized increases in cladding stress due to PCMI in the presence of fuel cracks and defects have been documented (Capps et al., 2016). To reproduce this analysis with smeared cracking models, the mechanical contact model currently employed in BISON will have to be investigated to include the effect of friction after gap closure.

Mechanistically modeling the effect of fuel fracture is difficult because of the limited available experimental data that exclusively investigate fuel behavior. By using data from integral fuel rod experiments, error is introduced through inaccuracies in the cladding behavioral models. This presents a unique and difficult challenge suited for continued improvement using high-fidelity fuel performance analysis. Accurately modeling stress evolution in the fuel is key to assessing fuel behavior up to gap closure and the subsequent deformation of the cladding due to PCMI.

CHAPTER 5: TRANSIENT OPERATION (LOSS-OF-COOLANT ACCIDENT)

5.1 Overview

The goal of identifying an alternative cladding material to Zircaloy for LWR fuel systems is to improve the reactor safety during high-temperature transient conditions. In order to provide insight into how FeCrAl cladding will perform compared to Zircaloy in this environment, fuel performance code capabilities can be extended, provided that thorough constitutive models are developed and implemented (Van Uffelen et al., 2008).

Because *in-situ* testing of LWR fuel rods under accident conditions is difficult and expensive, various test reactors and transient effects programs are utilized to develop specific thermo-mechanical models of the fuel and cladding behavior. These models can be incorporated into fuel performance codes, which can then be used to screen fuel rods for failure over a range of postulated transient scenarios. Of the scenarios which are typically considered, two design basis accidents, the loss-of-coolant accident and the reactivity insertion accident, are typically investigated to ensure reactor safety (OECD, 2012).

While each of these accidents can ultimately lead to fuel failure, the target of this analysis is the cladding behavior in the high-temperature environment sustained during a potential large-break loss-of-coolant (LBLOCA) accident. In this analysis, conditions from a mitigated LBLOCA are extended to compare the beyond design basis accident response of FeCrAl as compared to standard Zircaloy cladding.

During a loss-of-coolant accident with Zircaloy cladding, as the reactor loses its capability to cool the fuel, fuel rod temperatures begin to increase. Eventually, if this increase in temperatures is unmitigated, then the cladding will begin to 'balloon', or deform outwards, due to the pressure differential between the interior of the fuel rod and the pressure remaining in the reactor pressure vessel. If this deformation persists, cladding burst can occur during these high temperature conditions from a combination of thermal creep and plasticity (Erbacher and Leistikow, 1987). If the temperature continues to increase further, the exothermic oxidation reaction of the Zircaloy cladding may become autocatalytic. This produces large amounts of heat, consumes the cladding, and produces hydrogen gas. Within this study, the cladding performance for both FeCrAl and Zircaloy cladding under these conditions are targeted.

Traditionally, separate fuel performance codes are utilized to simulate the fuel rod behavior under steady-state and transient conditions either in conjunction with each other, or to provide a stand-alone analysis. Transitioning the state of the fuel rod from normal operation into the transient environment is necessary to evaluate the unique condition of the fuel at a variety of fuel burnups. To accomplish this, these simulation conditions contain long-term steady-state reactor operation before transitioning into the accident scenario. This allows

the state of the integral fuel rod at different specified burnups to be incorporated into the transient analysis.

Simulations of Zircaloy cladding behavior under LOCA conditions have been performed by Pastore and co-workers using the BISON fuel performance code (Pastore et al., 2015) with the purpose of comparing modeling predictions to the REBEKA cladding burst tests. Figure 65 shows azimuthally and axially varying temperatures on the cladding surface as well as the cladding creep strain, and the cladding elements determined to have ruptured. This analysis was performed using specifications from the REBEKA cladding burst test suite and demonstrate that the BISON fuel performance code has a framework in place to implement additional models and assess fuel and cladding behavior in transient conditions.

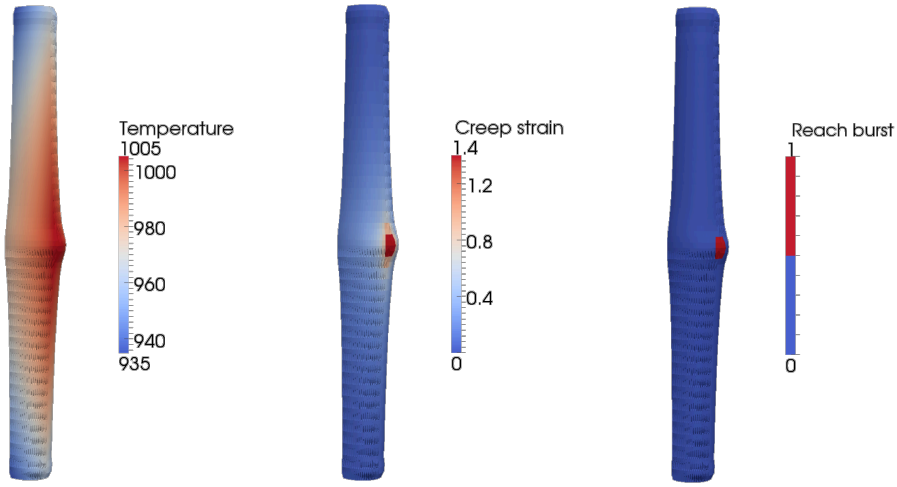

Figure 65. BISON simulation showing local temperature, creep strain, and area of cladding burst for Zircaloy cladding under LOCA conditions, as reproduced from (Pastore et al., 2015).

To accurately simulate the cladding behavior under a loss of coolant accident, several key models are needed. These include chemical and phase changes of the cladding alloy (such as oxidation), high temperature constitutive behavior, and cladding rupture criteria. The conditions mentioned in this analysis only consider azimuthally uniform heat transfer conditions, and, as such, utilize axisymmetric fuel rod geometries. Previous experimental analysis shows that azimuthally varying the cladding temperature can significantly reduce the cladding strain at which burst occurs. This is an important consideration for future work targeting the effect of fuel pellet eccentricity, nonuniform temperature profiles during core reflooding, and multi-rod failure analysis (Erbacher and Leistikow, 1987).

Section 5.2 discusses, in detail, the construction of the constitutive models for both cladding types. This section also provides a comparison of FeCrAl cladding burst simulations in BISON against results from the ORNL Severe Accident Test Station. Section 5.3 includes the identification and development of the representative boundary conditions used to simulate the normal and transient reactor operation. Section 5.4 provides

a summary of the results from the steady-state reactor operation. Sections 5.5 summarizes the results of the LOCA analysis up to cladding rupture and Section 5.6 details the results of extending these simulations by calculating the thermal solution following mechanical failure. A summary of the work performed and future model improvements is discussed in Section 5.7.

5.2 High-Temperature Constitutive Models

In order to assess the condition of the cladding materials under LOCA conditions, high-temperature behavioral models were developed as needed and implemented into BISON. These models for Zircaloy and FeCrAl include high-temperature thermal creep, plasticity, failure, and oxidation. Additionally, the models were evaluated against data from cladding burst tests to assess their accuracy.

5.2.1 High-Temperature Thermal Creep Model

For these simulations, both the FeCrAl and Zircaloy cladding utilize two separate models for the thermal creep calculation. These models use a separate calculation during lower temperature steady-state conditions, and under transient conditions, transition into high-temperature models.

For the FeCrAl cladding, the Arrhenius-based relationship describing the C35M thermal creep behavior in Section 3.8 is used, which is recommended for temperatures up to 870 K (Field et al., 2017). Above 900 K, the original creep relation described by Saunders et al. (Saunders et al., 1997), described in Section 2.6, is used. To transition between the high and low temperature creep relations, an additional Arrhenius-based relation has been fit and implemented. This transition function is used to ensure that the creep calculation remains a continuous function and does not hinder code convergence. Equation 21 shows the general form of the thermal creep equation used in these calculations, as reproduced from Eq. (4) in Sect. 2.5. Tabulated values used in the thermal creep calculation for FeCrAl cladding are shown in Table 9.

$$\varepsilon_{c,th} = C \cdot \sigma^n \cdot \exp\left(-\frac{Q}{kT}\right) \cdot t \tag{21}$$

where C is the creep pre-exponential (s^{-1}–Pa^{-n}), σ is the effective stress (Pa), n is the stress exponent fitting parameter, Q is the creep activation energy (eV), T is the temperature in K, t is the time in seconds, and k is the Boltzmann constant ($eV\text{-}K^{-1}$). Figure 66 shows the distinct increase in the thermal creep rate corresponding to the high-temperature regime for three varying stresses. Because the same stress exponent is used at all temperatures, the stress scaling between the curves remains constant.

Table 9. Thermal Creep Parameters for FeCrAl Cladding

Cladding Temperature (K)	Creep Prefactor, A (Pa^{-n}-s^{-1})	Activation Energy, Q (eV)	Stress Exponent, n (unitless)
<= 860	2.89e-36	2.560	
860 < T < 890	2.20e-12	6.635	5.5
=> 890	5.96e-27	4.062	

Similarly, for the Zircaloy cladding, the Limback thermal creep model described in Section 2.5 is used up to 700 K. Above 900K, a cladding thermal creep model derived from cladding tests under LOCA conditions is used, as described by (Erbacher et al., 1982). Between these temperatures, a weighting term is used to interpolate between the different functions. The LOCA thermal creep model currently implemented in BISON takes the same form as the model for the FeCrAl (Eq. (21)). This model also takes into account the volumetric fraction of the α and β phase in the Zircaloy cladding based on the time and temperature variation rate (Pastore et al., 2015). Additionally, this calculation also includes an anisotropic reduction factor for the pure – α phase (Erbacher et al., 1982).

Table 10. High-Temperature Creep Parameters for Zircaloy-4 Cladding (Erbacher et al., 1982) [adapted from (Pastore et al., 2015)]

Zircaloy Phase	Creep Prefactor, A (Pa^{-n}-s^{-1})	Activation Energy, Q (eV)	Stress Exponent, n (unitless)
α	3.99e-32	3.33 + 2.56e-4 (T-923.15)	5.89
α-β (50%-50%)	2.51e-15	1.06	2.33
β	1.65e-22	1.47	3.78
Note: in the mixed α-β phase if the strain rate exceeds 3e-3s^{-1}, interpolation is performed directly between the individual α and β phases			

Figure 66 shows the thermal creep rate for both cladding materials from 600 K – 1220 K for increasing stresses. This considers only the pure α-phase Zircaloy thermal creep constants. Zircaloy exhibits much more thermal creep at lower temperature, and this trend does persist with increasing temperature, although with a decrease in the difference between the thermal creep rates of Zircaloy versus FeCrAl. As the temperature reaches nearly 1200 K, the thermal creep rate for the FeCrAl is about an order of magnitude less than Zircaloy. This shows the Zircaloy cladding will experience much more thermal creep deformation than the FeCrAl cladding over burst relevant conditions.

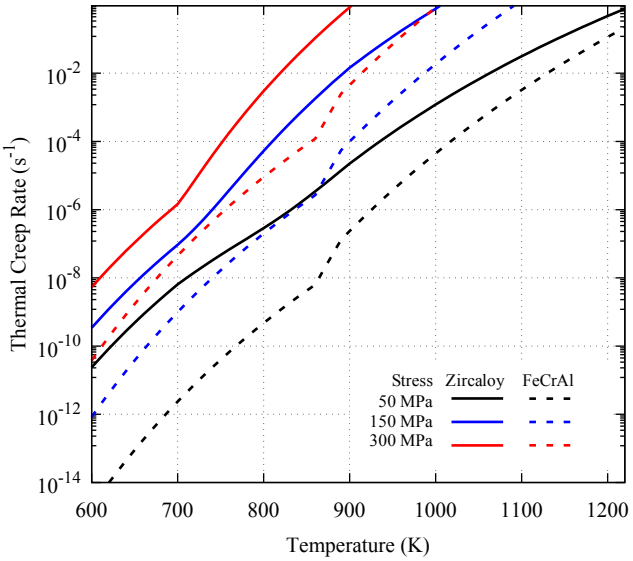

Figure 66. The thermal creep behavior for both the FeCrAl and the Zircaloy is divided into a separate low-temperature and high-temperature contribution with interpolation between the two regions.

5.2.2 Cladding Plasticity and Failure Models

In order to calculate the plastic deformation and assess failure of the cladding materials, isotropic plasticity models are used to define the stress-strain relationship after the material reaches the yield point. For this analysis, data from FeCrAl material testing (Maloy et al., 2016; Yamamoto et al., 2015) is used to develop a power-law strain hardening model which is implemented into BISON. The ultimate tensile strength is used as the failure criteria for the FeCrAl cladding. As the strain progresses beyond the yield point of the material, the simulations will eventually reach the failure criteria; when this stress is reached, the simulation is terminated. This is based on observations from prior burst testing experiments where very little necking occurs in the cladding before rupture (Massey et al., 2016). The yield strength and ultimate tensile strength of FeCrAl are shown in Figure 67(a) and (b), respectively. Both the yield and ultimate strength begins to rapidly decrease as the temperature approaches ~2/3 of the alloy melting temperature. For this analysis, the C35M (Rolled) properties are used to simulate the FeCrAl cladding.

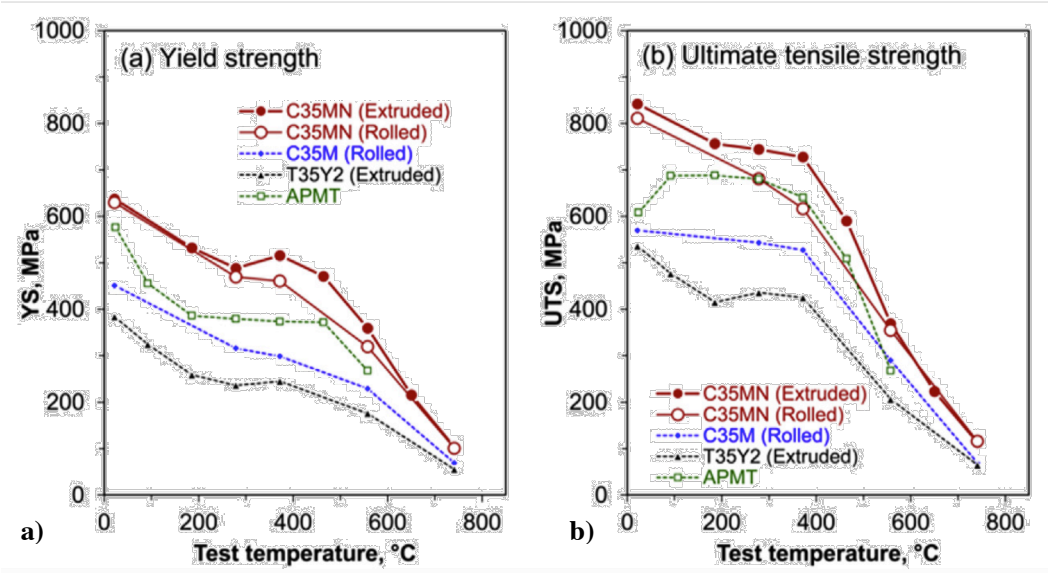

Figure 67. The measured yield strength (a) and ultimate tensile strength (b) for various FeCrAl alloys as a function of temperature. [Reproduced from (Yamamoto et al., 2015)]

In order to utilize this method of cladding failure, the uniform plastic elongation was obtained from an similar FeCrAl sample (Maloy et al., 2016) and used to derive a series of power-law strain hardening relations for the alloy at several different temperatues. These relations were implemented into BISON and interpolated to provide a more thorough description of the temperature-dependant plastic behavior of the FeCrAl cladding. This model does not consider any change in the yield strength or ultimate tensile strength due to irradiation hardening. While irradiation hardening is known to increase both the yield and tensile strength at reactor operating temperatures, assessing the appropriate values to use during an accident is complicated by the anticipated thermal annealing of the irradiation damaged microstructure.

To demonstrate the power-lar strain hardening and FeCrAl cladding failure criteria, a rudimentary simulation of a tension test was performed in BISON for the FeCrAl alloy. This tests consists of a coarse finite-element tensile specimen where the bottom is fixed and the top of the test specimen is subject to a slowly increasing strain. This places the specimen in uniaxial tension, and the yield and subsequent failure of the material can be modeled, as shown in Figure 68. In this simulation, the tensile test was performed at four separate temperatures ranging from room temperature to the approximate cladding rupture temperature expected during a LOCA. These simulations end with assumed cladding failure at the calculated ultimate tensile strength. The results of these BISON modeled tensile tests show a decreasing yield strength and ultimate tensile strength with increasing temperature and show the variation in uniform elongation of the alloy, expected at cladding failure.

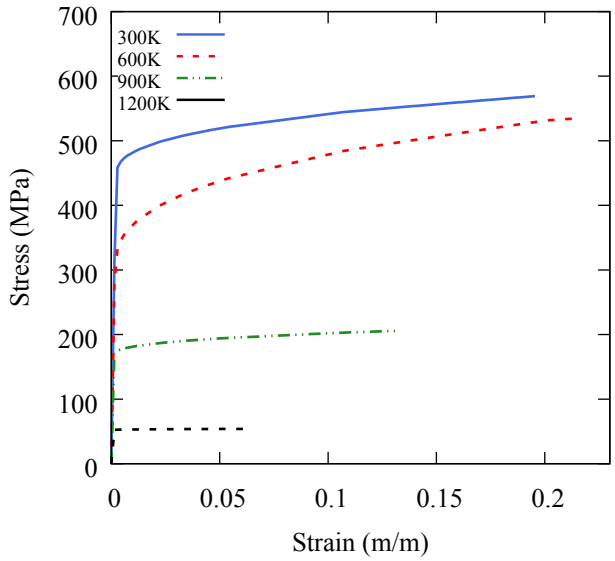

Figure 68. BISON model predictions for the stress strain response of a FeCrAl subject to a simulated tensile test, as a function of test temperature. These simulations end when the ultimate tensile strength is reached.

In order to better predict the high-temperature failure of the FeCrAl cladding, the ultimate tensile strength of the alloy was re-examined. This was motivated by a lack of data at higher temperatures where the alloy is expected to lose strength much faster than a simple linear interpolation to the melting temperature would predict. Figure 69 shows the ultimate tensile strength implemented into BISON. This shows that above 1000 K there is no data, so the expected behavior of the alloy must be used. In the first iteration of this model, the ultimate tensile strength was simply interpolated to the melting temperature where the alloy is assumed to have no remaining strength. This results in an overprediction of the ultimate tensile stress. Next, the ultimate tensile strength was estimated based on the high temperature performance of stainless steels, which lose much of their strength before the alloy reaches the melting temperature. This was compared against recent results generated from fitting directly to burst test data (Gamble et al., 2017), and it agrees well.

While this is an early implementation for the failure criteria of FeCrAl cladding, a more thorough examination of the material behavior at high temperatures could be made with more ultimate tensile strength data.

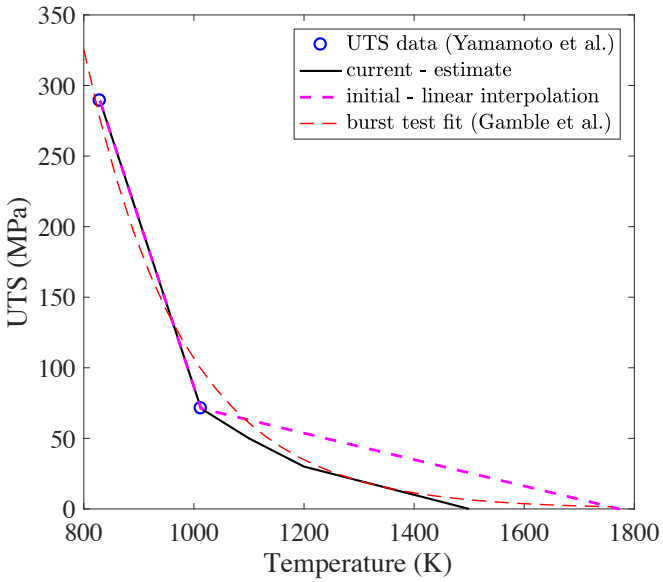

Figure 69. Ultimate tensile strength of FeCrAl as a function of temperature showing two iterations of the model implemented in BISON for high temperatures (initial versus current), compared to a fit to available data performed by Gamble and co-workers (Gamble et al., 2017) and UTS data from (Yamamoto et al., 2015).

To calculate the plastic behavior of the Zircaloy cladding, a much more thorough model, the PNNL stress-strain correlation, developed at Pacific Northwest National Laboratory for the FRAPCON fuel performance code (Geelhood et al., 2008), is currently implemented in BISON (Hales et al., 2014) and used for this analysis. This model utilizes a strain-rate dependent strain hardening model with a variable (temperature, cold work, compositions, etc.) strain hardening exponent and strength coefficient to predict the Zircaloy response at higher fuel burnups.

Failure of Zircaloy cladding is determined from burst stress data that was developed from the REBEKA burst test experiment (Erbacher et al., 1982), in addition to a strain rate failure criteria for low-stress failure. This burst stress function is shown in Equation 22, and is dependent of the cladding phase, temperature, and the fraction of oxygen dissolved into the cladding.

$$\sigma_B = a \cdot exp(-bT) \cdot exp\left(-\left(\frac{f_{wt,ox} - 0.0012}{9.5 \cdot 10^{-4}}\right)^2\right) \quad (22)$$

Where σ_B is the cladding burst stress in MPa, a and b are burst stress parameters (shown in Table 11) based on the phase of the Zircaloy, T is the temperature in K, and $f_{wt,ox}$ is the weight fraction of oxygen dissolved in the cladding. In this expression, the initial oxygen weight fraction of the cladding is assumed to be 0.0012. In BISON, the oxygen weight fraction in the cladding is calculated from the oxygen mass gain from the cladding

oxidation model. As previously mentioned, the Zircaloy phase fraction is calculated using a separate model in BISON (Pastore et al., 2015).

Table 11. Phase Dependent Burst Stress Parameters for Zircaloy-4 (Erbacher et al., 1982)

Phase	a (MPa)	$b \times 10^3$ (K^{-1})
α	830	1.0
α-β (50%-50%)	3000	3.0
β	2300	3.0

Figure 70 shows the burst stress function for three ranges of heating rates compared to experimental burst test data. The variation in the heating rate influences the onset and rate of the phase change. This figure shows a summary of unirradiated cladding burst tests by (Erbacher et al., 1982) and Chapman (Chapman et al., 1979), and a small amount of irradiated cladding burst tests described by (Bennett et al., 1979). The burst test data summarized by Bennett includes spent fuel cladding from the H.B. Robinson and Oconee nuclear reactors and shows a remarkably lower burst stresses at lower temperatures for high heating rates. This is included to provide a comparison to used fuel, as these other experiments do not use irradiated specimens. Although the fuel burnup is not believed to greatly influence the cladding burst behavior, these burst test discrepancies can possibly be accounted for based on the higher oxygen weight fraction in the cladding as the cladding oxidizes during operation, and from an azimuthally varying temperature during testing (Erbacher and Leistikow, 1987). This shows the burst stress failure criterion provides a somewhat liberal determination of stress at which the Zircaloy cladding will fail.

At high temperatures, the cladding thermal creep model may produce significant stress relaxation such that the burst stress cannot be reached. Because this model may not accurately assess the cladding failure in low-stress conditions, an additional strain-rate failure criterion ($\dot{\varepsilon_B} = 2.78 \cdot 10^{-2} \ \ s^{-1}$) is used (Hales et al., 2014; Pastore et al., 2015). It has also been suggested to include a limiting strain along with the strain rate criteria (Van Uffelen and Suzuki, 2012), and although this is not included here, it will be examined as this work is extended.

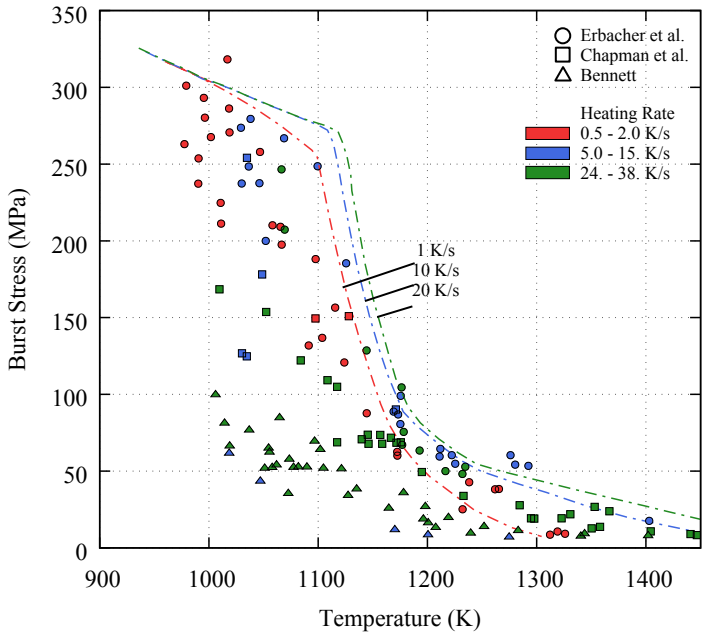

Figure 70. The burst stress failure criteria for Zircaloy cladding as a function of temperature and heating rate. In this plot, three separate sets of burst test data are shown for different heating rate (Bennett et al., 1979; Chapman et al., 1979; Erbacher et al., 1982). The dashed curves represent the burst stress relation from Erbacher et al. for three different heating rates. Note: the data from Bennett is based on previous burst testing of archive and used fuel cladding.

5.2.3 Comparison to ORNL Severe Accident Test Station

In order to benchmark the current FeCrAl cladding behavioral models implemented in BISON against experimental data, additional simulations were performed to replicate a cladding burst experiment. These burst tests, performed at Oak Ridge National Laboratory using the Severe Accident Test Station (Massey et al., 2016), utilize a 30 cm long, 9.5 mm diameter pressurized cladding tube in an infrared furnace with flowing steam (.1 MPa) over the outer surface. The cladding tubes are pressurized using helium gas and contain zirconia pellets.

Figure 71(a) is an example of the 3D finite element model used for the burst test simulations. The green outer elements are the FeCrAl cladding, and the grey elements in the fuel rod interior are Zirconia pellets. Figure 71(b-d) shows an example of the change in relevant conditions for a single burst test. The cladding temperature and pressure are increased as the simulation starts, up to 50 seconds and held constant at ~573 K. At ~140 seconds, the plenum pressure inside the cladding tube is increased. After this point, the tube contains the final amount of gas, and at ~350 seconds the cladding temperature begins to increase at 5K/s, increasing the gas pressure. For these simulations the cladding temperature is increased until the cladding tube ruptures.

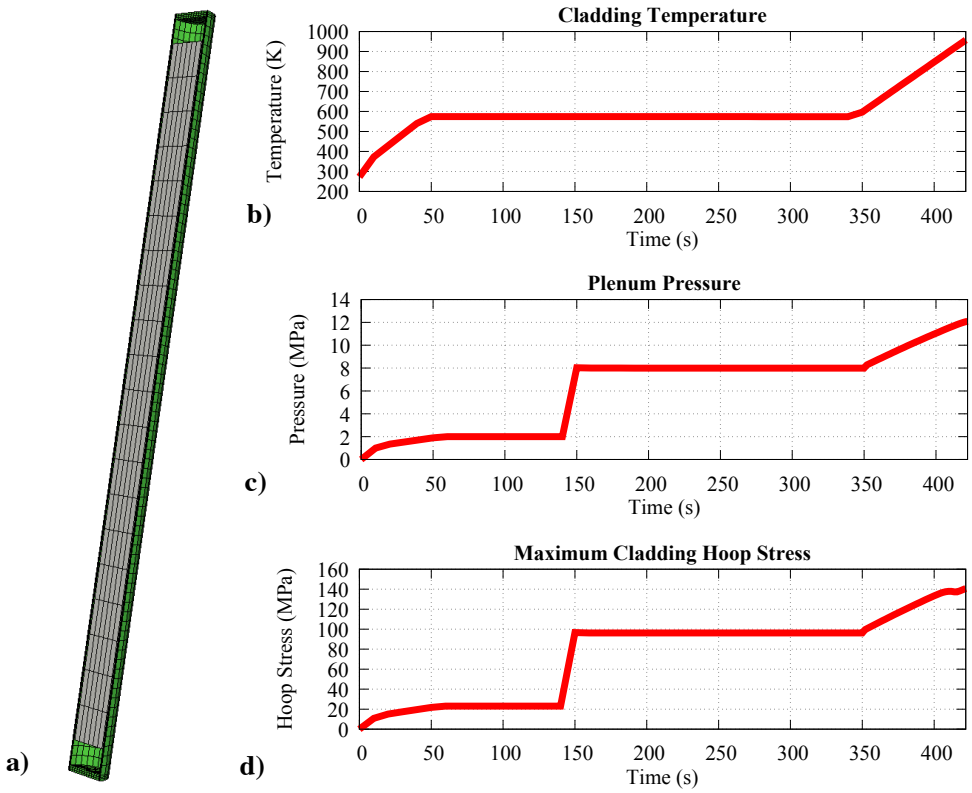

Figure 71. (a) Cladding tube mesh used in BISON to simulate a FeCrAl tube burst test experiment, (b) evolution of the cladding temperature, (c) gas pressure, and (d) maximum cladding hoop stress as a function of time.

A series of these simulations was performed for a range of different cladding tube internal pressures. Figure 72 shows the cladding hoop stress and temperature at rupture for the cladding burst experiment and associated simulations of this experiment using the aforementioned thermal creep, plasticity, and failure models.

The results of these simulations agree quite well with the experiment, especially for the higher cladding hoop stresses. As the temperature at failure increases, the results predicted by BISON begin to deviate, presumably because of the estimate used to extend the ultimate tensile strength. Although this estimate results in conservative estimation of the FeCrAl cladding failure, additional high-temperature yield and ultimate tensile strength might improve this comparison.

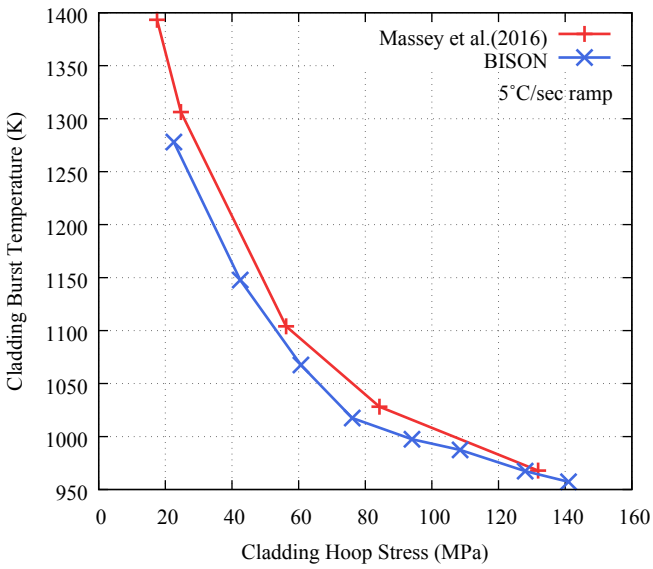

Figure 72. Cladding burst temperature versus cladding hoop stress of FeCrAl cladding as measured by Massey in the ORNL Severe Accident test Station (red) (Massey et al., 2016) versus BISON predictions of failure in the simulated tests (blue).

5.2.4 Oxidation Models

The oxidation behavior for both cladding types has been implemented into BISON in order to calculate the weight gain of oxygen in the cladding, the thickness of the oxide layer on the cladding, and the thickness of the metal consumed. For both cladding types, a low temperature and high temperature oxidation model is included.

The high temperature data is based on measurements of the Kanthal APMT alloy, which have been modified using a scale factor to adjust for the alloy composition (Field et al., 2017). Figure 73 shows the results of a series of oxidation tests carried out in 1200˚C steam for a variety of compositions of FeCrAl alloys, with varying chromium and aluminum content. This plot shows the alloys which form a protective passivating oxide layer and indicate the oxide layer thickness that forms in relation to Kanthal APMT. For the expected alloy (>10% Cr 5-6% Al), a scale factor of 2.3 is used and assumed to be conservative.

In order to simulate FeCrAl in the BWR environment, data is used from an investigation of the oxidation of an Fe-13Cr-4Al alloy in hydrogen water chemistry (Terrani et al., 2016a). The high temperature and low temperature relations are then connected as the high-temperature reaction is extended down to 1173K and the low-temperature is interpolated using an Arrhenius relation from the single present data point to the lowest high-temperature point. This is interpolated to the lowest temperature where alumina is expected to become the dominant oxidation layer formed (Engkvist et al., 2010; Rybicki and Smialek, 1989). Without much data in the intermediate temperature region, it is difficult to determine the accuracy of this assumption, however, the oxidation rate constants (shown

in Figure 74) indicate that, even at elevated temperatures, much less oxidation is expected than for Zircaloy.

To simulate the Zircaloy cladding for low temperatures, linear oxidation kinetics are considered and implemented using a specific model for a boiling water reactor (Lanning et al., 1997). This model uses linear kinetics because it assumes that the transition thickness from cubic to linear scaling is negligible. It should be noted that this BWR specific model predicts significantly less mass gain than corresponding models for PWRs, consistent with the lower cladding temperatures in a BWR.

At higher cladding temperatures (>673 K) the Leistikow et al. (Leistikow et al., 1983) oxidation model is implemented as described by Pastore and Shanz, respectively (Pastore et al., 2015; Schanz, 2003). To provide a conservative estimate of the oxidation formation after increase past the normal operating temperatures, this model is extended to lower cladding temperatures than originally intended (~873K).

Figure 74 shows the parabolic oxidation rate constants for both of these alloys according to the reciprocal temperature. Because the low-temperature zircaloy only uses linear oxidation kinetics, it is not included. This shows the profile of the interpolation of the FeCrAl oxidation behavior up to higher temperatures and, as expected, the oxidation rate constant remains much lower for the FeCrAl than the Zircaloy.

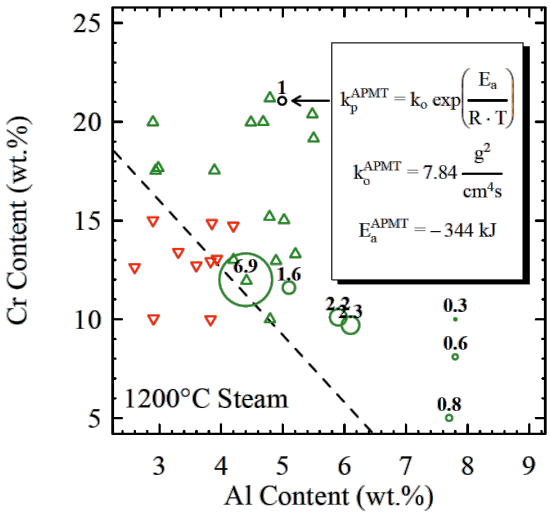

Figure 73. The oxidation behavior of various FeCrAl alloys in 1200˚C as a function aluminum and chromium content. The dashed line is an artificial division between the alloys that form a passivating (green markers) and non-passivating (red markers) oxidation layer. Green circle markers show the magnitude of the oxidation kinetics relative to Kanthal APMT. [Reproduced from (Field et al., 2017)]

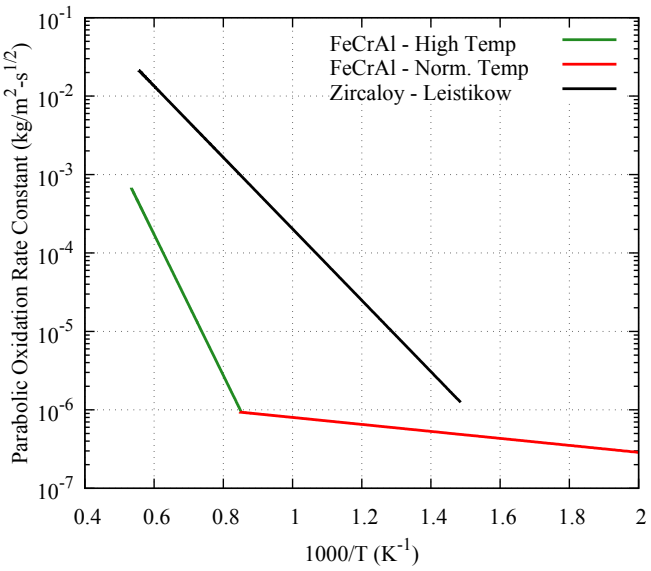

Figure 74. The parabolic oxidation rate constant for both the FeCrAl and Zircaloy as a function of inverse temperature. The FeCrAl cladding has significantly lower parabolic oxidation rate constants than the model used for Zircaloy. The low temperature (<673 K) oxidation model for Zircaloy cladding is described by linear oxidation kinetics and is not plotted here.

5.3 LOCA Operating Conditions

In order to simulate the LOCA, representative boundary conditions are applied to the axisymmetric fuel rod geometries from Chapters 2 and 3, reviewed in Table 1 from Chapter 2. These fuel rod designs are estimates of those from a BWR/4 which have been modified to due to limited data and, in the case of the FeCrAl cladded fuel rod, to account for the parasitic neutron absorption for the cladding alloy.

The postulated accident and associated conditions are derived from a study on the effect of fuel thermal conductivity on the temperature progression of the fuel and cladding during a LBLOCA in a BWR (Terrani et al., 2014a). Figure 75 shows a diagram of the coolant system for this particular loss of coolant accident. Here, there is an assumed double-ended guillotine break in the coolant pipe between the pressure vessel and the recirculation pump isolation valve. The onset for this accident is actuated at three separate fuel burnups to determine the sensitivity of the cladding behavior to the integral fuel rod state. The power production for this fuel rod is controlled with a power history and axial power profile, while the cladding temperature is controlled by the coolant temperature and coolant heat transfer coefficient.

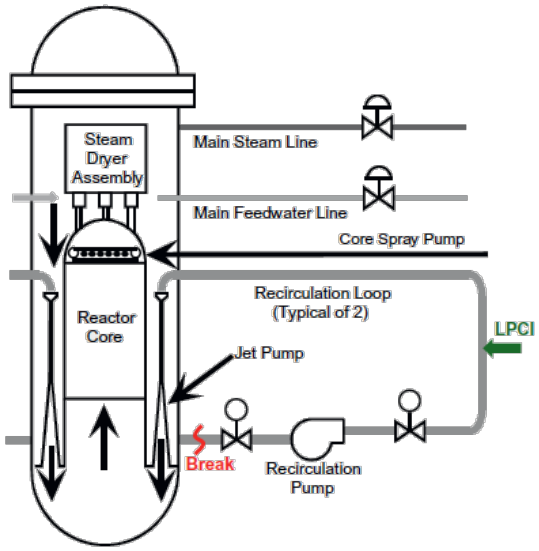

Figure 75. The transient boundary conditions provided from TRACE simulate a break (marked in red) in the recirculation suction line between the vessel and the recirculation pump isolation valves for a BWR. [Reproduced from (Terrani et al., 2014a)]

The progression of the peak cladding temperature from this previous analysis is shown in Figure 76. The reactor is operated using steady state conditions until the accident is initiated at the time of 0s. Here, the recirculation pipe is assumed to be broken and the reactor is scrammed. As power in the core is reduced and the recirculation pumps slowly blowdown, the cladding temperatures initially decline. However, as the coolant flow slowly stagnates, the cladding temperatures begin to rise. The low-pressure coolant injection system is actuated at ~91s and eventually quenches the core.

In order to determine the difference in cladding performance during the unmitigated accident, these simulations do not consider the initiation of the low-pressure coolant injection system; the fuel rod temperatures are allowed to increase until cladding failure consistent with a beyond design basis accident scenario.

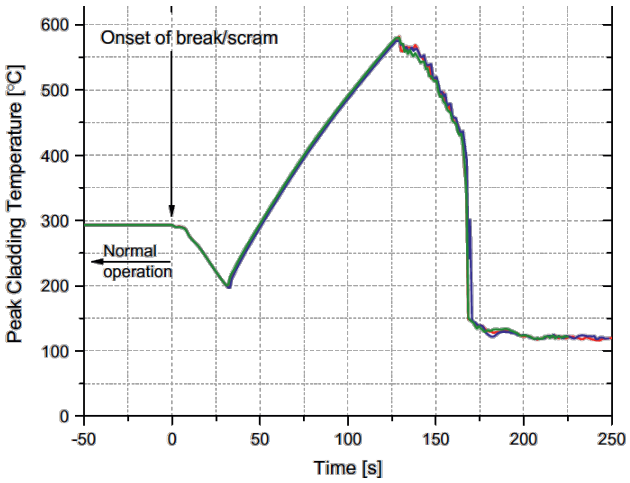

Figure 76. Peak cladding temperature as a function of time, before and after initiation of a large break LOCA. Note that the low-pressure coolant injection system is actuated at ~91 seconds, which eventually quenches the core and reduces fuel cladding temperatures. The different lines in this figure denote different thermal conductivities of the fuel as described in the work by Terrani and coworkers. [Reproduced from (Terrani et al., 2014a)]

The power history and axial power profile used in this analysis is shown in Figure 77. The fuel rod power ramps up to steady-state operation at 20 kW/m over 100 hours and held constant until the designated burnup is reached. At the onset of the accident conditions, the reactor core is screamed and the fuel power is reduced. Equation 23 is used to calculate the assumed power production due decay heat (El-Wakil, 1978).

$$Q_{decay} = 9.5 \times 10^{-2} \cdot Q_0 \cdot t^{-0.26} \quad (23)$$

Where Q_{decay} is the decay heat production in the fuel (kW/m), Q_0 is the steady state heat production (in this case 20 kW/m), and t is the time after the reactor scram (seconds). While this is not the most accurate calculation for decay heat production, it does provide a representative value, which, for this particular case this leads to ~ 2 kW/m after the reactor scram. The axial power profile, shown in Figure 77(b) remains static in these calculations. As discussed later, this eventually leads to a single axial length of the fuel rod which experiences considerably higher temperatures, greater burnup, and during the transient, even greater decay heat production.

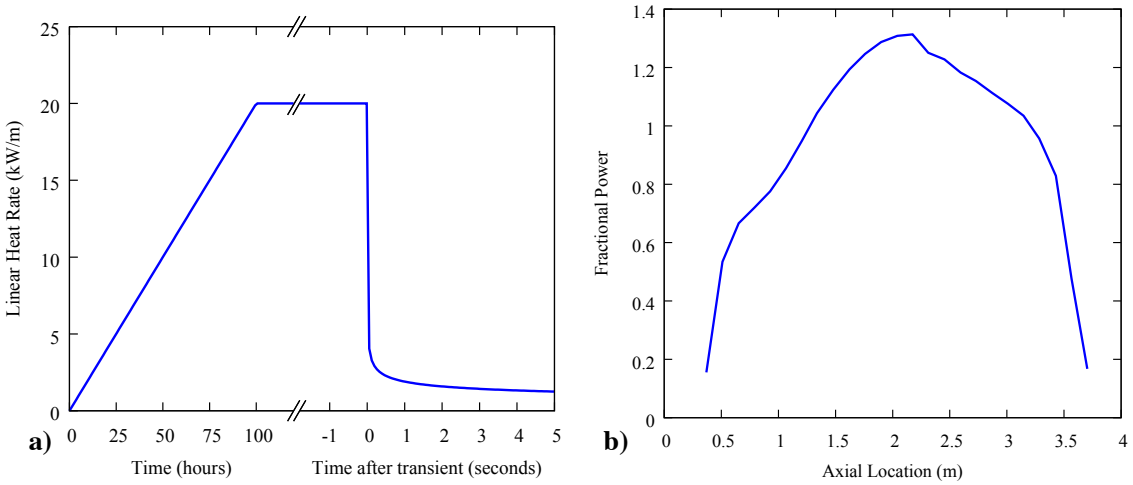

Figure 77. The power history of fuel rods in this LOCA analysis, (a) the Linear heat rate is divided into three regions: the initial ramp to operating power, constant operation at 20kW/m, and the reactor scram at the beginning of the transient conditions and the subsequent decay heat production. The axial power profile (b) is assumed to be constant for all three regions.

Pertinent reactor and fuel rod properties, identical to those described in Chapter 2 and typical for a BWR, are summarized in **Table 12**.

Table 12. Loss-of-Coolant Accident Reactor and Fuel Properties

Parameter	Value	Unit
Coolant Pressure	7.136	MPa
Initial Plenum Pressure	0.5	MPa
UO_2 Density	95%	T.D.

5.4 Steady-State Operation Results

For these simulations, before the onset of the transient conditions, the fuel of both cladding types is operated to three specified burnups, namely, 20 MWd/kgU, 40 MWd/kgU, and 60 MWd/kgU. This is performed to compare the accident progression and failure of both cladding types as a result of the fuel rod state (temperature, pressure gap thickness, etc.). Because a comparison of the Zircaloy and FeCrAl cladding behavior under constant operating conditions was thoroughly discussed in Chapter 3, only condensed results are presented here.

Figure 78 shows the average fuel centerline temperature (a) and the minimum gap thickness (b) for these fuel rods up to a burnup of 60 MWd/kgU. The sharp, nearly vertical, drops in the fuel temperatures occur quickly during the postulated accident and will be discussed further in the next section. The average fuel rod temperatures remain similar for much of the simulation. There is a small deviation due to the gap closure behavior between the

cladding types. The Zircaloy cladding immediately begins to creep-down, closing the gap and improving the heat transfer across the fuel rod gap. This results in a lower (~50K) average fuel centerline temperature over much of the simulated fuel burnup.

The gap closure behavior of both cladding materials is shown in Figure 78(b). Although this suggests gap closure occurs at ~13 MWd/kgU and ~27 MWd/kgU for the Zircaloy and FeCrAl, respectively, this effect is localized to the highest power region, as described by the axial power profile. This is a consequence of using a static axial power profile over the entire simulation, and concentrates the neutron flux, burnup, and temperature in a small section of the fuel rod. In this fuel rod section, the fuel expands more thermally and experiences more fuel relocation and fission product swelling. As well, in this location, the cladding experiences more dimensional change due to irradiation (swelling/growth) and irradiation creep deformation.

The maximum oxidation thickness that that forms on the cladding surface is shown in Figure 79. The Zircaloy cladding forms ~23 µm of oxidation by the end of the simulations, while the FeCrAl forms ~4µm. As previously noted, Zircaloy cladding in the BWR environment is expected for form significantly less oxidation than in the PWR (Lanning et al., 1997). Because of the linear scaling, the oxidation layer in the Zircaloy continues to grow at a constant rate. For the FeCrAl, however, due to the parabolic kinetics associated with oxide layer formation, the growth rate diminishes with increasing thickness.

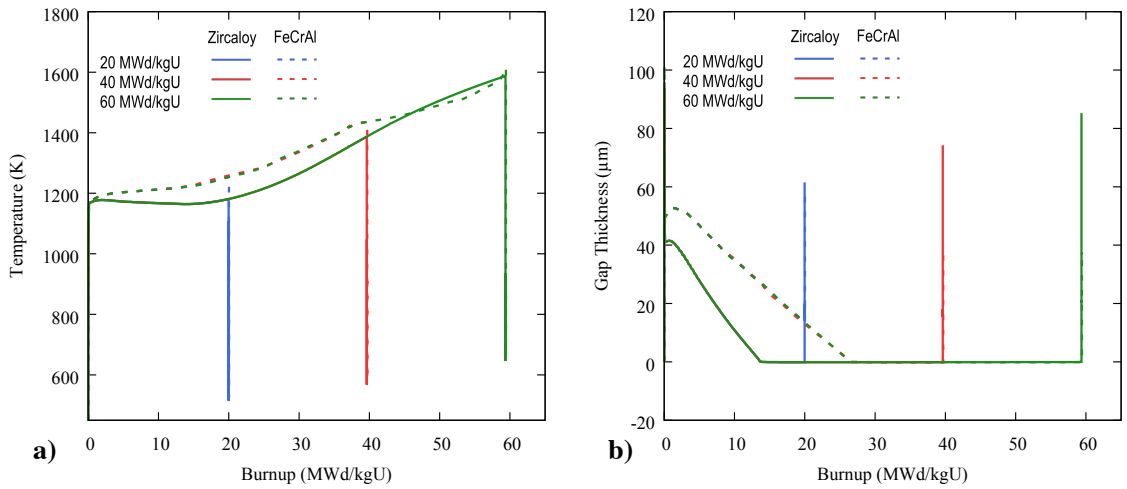

Figure 78. The average fuel temperature (a) for the FeCrAl cladded fuel rods is much larger for much of the fuel utilization. The onset of gap closure (b) occurs much sooner for the Zircaloy cladded fuel rods than the FeCrAl.

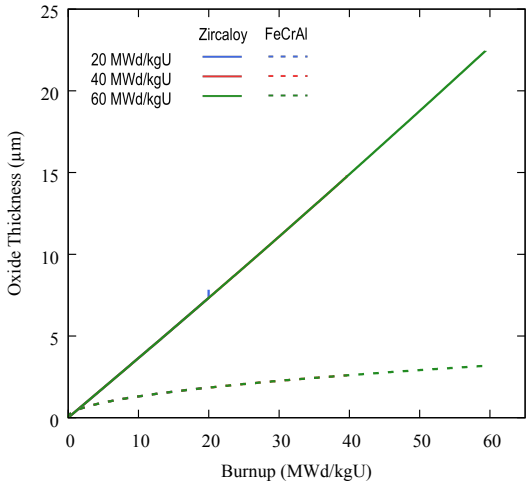

Figure 79. The maximum cladding oxidation thickness for the Zircaloy versus FeCrAl cladding, as a function of burnup.

5.5 LOCA Results

After the steady-state irradiation period, at a specified fuel burnup, the accident conditions are initiated based on the scenario presented in Figure 76, although this analysis does not initiate the low-pressure injection system at ~91 seconds after the accident. Figure 80 shows the average fuel centerline temperature (a) and the maximum cladding temperature (b) during the transient. In these figures, the reactor is scrammed at 0s, and the reactor power then decays according to the fission product decay heat relation provided in Eq. (23). The coolant flow slowly decreases as the core recirculation pumps stop. As the coolant flow stagnates, the coolant temperatures increase, and the coolant heat transfer coefficient is decreased.

Figure 80(a) shows the variation in the fuel temperatures during the steady-state operation due to the fuel rod condition. After the reactor is scrammed, the fuel temperatures slowly decrease as the heat is removed while the coolant pumps stop. As the coolant stagnates in the core, fuel temperatures begin to rise and, eventually, converge, independent of cladding type.

The peak cladding temperatures (Figure 80(b)) show a similar trend after the accident conditions have been initialized. The cladding temperatures slowly decrease after the reactor has scrammed, reaching a minimum at ~41 seconds. This plot also shows the cladding temperatures from the TRACE simulation that actuated the low-pressure injection at approximately 91 seconds (Terrani et al., 2014a). In the TRACE simulation the cladding temperatures begin to decrease at ~140 seconds as the core is re-flooded. However, in our BISON analysis the temperatures continue to increase until the cladding fails. As previously mentioned, these simulations are terminated when the burst criterion

is reached. These results show progressively lower temperatures for the increasing fuel burnups. These simulations also show very similar burst times for both cladding types.

Figure 81 shows the maximum fuel cladding gap thickness (a) and the maximum cladding hoops stress (b) during the accident conditions simulated with BISON. All of the fuel rods experience gap closure by the time the accident conditions are initiated, except the FeCrAl fuel rod at the lowest burnup of 20 MWd/kgU. After the onset of the accident conditions, the fuel cools down and the coolant system pressure rapidly drops. As the fuel contracts and the cladding is expanded due to the change in pressure differential, the fuel cladding gap is reopened. For the Zircaloy, as the fuel rod temperatures begin to increase, the pressure differential between the fuel rod plenum and coolant system allow the fuel to begin rapidly expanding due to thermal creep. The FeCrAl cladding does not experience the same magnitude of thermal creep; the thermal expansion of the cladding and increase in rod internal gas pressure drive the increase in gap thickness.

Leading up to the accident scenario, the maximum cladding hoop stress (Figure 81(b)) is initially in a tensile state due to mechanical interaction between the fuel and cladding. After the onset of the LBLOCA conditions, the gap is reopened, as the reactor coolant pressure is reduced to atmospheric pressure. This generates significant hoop stresses in the cladding, as the fuel rod plenum pressure begins to increase with the fuel temperatures. In these simulations, the FeCrAl cladded fuel rods fail at much larger stresses their Zircaloy counterparts.

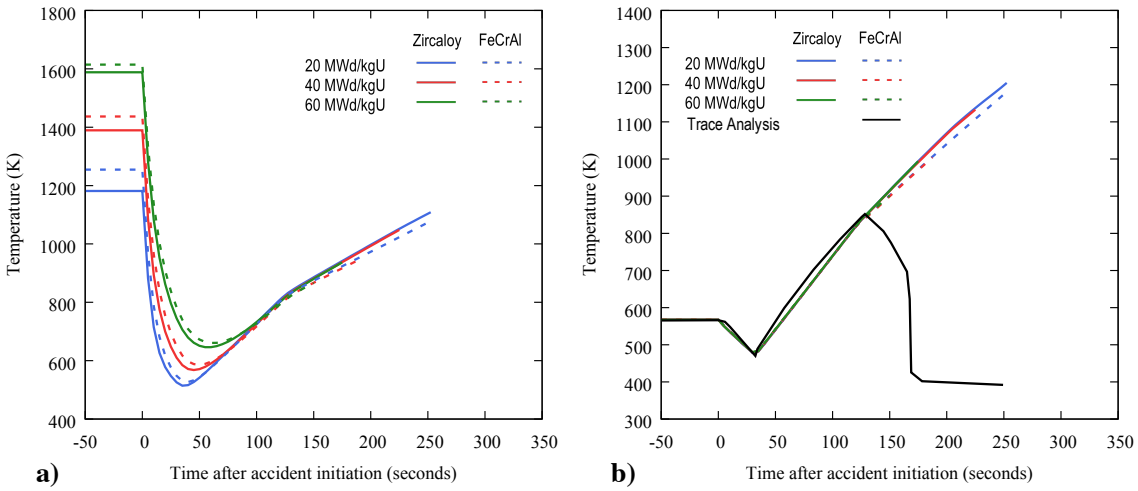

Figure 80. The maximum fuel centerline temperature (a) and the maximum cladding temperature (b) for both cladding types as a function of time after the accident. The results from the TRACE simulation are (black line) included in b) to provide a comparison.

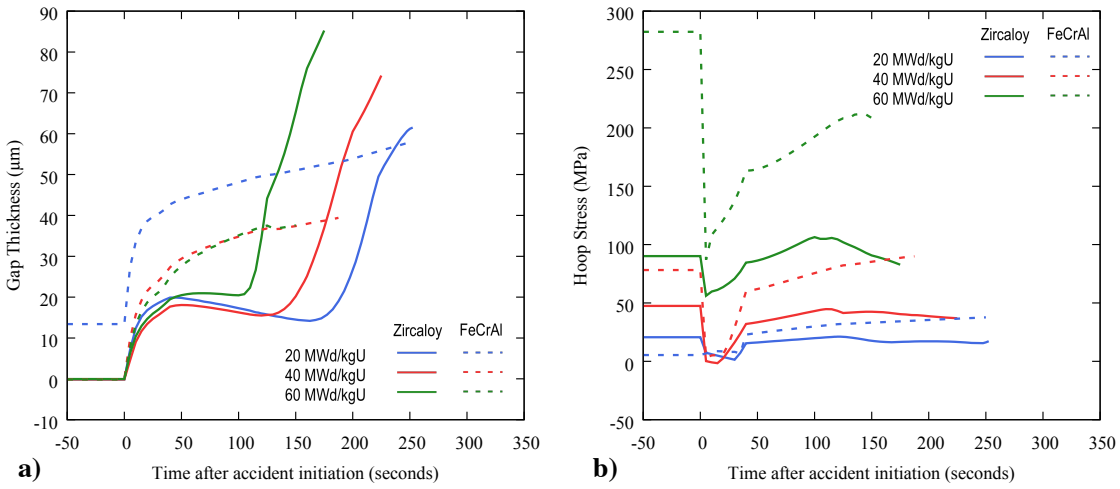

Figure 81. After the reactor is scrammed, the fuel contracts and the fuel cladding gap (a) is reopened. The Zircaloy cladding shows a much sharper increase in the gap thickness as the accident conditions progress. The maximum cladding hoop stress (b) is reduced as the accident conditions are initiated, however, as the accident progresses, the hoop stress in the FeCrAl cladding increases until failure.

These results show that the FeCrAl cladded fuel rods fail at similar times to the Zircaloy cladding, however, they fail at much larger cladding hoop stresses. The next section describes a brief analysis of the subsequent high-temperature oxidation behavior of the cladding materials.

5.6 Results of Extended Simulation

This analysis is extended further after the prediction of cladding rupture by considering only the thermal solution with extended time duration without operation of the emergency core cooling systems. In order to perform this analysis, the fuel and cladding mechanical strains are held constant, and the thermal solution is advanced. To simulate the post-burst behavior, the plenum pressure in the fuel rod is set equal to the coolant system pressure. This analysis is performed to elucidate the cladding oxidation behavior after burst, without the code convergence issues of high temperature mechanics. Although it is included in all simulations in this chapter, the heat production due to the exothermic cladding oxidation reaction produces very little heat until the cladding reaches sufficiently high temperatures. The calculation for the heat deposition is further described in Appendix C. These simulations are terminated when the peak cladding temperature reaches 2000 K, since by this temperature, the FeCrAl cladding would have melted.

Figure 82 shows the average fuel temperature (a) and the peak cladding temperature (b) for both fuel rods over this extended time period during the beyond design basis accident. The fuel centerline temperatures begin to deviate as the Zircaloy cladding oxidation reaction

begins and continues to become autocatalytic. For these condition, the FeCrAl cladding reaches 2000 K approximately 150 seconds later.

Figure 83 shows the cladding oxidation thickness during this extended period. The FeCrAl cladding exhibits very little additional oxidation under the transient conditions, while the Zircaloy cladding increases in a highly non-linear manner with at least an additional 20 µm of oxide thickness.

Using the calculations from the oxygen weight gain in the cladding, and assuming stoichiometric oxide formation, the hydrogen gas production per fuel rod is calculated to be ~.8g H_2 for the Zircaloy cladding and ~.05g H_2 FeCrAl cladding. Extrapolating this to an entire BWR core would yield ~ 44 kg for the Zircaloy cladding versus a much-reduced production of ~2.75 kg for the FeCrAl cladding.

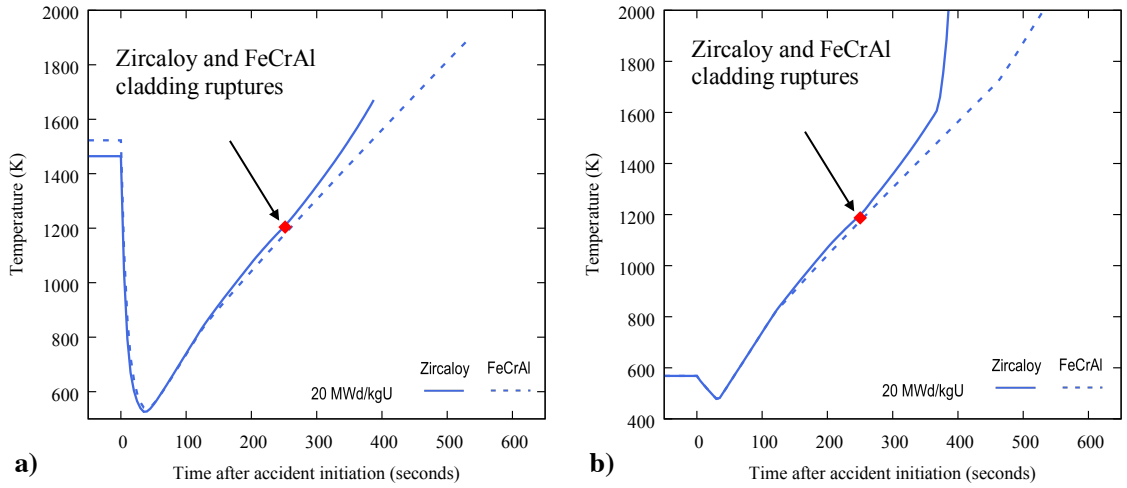

Figure 82. (a) The predicted maximum fuel centerline temperature and (b) the maximum cladding temperature for Zircaloy or FeCrAl cladded rods as a function of time following initiation of the beyond design basis LBLOCA conditions.

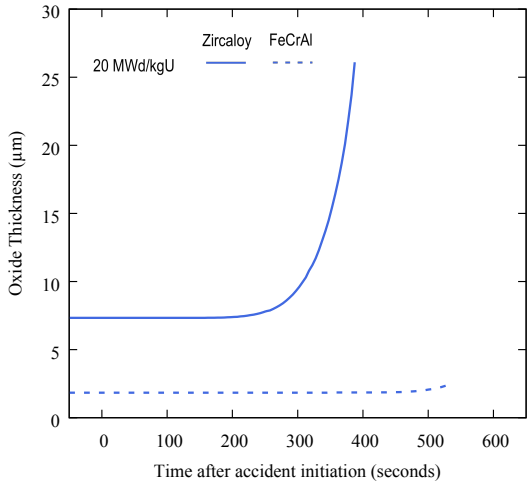

Figure 83. The maximum oxidation thickness rapidly increases for the Zircaloy after these simulations are restarted. The FeCrAl cladding, however, shows a nearly negligible increase in oxide thickness under the transient conditions.

These results provide an initial comparison of the behavior of FeCrAl and Zircaloy cladding under beyond design basis conditions. The analysis indicates that for this accident progression, the cladding materials rupture at similar times although the behavior leading up to rupture is different. The conditions of these simulations are very unique because the fuel burnup is concentrated in a small area of the fuel rod, due to the static axial power profile. This increases the heat generation due to fission product decay, and subsequently influences the mechanical behavior of the cladding in that region and the cladding oxidation. Future investigations of these cladding materials under LOCA conditions should provide a more uniform axial distribution of power over the fuel rod.

5.7 Summary

This chapter documents initial efforts to extend the steady-state modeling capabilities established for FeCrAl cladding in the BISON fuel performance code to high temperature transient conditions. In order to compare the behavior of FeCrAl and Zircaloy cladding during a simulated a loss-of-coolant accident, high-temperature constitutive models, failure criteria, and boundary conditions were implemented.

These results show that the FeCrAl cladding will generally burst at a similar time and temperature as the Zircaloy cladding under the specific reactor operating and accident conditions that were simulated, but experience significantly larger cladding hoop stresses. As expected, the main driving force for differences in burst behavior between the various fuel burnups is the pressure differential across the cladding as the transient conditions evolve. The FeCrAl cladding thickness used in this analysis is thinner than the thickness expected to be deployed in commercial reactors, which would tend to increase the difference in cladding failure time for the FeCrAl rods during the accident. This analysis

also demonstrated the ability to simulate beyond the cladding burst behavior using the thermal solution only. By extending this analysis, it was shown that because the FeCrAl cladding possesses much slower oxidation reaction kinetics there is very little increase in the oxide thickness and the cladding produces significantly less hydrogen gas.

To further enhance this analysis, additional improvements to the FeCrAl constitutive models are necessary. The development of the power law strain-hardening plasticity model consisted of a combination of different FeCrAl cladding property tests. Although these tests are conducted on similar alloys, no single test was able to provide a complete description of the temperature-dependent plastic behavior of the FeCrAl alloy. Because of this, it is expected that the behavior of the target alloys will differ from the model that is implemented. The cladding failure models should also be subject to more thorough investigation to determine if strain-based failure models are more applicable. The current burst stress and ultimate tensile strength models lead to situations under low-stress conditions the failure time and temperature are greatly over predicted due to stress relief mechanisms in the cladding.

The operating conditions used in this analysis generate unique results because the fuel burnup is concentrated in a small area of the fuel rod due to the static axial power profile. This increases the heat generation due to fission product decay, and subsequently influences the mechanical behavior of the cladding in that region and the cladding oxidation. These simulations also do not contain the axial variation in the coolant temperature typical of a boiling water reactor. Because the temperature profile is constant axially along the fuel rod, the location of the fuel rupture is especially sensitive to the axial peaking factors. For future simulations, a combination of axial power profiles to more evenly distribute the fuel power axially over the fuel rod are expected to provide a more accurate set of conditions to model the accident progression. Coupling to a reactor systems or thermal hydraulics code would better define the cladding temperature evolution under transient conditions and would also allow evaluation of different accident scenarios.

Additionally, neither the thermal or mechanical properties of the cladding oxides have been implemented into these simulations. While the FeCrAl cladding is not expected to develop a significant oxide thickness, Zircaloy cladding is. As the cladding is oxidized and the metal is consumed, the cladding is thinned and replaced with a brittle oxide ceramic with lower thermal conductivity. Ongoing work is being performed to incorporate a discrete oxide layer directly into the finite element simulations. This may consist of either a discrete meshed oxide layer or a smeared oxide approach. A discrete oxide layer bonded to the outside of the cladding can simulate the oxide growth and cladding consumption, although there are concerns about the ability to achieve and maintain code convergence. Alternatively, a smeared oxide/cladding layer may be implemented where the material properties in the outer element of the cladding are slowly changed into the oxide. While this is computationally more efficient, accurate assessment of the growth and consumption strains will be required.

This work aims to initiate an analysis about the increase in coping time gained by using FeCrAl cladding through the use of a fuel performance code. While this work does not utilize the boundary conditions necessary to provide quantifiable results, it does showcase several areas where additional data is needed.

CHAPTER 6: CONCLUSION AND FUTURE WORK

This work has sought to identify the operational characteristics of FeCrAl cladding based on the current available materials property data for FeCrAl alloy(s) during steady-state and transient reactor operating conditions using the finite-element fuel performance code, BISON. This is performed in order to provide guidance on cladding performance sensitivities and to identify areas where more thorough material property investigation is necessary for future fuel performance modeling analysis.

The findings of this work show that, under steady-state conditions, FeCrAl cladding may possesses much lower creep rates than Zircaloy cladding, and this creep behavior of the cladding tube normally determines gap closure. For FeCrAl clad rods, the models predict that the fuel cladding gap remains open for much longer and leads to increased temperatures. Altering the fuel design, however, can help achieve similar performance to Zircaloy clad rods.

The magnitude of the hoop stress that forms after gap closure occurs for the FeCrAl cladding was found to be much more sensitive to the fuel creep model than for Zircaloy cladding. To provide insight into this effect, an investigation of the fuel creep model was performed. Due to a lack of consensus in the literature over the expected fuel behavior from fission-induced creep, an additional facet of this study evaluated the difference in the cladding stress evolution by modifying the fuel creep calculation. This showed that at LWR relevant conditions, fission-induced creep is the dominant contributor to fuel creep deformation. Due to the uncertainty in the formulation for this model, it is suggested that fuel creep test data be compiled and compared to better determine which formulation (athermal vs temperature-dependent) is most appropriate to measure the fission-induced creep.

Because of the uncertainty in modeling the fuel compliance and the nonconventional fuel diameter expected for the FeCrAl cladded fuel rods, explicit fracture models were considered to provide a mechanistic basis to calculate fuel expansion and the stress relief necessary to properly evaluate fuel creep. The nonconventional fuel size of the FeCrAl cladded fuel rod design arises because of the desire to offset the higher rate of parasitic neutron absorption in FeCrAl (neutronic penalty) using thinner cladding and greater fuel mass to achieve equivalent reactor cycle lengths to Zircaloy cladding. Such fuel designs may fall outside the experimental database on which empirical fuel relocation models for standard LWR fuel have been calibrated. The fuel relocation models aim to predict the fuel expansion from fracture and the gradual movement of the fractured fuel. A series of simulations were performed comparing different models accounting for the fracture behavior of the fuel to test rod measurements. While this work has not yet led to an improved solution methodology, this work has succeeded in initiating the incorporation of explicit fracture into the fuel performance code.

To assess the FeCrAl cladding performance under transient conditions, a loss-of-coolant accident was simulated. In order to simulate this, additional reactor operating and boundary

conditions were implemented along with constitutive models to simulate high-temperature creep, plasticity, oxidation, and failure. After comparing the FeCrAl and zircaloy cladding, these simulations show that the burst temperature and stresses were generally similar for both cladding types. Additional code capabilities were implemented to elucidate high-temperature cladding behavior beyond the cladding burst. Here, it was shown that after the oxidation reaction of zircaloy cladding becomes autocatalytic, the FeCrAl cladded fuel rods can be expected to remain intact slightly longer. Because the FeCrAl cladding possesses much slower oxidation reaction kinetics than Zircaloy, there is very little increase in the oxide thickness and the cladding produces significantly less hydrogen gas. Although the operating conditions used in this analysis were extremely simplified, a framework is in place to simulate and compare the cladding performance for additional accident scenarios.

There are many aspects of this work that are intended to guide the further development of models used in the BISON fuel performance code to move closer to achieving predictive capabilities. Much of this work centers on the implementation of more accurate material properties and the deployment of new modeling techniques, such as the evaluation of an explicit oxide layer.

Additional work is needed to compile data from fuel creep tests and calibrate the current fuel model. Pellet cladding mechanical interaction can play a large role in the failure of fuel rods under normal LWR operating conditions (OECD, 2012), and more investigation is necessary to ensure fuel creep deformation is accurately accounted for under these conditions. Likewise, further enhancements to the explicit fracture models for the fuel are currently planned to expand current fracture capabilities and perform an assessment of the effect of cracking on the cladding stress state using these smeared cracking models.

To expand these capabilities, several new model aspects should be considered including modification of the Poisson's Ratio and thermal conductivity for cracked elements based on the crack size or strain. In order to improve the behavior of elements as they are stretched due to crack opening and closing, the value of the Poisson's Ratio should decay using a method similar to that used for isotropic softening (Hales et al., 2014) or proposed by (Jankus and Weeks, 1972). Because the cracks are filled with gas, the heat transfer across cracks is lower than that of the solid conduction in UO_2 fuel. In order to simulate this effect using the smeared cracking model, the thermal conductivity of cracked elements should also be reduced based on the heat transfer characteristics of the gas and fuel.

Additional capabilities planned for code development include crack healing and a possible coupling to the fission gas release model. Crack healing is an important aspect of the fracture mechanics affecting re-cohesion or re-sintering of the cracked surface and may result in better agreement with the experimental results as elastic properties recover. Currently, BISON does not include a representative crack healing model, and as such it is not currently possible to simulate the fuel "ratcheting" behavior associated with continued power cycling. In order to include this contribution to the diametral expansion, crack healing criteria will need to be developed and implemented into the smeared cracking model.

Coupling to the fission gas release model provides another area where explicit fracture can offer a more mechanistic model improvement. As crack networks propagate both radially and circumferentially through the fuel pellet, new free surfaces are created which may serve as sites to allow more gaseous fission products to diffuse from the fuel (Pastore et al., 2013). Although this fission gas release mechanism has never been thoroughly evaluated experimentally, it is expected to play a role in the transient fission gas release occurring during reactor power maneuvering (Maki and Meyer, 1978).

An assessment is planned to determine the impact of fuel cracks during mechanical interaction by applying a frictional contact model between the fuel and cladding. As well, additional analyses are needed to further identify the cladding stress development due to mechanical contact between cladding and fuel cracks. Localized increases in cladding stress due to PCMI in the presence of fuel cracks and defects have been documented using discrete cracking models (Capps et al., 2016). Future work is planned to reproduce this analysis using smeared cracking models; the mechanical contact model currently employed in BISON will have to be investigated to include the effect of friction after gap closure.

The current loss of coolant analysis work examined a limiting scenario because of the boundary conditions used. A more comprehensive analysis using representative boundary conditions should be performed. This can be accomplished by coupling to a reactor systems or thermal hydraulics code, which may help better define the cladding temperature evolution under transient conditions and would also allow evaluation of different accident scenarios.

The high-temperature cladding failure models should also be subject to more thorough investigation to determine if strain-based failure criteria are more appropriate than the criteria used in this work. The current burst stress and ultimate tensile strength models lead to situations where, under low-stress conditions, the failure time and temperature are greatly over predicted due to stress relief mechanisms that occur in the cladding. Implementing a strain-based failure criterion in conjunction with the burst stress criterion may help more conservatively predict cladding failure due to rupture.

The impact of cladding consumption during the formation of the oxidation layer on the cladding exterior should also be examined. Neither the thermal or mechanical properties of the cladding oxides are considered in this current work. While the FeCrAl cladding is not expected to develop a significant oxide thickness, Zircaloy cladding does. As the cladding is oxidized and the metal is consumed, the cladding is thinned and replaced with a brittle oxide ceramic with much lower thermal conductivity. Ongoing work is being performed to incorporate a discrete oxide layer directly into the finite element simulations. This may consist of either a discrete meshed oxide layer or a smeared oxide approach. A discrete oxide layer bonded to the outside of the cladding can simulate the oxide growth and cladding consumption, although there are concerns about the ability to achieve and maintain code convergence. Alternatively, a smeared oxide/cladding layer may be implemented where the material properties in the outer element of the cladding are slowly

changed into the oxide. While this is computationally more efficient, accurate assessment of the growth and consumption strains will be required.

Thus, this work has shown that although the behavior of the FeCrAl alloy cladding varies greatly relative to Zircaloy in some of these analyses, it is possible to utilize material properties as engineering parameters to tailor the overall fuel rod response under certain conditions (high temperature, stress, or neutron fluence). This may include modifying such properties as the cladding composition, texture, grain size, or possibly the addition of a dopant.

In order to optimize FeCrAl alloys as an alternative cladding material to Zircaloy, engineering design improvements are possible to better capitalize on the characteristic strength and creep strength of the alloys. This might involve tailoring material properties such as composition, microstructure, and in the case of fuel, microstructure and porosity, or even altering the geometric design of the fuel rod, which might delay the onset of gap closure or mitigate mechanical interaction. In order to apply alternative cladding materials to currently operating reactors, design consideration should be given to both.

LIST OF REFERENCES

Adamson, R.B., 2010. Zirconium Production and Technology: The Kroll Medal Papers, 1975-2010. ASTM International.

Ainscough, J.B., Oldfield, B.W., Ware, J.O., 1973. Isothermal grain growth kinetics in sintered UO2 pellets. J Nucl Mater 49, 117-128.

Andresen, P.L., Rebak, R.B., Dolley, E., 2014. SCC Resistance of Irradiated and Unirradiated High Cr Ferritic Steels. Paper C2014-3760, Corrosion/2014, San Antonio, TX, 09-13.

Bennett, G.L., U. S. Nuclear Regulatory Commission, Division of Reactor Safety Research, 1979. Summary of NRC LWR safety research programs on fuel behavior, metallurgy/materials and operational safety.

Beyer, C., Hann, C., Lanning, D., Panisko, F., Parchen, L., 1975. GAPCON-THERMAL-2: a computer program for calculating the thermal behavior of an oxide fuel rod. Battelle Pacific Northwest Labs., Richland, Wash.(USA).

Bohaboy, P., Asamoto, R., Conti, A., 1969. COMPRESSIVE CREEP CHARACTERISTICS OF STOICHIOMETRIC URANIUM DIOXIDE. General Electric Co., Sunnyvale, Calif. Breeder Reactor Development Operation.

Bragg-Sitton, S.M., Todosow, M., Montgomery, R., Stanek, C.R., Montgomery, R., Carmack, W.J., 2016. Metrics for the technical performance evaluation of light water reactor accident-tolerant fuel. Nuclear Technology 195, 111-123.

Brucklacher, D., Dienst, W., 1970. Kontinuierliche messung des kriechens von UO2 unter bestrahlung. J Nucl Mater 36, 244-247.

Capps, N., Montgomery, R., Sunderland, D., Pytel, M., Wirth, B.D., 2016. Evaluation of missing pellet surface geometry on cladding stress distribution and magnitude. Nucl Eng Des 305, 51-63.

Carmack, J., Goldner, F., Bragg-Sitton, S.M., Snead, L.L., 2013. Overview of the US DOE accident tolerant fuel development program. Idaho National Laboratory (INL).

Cathcart, J., Pawel, R., McKee, R., Druschel, R., Yurek, G., Campbell, J., Jury, S., 1977. Zirconium metal-water oxidation kinetics. IV. Reaction rate studies. Oak Ridge National Lab.

Chapman, R., Crowley, J., Longest, A., Hofmann, G., 1979. Zirconium Cladding Deformation in a Steam Environment with Transient Heating, Zirconium Cladding Deformation in a Steam Environment with Transient Heating.

Clayton, J.C., 1993. The Shippingport Pressurized Water Reactor and Light Water Breeder Reactor. ; Bettis Atomic Power Lab., West Mifflin, PA (United States).

Clough, D., 1970. IRRADIATION INDUCED CREEP OF CERAMIC FUELS. United Kingdom Atomic Energy Authority, Harwell, Eng.

Cunningham, M., Beyer, C., Medvedev, P., Berna, G., 2001. FRAPTRAN: A computer code for the transient analysis of oxide fuel rods. NUREGICR-6739 1.

Cunningham, M., Williford, R., Hann, C., 1979. Effects of fill gas composition and pellet eccentricity: comparison between instrumented fuel assemblies IFA-431 and IFA-432. Battelle Pacific Northwest Labs., Richland, WA (USA).

Dienst, W., 1977. Irradiation induced creep of ceramic nuclear fuels. J Nucl Mater 65, 1-8.

El-Wakil, M.M., 1978. Nuclear heat transport. American Nuclear Society.

Engkvist, J., Canovic, S., Hellström, K., Järdnäs, A., Svensson, J.-E., Johansson, L.-G., Olsson, M., Halvarsson, M., 2010. Alumina scale formation on a powder metallurgical FeCrAl alloy (Kanthal APMT) at 900–1,100 C in dry O 2 and in O 2+ H 2 O. Oxid Met 73, 233-253.

EPRI, 2008. The Path to Zero Defects: EPRI Fuel Reliability Guidelines. Electric Power Research Institute.

Erbacher, F., Leistikow, S., 1987. Zircaloy Fuel Cladding Behavior in a Loss-of-Coolant Accident: A Review, Zircaloy Fuel Cladding Behavior in a Loss-of-Coolant Accident: A Review.

Erbacher, F., Neitzel, H., Rosinger, H., Schmidt, H., Wiehr, K., 1982. Burst Criterion of Zircaloy Fuel Claddings in a Loss-of-Coolant Accident, Burst Criterion of Zircaloy Fuel Claddings in a Loss-of-Coolant Accident.

Field, K.G., Briggs, S.A., Edmondson, P., Hu, X., Littrell, K.C., Howard, R., Parish, C.M., Yamamoto, Y., 2015. Evaluation on the Effect of Composition on Radiation Hardening and Embrittlement in Model FeCrAl Alloys. Oak Ridge National Lab.(ORNL).

Field, K.G., Snead, M.A., Yamamoto, Y., Terrani, K.A., 2017. Handbook on the Material Properties of FeCrAl Alloys for Nuclear Power Production Applications.

Franklin, D., 1982. Zircaloy-4 cladding deformation during power reactor irradiation, Zirconium in the Nuclear Industry. ASTM International.

Gamble, K.A., Barani, T., Pizzocri, D., Hales, J.D., Terrani, K.A., Pastore, G., 2017. An investigation of FeCrAl cladding behavior under normal operating and loss of coolant conditions. J Nucl Mater 491, 55-66.

Garner, F.A., Toloczko, M.B., Sencer, B.H., 2000. Comparison of swelling and irradiation creep behavior of fcc-austenitic and bcc-ferritic/martensitic alloys at high neutron exposure. J Nucl Mater 276, 123-142.

Gaston, D., Newman, C., Hansen, G., Lebrun-Grandie, D., 2009. MOOSE: A parallel computational framework for coupled systems of nonlinear equations. Nucl Eng Des 239, 1768-1778.

Geelhood, K., Luscher, W.G., Beyer, C., Flanagan, M., 2011. FRAPCON-3.4: A Computer Code for the Calculation of Steady State Thermal-mechanical Behavior of Oxide Fuel Rods for High Burnup. US Nuclear Regulatory Commission, Office of Nuclear Regulatory Research Richland, WA.

Geelhood, K.J., Beyer, C.E., Luscher, W.G., 2008. PNNL stress/strain correlation for Zircaloy. Pacific Northwest National Laboratory (PNNL), Richland, WA (US).

George, N.M., Powers, J.J., Maldonado, G.I., Worrall, A., Terrani, K.A., 2015a. Development of a Full-core Reactivity Equivalence for FeCrAl Enhanced Accident Tolerant Fuel in BWRs. Oak Ridge National Laboratory (ORNL).

George, N.M., Sweet, R.T., Powers, J.J., Worrall, A., Terrani, K.A., Wirth, B.D., Maldonado, G.I., 2017. Full-Core Analysis for FeCrAl Enhanced Accident Tolerant Fuel in BWRs. Nucl Eng Des.

George, N.M., Terrani, K., Powers, J., Worrall, A., Maldonado, I., 2015b. Neutronic analysis of candidate accident-tolerant cladding concepts in pressurized water reactors. Ann Nucl Energy 75, 703-712.

Gittus, J.H., 1972. Theoretical analysis of the strains produced in nuclear fuel cladding tubes by the expansion of cracked cylindrical fuel pellets. Nucl Eng Des 18, 69-82.
GNF-A, 2010. The PRIME Model for Analysis of Fuel Rod Thermal – Mechanical Performance, NEDO-33256-A Revision 1, NEDO-33257-A Revision 1, & NEDO-33258-A Revision 1.
Hagrman, D.T., Allison, C.M., Berna, G.A., 1995. SCDAP/RELAP5/MOD 3.1 code manual: MATPRO, A library of materials properties for Light-Water-Reactor accident analysis. Volume 4.
Hales, J., Novascone, S., Pastore, G., Perez, D., Spencer, B., Williamson, R., 2014. BISON theory manual: The equations behind nuclear fuel analysis. Fuels Modeling & Simulation Department, Idaho National Laboratory, Idaho Falls, Idaho.
Heinisch, H.L., Greenwood, L.R., Weber, W.J., Williford, R.E., 2004. Displacement damage in silicon carbide irradiated in fission reactors. J Nucl Mater 327, 175-181.
Hofmann, P., 1998. Current knowledge of core degradation phenomena, a review. J Nucl Mater 270, 194-211.
Hoppe, N., Billaux, M., van Vliet, J., Shihab, S., 1995. COMETHE, Version 4D Release 022 (4.4-0.22), Volume 1, General Description. BN 9409844/220–A, April.
Hu, X., Terrani, K.A., Wirth, B.D., Snead, L.L., 2015. Hydrogen permeation in FeCrAl alloys for LWR cladding application. J Nucl Mater 461, 282-291.
IAEA, 2010. Review of Fuel Failures in Water Cooled Reactors. INTERNATIONAL ATOMIC ENERGY AGENCY, Vienna.
IAEA, 2011. Power Uprate in Nuclear Power Plants: Guidelines and Experience. INTERNATIONAL ATOMIC ENERGY AGENCY, Vienna.
Jackson, P., Turnbull, J., White, R., 1990. Enigma fuel performance code. Nuclear Energy 29, 107-114.
Jankus, V., Weeks, R., 1972. LIFE-II—A computer analysis of fast-reactor fuel-element behavior as a function of reactor operating history. Nucl Eng Des 18, 83-96.
Kanthal, Kanthal Alkrothal 720 Datasheet. Sandvik AB, Hallstahammar, Sweden.
Kanthal, Kanthal APMT Datasheet. Sandvik AB, Hallstahammar, Sweden.
Karoutas, Z., Brown, J., Atwood, A., Hallstadius, L., Lahoda, E., Ray, S., Bradfute, J., 2018. The maturing of nuclear fuel: Past to Accident Tolerant Fuel. Progress in Nuclear Energy 102, 68-78.
Lanning, D., Beyer, C., Painter, C., 1997. FRAPCON-3: modifications to fuel rod material properties and performance models for high-burnup application. NUREG0CR-6534 1.
Larsen, N.H., 1978. Core design and operating data for Cycles 1 and 2 of Peach Bottom 2, p. Medium: ED; Size: Pages: 207.
Lassmann, K., 1980. The Structure of Fuel-Element Codes. Nucl Eng Des 57, 17-39.
Lassmann, K., O'carroll, C., Van de Laar, J., Walker, C., 1994. The radial distribution of plutonium in high burnup UO2 fuels. J Nucl Mater 208, 223-231.
Lassmann, K., Walker, C.T., van de Laar, J., Lindström, F., 1995. Modelling the high burnup UO2 structure in LWR fuel. J Nucl Mater 226, 1-8.
Leistikow, S., Schanz, G., Berg, H., Aly, A., 1983. Comprehensive presentation of extended Zircaloy-4 steam oxidation results (600-1600 deg. C).

Limbäck, M., Andersson, T., 1996. A model for analysis of the effect of final annealing on the in-and out-of-reactor creep behavior of zircaloy cladding, Zirconium in the Nuclear Industry: Eleventh International Symposium. ASTM International.

Liu, W., Rashid, J., 2017. Continued Improvements in Numerical/Mechanical BISON Models, CASL Milestone Report: L3_FMC_FUEL_P15_08.

Long, Y., Kersting, P.J., Linsuain, O., Schutte, H., Rumschlag, D.T., Keiser, K.B., Mitchell, D., Oelrich, R.L., 2013. PAD5: Westinghouse high burnup fuel performance models.

Mader, E.V., 2016. Fuel Reliability Status & the Promise Initiative, CASL Industry Council: CASL-U-2016-1093-000.

Maki, J.T., Meyer, J.E., 1978. LWR fuel performance analysis: fuel cracking and relocation. MIT Energy Laboratory.

Maloy, S.A., Aydogan, E., Anderoglu, O., Lavender, C., Yamamoto, Y., 2016. Viability of thin wall tube forming of ATF FeCrAl. ; Los Alamos National Lab. (LANL), Los Alamos, NM (United States); Pacific Northwest National Lab. (PNNL), Richland, WA (United States); Oak Ridge National Lab. (ORNL), Oak Ridge, TN (United States), p. Medium: ED; Size: 35 p.

Marion, A., 2006. A. Marion to H. N. Berkow, June 13, 2006, in *Re-submittal of Safety Evaluation by the Office of Nuclear Reactor Regulation of Electric Power Research Institute (EPRI) Topical Report TR-1002865, "Topical Report on Reactivity Initiated Accidents: Bases for RIA Fuel Rod Failures and Core Coolability Criteria"*.

Massey, C.P., Terrani, K.A., Dryepondt, S.N., Pint, B.A., 2016. Cladding burst behavior of Fe-based alloys under LOCA. J Nucl Mater 470, 128-138.

Matsuo, Y., 1987. Thermal creep of zircaloy-4 cladding under internal pressure. Journal of Nuclear Science and Technology 24, 111-119.

Moalem, M., Olander, D.R., 1991. Oxidation of Zircaloy by steam. J Nucl Mater 182, 170-194.

Moore, R., Notz, K., 1989. Physical characteristics of GE BWR fuel assemblies. ORNL/TM-10902 (2nd ed.) Oak Ridge National Laboratory, Oak Ridge, TN.

OECD, 2012. Nuclear Fuel Safety Criteria Technical Review (Second Edition). OECD Publishing.

OECD Nuclear Energy Agency Nuclear Science Committee, 2007. Handbook on Lead-bismuth Eutectic Alloy and Lead Properties, Materials Compatibility, Thermal-hydraulics and Technologies. OECD Nuclear Energy Agency.

Oguma, M., 1983. Cracking and Relocation Behavior of Nuclear-Fuel Pellets during Rise to Power. Nucl Eng Des 76, 35-45.

Olander, D.R., 1976. Fundamental aspects of nuclear reactor fuel elements. California Univ., Berkeley (USA). Dept. of Nuclear Engineering.

Ott, L.J., Robb, K.R., Wang, D., 2014. Preliminary assessment of accident-tolerant fuels on LWR performance during normal operation and under DB and BDB accident conditions. J Nucl Mater 448, 520-533.

Pastore, G., Hales, J., Novascone, S., Perez, D., Spencer, B., Williamson, R., 2013. Analysis of fission gas release in LWR fuel using the BISON code. Idaho National Laboratory (INL).

Pastore, G., Novascone, S., Williamson, R., Hales, J., Spencer, B., Stafford, S., 2015. Modeling of fuel behavior during loss-of-coolant accidents using the BISON code, 2015 LWR Fuel Performance Meeting—Top Fuel, Zurich, Switzerland.
Pasupathi, V., Klingensmith, R., 1981. Investigation of stainless steel clad fuel rod failures and fuel performance in the Connecticut Yankee Reactor. Final report. Battelle Columbus Labs., OH (USA).
Perrin, J., Wilson, W., 1971. EFFECT OF IRRADIATION ON THE CREEP OF URANIUM DIOXIDE. Battelle Memorial Inst., Columbus, Ohio.
Rashid, Y., 1974. Mathematical modeling and analysis of fuel rods. Nucl Eng Des 29, 22-32.
Rashid, Y., Dunham, R., Montgomery, R., 2004. Fuel analysis and licensing code: FALCON MOD01. EPRI Report 1011308.
Rashid, Y.R., 1968. Ultimate strength analysis of prestressed concrete pressure vessels. Nucl Eng Des 7, 334-344.
Rebak, R.B., 2018. Versatile Oxide Films Protect FeCrAl Alloys Under Normal Operation and Accident Conditions in Light Water Power Reactors. JOM 70, 176-185.
Robb, K.R., 2015. Analysis of the FeCrAl Accident Tolerant Fuel Concept Benefits during BWR Station Blackout Accidents, United States.
Roberts, J.T.A., 2013. Structural Materials in Nuclear Power Systems. Springer US.
Rybicki, G.C., Smialek, J.L., 1989. Effect of theθ-α-Al2O3 transformation on the oxidation behavior ofβ-NiAl + Zr. Oxid Met 31, 275-304.
Sartori, E., Killeen, J., Turnbull, J., 2010. International Fuel Performance Experiments (IFPE) Database. OECD-NEA.
Saunders, S.R.J., Evans, H.E., Li, M., Gohil, D.D., Osgerby, S., 1997. Oxidation growth stresses in an alumina-forming ferritic steel measured by creep deflection. Oxid Met 48, 189-200.
Schanz, G., 2003. Recommendations and supporting information on the choice of zirconium oxidation models in severe accident codes.
Solomon, A., Gebner, R., 1972. Instrumented Capsule for Measuring Fission-Induced Creep of Oxide Fuels. Nuclear Technology 13, 177-184.
Solomon, A.A., Routbort, J.L., Voglewede, J.C., 1971. Fission-Induced Creep of UO2 and Its Significance to Fuel-Element Performance. Argonne National Lab., Argonne, Illinois
Strasser, A., Santucci, J., Lindquist, K., Yario, W., Stern, G., Goldstein, L., Joseph, L., 1982. An Evaluation of stainless steel cladding for use in current design LWRs. Electric Power Research Institute, Palo Alto, Calif.
Suzuki, M., Saitou, H., 1997. Light Water Reactor Fuel Analysis Code: FEMAXI-6 (Ver. 1): Detailed Structure and User's Manual. Japan Atomic Energy Research Institute.
Sweet, R., George, N., Maldonado, G., Terrani, K., Wirth, B., 2018. Fuel performance simulation of iron-chrome-aluminum (FeCrAl) cladding during steady-state LWR operation. Nucl Eng Des 328, 10-26.
Swiler, L.P., Williamson, R.L., Perez, D.M., 2013. Calibration of a Fuel Relocation Model in BISON. Sandia National Laboratories (SNL-NM), Albuquerque, NM (United States).

Sykes, E., Sawbridge, P., 1969. IRRADIATION CREEP OF URANIUM DIOXIDE. Central Electricity Generating Board, Berkeley (England). Berkeley Nuclear Labs.
Terrani, K., 2018. Accident tolerant fuel cladding development: Promise, status, and challenges. J Nucl Mater.
Terrani, K., Pint, B., Kim, Y.-J., Unocic, K., Yang, Y., Silva, C., Meyer, H., Rebak, R., 2016a. Uniform corrosion of FeCrAl alloys in LWR coolant environments. J Nucl Mater 479, 36-47.
Terrani, K.A., Balooch, M., Yagnik, S., McGrath, M., Olander, D.R., 2011. A Method for Accurate Determination of In-Pile UO2 Thermal Conductivity as A Function of Temperature, Burnup, and Flux, EHPG 2011, Sandefjord, Norway.
Terrani, K.A., Karlsen, T.M., Yamamoto, Y., 2015. Report on Design and Preliminary Data of Halden In-Pile Creep Rig, ORNL/TM-2015/507, Oak Ridge National Laboratory.
Terrani, K.A., Wang, D., Ott, L.J., Montgomery, R.O., 2014a. The effect of fuel thermal conductivity on the behavior of LWR cores during loss-of-coolant accidents. J Nucl Mater 448, 512-519.
Terrani, K.A., Yamamoto, Y., 2016. Input Correlations for Irradiation Creep of FeCrAl and SiC Based on In-Pile Halden Test Results. Oak Ridge National Laboratory (ORNL), Oak Ridge, TN (United States).
Terrani, K.A., Yamamoto, Y., Gussev, M., 2016b. Characterization Report on FeCrAl Cladding for Halden Irradiation, ORNL/TM-2016/343. Oak Ridge National Laboratory.
Terrani, K.A., Zinkle, S.J., Snead, L.L., 2014b. Advanced oxidation-resistant iron-based alloys for LWR fuel cladding. J Nucl Mater 448, 420-435.
Thompson, Z.T., Terrani, K.A., Yamamoto, Y., 2015. Elastic Modulus Measurement of ORNL ATF FeCrAl Alloys. Oak Ridge National Laboratory (ORNL), Oak Ridge, TN (United States).
Thouvenin, G., Ricaud, J., Michel, B., Plancq, D., Thevenin, P., 2006. ALCYONE: the PLEIADES fuel performance code dedicated to multidimensional PWR studies. Proceedings of Top Fuel.
Todreas, N.E., Kazimi, M.S., 2012. Nuclear Systems: Thermal Hydraulic Fundamentals, Second Edition. Taylor & Francis.
Turnbull, J.A., 1998. An Empirical Model of UO2 Thermal conductivity Based on Laser Flash Measurements of Thermal Diffusivity, TR-111347., EPRI, Palo Alto, CA.
U.S. EIA, 2018. Monthly energy review. United States Energy Information Administration.
U.S. Nuclear Regulatory Commission, 2007. Chapter 4, Section 2 : Fuel System Design, Standard review plan for the review of safety analysis reports for nuclear power plants : LWR edition. U.S. Nuclear Regulatory Commission; NTIS, Washington, D.C; Springfield, Va.
Van Uffelen, P., Győri, C., Schubert, A., van de Laar, J., Hózer, Z., Spykman, G., 2008. Extending the application range of a fuel performance code from normal operating to design basis accident conditions. J Nucl Mater 383, 137-143.

Van Uffelen, P., Suzuki, M., 2012. 3.19 - Oxide Fuel Performance Modeling and Simulations A2 - Konings, Rudy J.M, Comprehensive Nuclear Materials. Elsevier, Oxford, pp. 535-577.

Walton, L., Husser, D., 1982. Fuel pellet fracture and relocation. FUEL ELEMENT PERFORMANCE COMPUTER MODELLING, 147.

Wiesenack, W., Vankeerberghen, M., Thankappan, R., 1996. Assessment of UO2 conductivity degradation based on in-pile temperature data, HWR-469. OECD Halden Reactor Project.

Williamson, R., Gamble, K., Perez, D., Novascone, S., Pastore, G., Gardner, R., Hales, J., Liu, W., Mai, A., 2016. Validating the BISON fuel performance code to integral LWR experiments. Nucl Eng Des 301, 232-244.

Williamson, R.L., Hales, J.D., Novascone, S.R., Tonks, M.R., Gaston, D.R., Permann, C.J., Andrs, D., Martineau, R.C., 2012. Multidimensional multiphysics simulation of nuclear fuel behavior. J Nucl Mater 423, 149-163.

Williford, R., 1982. Experimental Verification of a Cracked Fuel Mechanical Model. Pacific Northwest National Laboratory (PNNL), Richland, WA (United States).

Williford, R., Mohr, C., Lanning, D., Cunningham, M., Rausch, W., Bradley, E., 1980. Analysis of fuel relocation for the NRC/PNL Halden assemblies IFA-431, IFA-432, and IFA-513. Pacific Northwest Labs., Richland, WA (USA).

Wu, X., Kozlowski, T., Hales, J.D., 2015. Neutronics and fuel performance evaluation of accident tolerant FeCrAl cladding under normal operation conditions. Ann Nucl Energy 85, 763-775.

Yamamoto, Y., Pint, B., Terrani, K., Field, K., Yang, Y., Snead, L., 2015. Development and property evaluation of nuclear grade wrought FeCrAl fuel cladding for light water reactors. J Nucl Mater 467, 703-716.

Yang, R., Cheng, B., Deshon, J., Edsinger, K., Ozer, O., 2006. Fuel R & D to Improve Fuel Reliability. Journal of Nuclear Science and Technology 43, 951-959.

Younker, I., Fratoni, M., 2016. Neutronic evaluation of coating and cladding materials for accident tolerant fuels. Progress in Nuclear Energy 88, 10-18.

Zinkle, S.J., Terrani, K.A., Gehin, J.C., Ott, L.J., Snead, L.L., 2014. Accident tolerant fuels for LWRs: A perspective. J Nucl Mater 448, 374-379.

APPENDIX

APPENDIX A – Effect of Helium or Lead-Bismuth Filled Cracks on Temperature Profile of LWR Fuel Pellets

INTRODUCTION

The purpose of nuclear fuel is to facilitate fission that in turn deposits a large amount of energy within that medium. That thermal energy is then transferred away from the fuel and may then be converted to electricity. Thermal conductivity of nuclear reactor fuel is of great importance throughout this process and has been a subject of long-term investigation. While a number of reliable thermal conductivity correlations are available (Turnbull, 1998; Wiesenack et al., 1996), more accurate measurements of thermal conductivity can improve predictive capability of fuel performance analysis tools. To this end a new experiment was designed and is currently ongoing at the Halden reactor in Norway (IFA-744). The details and the goals of the experiment are detailed out elsewhere (Terrani et al., 2011). An important distinction of this experiment from the past in-pile measurements is that the fuel-cladding gap in some of the experimental rodlets is filled with a liquid metal (LM) instead of He gas that is typically used within this volume. The LM consists of the eutectic mixture of lead and bismuth (LBE).

In order to accurately interpret the results of in-pile temperature data from the LM-bonded fuel rods, one needs to investigate the effect of micro cracking that will inevitably occur in the fuel. In particular, it is important to quantify the error in the temperature data that might be introduced by penetration of LM into the radial or circumferential cracks. The purpose of this study is to investigate the effect of radial and circumferential micro cracks on the temperature profile in the urania pellets when they are filled with He or LM.

METHODOLOGY
GEOMETRY

2-D(r,θ) coordinate simulations were made to analyze the temperature effects of prescribed cracks inside UO_2 fuel pellets filled with He gas or a liquid metal. Fuel rod geometries were created using the parameters in Table 13. Cracks were created in several models to examine the effects of the crack type (radial and circumferential) and width (25 and 50μm).

Table 13. Uncracked Fuel Geometry

Fuel Radius (mm)	4.1
Cladding Inner Radius (mm)	4.2
Cladding Outer Radius (mm)	5.2

In order to ensure the fuel volume (and the power density) was conserved, the fuel outer radius was increased for the cracked geometries to account for the volume of the cracks. The cladding inner and outer radii, however, were not changed. The increase in fuel radius is shown in Table 14. Examples of meshes for cracked fuel geometries are shown in Figure 84.

Table 14. Fuel Radius Increase

Crack Type	Crack Width (μm)	Fuel Radius Increase
Circumferential	25	0.41%
	50	0.81%
Radial	25	0.26%
	50	0.53%

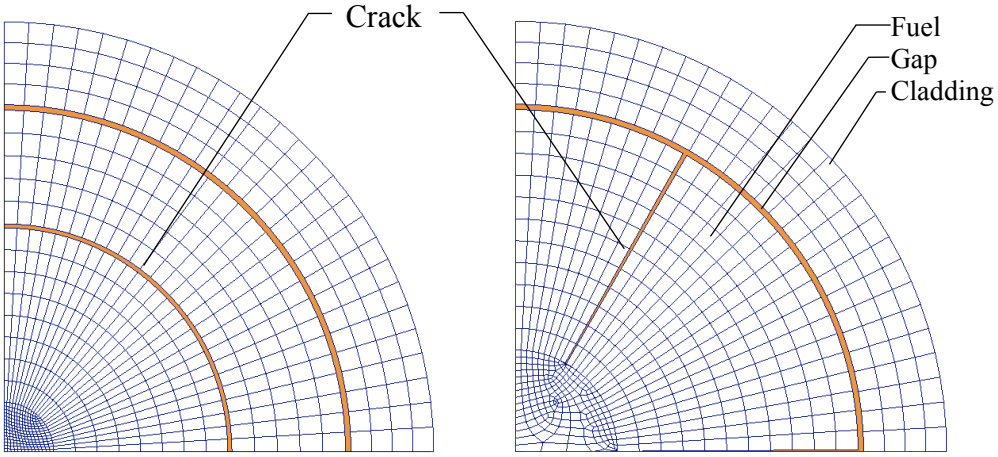

Figure 84. 90 degree r-θ models showing the 50μm circumferential (left) and 50μm radial cracks (right) (Note: mesh over cracks is removed for visualization).

To produce the radially cracked fuel geometries, there were 6 cracks equally spaced cracks created per pellet and the crack penetration length was assumed to be at 70% of the fuel radius. Crack width for these geometries is measured at the pellet surface and reduces

towards the center with a constant solid angle. The circumferential cracks were centered at 2/3 of the fuel radius and extend azimuthally through the entire pellet.

THERMAL PROPERTIES

Thermal conductivities of the materials considered are summarized in Table 15. The temperature-dependent thermal conductivities for the helium and lead-bismuth eutectic are applied to both the fuel-cladding gap and the crack area in their respective simulations. The fuel and the cladding materials were assigned temperature-independent conductivities to reflect UO_2 and Zircaloy respectively, and their conductivities were held constant to better resolve small temperature changes from the cracks.

Table 15. Fuel Rod Material Thermal Conductivities

Material	Thermal Conductivity, $k\left(\frac{W}{m-K}\right)$
LBE[1]	$3.61 + 1.517E\text{-}2 \cdot T - 1.741E\text{-}6 \cdot T^2$
He[2]	$2.639E\text{-}3 \cdot T^{0.7085}$
UO_2	3.5
Zry	17.3

[1](OECD Nuclear Energy Agency Nuclear Science Committee, 2007) [2](Hagrman et al., 1995)

OPERATING CONDITIONS

For these simulations, simple reactor operating conditions were applied. The linear heat rate of the fuel is increased from 0 to 25kW/m over 80000s and then held constant for another 20000s. A temperature of 350°C was applied to the outside of the cladding as the boundary condition.

RESULTS
FINITE ELEMENT RESULTS

The fuel centerline temperatures generated using BISON are shown in Figure **85** and are organized based on the gap material. These temperatures are evaluated at the end of the simulation. This plot shows that for both types of cracks, the fuel centerline temperature decreases.

In the circumferentially cracked fuel, this decrease in temperature is partly due to the increase in the fuel diameter and the subsequent decrease in the gap thickness allowing for better heat transfer to the cladding. In the radially cracked fuel, the temperature decrease is driven by both the decrease in gap thickness (similar to the circumferentially cracked fuel) and radial heat conduction across the cracks.

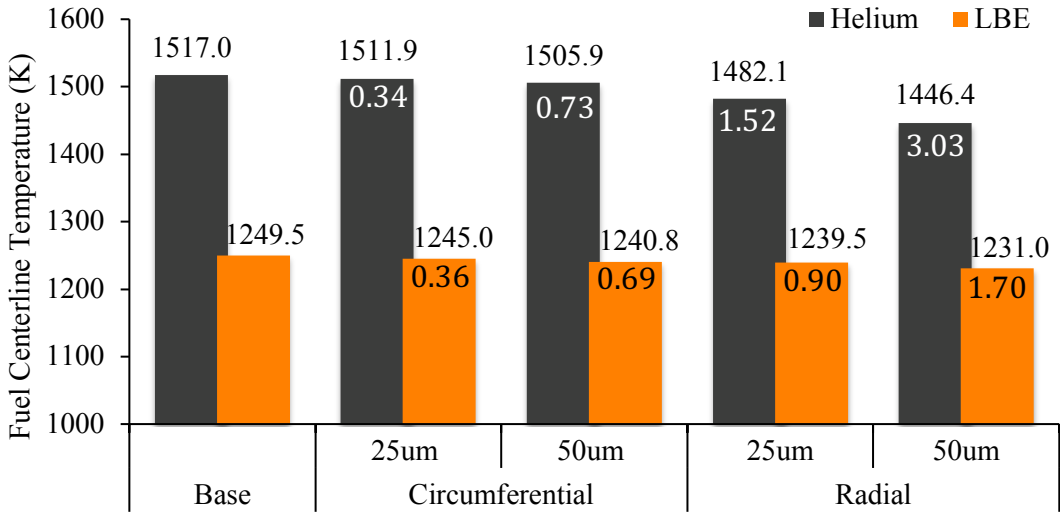

Figure 85. Comparison of fuel centerlines between helium and LBE filled fuel rods organized by crack type.

Figure 86 compares the azimuthal temperature profile across the outer surface of a fuel pellet for the uncracked and radially cracked cases and shows a 2-D temperature map for the 50µm crack width case for both gap materials. This plot shows that for the LBE filled rod, because the LBE conducts heat better than the fuel, the crack cools the center of the fuel and heats the periphery locally. In contrast, for the case of helium filled rod, the helium in the gap adjacent to the crack has a lower temperature. This is because the helium has lower thermal conductivity than the fuel and a smaller heat flux is supplied via the gas-filled crack to the periphery of the fuel. This is important; it shows that the radial cracks in helium filled rods can actually increase the fuel temperature. However, the increase in fuel radius using this simplified model to preserve the fuel volume when cracks are introduced, reduces the temperature drop across the gas-filled gap and cools the fuel. One might attribute an equivalent effect to fuel relocation once cracks develop in the pellet as a result of operation. This effect is compared with the circumferentially cracked fuel pellet case later in this document.

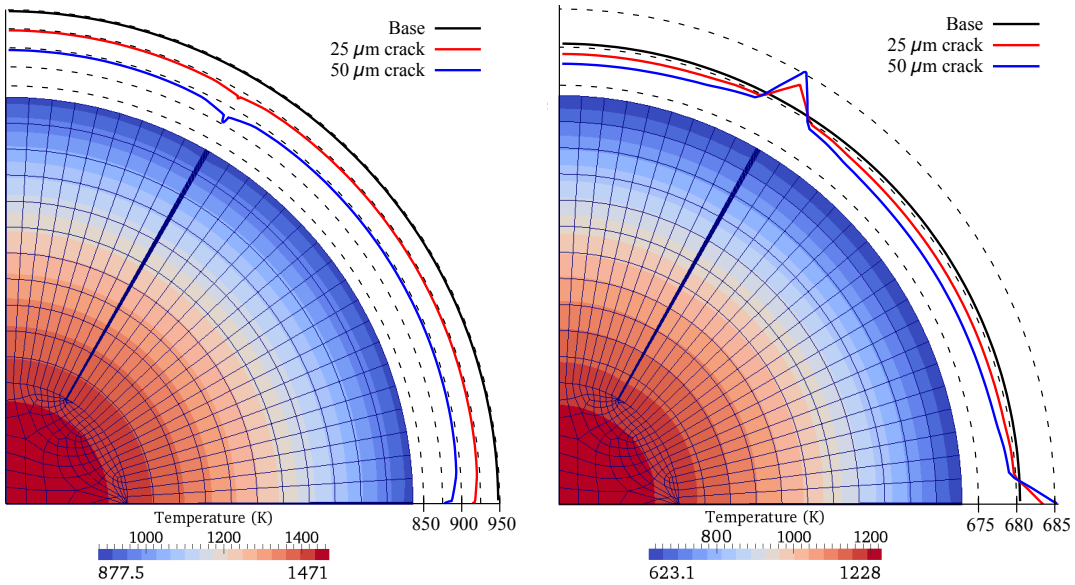

Figure 86. Plot of the azimuthal temperature profile across the outer fuel surface for radially cracked and uncracked fuel and 2-D temperature map of 50μm radial cracks for helium (left) and LBE (right) filled gaps (all temperatures in K).

Plots of the radial temperature profiles for the radially cracked fuel of both gap materials are shown in Figure 87. The temperature profiles are plotted as a function of radius at a location midway between two radial cracks. The temperature profiles for the helium filled cases show a constant shape, offset by the difference in the temperature drop inside of the gap. This shows that much of the temperature change in this case is driven by the change in the fuel radius and the corresponding change in the gap thickness, instead of any changes due to radial heat conduction across the crack. This should be expected due to the poor thermal conductivity of the helium as compared to the UO_2 fuel. The temperature profiles across the LBE-filled rods, however, show that the cracks cause a decrease in temperature at the fuel center and a slight increase in temperature at the fuel periphery. Essentially, the high heat flux through the radial cracks cools the fuel centerline and heats the outside of the fuel.

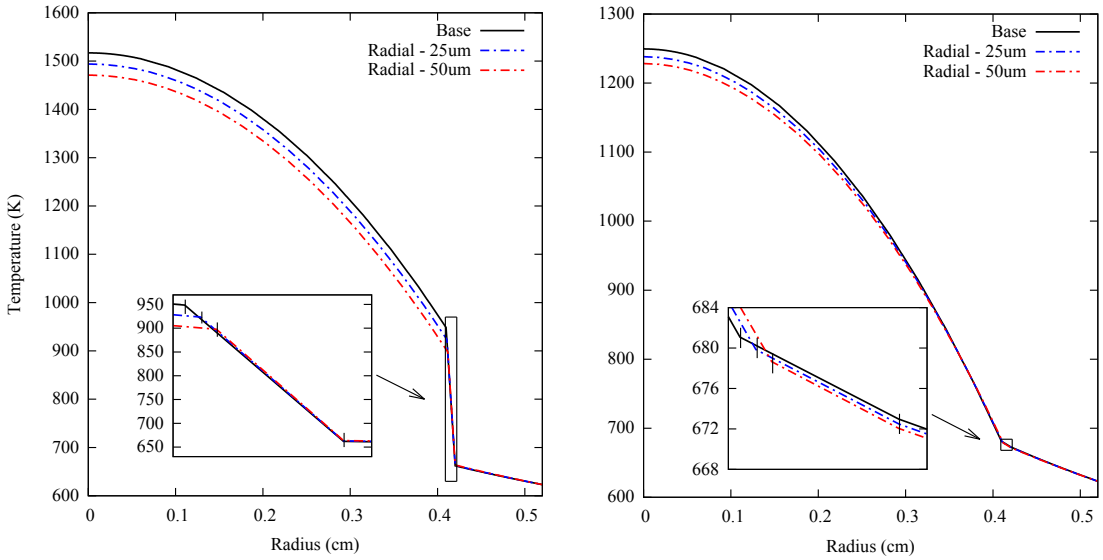

Figure 87. Temperature profiles for radially-cracked fuel with helium (left) and LBE (right) filled gap.

The temperature profiles for the circumferential cracks are shown in Figure 88 and Figure 89. The addition of circumferential cracks of a certain thickness is accompanied by an equivalent reduction in the gap width. Therefore, it is as if the thermal resistance across the original pellet cladding gap was split into two and added as separate resistances across the circumferential crack and the remaining pellet-cladding gap. The edges of the cracks are marked in black in the magnified region of the plots in Figure 89. This plot shows the dramatic temperature jump caused by the circumferential cracks in helium filled rods, and a much smaller temperature jump in case of LBE.

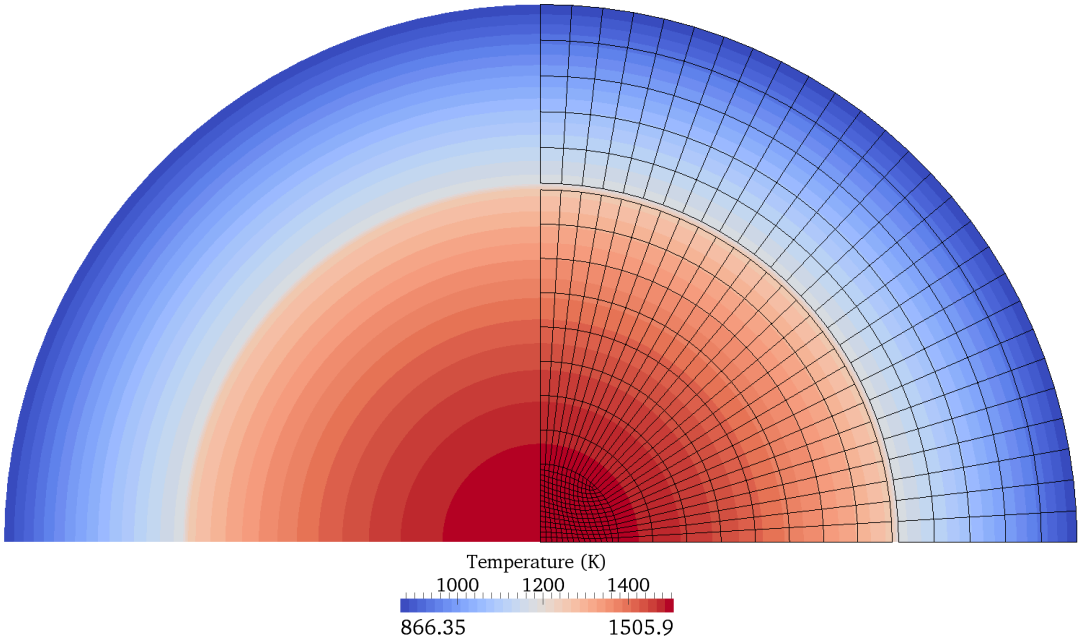

Figure 88. 2-D temperature map for 50μm circumferentially cracked fuel with helium filled cracks showing the fuel and crack mesh (Note: cladding is not shown).

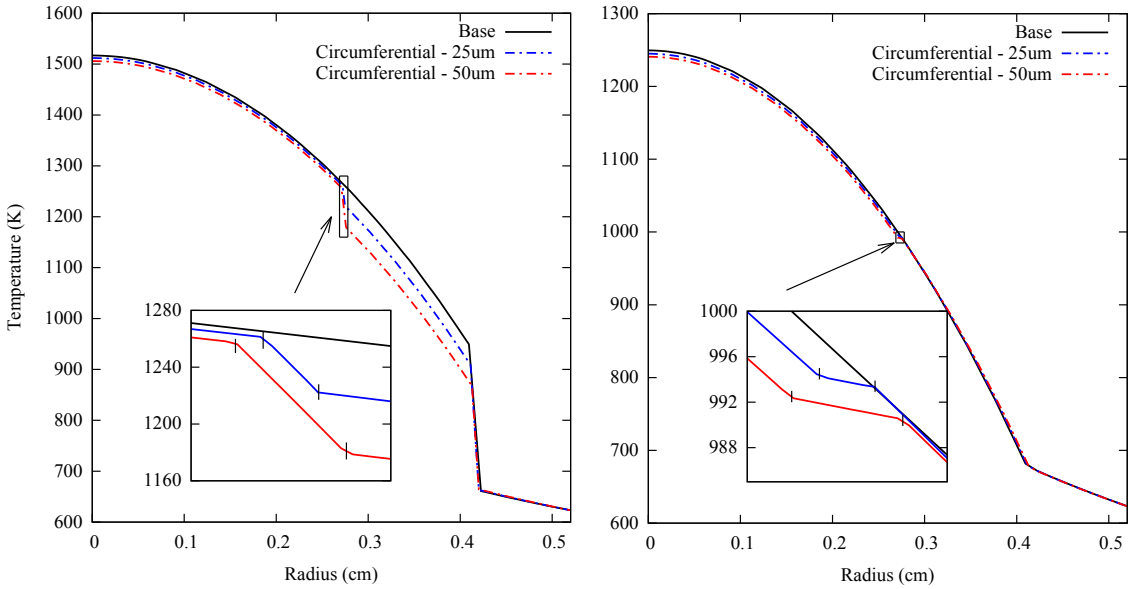

Figure 89. Temperature profiles for circumferentially-cracked fuel with helium (left) and LBE (right) filled gap.

As mentioned earlier, the fuel centerline temperatures are lower for radially cracked geometries than the corresponding circumferentially cracked geometries, even though the fuel radii are increased less for the radial cracks. In case of He-filled gaps, the circumferentially cracked geometries have to conduct the heat radially across the crack and the gap that roughly add up to the same thermal resistance as the case of crack free pellet.

However, although He-filled radial cracks do not contribute significantly to heat transfer, the reduction in the gap thickness to preserve the fuel volume significantly reduces the fuel centerline temperature. The same logic as for the He-filled circumferential cracks can be applied for the LBE-filled counterparts. However, in case of LBE-filled radial cracks, the reduction in pellet-gap thickness only slightly reduces the fuel centerline temperature, while the ability of high thermal conductivity crack to facilitate a high heat flux away from the center of the pellet is more pronounced.

1D ANALYTICAL RESULTS

These simulation results have also been compared to results from 1-D analytical heat transfer calculations for consistency. The thermal conductivities used for the following calculations are in Table 16 and the dimensions are the same as those used in the BISON calculations (Table 13) and are adjusted to conserve fuel volume. Thermal conductivities used in the analytical calculations were selected in order to simplify the calculation and are evaluated at relevant temperatures.

Table 16. Fuel Rod Material Constant Thermal Conductivities

Material	Thermal Conductivity, $k\left(\frac{W}{m-K}\right)$
LBE	13.4
He	0.328
UO_2	3.5
Zry	17.3

The fuel centerline temperature for uncracked fuel can be calculated by considering heat conduction radially through the fuel rod as a network of thermal resistances. The network is composed of the individual thermal resistances of each body combined together (**Eq.1**), comparable to Ohm's Law of electrical resistors in series. This analogy to current flow in a circuit allows the temperature change across the rod to be calculated as (Todreas and Kazimi, 2012):

$$T_{cl} = \frac{LHR}{2\pi}\left(\frac{1}{2k_{fuel}} + \frac{\ln\left(\frac{r_{c,i}}{r_f}\right)}{k_{gap}} + \frac{\ln\left(\frac{r_{c,o}}{r_{c,i}}\right)}{k_{clad}}\right) + T_{surf} \quad (1)$$

where LHR is the linear heat rate (W/m), k is the thermal conductivity (W/m-K) for the materials, T_{surf} is the cladding outer surface temperature (K), and r is the radius for the fuel and cladding inner and outer surfaces (m).

The centerline temperature for radially cracked fuel can be calculated similarly by implementing the radial cracks as a parallel thermal resistance with the fuel. The cracks are given the thermal conductivity of the gap, and both thermal conductivities are scaled by their solid angle. This approach includes the crack region in the heat generation calculation, but because the combined area of the cracks is so small compared to the area of the fuel this contribution is deemed negligible. The result is equation **(2)**:

$$T_{cl} = \frac{LHR}{2\pi}\left(\frac{1}{2\left((1-\chi)k_{fuel}+\chi\, k_{gap}\right)} + \frac{\ln\left(\frac{r_{c,i}}{r_f}\right)}{k_{gap}} + \frac{\ln\left(\frac{r_{c,o}}{r_{c,i}}\right)}{k_{clad}}\right) + T_{surf} \quad (2)$$

where χ is the fraction of the solid angle that the cracks occupy.

For the fuel with circumferential cracks a similar approach was taken. The fuel centerline temperature was determined by combining the contributions from the inner region of the fuel, the circumferential crack, the outer region of the fuel, the gap, and the cladding. The difference here was the addition of new crack and fuel regions to the thermal resistances, and the scaling of the linear heat rate in the inner regions. The linear heat rate is scaled in the inner fuel region and the circumferential crack region based on the heat generation in the inner region of the fuel, assuming a uniform heat generation rate. This was used in order to resolve effects from two separate heat generation contributions from the separate fuel regions. Using this, the centerline temperature for the circumferentially cracked fuel can be calculated as:

$$\mathrm{T_{cl}} = \frac{\mathrm{LHR}}{2\pi}\left(\frac{\mathrm{A_f}}{2\mathrm{k_{fuel}}} + \frac{\mathrm{A_f}\ln\left(\frac{\mathrm{r_{cr,o}}}{\mathrm{r_{cr,i}}}\right)}{\mathrm{k_{gap}}} + \frac{\left[1-\left(\frac{\mathrm{r_{cr,o}}}{\mathrm{r_f}}\right)^2\right]}{2\mathrm{k_{fuel}}} + \frac{\ln\left(\frac{\mathrm{r_{c,i}}}{\mathrm{r_f}}\right)}{\mathrm{k_{gap}}} + \frac{\ln\left(\frac{\mathrm{r_{c,o}}}{\mathrm{r_{c,i}}}\right)}{\mathrm{k_{clad}}}\right) + \mathrm{T_{surf}} \quad (3)$$

Where $r_{cr,i}$ and $r_{cr,o}$ are the inner and outer radii of the circumferential crack and A_f is the fraction of area occupied by the inner fuel region:

$$\mathrm{A_f} = \frac{\mathrm{r_{cr,i}^2}}{\mathrm{r_f^2} - (\mathrm{r_{cr,o}^2} - \mathrm{r_{cr,i}^2})} \quad (4)$$

The comparison between these calculated values and the values from BISON are shown in Table 17, and seem to agree reasonably well. The main differences between the two approaches are the gap conductivity model that BISON uses and the thermal conductivities used. These analytical calculations use only heat conduction to model the heat transfer in the gap region and the thermal conductivities are evaluated at approximate temperatures.

Table 17. Comparison Between Calculated and BISON fuel Centerline Temperatures

Gap Material	Crack Type	Width	Calculated Temperature (K)	BISON Temperature (K)	% Difference
He	Uncracked		1533.1	1517.0	1.05%
	Circumferential	25um	1529.1	1511.9	1.13%
		50um	1524.6	1505.9	1.23%
	Radial	25um	1504.1	1494.0	0.67%
		50um	1475.2	1471.1	0.28%
LM	Uncracked		1247.8	1249.5	0.13%
	Circumferential	25um	1244.1	1245.0	0.07%
		50um	1240.3	1240.8	0.04%
	Radial	25um	1237.9	1238.2	0.03%
		50um	1228.2	1228.3	0.01%

CONCLUSIONS

The fuel performance code BISON was used to examine the temperature effect due to cracks in fuel. This study shows that radial cracks in fuel have the most dramatic effect on fuel temperature, especially when the gap material has a low thermal conductivity and cracks lead to relocation of the pellet. For the purposes of IFA-744 experiment, it is shown that thin LBE-filled radial and circumferential cracks will reduce the fuel centerline temperature by ~1%.

In order to further quantify the effects of cracking on fuel temperatures, a more comprehensive study could be performed to determine the effects from the number, size, and length of radial cracks, and the width and position of the circumferential cracks. Additionally, networks of radial and circumferential cracks may be simultaneously examined.

ACKNOWLEDGEMENTS

Comments and useful discussions were provided by Wolfgang Wiesenack at Halden Reactor Project and Suresh Yagnik at Electric Power Research Institute. The work presented in this paper was supported by the Consortium for Advanced Simulation of Light Water Reactors (www.casl.gov), an Energy Innovation Hub for Modeling and Simulation of Nuclear Reactors under U.S. Department of Energy Contract No. DE-AC05-00OR22725. This material is based upon work supported under an Integrated University Program Graduate Fellowship.

APPENDIX B – Integral Fuel Rod Experiment Evaluation (IFA-796)

To continue the process of characterizing candidate accident tolerant fuel materials, irradiation testing, using an instrumented fuel assembly (IFA-796), has been scheduled in the Halden Boiling Water Reactor. The IFA-796 test is designed to irradiate six fuel rod positions, to be filled with a combination of fuel rods and fuel rod segments, consisting of various accident tolerant fuel cladding concepts. In order to support ongoing experimental characterization of FeCrAl cladding behavior, fuel performance simulations have been performed for relevant FeCrAl cladded fuel rods under anticipated reactor conditions.

This milestone report consists of two separate analyses. The first analysis consists of fuel performance simulations of IFA-796 rod 4 and two segments of rod 3. These simulations utilize previously implemented material models for the C35M FeCrAl alloy and UO_2 to provide a bounding behavior analysis corresponding to variation of the initial fuel cladding gap thickness within the fuel rod. The second analysis is an assessment of the fuel and cladding stress states after modification of the fuel creep model that is currently implemented in the BISON fuel performance code. This is performed to more accurately determine the mechanical response of the fuel and cladding after pellet-cladding mechanical interaction (PCMI) occurs.

MODELING APPROACH

We have used the BISON fuel performance code to simulate the FeCrAl cladded fuel rod and fuel rod segments in IFA-796 (Williamson et al., 2012). This fuel assembly is expected to contain three separate specimens with FeCrAl cladding. The first two specimens are segments of a fuel rod loaded at different axial positions in the Rod 3 location of the IFA-796 test rig. The third specimen is a full-size test rod spanning all four available segment locations in the Rod 4 location. A range of values for cladding thickness and fuel radius are assumed based on the measured variability of the cladding wall thickness across its periphery and the radius of the fuel pellets as manufactured. The values used for these simulations are organized to provide bounding behavior if the fuel rod was manufactured to have the largest possible gap thickness, the smallest possible gap thickness, and an average gap thickness. The fuel rod geometry specifications gathered from personal correspondence and an IFA-796 characterization report (Terrani et al., 2016b) are shown in Table 18.

Table 18. IFA-796 Fuel Rod Geometry

Simulation	Fuel Radius (μm)	Gap thickness (μm)	Cladding Thickness (μm)	Fuel Rod Outer Diameter (mm)	Fuel Stack Height (cm)	Cladding Length (cm)
Rod 4 - Max Gap	4335	65	371	9.542		
Rod 4 - Avg Gap	4338.5	54.5	381	9.548	50	60
Rod 4 - Min Gap	4342	44	391	9.554		
Rod 3 - Max Gap	4335	65	371	9.542		
Rod 3 - Avg Gap	4338.5	54.5	381	9.548	13.3	16
Rod 3 - Min Gap	4342	44	391	9.554		

To model the C36M3 FeCrAl cladding and UO_2 fuel, these simulations use several previously developed materials models currently implemented in BISON (Gamble et al., 2017). The cladding models used include: C35M Elastic modulus and poisons ratio (Thompson et al., 2015), Kanthal APMT thermal expansion (Kanthal), C35M thermal creep (Terrani and Yamamoto, 2016), and irradiation creep and swelling (Sweet et al., 2018). Material properties used to simulate UO_2, including thermal and mechanical behavior models, fission gas release, fission product swelling, and fuel pellet relocation, are included in BISON and documented by Hales et al. (Hales et al., 2014). These simulations use frictionless mechanical contact, which may influence the axial elongation of the cladding after mechanical contact has occurred.

The fuel rods are simulated under a constant linear heat rate of 20 kW/m, although the original linear heat rate target was nearly 25 kW/m, and use a flat axial power profile. This experiment targets a final fuel burnup of ~ 40 MWd/kgU, the fuel rods are simulated to a fuel average burnup of 60 MWd/kgU.

The IFA-796 irradiation rig is connected to a test loop designed to utilize prototypic PWR conditions. The reactor operating parameters are summarized in Table 19. A simple coolant temperature profile is applied along rod 4; the different sections of rod 3 use a temperature profile based on their axial location.

Table 19. IFA-796 fuel parameters and PWR loop conditions

Quantity	Value
Coolant Pressure	15.5 MPa
Coolant Temperature	Inlet: 568K Outlet: 593K
Initial Plenum Pressure	1 MPa
Fuel Density	95% T.D.
Average Fuel Grain Size	10 μm
UO_2 Fuel Enrichment	5%

UO_2 Creep Model

The UO_2 creep model included in BISON is a modified version of the FCREEP combined thermal and irradiation creep model (eq. 1) described by Hagrman et al. (Hagrman et al., 1995). FCREEP is assessed in order to identify sensitivity of the cladding stress state to uncertainties in the fuel compliance, specifically the contribution from fission-induced creep. This model is defined as the summation of the three separate creep contributions shown in eq. 1; fission-enhanced thermal creep (first term), thermal creep (second term), and fission-induced creep (third term).

$$\dot{\varepsilon}_{total} = \frac{A_1+A_2\dot{F}}{(A_3+D)G^2}\sigma e^{\left(\frac{-Q_1}{RT}\right)} + \frac{A_4}{(A_6+D)}\sigma^{4.5}e^{\left(\frac{-Q_2}{RT}\right)} + A_7\dot{F}\sigma e^{\left(\frac{-Q_3}{RT}\right)} \quad (1)$$

Where the various A parameters, are fitting parameters, $\dot{F}$ is the fission rate (m^{-3}-s^{-1}), σ is the effective stress (Pa), the Q variables are creep activation energies (J-mol^{-1}), T is the temperature (K), R is the gas constant (J-K^{-1}-mol^{-1}), D is the percent of theoretical fuel density, and G is the grain size (μm). While there is an effect of the fuel stoichiometry on the creep activation energies (Q) for this model, only an oxide-to-metal ratio of 2 is considered. Values for the material constants are shown in Table 20.

Table 20. Tabulated constants for the fuel creep and modified fission-induced creep

Parameter	Value	Units
A_1	0.3919	μm^2-Pa^{-1}-s^{-1}
A_2	1.31e-19	μm^2-m^3-Pa^{-1}
A_3	-87.7	*dimensionless*
A_4	2.0391e-25	Pa$^{-4.5}$-s^{-1}
A_6	-90.5	*dimensionless*
A_7	3.72264e-35	m^3-Pa^{-1}
A_8	1.49977e-36	m^3-Pa^{-1}
Q_1	4.5294e4	J/mol
Q_2	6.6432e4	J/mol
Q_3	2.6167e-3	J/mol

The fission-induced creep contribution is generally thought to be athermal (Solomon et al., 1971), although there is some variability in reporting a temperature dependence (Dienst, 1977). This is especially important because the contribution from fission-induced creep dominates the total creep response approaching 1000˚C, where irradiation-enhanced creep becomes dominant.

In order to determine the differences from including athermal fission-induced creep in the creep rate calculation, the contribution in Eq. 1 was replaced by the athermal contribution from Solomon et al., shown in Equation 2. Figure 90 shows an example of the individual contributions in the combined thermal and irradiation creep model and eq. 2 for some

common fuel parameters.

$$\dot{\varepsilon}_{3,b} = A_8 \dot{F} \sigma \tag{2}$$

Where the A parameter is a fitting parameter, $\dot{F}$ is the fission rate (m^{-3}-s^{-1}), and σ is the effective stress (Pa).

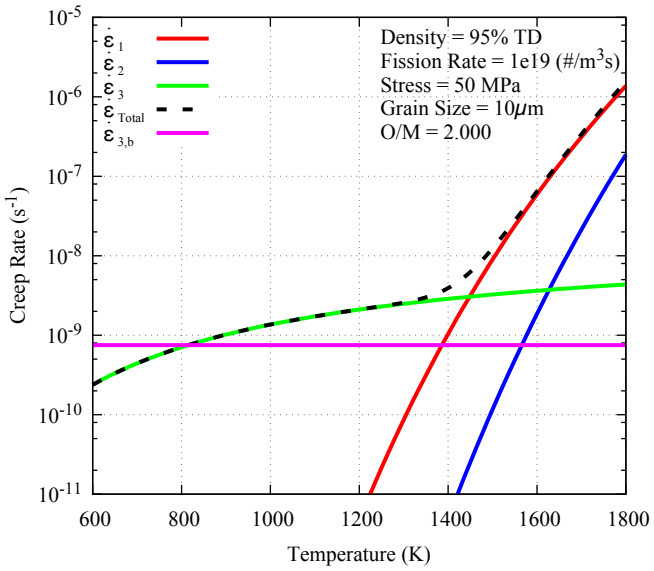

Figure 90. Plot of the individual contributions ($\dot{\varepsilon}_1, \dot{\varepsilon}_2, \dot{\varepsilon}_3$) to the total fuel creep rate ($\dot{\varepsilon}_{Total}$) in the model described by Hagrman (Hagrman et al., 1995) and a comparison with the athermal irradiation-induced fuel creep ($\dot{\varepsilon}_{3,b}$) contribution described by Solomon (Solomon et al., 1971).

For the analysis described in Sections 3.1 and 3.2, the modified fuel creep model described in this section is used. Section 3.3 shows the effect that making this modification has on the cladding radial deformation and hoop stress after pellet-cladding contact has occurred. Because BISON does not currently track the size evolution of individual fuel grains during the simulations, a static value for the grain size is assumed for the entire fuel stack. Section 3.3 also contains a short evaluation of this assumption by dividing the fuel stack into radial zones and prescribing a different grain size to each zone.

RESULTS AND DISCUSSION

The BISON fuel performance code was used to provide engineering analysis on the full-length rod 4 and the top-mid and bottom segments of rod 3 in the IFA-796 fuel assembly. The following results and discussion provide a systematic description of several relevant fuel rod performance indicators over the simulations including: the maximum fuel centerline temperature, cladding elongation, cladding radial deformation, maximum cladding hoop stress, fission gas release, and plenum pressure. Although the target

discharge burnup for these test rods is 40 MWd/kgU, the BISON simulations of the fuel performance of these rods has been extended to 60 MWd/kgU to show possible fuel rod behavior if the target burnup is surpassed. It is once again pertinent to indicate that frictionless contact has been modeled for all cases within this report, and this will impact the predictions of axial deformation after the fuel – cladding gap has closed. The target burnup is displayed in these plots using a grey vertical line.

Rod 3 – Top-mid Section

The top-mid segment of rod 3 was simulated to 60 MWd/kgU. The peak fuel centerline temperature for all three fuel rod geometries over the fuel utilization is shown in Figure 91. As the fuel rod is initially heated, a difference among the simulations can be observed based on the fuel rod gap thickness. The fuel centerline temperatures continue to increase, even as the UO_2 thermal conductivity degrades, despite solid fission product swelling and fuel relocation increasing the fuel pellet diameter. As the gap closes, heat transfer between the fuel and cladding improves, working to slow the increase in fuel temperatures until gap closure occurs. The onset of gap closure for the *Minimum Gap* simulation begins at ~35 MWd/kgU where the edge of the smeared pellet fuel stack expands to locally contact the cladding. At ~40 MWd/kgU gap closure in the simulation is fully established with the rest of the fuel column in contact with the FeCrAl cladding. This occurs for the *Average Gap* and *Maximum Gap* simulations as well, with the onset of gap closure occurring at ~42 MWd/kgU and ~50 MWd/kgU and fully established mechanical contact occurring at ~46 MWd/kgU and ~55 MWd/kgU, respectively. Because the fuel temperatures in these simulations are low (< 1300K), they release very small amounts of gaseous fission products to the to the fuel rod plenum; the gap conductivity remains relatively unaffected.

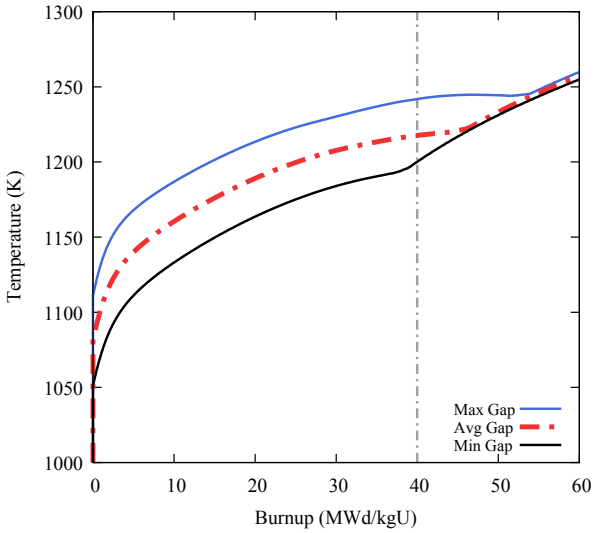

Figure 91. The peak fuel centerline temperatures for the top-mid section of fuel rod 3 show an expected difference based on the variation of the gap thickness among the simulations.

Figure 92 shows the cladding radial expansion and the cladding elongation over the simulated fuel utilization. As indicated in Figure 92a, the cladding radius initially increases (~14 μm) due to thermal expansion as the cladding is heated to the coolant temperature. After the cladding is heated, it expands slightly (< 2 μm) due to irradiation swelling. As mechanical contact occurs and the edge of the fuel pellet stack pushes on the cladding, the cladding begins to radially deform locally. Shortly after the onset of mechanical interaction has occurred, mechanical contact is fully established between the cladding wall and the fuel stack. As the fuel continues to radially expand, the axial elongation (shown in Figure 92b) due to irradiation swelling is offset. The initially cladding elongation is also due to thermal expansion as the cladding is heated from room temperature to reactor coolant temperature. During constant power operation, the cladding continues to expand due to isotropic irradiation swelling until mechanical contact is established. Here, the cladding is radially deformed, and the cladding axially contracts.

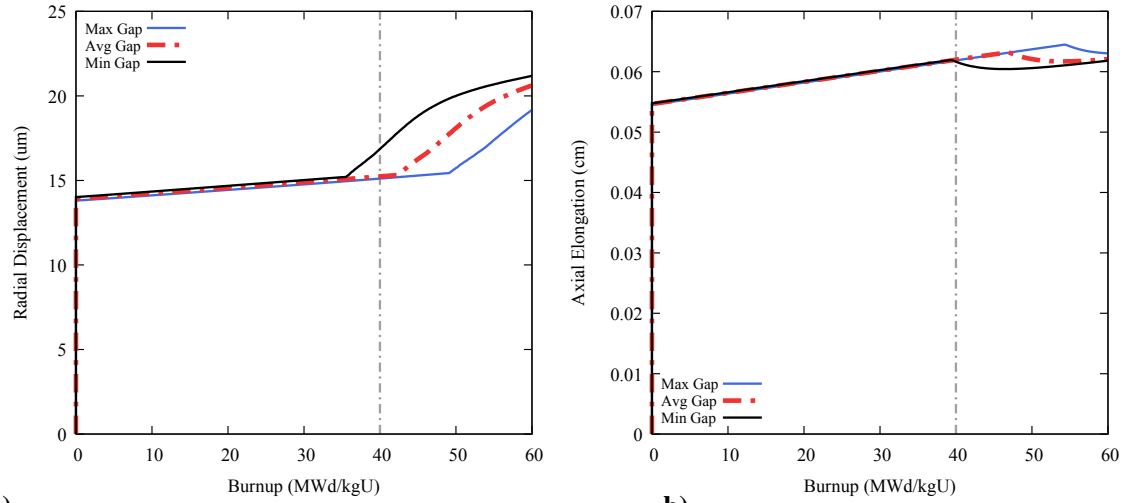

Figure 92. The maximum radial displacement (a) from these simulations is dominated by the initial thermal expansion until mechanical contact with the fuel begins to push the cladding radially. Likewise, axial elongation of the cladding (b) increases initially due to thermal expansion; however, as mechnical contact increases the fuel radial displacment, the elongation is decreased.

The maximum cladding hoop stress over the simulated fuel irradiation, shown in Figure 93, initially becomes compressive due to the large pressure differential between the coolant and fuel rod plenum. There is a slight difference among the hoop stresses in these simulations because of the difference in cladding geometries that results in a different onset burnup for gap closure. There is also a decrease in the hoop stress over time, attributable to the increasing radius due to isotropic irradiation swelling. After gap closure occurs, the hoop stress quickly becomes tensile as the fuel pushes radially on the cladding. Only the minimum gap simulation shows gap closure (~35 MWd/kgU) before the target burnup is reached.

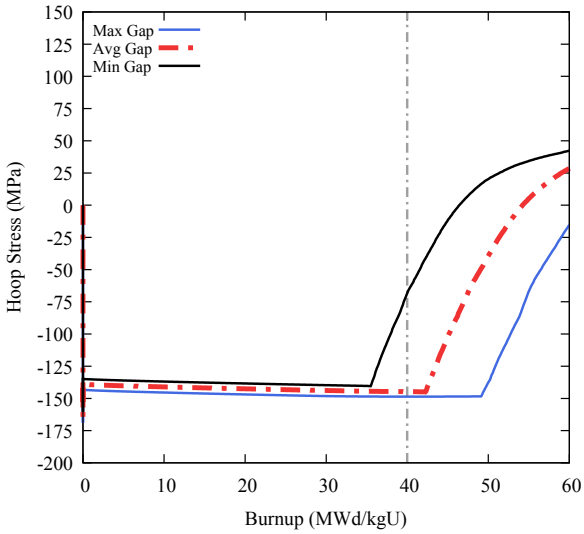

Figure 93. The maximum hoop stress in the cladding is initially compressive due to the pressure difference across the cladding from the coolant system and the fuel rod plenum. It remains compressive until mechanical contact occurs.

Figure 94 shows the calculated results for fission gas release and plenum pressure for rod 3. As indicated in Figure 94a, a relatively low amount of fission gas is released as expected from the low fuel temperatures (< 1300K). As well, the modeling predicts that the onset of fission gas release occurs late in the fuel lifetime, at burnup levels near the IFA-796 irradiation target. The low fuel temperatures expected from these fuel rods delays the onset of gas release and also facilitate a smaller amount of fission gas being released to the plenum over the irradiation (< 2% total fission gas production).

As the fuel rod is heated from room temperature to the reactor coolant temperature, the fuel rod plenum pressure (shown in Figure 94b) increases from 1 MPa to ~2.5 MPa. Fuel expansion due to fission product swelling and fuel relocation only increases the plenum pressure slightly up to ~35 MWd/kgU. Even though there is only a small amount of fission gas released to the plenum, there is an increase in pressure near the end of the simulation.

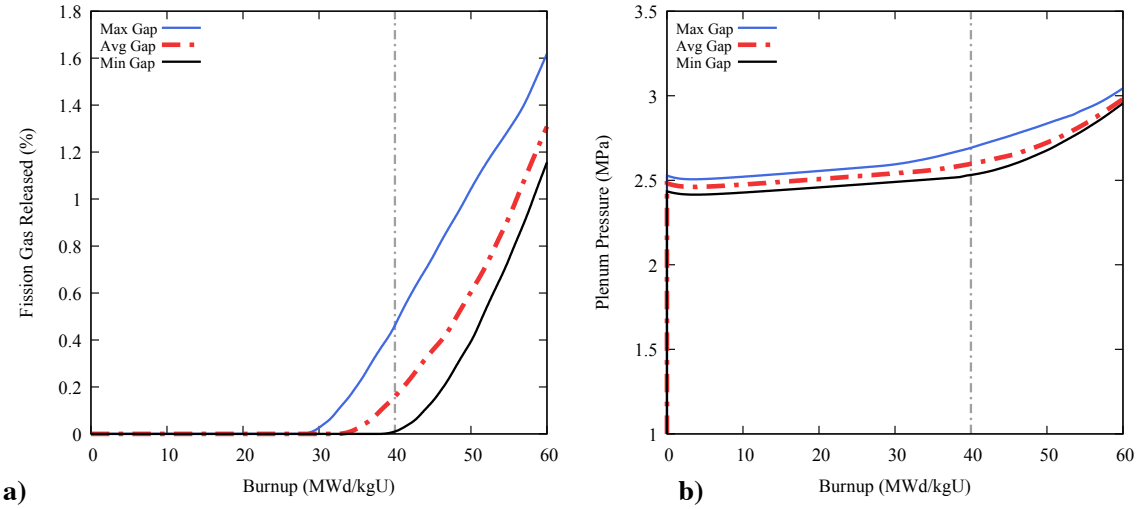

Figure 94. The onset of fission gas release to the fuel rod plenum (a) begins late in the simulation and the amount of gas released remains low (< 1.6%) for all three fuel rod geometries. As there is only a small amount of fission gas released, the fuel rod plenum pressure (b) is only slightly increased starting near the end of the simulations.

The results from these BISON simulations indicate a range of behavior that may be expected during the irradiation of the top-mid section of rod 3 in IFA-796 based on the fuel rod geometry. The *Avg Gap* simulations from the bottom and top-mid sections of fuel rod 3 are compared in order to identify differences in expected integral fuel rod behavior arising from an increase in the coolant temperature profile. For the top-mid section of rod 3, the coolant temperature profile ranges linearly from ~580K to ~587K. In order to simulate the bottom section, the temperature is decreased to 568K to ~574K. Because the temperature difference is so small (~12K), many of the performance aspects examined between the two fuel rod segments are nearly identical.

Figure 95a shows a comparison of the peak fuel centerline temperatures for the *Avg Gap* simulation of the rod 3 segments. The peak fuel centerline temperature for the Top-mid rod segment is consistently 10-15K higher that the temperatures in the Bottom segment. As such, thermally driven phenomena, such as fuel and cladding thermal expansion and fission gas release are slightly decreased. Figure 95b shows the maximum cladding hoop stress and gap closure behavior for these fuel rods is expected to be very similar.

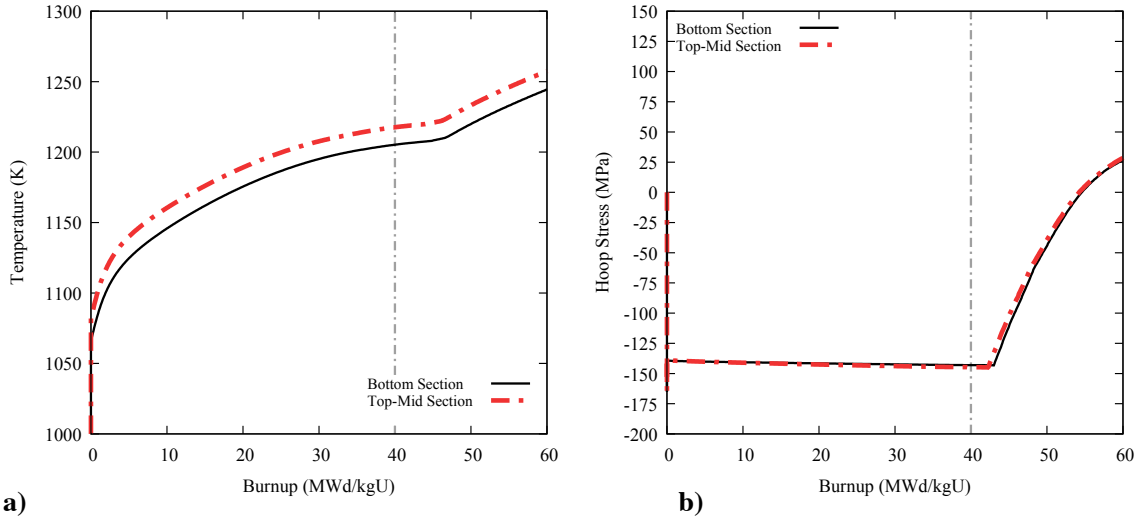

Figure 95. The maximum fuel centerline temperature (a) shows a slight difference between simulations due to the difference in coolant temperatures. The maximum cladding hoop stress (b) for both of the simulations look nearly identical, showing very similar expected mechanical performance for both fuel rod segments.

Rod 4

IFA-796 rod 4 is a full-length rod (60 cm), spanning 4 sections of the irradiation test rig. Much like the previously discussed results for the segments of rod 3, the fuel temperatures vary based on the fuel rod radial geometry. Initially, the fuel temperatures increase as the fuel power is ramped to 20 kW/m and held constant. Figure 96 shows the peak fuel centerline temperature for each of the Rod 4 simulations. For each successive simulation with a larger initial gap thickness, the fuel temperature is greater. The fuel rod gap behavior dominates the heat transfer between the fuel and the cladding until the gap is closed later in the simulations. During this time, the fuel radius changes due to thermal expansion, densification, fission product swelling, and relocation. Even as the fuel radius is changing however, the thermal conductivity of the fuel is continuously decreasing with increasing fuel utilization. This causes the peak fuel centerline temperature to increase even after gap closure has occurred. Because fuel radial geometry and linear heat rate are the same for rod 4 as the previously discussed rod 3 segments, the fuel centerline temperatures and gap closure times for each of the three simulations is similar.

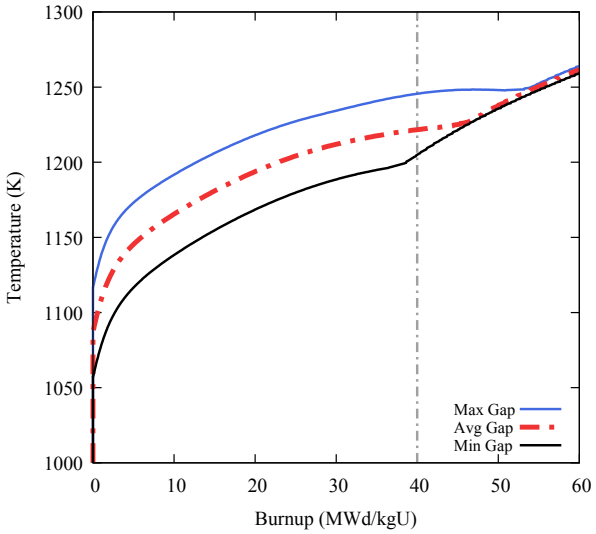

Figure 96. The peak fuel centerline temperature for the rod 4 simulations, as expected, is greater for fuel geometries with correspondingly larger initial gap thicknesses and shows a very similar progression to the rod 3 simulations.

The maximum cladding radial deformation, shown in Figure 97a, is also very similar to the simulations of rod 3 because of the same radial geometry. The cladding thermally expands as it is heated from room temperature to the coolant temperature. Isotropic irradiation swelling acts to further expand the cladding radius, albeit slowly, until mechanical contact occurs. As marked by the sharp increase in radial displacement, the onset of mechanical contact occurs for the *Min Gap, Avg Gap and Max Gap* simulations at ~35 MWd/kgU, 42 MWd/kgU, and 50 MWd/kgU respectively.

The cladding axial elongation, shown in Figure 97b, displays a similar profile to rod 3, however, because the cladding in rod 4 is longer, the magnitude of the elongation is greater. Again, the initial thermal expansion dominates the cladding axial elongation. The cladding axially expands due to irradiation swelling until mechanical contact occurs. After gap closure is fully established with the full fuel stack pushing on the cladding tube wall, the cladding length will be reduced with increasing radial deformation.

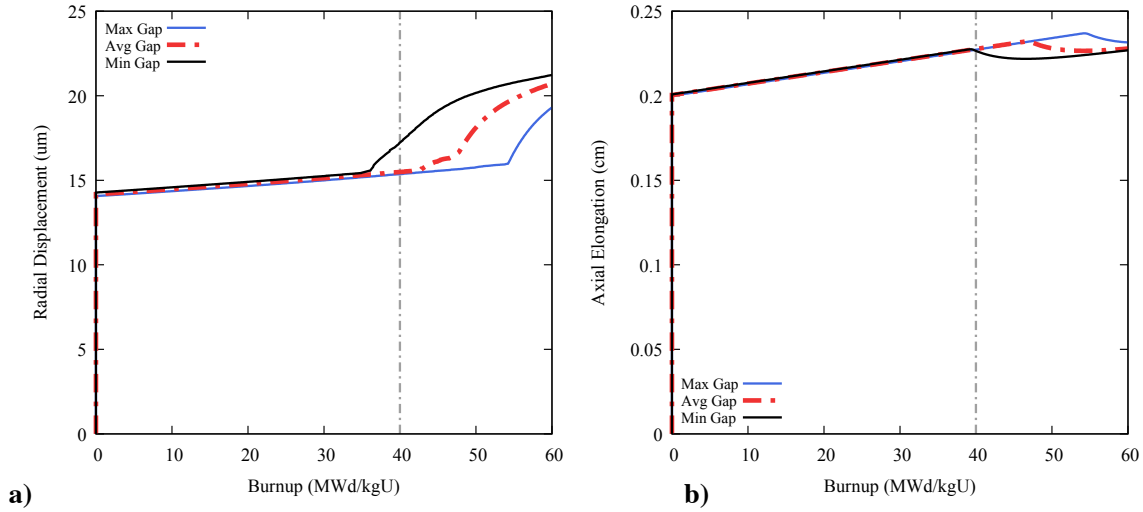

Figure 97. The maximum radial displacement (a) in the cladding initally increases due to thermal expansion. Isotropic irradiation swelling slightly expands the cladding radius until mechanical contact occurs. Thermal expansion is also responsible for the initial cladding elongaiton (b). Similiarly, the cladding expands due to irradiation swelling until mechanical contact occurs and the radial expansion decreases the elongation.

The maximum value of the cladding hoop stress (Figure 98) initially becomes compressive as the coolant system pressure is much larger than the fuel rod plenum pressure. As reactor operation continues, the cladding hoop stress remains compressive until fuel cladding mechanical contact occurs. After mechanical contact is established, the maximum cladding hoop stress quickly begins to increase, even becoming tensile by 60 MWd/kgU in the *Avg* and *Min Gap* simulations. Of course, much of this behavior is well beyond the 40 MWd/kgU target fuel burnup for this irradiation.

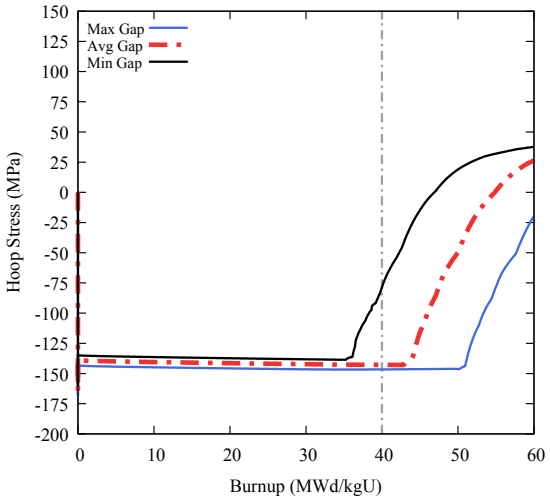

Figure 98. The hoop stress in the cladding initially becomes compressive due to the pressure difference between the fuel rod plenum and the coolant system. After mechanical contact occurs, the hoop stress quickly becomes tensile, and eventually saturates due to the stress sensitivity of the fuel creep model.

The percentage of fission gas released from the fuel is shown in Figure 99a. As indicated in the figure and discussed previously, very little fission gas release is expected in these fuel rods due to the low fuel temperatures. This means fission gas release will have a very small impact on the fuel rod plenum pressure (Figure 99b) and will not contribute much to gap conductivity degradation. Because of the low fuel temperatures, the onset of fission gas release will also occur late in the fuel life, near the target burnup for IFA-796.

Figure 99b shows the fuel rod plenum pressure over the expected fuel utilization. The plenum pressure increases and the fuel, cladding, and rod fill gas heat to operating temperature. After this, the plenum pressure increases slightly as the plenum volume is decreased from fuel expansion. Starting near 40 MWd/kgU and continuing to the end of the simulation, there is a slight pressure increase from the fission gas released to the plenum.

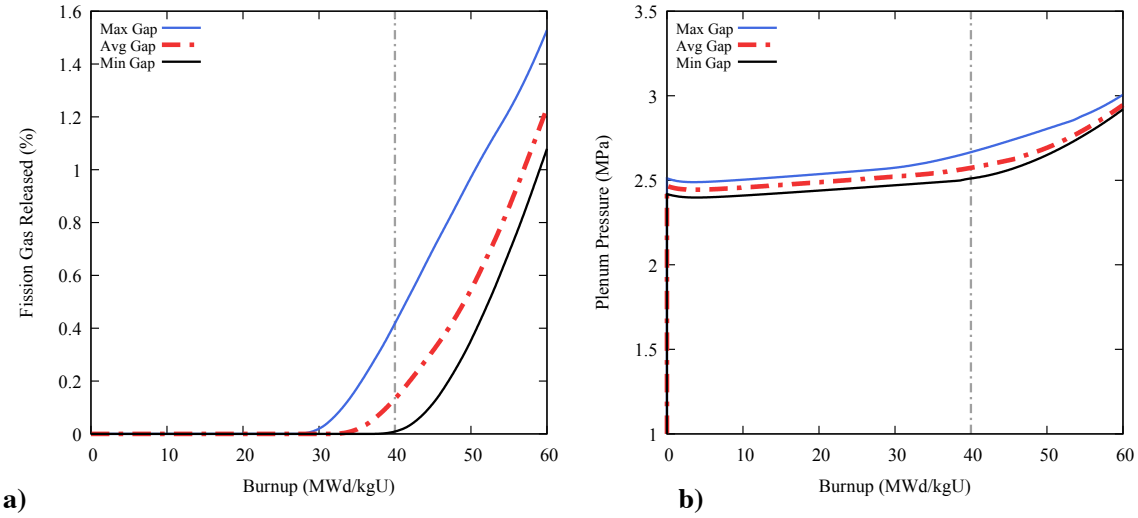

Figure 99. Due to the low (< 1300 K) fuel temperatures, the onset of fission gas release (a) is expected to occur near the IFA-796 target burnup, and the total amount of fission gas released is expected to be less than 1.6%. The fuel rod plenum pressure increases from 1 MPa to ~ 2.5 MPa as the fuel rod is initially heated. Fuel expansion gradually decreases the plenum volume, thereby increasing the plenum pressure, until fission gas is released from the fuel.

Rod 4 – Fuel Creep Analysis

For this scoping analysis, the performance impact of modifying the fuel creep model on the average gap thickness simulation using rod 4 geometry is identified.

Figure 100 shows the maximum cladding radial displacement (a) and cladding hoop stress (b) for the *Avg Gap* simulation of IFA-796 rod 4, and compares the original fuel creep model and the modified fuel creep model. As mentioned previously, the only difference between these fuel creep models is the contribution of the fission-induced creep term. There is no noticeable change in the cladding behavior before mechanical contact has occurred. There is a slight increase in the radial displacement after the fuel comes into contact with cladding, as the fuel is actually less compliant after modifying the creep model. Using the modified fuel creep models, the fuel deforms less due to mechanical contact, expanding the cladding further than the original model and generating somewhat higher hoop stresses in the cladding. More work is set to be performed to benchmark this model in order to correctly determine cladding behavior after mechanical contact has occurred.

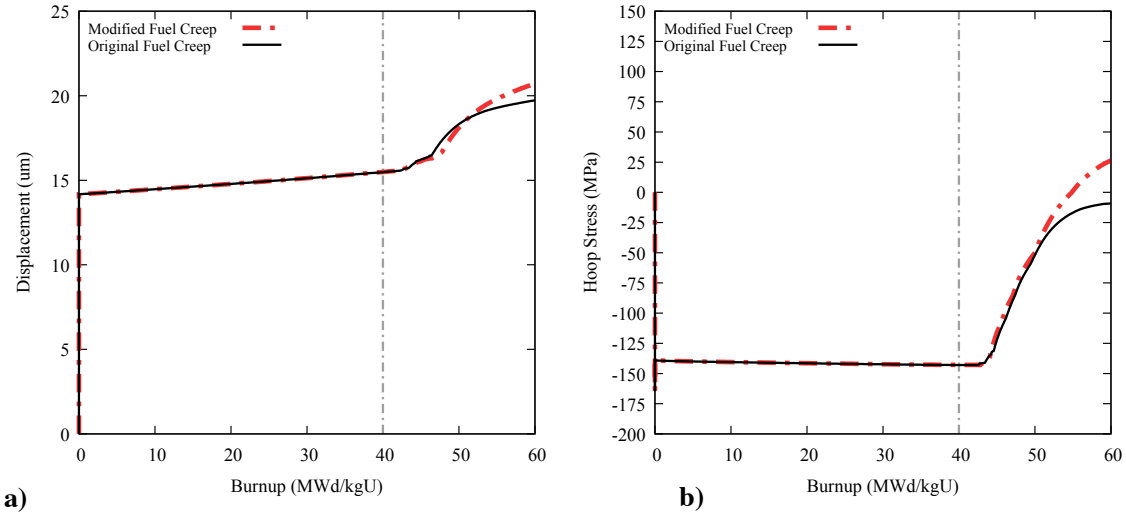

Figure 100. By modifying the fission-induced creep contribution in the fuel, the maximum cladding radial displacement (a) and maximum cladding hoop stress (b) are increased compared to the original fission-induced creep contribution after mechanical contact has occurred at ~ 42 MWd/kgU.

Next, the effect grain size within the fuel creep model was analyzed for rod 4. Because it is currently impractical to track individual grain evolution in a continuum-scale fuel performance code, BISON uses a static value for the grain size in fuel creep calculations. This short analysis applied a simple linear grain size profile to the Rod 4 fuel geometry. To perform this, the fuel is divided into four concentric zones, where each has a different grain diameter. A radial slice from the axisymmetric fuel rod mesh is shown in Figure 101. Starting from the innermost zone and proceeding toward the fuel periphery the grain diameters for each zone are: 10µm, 7.33 µm, 4.66 µm, and 2 µm. The values from this simplified profile are chosen to determine the effect of grain subdivision approaching the periphery of the fuel pellet. Grain growth here is neglected because, according to Ainscough et al., the 10 µm grain size should be very near the limiting grain size for these temperatures (Ainscough et al., 1973).

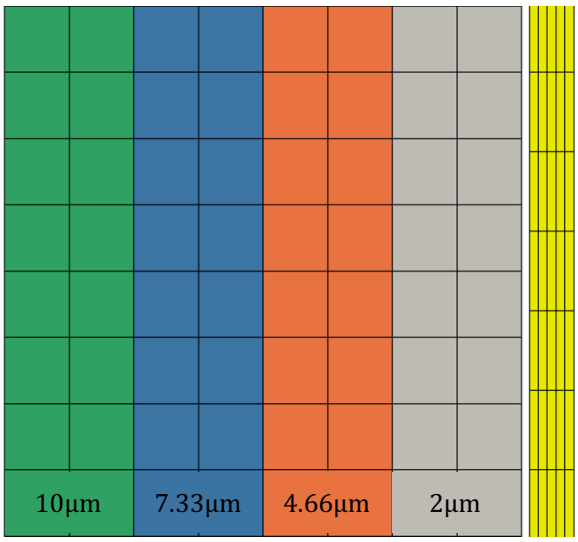

Figure 101. This axial segment of the axisymmetric fuel rod mesh shows the four regions of the UO_2 fuel and the FeCrAl cladding which are considered in this analysis. Starting from the center (green) and progressing toward the FeCrAl cladding (yellow) all four fuel zones has a progressively smaller grain size.

The resulting cladding hoop stress profiles for these simulations, shown in Figure 102, show similar results even when including this modification to the fuel geometry. This shows that the magnitude of the fuel creep calculated from modifying the first term in equation 1 (grain boundary sliding and vacancy diffusion) shows little to no effect on the fuel in these particular simulations and the corresponding experimental conditions. This highlights the importance of accurately determining the fission-induced creep contribution, as it dominates the total creep response under these anticipated low fuel temperatures (<1300K).

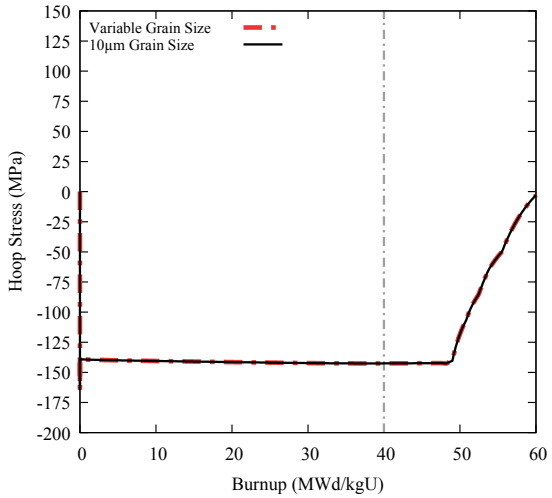

Figure 102. The maximum cladding hoop stress in these simulations remains unaffected by the differing grain sizes. This indicates that nearly the entire creep response is due to the contribution from fission-induced creep.

SUMMARY and CONCLUSIONS

Three FeCrAl cladded fuel rods from IFA-796 were simulated using the BISON fuel performance code. These simulations use models developed from available data on the C35M alloy and expected reactor operating conditions for the PWR test loop used in the experiment. Due to small variations in the fuel diameter and cladding thickness during manufacture, a range of values were used in the fuel rod geometry in these simulations. The analysis performed in Sections 3.1 and 3.2 show that the expected temperature during steady state operation for both rod 3 and rod 4 should This analysis also shows an almost negligible difference in the performance of the rod 3 segments based on the axial location.

Effects from modifying the fuel creep model were identified for the BISON simulations of the IFA-796 rod 4 experiment, but show that varying the creep model (within the range investigated here) only provide a minimal increase in the fuel radius and maximum cladding hoop stress. Continued investigation of fuel behavioral models will include benchmarking the modified fuel creep model against available experimental data, as well as an investigation of the role that fuel cracking will play in the compliance of the fuel. Correctly calculating stress evolution in the fuel is key to assessing fuel behavior up to gap closure and the subsequent deformation of the cladding due to PCMI. The inclusion of frictional contact should also be investigated to determine the axial elongation of the fuel rods for comparison with data from this experiment.

APPENDIX C – Oxidation Reaction Energy Deposition Model

In order to calculate the heat produced due to the cladding oxidation reaction, a model was developed which couples the oxygen weight gain to the heat production source term in the fuel performance code.

This model includes a number of simplifying assumptions, including that the oxide formation is purely stoichiometric, heat is dispersed over the entire cladding thickness, and that the cladding materials only react with H_2O.

For the FeCrAl cladding in particular, the contribution to the enthalpy change associated with the heat of formation for the FeCrAl alloy is neglected, such that a conservative bounding assumption is that only aluminum will undergo oxidation at high temperatures (>900K).

The same assumptions are used to evaluate the hydrogen production in the cladding. For the Zircaloy, the following reaction is considered:

$$Zr + H_2O \rightarrow ZrO_2 + H_2 + Q \quad \text{(1A)}$$

$$Al + H_2O \rightarrow Al_2O_3 + H_2 + Q \quad \text{(1B)}$$

From the mass of the metal oxide produced, the mass of metal consumed, the hydrogen gas produced, and the heat produced are all then determined using the reaction in Equation 1A and 1B, for Zircaloy and FeCrAl, respectively. To calculate the mass of the zirconium oxide, the oxidation weight gain and oxide density are used from the cladding model. The heat production for Zircaloy is taken from (Hagrman et al., 1995). For the FeCrAl cladding, because at high temperatures only alumina is expected to form, the reaction is only considered as shown in Equation 1B.

The heat produced and the mass of hydrogen produced in these models is summarized in Table 21. Because these reactions consider the intermediate dissolution of H_2O on the reaction energetics, these values are assumed to be somewhat conservative.

In order to apply these models, a simple test comparison is made to the work of Terrani and co-workers for zircaloy cladding (Terrani et al., 2014b) based on the decay heat production in 1173K steam. To simulate the impact of time after reactor shutdown on the decay and oxidation heat, a simple decay heat relation (El-Wakil, 1978) is used to calculate the linear heat rate in the fuel after different holding times.

Table 21. Values used in the heat production and hydrogen generation model

Cladding Type	Heat produced per kg metal (MJ/kg)	Hydrogen produced per kg metal (kg/kg)
Zircaloy	6.45	4.42e-2
FeCrAl	15.15	.1111

Figure 103 shows results from a comparison of the cladding temperature evolution as a function of tome in 1173 K steam for different reactor cool down periods, as compared to the work of and Terrani and co-workers for a PWR fuel geometry.

This model generally over predicts the initial cladding temperature increase, but the prediction of this model agrees well with Terrani for the time to initiate the autocatalytic reaction is for the 2, 8, and 24 hr, respectively. For the 72 hr simulation, the autocatalytic event is mitigated. This could arise because of the difference in the oxidation kinetics used; Terrani and coworkers use Cathcart (Cathcart et al., 1977), while this work uses Leistikow (Leistikow et al., 1983).

Figure 104 shows the application of the FeCrAl and Zircaloy cladding oxidation models to the BWR fuel geometries considered in this work. Again, the simulations have been performed assuming a 2,8, or 24-hour reactor cooling prior to the initiation of high temperature steam exposure. As expected, the FeCrAl models, which involve the formation of a passivating oxide layer, rapidly reach a saturation temperature that varies based on the difference in remaining decay heat generation. The Zircaloy cladding, however, experiences a similar temperature increase to the previous PWR analysis, rapidly increasing as the oxidation becomes the dominant source of heat production.

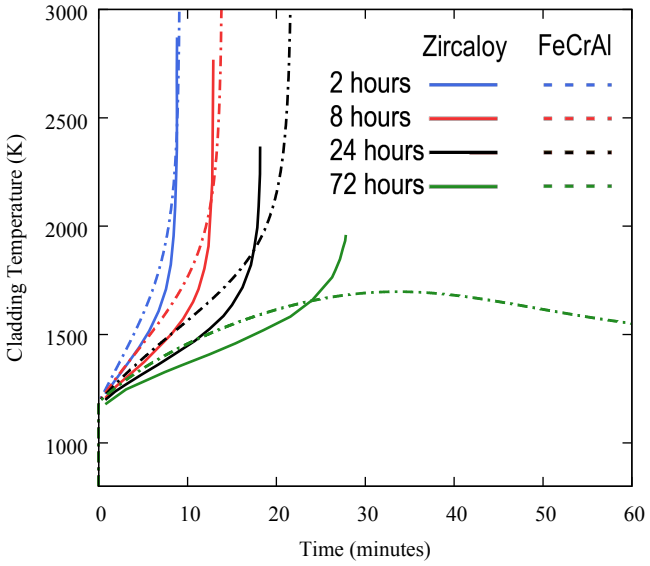

Figure 103. Comparison of the Zircaloy cladding temperature evolution due to decay heat and exothermic oxidation reactions between these results (dashed) versus Terrani and coworkers (solid) (Terrani et al., 2014b) based on the cooling period after the reactor scram of 2, 8, 24,or 72 hr.

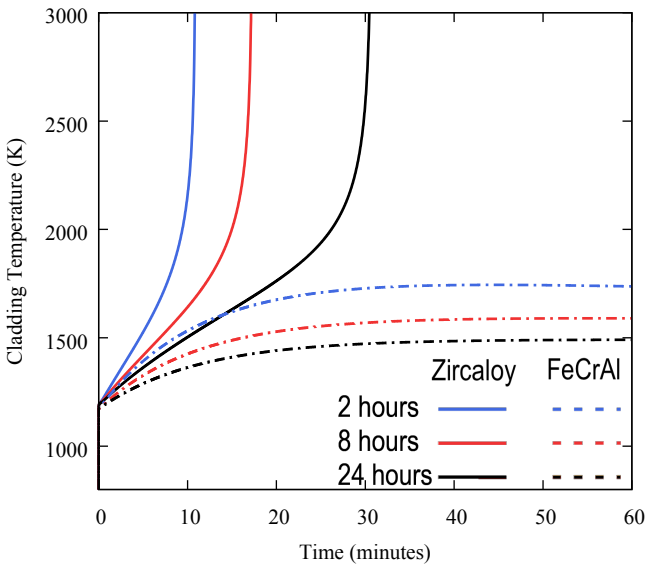

Figure 104. The cladding temperature evolution for the FeCrAl (dashed) versus Zircaloy (solid) cladding due to the decay heat and exothermic oxidation reaction based on 2, 8, or 24 hr cooling times after the reactor scram.

This scoping study was performed to provide a benchmark comparison and demonstrate that the energy deposition model could initiate the autocatalytic reaction of Zircaloy cladding.

VITA

Ryan Terrence Sweet was born in Port Orchard, Washington to Alan and Patricia Sweet on November 23rd, 1990. He has one older brother, Brendan. He graduated from White County High School in 2009, and attended The University of Tennessee in Knoxville, TN. He completed his Bachelor of Science in Nuclear Engineering in 2013. He began graduate school in Fall of 2013, working as a graduate research assistant under Professor Brian Wirth. From 2014 to 2017, he was the recipient of a Nuclear Engineering University Program Fellowship focusing on the fuel performance evaluation of iron-chromium-aluminum alloys as reactor fuel cladding. He completed his Doctor of Philosophy in Nuclear Engineering in 2018.